REPORT DOCUMENTATION PAGE

Form Approved
OMB No. 0704-0188

1. AGENCY USE ONLY *(Leave blank)*	2. REPORT DATE 22 May 97	3. REPORT TYPE AND DATES COVERED

4. TITLE AND SUBTITLE
COMBINED RADAR-RADIOMETER RAINFALL RETRIEVAL FOR TRMM
USING STRUCTURE FUNCTION-BASED OPTIMIZATION

5. FUNDING NUMBERS

6. AUTHOR(S)
MICHAEL R. FARRAR

7. PERFORMING ORGANIZATION NAME(S) AND ADDRESS(ES)
FLORIDA STATE UNIVERSITY COLLERGE OF ARTS AND SCIENCES

8. PERFORMING ORGANIZATION REPORT NUMBER

97-043

9. SPONSORING/MONITORING AGENCY NAME(S) AND ADDRESS(ES)
DEPARTMENT OF THE AIR FORCE
AFIT/CI
2950 P STREET
WRIGHT-PATTERSON AFB OH 45433-7765

10. SPONSORING/MONITORING AGENCY REPORT NUMBER

11. SUPPLEMENTARY NOTES

12a. DISTRIBUTION AVAILABILITY STATEMENT

DISTRIBUTION STATEMENT A

Approved for public release;
Distribution Unlimited

12b. DISTRIBUTION CODE

13. ABSTRACT *(Maximum 200 words)*

19970528 069

14. SUBJECT TERMS

15. NUMBER OF PAGES
190

16. PRICE CODE

17. SECURITY CLASSIFICATION OF REPORT	18. SECURITY CLASSIFICATION OF THIS PAGE	19. SECURITY CLASSIFICATION OF ABSTRACT	20. LIMITATION OF ABSTRACT

COMBINED RADAR-RADIOMETER RAINFALL RETRIEVAL FOR TRMM USING STRUCTURE FUNCTION-BASED OPTIMIZATION

Name: Michael R. Farrar
Department: Meteorology
Major Professor: Eric A. Smith
Degree: Ph. D.
Term Degree Awarded: Summer, 1997

ABSTRACT

The Tropical Rainfall Measuring Mission (TRMM) satellite, a joint US-Japanese mission to explore tropical rainfall and its effects on the earth's energy budget, general circulation, and climate, represents the first dual deployment of a precipitation radar and passive microwave radiometer on an earth-viewing satellite. While both radiometers and radars have been widely used *independently* to retrieve rainfall, previous attempts to combine the two types of measurements have mostly maintained independent treatment of the data, as these instruments are designed to measure precipitation based on different physical principles.

A method has been developed which objectively combines the measurements within the context of a unified radiative transfer equation (RTE) model, by treating the radar as a radiation source within the RTE model's source function. The retrieval method, referred to as "tall vector" inversion, uses a physical inversion scheme which initially searches a cloud-radiation database of profiles, produced by a 3-dimensional non-hydrostatic cloud model simulation of a tropical storm, to find first guess hydrometeor profiles whose brightness temperatures (TBs) and reflectivities (Zs) best match the radiometer and radar measurements as determined by a combined normalized error function. The first guess profiles, expressed in terms of structure functions, are modified within a

steepest descent optimization scheme, using the structure function coefficients as the optimization control variables, until the error function cannot be reduced. The solution hydrometeor profiles are then subjected to a set of gravity fallout equations to calculate the surface rainfall rates. Precipitation type is also diagnosed from an algorithm using TB threshold tests in conjunction with radar-derived bright band information.

As measurements from the TRMM sensors are not yet available, measurements from similar aircraft prototype instruments deployed for the TOGA-COARE field experiment are used in the evaluation of the algorithm. A statistical analysis of the TOGA-COARE retrieval results found that the optimization improved the average agreement between the measured and first guess TBs and Zs by approximately 20%. Also the determination of the precipitation type matched independent observations for specific test cases, and in a bulk statistical sense was consistent with observations and theoretical considerations. The combination of the TB and Z measurements reduce weaknesses inherent to single instrument retrievals, by reduction of the vertical non-uniqueness problems inherent to passive-only retrievals, and reduction of the sensitivity to microphysical assumptions inherent to radar-only retrievals. These and other features discussed within this study indicate the potential of combined retrieval, namely that a merged inversion algorithm is greater than the sum of its parts.

THE FLORIDA STATE UNIVERSITY
COLLEGE OF ARTS AND SCIENCES

Combined Radar-Radiometer Rainfall Retrieval for TRMM Using Structure Function-Based Optimization

by

Michael R. Farrar

A Dissertation submitted to the
Department of Meteorology
in partial fulfillment of the
requirements for the degree of
Doctor of Philosophy

Degree Awarded:
Summer Semester, 1997

The members of the Committee approve the dissertation of Michael R. Farrar defended on April 15, 1997.

Eric A. Smith
Professor Directing Dissertation
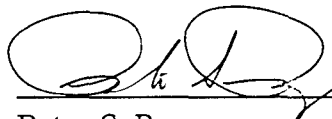
Steven L. Blumsack
Outside Committee Member
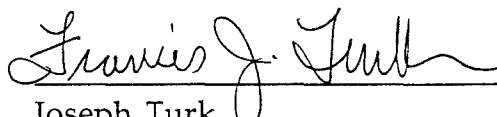
Kevin A. Kloesel
Committee Member

T.N. Krishnamurti
Committee Member

Peter S. Ray
Committee Member

Joseph Turk
Committee Member

ACKNOWLEDGEMENTS

First and foremost I wish to express my gratitude and love to my wife Tammy and my sons Nick and Jake, who endured long periods of time when I was working hard at school and was consequently not there for them at home. Without their love and picking up the slack without me around, I surely would not have been able to complete this dissertation. I also wish to thank my parents, Carolyn Gray and Mickey Farrar, who brought me into this world, and in spite of all I put them through, allowed me to stay here. I will do my best to raise my own sons as well as they did with me, which is the best way I know to thank them for all they have done.

I wish to thank Eric Smith, my major professor and mentor, who guided me during the research and composition of this dissertation. I am grateful not just for the scientific knowledge I learned, but also for his insights on academia, publishing, and the general in-and-outs of the research business. Thanks also go to Steve Blumsack, Kevin Kloesel, T.N. Krishnamurti, Peter Ray, and Joe Turk, the other members of my committee whose contributions helped improve the quality of the dissertation.

I wish to express my appreciation to all members of our research lab who contributed to the positive outcome of this dissertation. Special thanks go to Xuwu Xiang and Song Yang for their direct contributions to this research, to Jim Merritt and Jim Lamm for their graphics and computational support, and to Barbara Benton, Harry Cooper, and Anna Smith for their friendship and helping me stay sane during this process.

TABLE OF CONTENTS

LIST OF TABLES

LIST OF FIGURES

ix

xiv

ABSTRACT

The Tropical Rainfall Measuring Mission (TRMM) satellite, a joint US-Japanese mission to explore tropical rainfall and its effects on the earth's energy budget, general circulation, and climate, represents the first dual deployment of a precipitation radar and passive microwave radiometer on an earth-viewing satellite. While both radiometers and radars have been widely used *independently* to retrieve rainfall, previous attempts to combine the two types of measurements have mostly maintained independent treatment of the data, as these instruments are designed to measure precipitation based on different physical principles.

A method has been developed which objectively combines the measurements within the context of a unified radiative transfer equation (RTE) model, by treating the radar as a radiation source within the RTE model's source function. The retrieval method, referred to as "tall vector" inversion, uses a physical inversion scheme which initially searches a cloud-radiation database of profiles, produced by a 3-dimensional non-hydrostatic cloud model simulation of a tropical storm, to find first guess hydrometeor profiles whose brightness temperatures (TBs) and reflectivities (Zs) best match the radiometer and radar measurements as determined by a combined normalized error function. The first guess profiles, expressed in terms of structure functions, are modified within a steepest descent optimization scheme, using the structure function coefficients as the optimization control variables, until the error function cannot be reduced. The solution hydrometeor profiles are then subjected to a set of gravity fallout equations to

calculate the surface rainfall rates. Precipitation type is also diagnosed from an algorithm using TB threshold tests in conjunction with radar-derived bright band information.

As measurements from the TRMM sensors are not yet available, measurements from similar aircraft prototype instruments deployed for the TOGA-COARE field experiment are used in the evaluation of the algorithm. A statistical analysis of the TOGA-COARE retrieval results found that the optimization improved the average agreement between the measured and first guess TBs and Zs by approximately 20%. Also the determination of the precipitation type matched independent observations for specific test cases, and in a bulk statistical sense was consistent with observations and theoretical considerations. The combination of the TB and Z measurements reduce weaknesses inherent to single instrument retrievals, by reduction of the vertical non-uniqueness problems inherent to passive-only retrievals, and reduction of the sensitivity to microphysical assumptions inherent to radar-only retrievals. These and other features discussed within this study indicate the potential of combined retrieval, namely that a merged inversion algorithm is greater than the sum of its parts.

CHAPTER 1

INTRODUCTION

Remote sensing of rainfall over the last few decades has primarily been restricted to techniques employing two types of instruments: ground-based active radars, and satellite-based passive radiometers of either the visible-infrared (VIS-IR) or passive microwave (PMW) type. A synopsis and brief history of both types of techniques are offered, followed by a discussion of how the strengths of these different methods can be merged within a new type of combined radar-radiometer retrieval that is being developed for the soon to be launched Tropical Rainfall Measuring Mission (TRMM) satellite, which will deploy both a non-coherent single-frequency (13.8 GHz) cross-track scanning precipitation radar along with a five-frequency conically scanning PMW radiometer, as described in Simpson et al. (1988, 1996).

1.1 Radar Methods

Prior to the entry of the U.S. into World War II in 1941, research and development had already begun on radar systems to detect and track aircraft. In addition to aircraft, these radars also detected rain drops in the atmosphere. Whereas this may have been an irritant to some radar operators interested only in aircraft, this was a boon to meteorologists -- and so radar meteorology was born.

Through a combination of theory and experimentation in the laboratory and in the field, Marshall et al. (1947) devised a method to determine

1

raindrop size distributions and relations between radar received power, reflectivity, and ultimately the surface rainfall rate. These experiments were analyzed and results reported by Marshall and Palmer (1948). The relationship between radar reflectivity (Z) and surface rainfall rate (R) was fit to an equation of the following form, consequently referred to as a Z-R relation:

$$Z = a\,R^b, \qquad (1)$$

where a and b are the constants of regression. This study produced the now famous Marshall-Palmer Z-R relation of

$$Z = 220\,R^{1.6} \qquad (2)$$

which is today still used as the standard Z-R relation for stratiform rain. Early parallel work was also conducted by Wexler (1947, 1948).

Since then, many improvements have been made on the technique, such as an adjustment to account for large errors of the Marshall-Palmer distribution at small diameters [Wexler and Atlas (1963)]. However the general form of the Z-R relation has remained unchanged. Various researchers have shown that the coefficients of Z-R relations vary significantly between rain types (convective, stratiform, orographic) and geographic location, such as Fujiwara (1965) and Stout and Mueller (1968). Numerous examples are tabulated and presented by Battan (1973).

The power returned from atmospheric scatterers is inversely proportional to the fourth power of the wavelength, as expressed by Rayleigh scattering theory [see Liou (1980)]. Therefore in order to achieve greater sensitivity, one method of seeking higher power returns is to use shorter wavelength radars. The disadvantage of this approach is that by decreasing the radar wavelength, the signal becomes increasingly attenuated by the rain

particles themselves. Hence methods designed to correct for this loss of signal due to attenuation have been employed in conjunction with radar retrievals at attenuating wavelengths. Hitschfeld and Bordan (1954) showed that large errors may result in this attenuation correction unless the radar constant and the atmospheric parameters, such as drop size distribution (DSD), are specified with a high degree of accuracy. Due to the difficulty of achieving such accuracy, rain measurements at attenuating wavelengths have generally been avoided for ground-based radars. However for space-borne radars such as to be used on TRMM, the constraint of small antennas, coupled with the desire of high resolution, has necessitated the use of shorter, attenuating wavelengths.

While attenuation is a function of the range (or path) of the signal, high range resolution in the attenuation measurement is difficult to obtain. Hence methods of attenuation correction are normally restricted to a path-integrated attenuation (PIA) measurement. A current radar method that has been used with aircraft-mounted radars, called the Surface Reference Technique (SRT), estimates the PIA through rain from the decrease in the radar return from the ocean surface, by comparing surface return powers measured in rain columns to those measured in adjacent rain-free areas. Discussions of the SRT are contained in Meneghini et al. (1983, 1987, 1989) and Fujita et al. (1985a, 1985b). Several methods have been developed which use variations of the SRT to estimate PIA, whereby this estimate is used to constrain the Hitschfeld and Bordan (1954) solution for the rain profile. Examples of this approach are presented by Meneghini and Nakamura (1990), Kozu and Nakamura (1991), Marzoug and Amayenc (1991), Kozu et al. (1991), and Iguchi and Meneghini (1994).

While the SRT has been shown to perform well under certain circumstances, its estimates of PIA are prone to noise, partly due to the variable effects of wind and rain on the ocean surface. Another source of error is due to the questionable underlying assumption that the roughness of the ocean surface under the rain area is equivalent to that under the rain-free area used for calibration of the SRT [see Meneghini et al. (1992)]. Hence other independent methods for the estimation of PIA have been considered. One such method, which uses the PMW brightness temperature at 10.7 GHz to estimate PIA, has been chosen for use with the initial TRMM combined algorithm, and is described by Smith et al. (1997a). As this method employs both radar and radiometer data, it is considered a combined method, although one which is designed around the modification of a radar method. More detailed discussions on this subject are presented in the subsequent sub-section introducing combined radar-radiometer retrieval.

1.2 Satellite Passive Radiometry

Satellite remote sensing of rainfall essentially began with the launch of TIROS-1, the first meteorological satellite, in 1960. Even though this satellite only viewed cloud tops with a VIS and IR sensor, one could make sensible deductions about rainfall from a simple premise; rain falls from clouds, and so where a satellite detects a cloud, there may be rain underneath. The basic approach was to relate a single cloud-top parameter, derived from VIS and/or IR values, to the rainfall rate at the surface, where this relationship was determined via statistical regression analysis. Lethbridge (1967) and Barrett (1970, 1973) were among the first to employ such techniques. Even after the advent of passive microwave radiometry, which provided a more direct

4

measurement of rainfall, research continued in rainfall estimation from VIS/IR measurements. For example, Negri et al. (1984) and Arkin and Meisner (1987) developed IR-based algorithms which are still used and studied today.

Rainfall estimation from VIS and IR data has one fundamental flaw; measurements at these wavelengths directly sense only cloud tops, not the rain underneath, which leads to several problems. First it is not necessarily raining underneath every point for which a satellite detects a cloud. Secondly, a satellite may measure identical values of VIS/IR radiation at the tops of clouds which have entirely different underlying rain structures.

The method chosen by many to alleviate these problems was to abandon the VIS/IR approach which *indirectly* diagnoses precipitation by its correlation with cloud tops, and instead use passive measurements in the microwave regime, a part of the radiation spectrum that can effectively penetrate the cloud tops and *directly* sense the raining hydrometeors themselves. The first satellite-based PMW radiometer available for use in rainfall retrievals was the Electrically Scanning Microwave Radiometer (ESMR), a single-channel 19 GHz instrument launched aboard Nimbus 5 in 1972. Another version of the ESMR operating at 37 GHz was launched aboard Nimbus 6 in 1975. Rainfall retrievals based on ESMR data were constructed in about the same manner as the early VIS-IR retrievals, which was to relate a single satellite-measured radiation value to a surface rainfall rate, either via a statistical regression or theoretical techniques based on emission signatures from hypothetical cloud structures. While the VIS-IR techniques did this with VIS or IR cloud-top radiation values, the PMW techniques used the microwave brightness temperatures (or TBs). Wilheit et al. (1977), Weinman

5

and Guetter (1977), Rodgers et al. (1979), and Jung (1980) were some of the first to develop algorithms designed to transform ESMR TBs into surface rainfall rate estimates. One drawback of the ESMR instruments was their limitation to a single frequency. As a single brightness temperature is effectively a weighted measurement of the entire hydrometeor column, it provides no insight into the vertical structure of the clouds and precipitation. Also each of the frequencies chosen has its own unique response to a column of liquid and frozen hydrometeors (discussed in detail in Chapter 4), which limits the utility of such a stand-alone single-frequency retrieval.

Hence the next logical step was a multi-frequency microwave sensor. The first was the Scanning Multichannel Scanning Radiometer (SMMR), launched aboard Nimbus 7 in 1978, and described in detail by Gloersen et al. (1984). This multichannel sensor allowed for algorithms which could use the different frequencies to explore the vertical structure of the precipitating column. However past thinking, which attempted to estimate only a single surface rainfall rate, was carried over in the use of this instrument. A number of techniques developed for use with SMMR data used multiple frequency brightness temperatures within a statistical regression to estimate a single surface rainfall rate. Such work includes that of Alishouse (1983), Prabhakara et al. (1986), and Hinton et al. (1992). The first attempt to exploit the multifrequency information of the SMMR in a rainfall algorithm was that of Olson (1989), which focused on rainfall within hurricanes. Another multifrequency algorithm addressing a wider variety of rainfall was developed by Kummerow et al. (1989), although it was designed for aircraft measurements.

The growth of multifrequency algorithms did not fully develop until the launch of the next generation sensor, the Special Sensor Microwave Imager (SSM/I) [described by Hollinger et al. (1990)]. The SSM/I is flown on the Department of Defense (DoD) operational satellites under the Defense Meteorological Satellite Program (DMSP); the first SSM/I was launched aboard DMSP satellite F-8 in 1987. The first rainfall retrieval algorithms using SSM/I data followed previous methods and produced a single rainfall rate at the surface, hereafter referred to as rainmap algorithms. For example, the original DoD operational algorithm, as described in CalVal (1989, 1991), is a regression-based rainmap algorithm. A study of the effects of spatial resolution effects on several of these algorithms is presented in Farrar et al. (1994).

An examination of microwave measurements of precipitating clouds reveals that radiation at the various PMW frequencies sample the depth of the column with fundamentally different weighting functions, which translates into effectively sampling different levels of the column. Figure 1.1 illustrates this for the four frequencies to be used by the TRMM PMW radiometer, where height of the peak of the weighting function in the vertical decreases with decreasing frequency. Hence measurements at these PMW frequencies are not really measuring the rainrate at the surface, but are actually sensing the vertical distribution of the hydrometeors. The reason the aforementioned rainmap algorithms can often provide reasonable estimates of surface rainrate is the inherent correlation between the broad vertical distribution of hydrometeors and the amount reaching the surface as rain, which is explored in detail in Chapter 4.
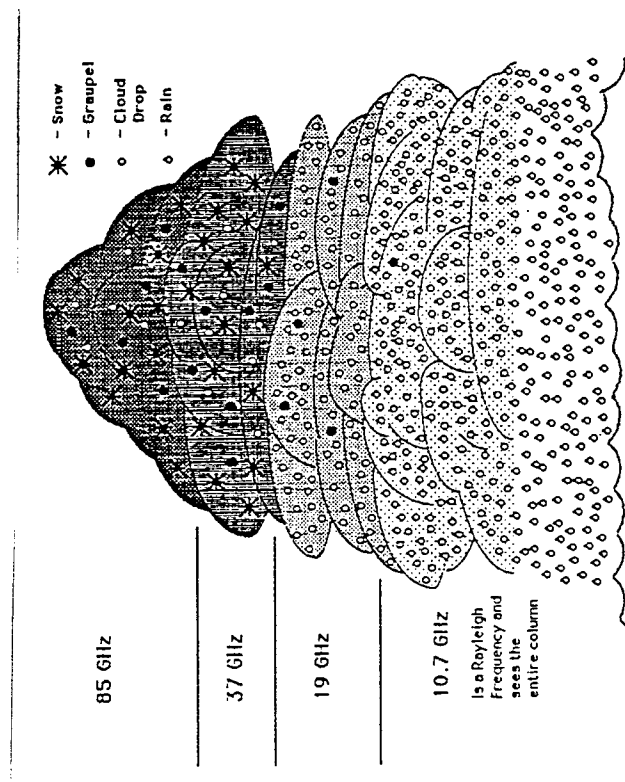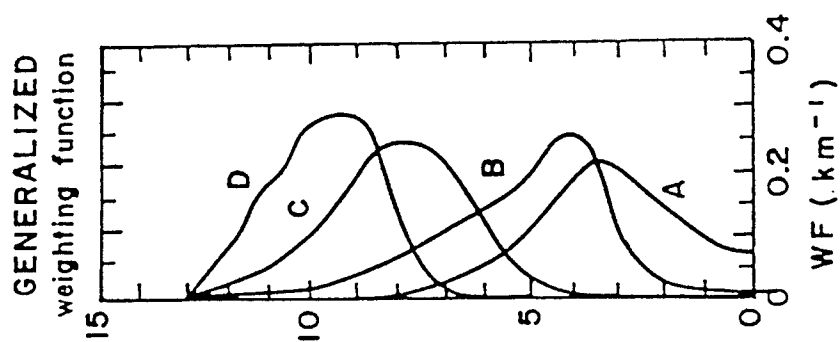
Figure 1.1: Generalized weighting functions with respect to a precipitating column for (a) 10.7, (b) 19.3, (c) 37.0, and (d) 85.5 GHz passive microwave TBs. [Left hand side of figure from Smith et al. (1994d)].

8

In contrast to rainmap algorithms are vertical profile algorithms, which take advantage of the vertical separation of the multiple TB weighting functions to retrieve a vertical profile of the hydrometeor information (instead of just a single surface rainrate value), as discussed in the studies of Smith and Mugnai (1988, 1989) and Mugnai et al. (1990). While the weighting function of each TB peaks at a different level, the broadness of the peaks and the fact that only four frequencies are used ensure that the vertical resolution of such profile algorithms will necessarily be coarse. Examples of such comprehensive multifrequency techniques, which approached rainfall retrieval from a profile approach, are given by Smith et al. (1992, 1994a-b), Mugnai et al. (1993), Kummerow and Giglio (1994a-b), Marzano et al. (1994), Evans et al. (1995), and Kummerow et al. (1996). A review of a number of rainmap and profile algorithms, including a discussion and comparison of their inherent differences and relative strengths and weaknesses, is given by Wilheit et al. (1994).

1.3 Combined Radar-Radiometer Retrieval

While rainfall retrieval techniques using only a single data type (radar, passive microwave, or VIS-IR) have been used for decades, combined methods exploiting the complementary strengths of each are relatively new [see Wilheit (1986)]. For example, Adler et al. (1991a, 1993, 1994) have developed an algorithm that combines retrievals from geosynchronous IR measurements with retrievals using SSM/I passive microwave measurements, whereby the IR retrievals are scaled statistically by factors derived from the microwave retrievals. One advantage of the geosynchronous platform is that the period between successive

measurements of the same location on the earth is typically no more than one hour, as opposed to a sun-synchronous polar orbiting satellite which views a point on the earth no more than twice a day. However as previously mentioned, microwave measurements have the advantage over IR of directly sensing the rain itself, and hence generally provide more accurate estimations of instantaneous rainfall than IR techniques. Hence this method attempts to improve upon the rainrates obtained from an IR retrieval by calibrating it with results from a PMW retrieval. Further development of this method is described by Kummerow and Giglio (1995).

Research in combined radar-radiometer retrievals has been quite limited until recently. Lu and Hai (1980) experimented with a ground-based radar-radiometer system (at 9.4 GHz) to measure rainfall, and showed that a combination of a radar retrieval, with an independent radiometer-derived estimate of path-integrated attenuation (PIA), provided improved results over radar-only and radiometer-only methods. Hai et al. (1985) went on to demonstrate further improvements by a dual-wavelength (9.4 and 35 GHz) radar system.

The first combined scheme using down-looking radar and radiometer measurements was performed by Weinman et al. (1990). The basic principle is the same as that of the radar methods previously described, whereby the standard radar technique of Hitschfeld and Bordan (1954) is constrained by an independent PIA estimate. The difference is that the PIA is estimated from a method using the passive microwave data, instead of a method such as the Surface Reference Technique which uses radar data. Subsequent studies have continued to explore this aircraft-borne combined retrieval approach, such as Kumagai et al. (1993) and Schols and Weinman (1994).

A different airborne radar-radiometer system was employed during the Convection and Precipitation/Electrification project over Florida in 1991, as described by Vivekanandan et al. (1993), Turk et al. (1994) and Marzano et al. (1994). While coincident radar and radiometer measurements were taken, these studies did not produce a true combined retrieval but instead compared independent radar and radiometer retrievals.

Although the method of constraining a radar-derived solution with a radiometer-derived PIA estimate employs both radar and radiometer data, it still maintains separate theoretical frameworks for the passive and active data. So in essence, these methods are actually the fusion of separate radar and radiometer techniques. Moreover the radar is the dominant element in the retrieval, with the radiometer providing only a supporting role with the PIA correction.

Another class of algorithms are now under development, in which the radar and radiometer measurements play an equivalent role in the inversion process. Olson et al. (1995) and Haddad et al. (1996) are developing separate profile retrieval schemes, whereby radar and radiometer measurements are inverted by producing Bayesian coefficients which are applied to a pre-existing profile database. An advantage of this approach is that since it does not use any inversion scheme, it is computationally efficient which can be important in an operational environment. However since this framework generates solution profiles by a weighted average of the profiles in the pre-existing database, it does not produce new independent profiles and hence is limited to the structures inherent to the pre-existing database.

Another approach is the subject of this research, as introduced by Farrar et al. (1996). This method allows the generation of independent profiles

relative to those in a pre-existing database used for initial guess information. The method represents hydrometeor profiles as structure functions, where the coefficients of the functions are used as the optimization control parameters in an optimization scheme. Hence new profiles are created as the coefficients of the structure functions are adjusted during the optimization. The other significant development in this algorithm is that it for the first time uses both radar and radiometer data within a single, unified radiative transfer framework, rather than in separate radiative frameworks.

Chapter 2 describes the retrieval algorithm methodology, followed by a discussion of the sensors and the datasets in Chapter 3. Knowledge gained through various tests using hydrometeor profiles from the high-resolution hurricane simulation database in conjunction with the unified active-passive RTE model are discussed in Chapter 4. The results of algorithm experiments using aircraft data from TOGA-COARE are given in Chapter 5. Finally a discussion and conclusions are given in Chapter 6.

CHAPTER 2

METHODOLOGY

Until now, retrieval of rainfall in the tropics by satellite-borne microwave sensors has been limited by several factors. The sun-synchronous orbits of these satellites have limited the sampling frequency in the tropical regions, while the satellites' altitude has limited the resolution of the data. Also these sensors have consisted of passive radiometers of only a few frequencies, strictly limiting the amount of independent information needed to infer the vertical structure of the sampled precipitating regions. The Tropical Rainfall Measuring Mission (TRMM), as described by Simpson et al. (1988, 1996), is a joint American-Japanese satellite mission designed to directly address these problems. It will fly in a low-inclination orbit, so that unlike measurements from a satellite in a standard polar orbit which have data gaps in equatorial regions, TRMM's measurements will blanket the tropics. Also by including a down-looking radar, higher resolution information on the vertical structure of observed precipitating rain columns will be available, when compared to previous passive-only satellite sensor suites.

The TRMM satellite will deploy a wide array of instruments, including the TRMM Microwave Imager (TMI), a five-frequency conically scanning passive microwave radiometer, and the Precipitation Radar (PR), a single-frequency (13.8 GHz) non-coherent cross-track scanning radar, the first of its kind to be deployed on a satellite. The combination of measurements from the TMI and PR will be the basis for the combined retrieval presented here.

13

Further details about the TMI and PR, as well as for some of TRMM's other instruments, are given in the Chapter 3.

As TRMM is not scheduled for launch until November 1997, rainfall retrievals using real TMI and PR data cannot yet be conducted. Instead, aircraft instruments designed to perform much like their future satellite-borne counterparts are used in the development and testing of the combined retrieval. TB measurements from the Advanced Microwave Precipitation Radiometer (AMPR) are used in lieu of those from the TMI. The AMPR, a cross-track scanning passive microwave radiometer which samples at four of the five TMI frequencies, is flown aboard a NASA ER-2 aircraft. Reflectivities from the Airborne Rain-Mapping Radar (ARMAR) are used in lieu of those from the PR. The ARMAR, a coherent cross-track scanning radar which operates at the TRMM PR frequency, is flown aboard a NASA DC-8 aircraft. Note that unlike the TRMM PR, the ARMAR is coherent and hence can produce Doppler vertical velocities in the presence of backscattering media (i.e., hydrometeors). More details about these aircraft sensors, as well as comparisons to their TRMM counterparts, are given in Chapter 3.

Combined precipitation retrievals using passive microwave (PMW) radiometer and radar measurements, from either the TRMM sensors or their aircraft-mounted predecessors, can be performed in several ways, as previously discussed in the introduction. In anticipation of the launch of the TRMM satellite, the TRMM project wished to have a workable combined algorithm in place prior to launch so that retrieval products could begin from the first day. The "Day-1" algorithm chosen was a Z-R radar method, similar to that described by Weinman et al. (1990), in which the radar portion of the algorithm is constrained by an estimate of path integrated attenuation (PIA)

14

derived from 10.7 GHz TMI measurements. The estimation of PIA from the 10.7 GHz channel of the TMI, for use in the Day-1 algorithm, is described by Smith et al. (1997); the Day-1 algorithm itself is described in Haddad et al. (1997).

While the Day-1 algorithm uses both radar and PMW radiometer data, it is still essentially a radar technique and does not make full use of the information provided by the PMW measurements. The combined technique which is the subject of this research takes the next step, by fully incorporating both radar and PMW radiometer measurements into a single data vector within a combined inversion scheme, where both data types are given equal weight. As the combined data vector includes the radar reflectivity measurements from each radar range gate and the TB measurements from each frequency of the PMW radiometer, it has been previously referred to as a "tall vector" in similar studies.

This combined data vector is used in the retrieval method in the following way. The process begins with the simulation of a precipitating storm by a cloud model, which generates a series of hydrometeor profiles present within the storm. Each of these hydrometeor profiles is input to a radiative transfer equation (RTE) model, which produces PMW TBs and radar Zs corresponding to each hydrometeor profile. The measured data vector is then compared to each set of TBs and Zs within the simulation database, where the set that matches the tall data vector most closely is selected as the first guess. The initial guess hydrometeor profiles are then iteratively altered within the context of an optimization scheme, producing a solution vector of TBs and Zs which provide an improved match with the measured data vector, when compared to the matchup using the unaltered initial guess

values. The final state of the solution hydrometeor profiles is then used as input to a rainfall submodel based on gravity fallout equations, which produces a solution surface rainfall rate. A preliminary description of the algorithm is presented by Farrar et al. (1996). A complete overview of the methodology is given in the next section, with detailed descriptions of important algorithm components given in the sections that follow.

2.1 Retrieval Overview

The combined retrieval scheme is presented in the form of a flowchart in Figure 2.1 to aid in the discussion of the process. The first step is a database of hydrometeor and vertical velocity profiles, produced from a high-resolution hurricane simulation using a 3-D non-hydrostatic cloud model. As the simulation produced cloud, hydrometeor, and vertical velocity structures present in all stages of tropical disturbances, including cirrus anvils, stratiform rain, and shallow and deep convection, the database serves as a limited representation of all types of these structures found in the tropical atmosphere. A complete description of the cloud model and the hydrometeor database is presented in section 2.2.

The next step is to use the microphysical hydrometeor profiles as input to a unified radar-radiometer Radiative Transfer Equation (RTE) model, in order to link a set of reflectivity (Z) profiles and upwelling microwave brightness temperatures (TB) with each set of corresponding hydrometeor profiles in the database. The unified model is described in detail by Smith et al. (1997b), with an overview presented in section 2.3.
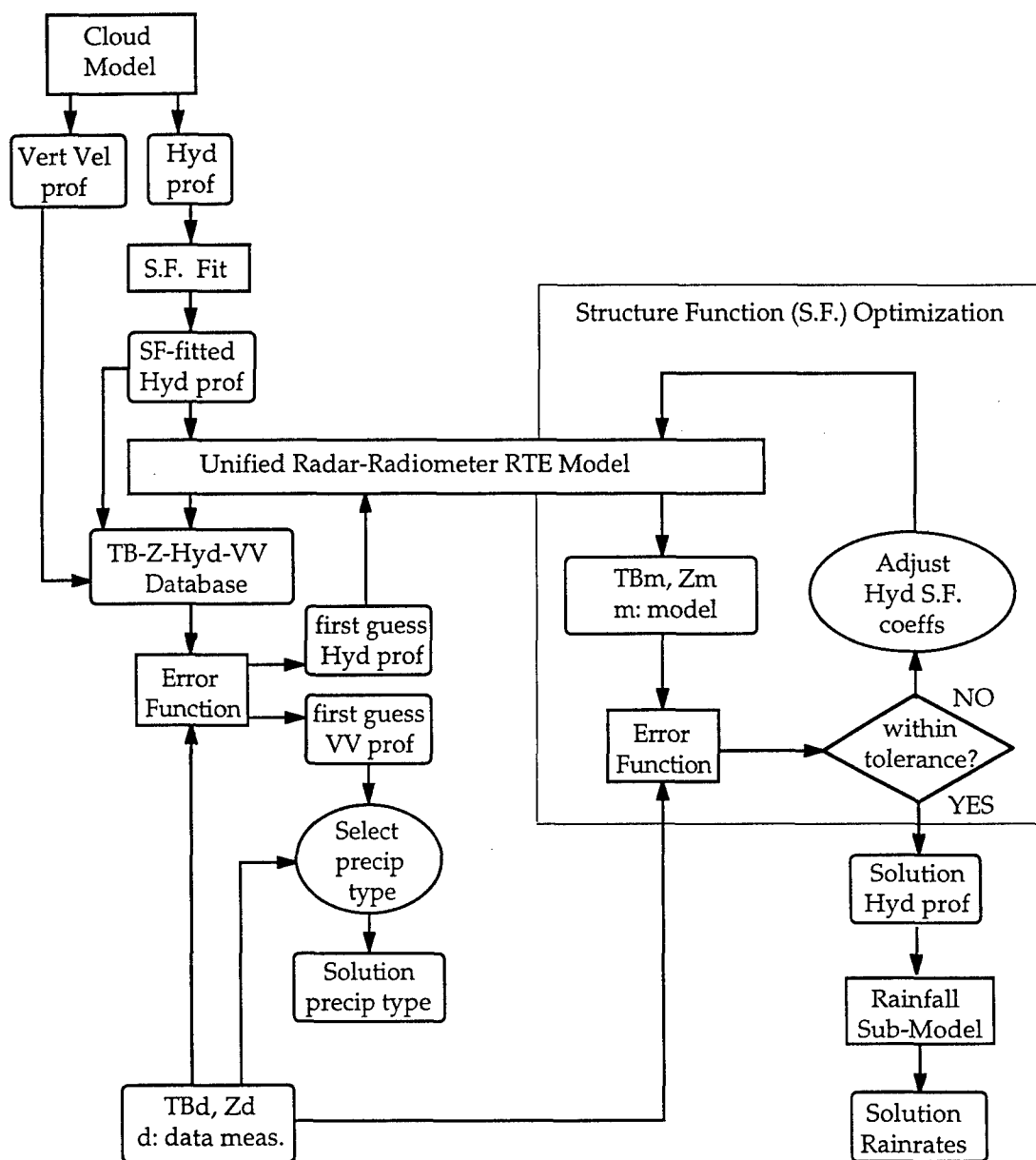
Figure 2.1: Retrieval Algorithm Flowchart

By inputting the hydrometeor profiles into the unified RTE model, a reflectivity profile and set of PMW TBs are produced for each set of hydrometeor profiles. These sets of corresponding brightness temperatures (TB), reflectivities (Z), hydrometeor (Hyd) concentration profiles, and vertical velocity (VV) profiles, form the initial guess database, indicated as the TB-Z-Hyd-VV Database in Figure 2.1. The actual TB and Z measurements from the AMPR and ARMAR, respectively, are then compared to all the matched sets in the TB-Z-Hyd-VV database using an error function; the set of database TBs and Zs which gives the minimum value of the error function is defined as the best match, and hence the corresponding matched hydrometeor and vertical velocity profiles are selected as the first guess profiles. The error function calculates the RMS differences between measured and modeled TB and Z data, and combines them by normalizing the RMS differences with the expected noise of the instruments and the model. Note that all measured and modeled Z values less than 0 dBZ are truncated to zero prior to calculation of the error function. A more detailed discussion of the error function is presented in section 2.4.

The first guess hydrometeor and cloud profiles are then fit to a series of structure functions, such that the hydrometeor and cloud profiles are expressed as a set of coefficients applied to a basis of structure functions. The profiles are then perturbed by altering the coefficients. These new perturbed profiles are then run through the unified RTE model, generating a new working set of TBs and Zs. This procedure is repeated under the control of an optimizer, using the structure function coefficients as the optimization control parameters, until the working set of TBs and Zs match the measurements within specified threshold limits as expressed by the

previously discussed error function, or until the optimization steps fail to provide a reduction of the error function. Section 2.5 provides a complete description of the structure functions and optimization scheme.

The end product from the optimization is a solution set of profiles of liquid and frozen hydrometeors, both suspended and precipitating. These solution hydrometeor profiles are input into a rainfall submodel, which use gravity fallout equations consistent with the cloud model to produce rainfall rates at the surface, with a complete description provided in Section 2.6. Also note that the solution hydrometeors can be used to obtain the latent heating profiles by taking vertical derivatives of the mass fluxes of precipitating liquid and ice, as described by Yang and Smith (1997).

As the hydrometeor profiles are altered during each step of the optimization, the modified profiles are input to the forward RTE model which produced a modified set of TBs and Zs. However as vertical velocity in not an input parameter to the forward RTE calculations, the vertical velocity profile from the initial guess database is not similarly modified. Hence as new vertical velocity profiles are not generated during the optimization, the first guess vertical velocity profile is retained for use in an experimental technique to determine precipitation type (i.e., convective vs. stratiform). The ARMAR Zs and AMPR TBs, along with the initial guess vertical velocity profile, is used as input into the precipitation type technique, described in detail in Section 2.7. An evaluation of the utility of the method based on retrieval results from TOGA COARE is presented in chapter 5.

2.2 Hydrometeor Database from Hurricane Simulation

The hydrometeor database was produced from a hurricane simulation using the University of Wisconsin Non-hydrostatic Modeling System (UW-NMS), a 3-D time-dependent cloud model described by Tripoli (1992a). The UW-NMS model is a modification of the model originally developed by Tripoli and Cotton (1982) and Cotton et al. (1982). The model employs a 2-way multiple nested grid system, allowing the inner nest to move along with a specified phenomena, such as the pressure minimum of an atmospheric disturbance.

The microphysics module is a modification of the version used in the Colorado State University-Regional Atmospheric Modeling System (CSU-RAMS) model, which is described by Flatau et al. (1989). Modifications made to the CSU-RAMS version include dividing the ice crystal category into pristine ice crystals and snow, allowing the aggregates to be included in the snow category, and representing the graupel with a constant-slope Marshall-Palmer distribution. This results in five categories of microphysical cloud/precipitation particles: (1) cloud drops, (2) rain drops, (3) graupel/hail, (4) pristine ice crystals, and (5) snow, where the snow category includes both ice crystal complexes (i.e., snow flakes) and aggregates of crystals and snow. Each of these particle types can grow independently, or interactively by coalescence (for liquid) or aggregation (for ice), as described by Tripoli (1992b). The characteristic radius [as described by Flatau et al. (1989)], particle densities, and size distribution functions for each microphysical category are given in Table 2.1.

Table 2.1: Hydrometeor Size Distribution Parameters and Particle Densities
[adapted from Panegrossi et al. (1997)]

Particle Type	Characteristic radius (m)	Size Distribution Function	Particle density $(kg\ m^{-3})$
cloud	1.0×10^{-5}	mono-dispersed	1.0×10^3
rain	2.7×10^{-4}	Marshall-Palmer	1.0×10^3
graupel	5.0×10^{-4}	Marshall-Palmer	6.0×10^2
pristine ice	1.17×10^{-4}	mono-dispersed	2.2×10^2
snow/aggregates	1.65×10^{-3}	Marshall-Palmer	3.0×10^1

Table 2.2: Hurricane Simulation Nested Grid Setup Parameters
[adapted from Tripoli (1992b)]

Parameter	Grid Number #1	#2	#3	#4
Period of Activation	0-56 hrs	0-56 hrs	8-56 hrs	50-56 hrs
Central Latitude	17.5° N	16.5° N	16.5° N	18.5° N
Central Longitude	71.0° W	68.0° W	68.0° W	69.7° W
# of Horizontal Boxes *	64	60	64	60
Horizontal Spacing *	60 km	20 km	10 km	3.3km
Horizontal Domain Length	3840 km	1200 km	640 km	198km
# of Vertical Boxes	42	42	42	42
Vertical Spacing	400-800 m	400-800 m	400-800 m	400-800m
Vertical Domain Height	30.5 km	30.5 km	30.5 km	30.5 km
Large Timestep	120 s	40 s	20 s	6.33 s
Small Timestep	40 s	13.3 s	6.67 s	2.11 s

* Note: Inner grids also contain an outer row of boxes for transferring boundary conditions with the outer grid. So for the high resolution grid #4 used in this research, the effective horizontal domain (including the boundary boxes) is 205 x 205 km from 62 x 62 boxes.

Table 2.3: Model Level Heights for High-Resolution Hurricane Simulation

Model Level	Height (km)	Model Level	Height (km)
1	30.574	22	13.774
2	29.774	23	12.974
3	28.974	24	12.174
4	28.174	25	11.374
5	27.374	26	10.574
6	26.574	27	9.774
7	25.774	28	8.974
8	24.974	29	8.174
9	24.174	30	7.374
10	23.374	31	6.574
11	22.574	32	5.774
12	21.774	33	4.973
13	20.974	34	4.179
14	20.174	35	3.432
15	19.374	36	2.756
16	18.574	37	2.142
17	17.774	38	1.584
18	16.974	39	1.076
19	16.174	40	0.615
20	15.374	41	0.195
21	14.574	42	0.000

The tropical cyclone simulation was carried out for approximately 56 hours of integration time. It began with an initial state where the wind speeds were assumed to be zero. The basic thermodynamic structure, taken from sounding profiles at Kingston, Jamaica, 36 hours prior to the passage of Hurricane Gilbert in September, 1988, was assumed to be horizontally homogeneous. The initial state was then perturbed by a modified Rankine vortex [described in Tripoli (1992b)] and allowed to evolve. Four nested grids

were used for the simulation. The outer grid (#1) was centered along the expected storm track; the medium grid (#2) was centered over the location of the initial perturbation; the next inner grid (#3) was implemented eight hours into the simulation when the cyclone stage began; the high-resolution grid (#4) was used in the last six hours of the simulation centered over the mature cyclone. Specifics on grid locations, resolution, and spacing are given in Table 2.2, while the vertical model level heights are given in Table 2.3.

Data from the high-resolution inner nest, with 3.3 km horizontal resolution, was used in order to best match up with the resolution of the ARMAR and AMPR data. A study using simulation data averaged to a lower resolution, in conjunction with SSM/I (Special Sensor Microwave/ Imager) measurements, is given by Panegrossi et al. (1997). While the profiles used were extracted from the inner nest centered about the eye, they still contained cloud and hydrometeor structures present in all stages of tropical disturbances, from stratiform and shallow convection to the deep convection of a fully formed eyewall.

From all the time steps in the high-resolution inner nest, six were selected as containing a representative sample of all hydrometeor structures found in the entire simulation. This subset, containing 20,081 matched sets of hydrometeor and atmospheric profiles, was then used as the simulation database for this study. The hydrometeor profiles are separated into the five categories previously described, expressed in terms of equivalent liquid water content. Figure 2.2(a) shows the average hydrometeor profile for each hydrometeor category, and Figure 2.2(b) shows the "maximum profile" defined as the maximum value of each hydrometeor category found at each level in the database. The peak of each hydrometeor category falls in the

expected relative location. The rain peak falls near the surface, with the cloud above; the graupel and snow peaks above the freezing level, with the pristine ice peaking above around the level of the cirrus anvil.

Another way of quantifying the hydrometeors is by their total Integrated Water Path (IWP), which is the vertical integral of their equivalent water content. A histogram of IWP of all database entries is given for each hydrometeor category in parts (a)-(e), and for surface rainrate in part (f), of Figure 2.3. As a significant portion of the profiles in the database are devoid of at least one hydrometeor category, these zero cases are removed from the histograms and their count is given in text in the upper portion of each panel. The notable exception is pristine ice [part (d)], which is contained in every profile in the database, due to the presence of a cirrus anvil in the entirety of the inner nest of the hurricane simulation.

This presents a problem when attempting to retrieve rainfall over areas without an overlying cirrus anvil, as there is no profile in the TB-Z-Hyd-VV database without high clouds to match with the measured data. This was resolved by duplicating the database with the upper levels of pristine ice and snow removed, which allowed the lower phenomena (e.g., shallow convection) to be represented both with and without an overlying layer of high cloud. Since most of the high cloud in the simulation was dynamically produced in the areas of deep convection and not by the same mechanisms producing the underlying low-level hydrometeors, the removal of the upper ice hydrometeors in a duplicate database does not destroy the dynamical integrity of the low-level simulation [Tripoli (1997), personal communication].

(a) Average of each Hydrometeor category

(b) Maximum of each Hydrometeor category
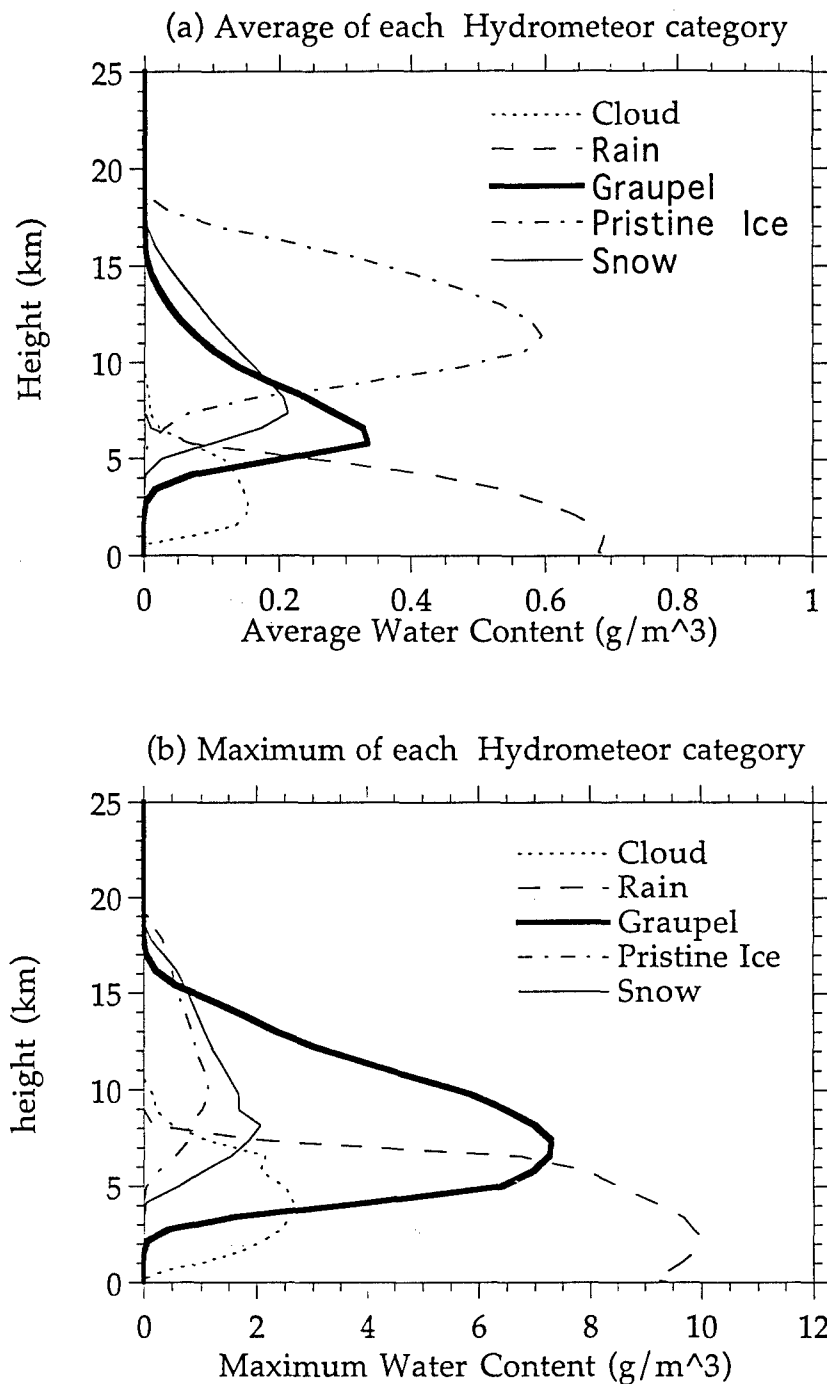
Figure 2.2: Average (a) and maximum (b) values of equivalent water content for each hydrometeor category in hurricane simulation database.

(a) Cloud

IWP < 1 kg/m^2 for 15149 profs
Max IWP = 13.8 kg/m^2

Count

3000
2000
1000
0

1 2 3 4 5 6 7 8 9
IWP (kg/m^2)

(b) Rain

IWP < 1 kg/m^2 for 11386 profs
Max IWP = 54.8 kg/m^2

Count

3000
2000
1000
0

1 10 20 30
IWP (kg/m^2)

(c) Graupel

IWP < 1 kg/m^2 for 15048 profs
Max IWP = 50.9 kg/m^2

Count

2000
1000
0

1 10 20 30
IWP (kg/m^2)

(d) Pristine Ice

Max IWP = 7.6 kg/m^2

Count

10000
8000
6000
4000
2000
0

0 1 2 3 4 5 6 7 8
IWP (kg/m^2)

(e) Snow

IWP < 1 kg/m^2 for 10119 profs
Max IWP = 10.7 kg/m^2

Count

5000
4000
3000
2000
1000
0

1 2 4 6 8 10
IWP (kg/m^2)

(f) Sfc Rainrate

RR < 10 mm/hr for 12830 profs
Max RR = 218 mm/hr

Count

3000
2000
1000
0

10 30 60 90 120 150
Rainrate (mm/hr)

Figure 2.3: Histogram of 20,081 database values of hydrometeor IWP (a)-(e) and surface rainrate (f). Some low-value bins reported separately as their large count overwhelmed the representation of the smaller count bins.
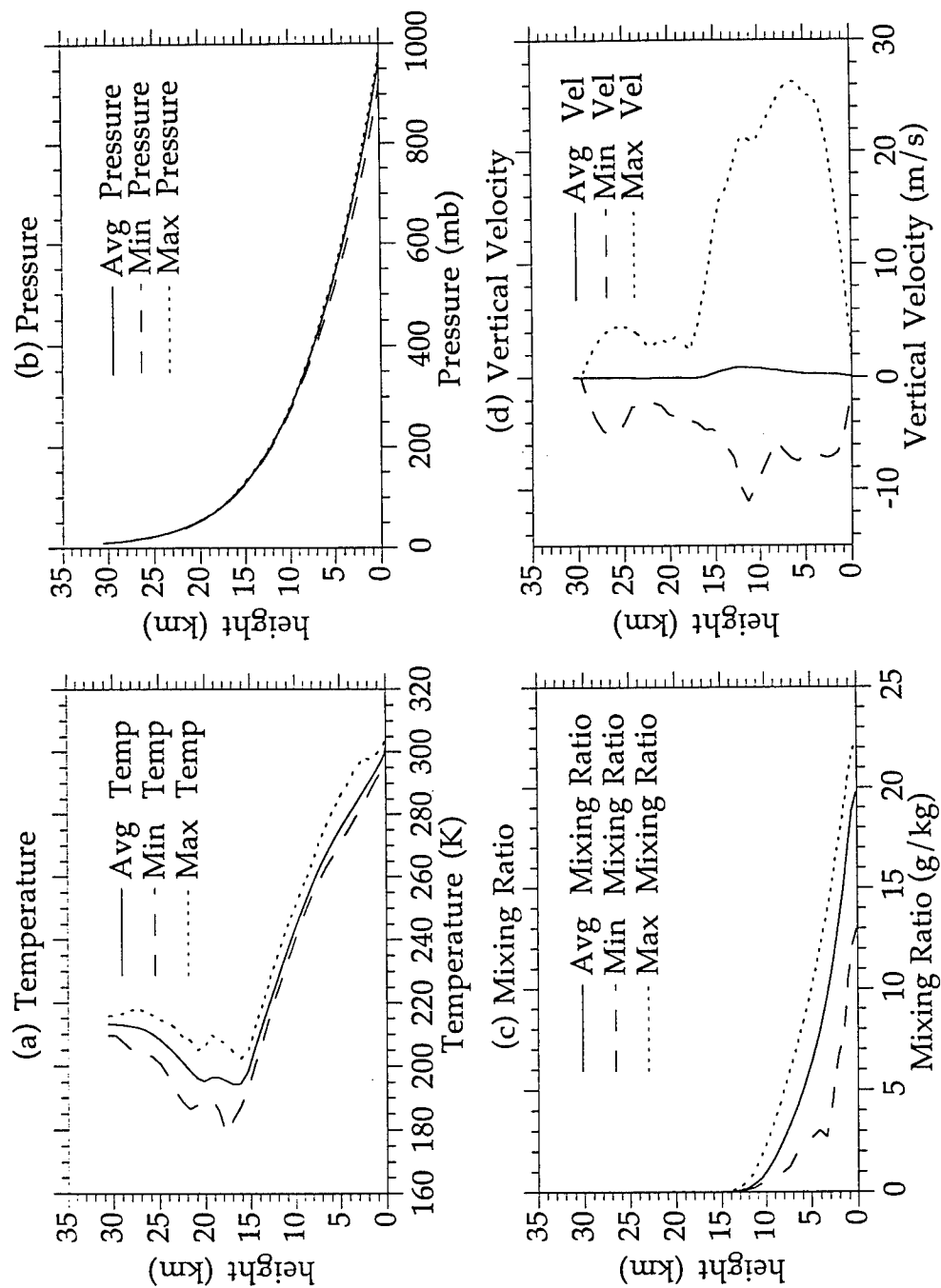
Figure 2.4: Profiles of average, minimum, and maximum values of (a) temperature, (b) pressure, (c) mixing ratio, and (d) vertical velocity from the simulation database.

27

As the simulations generated a complete dynamical structure of the atmosphere, other atmospheric variables were available at each simulation grid point. In addition to the previously discussed hydrometeor concentrations, the simulation also produced a set of atmospheric profiles for temperature, pressure, water vapor mixing ratio, and vertical velocity. The average of each profile from the database, along with minimum and maximum values detected at each level, are given in Figure 2.4. Features illustrated are what one would expect from a tropical atmosphere, such as heavy moisture in the lower atmosphere dropping off sharply with height, to minute concentration at the tropopause. However the fact that this is a hurricane simulation does lead to warmer average temperatures in the troposphere, as noted by an average freezing level height of near 6 km, when compared to the freezing level height of 4.5 km normally found in the tropics and typical of soundings taken during TOGA COARE. The average mixing ratio in the troposphere is also more moist for the hurricane simulation than that from typical soundings taken in TOGA COARE. There are also instances of very large upward vertical velocities associated with the intense convention around the hurricane eyewall, as exhibited by the maximum vertical velocities detected in the database. Impacts of these atmospheric properties on the retrieval process are discussed in Chapter 4.

2.3 Unified Radar-Radiometer RTE Model

A unified radar-radiometer Radiative Transfer Equation (RTE) model has been developed to simulate both the passive microwave brightness temperatures and the radar reflectivities at multiple range-gates for a precipitating cloud. The unified model is a modification of a solar radiation

model originally described by Xiang et al. (1994), and subsequently modified for PMW rain profile retrieval as given by Smith et al. (1994a). In the new model, the radar is treated as a radiation source, analogous to the sun as a source for solar radiation. Hence radar reflectivities are generated by treating the radar as a quasi-direct beam radiation source. By incorporating the passive and active portions within a unified model framework, the unified model allows absorption, scattering, and passive thermal sources to contribute to both the passive and active radiative transfer processes. A complete description of the unified model is given by Smith et al. (1997b).

The plane-parallel RTE for the combined radiometer-radar simulation is:

$$\mu \frac{dTB\,(\tau, \mu, \phi)}{d\tau} = -TB\,(\tau, \mu, \phi) + J\,(\tau, \mu, \phi) \qquad (3a)$$

where the source function J is given by

$$J = \frac{\omega}{4\pi} \int_0^{2\pi} \int_{-1}^{+1} P(\mu, \phi; \mu', \phi')\, TB\,(\tau, \mu', \phi')\, d\mu'\, d\phi'$$

$$+ (1-\omega)T(\tau) + \frac{\omega}{4\pi} TB\,(R_0)\, P\,(\mu, \phi\,;\, \mu_0, \phi_0)\, e^{-\tau/\mu_0} \qquad (3b)$$

In the above equations, $TB(\tau, \mu, \phi)$ is the brightness temperature representation of diffuse radiance, ω the single-scattering albedo, $P(\mu, \phi; \mu', \phi')$ the phase function, μ the cosine of zenith angle, ϕ the azimuth angle, τ the optical depth, $T(\tau)$ the environmental temperature at τ, (μ_0, ϕ_0) the direction of radar beam, and R_0 the radar direct irradiance incident to the atmospheric scattering volume. This latter term, as shown in Battan (1973), can be expressed as

$$R_0 = \frac{G\,P_t}{4\pi\,r^2} \qquad (4)$$

where r is the distance between radar set and scattering volume, P_t the transmitted radar power, and G the antenna gain. To convert R_0 into $TB(R_0)$ as required in Eq. (1b), the following relation is used:

$$TB(R_0) = \frac{C_2 \lambda^4}{C_1 \Delta\lambda} R_0 \qquad (5)$$

where λ is the radar wavelength, C_1 and C_2 the constants of the Planck function, equaling 3.742 E-16 [W•m^2] and 1.438 E-2 [m•deg(K)], and $\Delta\lambda$ the effective radar bandwidth in terms of wavelength. All units used in equations (2) and (3) are based on the SI convention.

The TB solved by the model is then transformed to radar reflectivity Z, which is the counterpart to the measurement from the TRMM radar, by

$$Z = 10^{18} \frac{C_1 \Delta\lambda}{\pi C_2 \lambda^4} TB \frac{A_t A_e}{C|k|^2} \qquad (6)$$

where A_e is the effective collector area, A_t the target cross section, C the radar constant [as defined by Battan (1973)], and k designates $(m^2 - 1)/(m^2 + 2)$, where m is the complex index of refraction. The reflectivity Z is expressed in units of [mm^6 m^{-3}]; all other quantities are in SI units.

2.4 TB-Reflectivity Error Function

As described in section 2.1, the first guess set of profiles is selected as those which produce the minimum value of an error function which quantifies the agreement between the AMPR-measured TBs with the simulation TBs, and between the ARMAR-measured Zs with the simulation Zs. The quantity chosen as the matchup criteria is root mean square (RMS) error. Calculating RMS error between the modeled and measured TBs is straightforward, as is the calculation of RMS error between the modeled and measured Zs. The problem lies in how to define a combined error function, which expresses the simultaneous agreement of both TBs and Zs. If combined in an ad hoc manner, the combined error function could be

arbitrarily weighted disproportionally toward either the TBs or the Zs, giving the other little weight in the combined error function.

To minimize this problem, each RMS difference is normalized by the expected error inherent in both the RTE model and the associated measuring instrument (i.e., AMPR or ARMAR). In this manner the calculated differences between the measured and modeled quantities will be expressed in terms of how much error would be expected due to random noise, so that in effect the combined error characteristics of the instruments and model select their relative weighting for themselves. Random error, or noise, is normally reported as one standard deviation from the mean. The equation to combine the unbiased noise effects of two independent quantities, such as the instrument measurement and the model-produced value, may be expressed as

$$\text{Noise(combined)} = \sqrt{\text{Noise}^2(\text{meas}) + \text{Noise}^2(\text{model})} \qquad (7)$$

Hence the error function for the brightness temperatures and reflectivities is given by the following two equations, respectively:

$$\text{ERR (TB)} = \sum_{i=1}^{4} \frac{\frac{1}{4}\left[\text{AMPR TB}_i(\text{K}) - \text{Model TB}_i(\text{K})\right]^2}{\sqrt{\text{Noise}^2(\text{AMPR TB}_i(\text{K})) + \text{Noise}^2(\text{Model TB}_i(\text{K}))}} \qquad (8a)$$

$$\text{ERR (Z)} = \sum_{i=\text{ibot}}^{\text{itop}} \frac{\frac{1}{(\text{ibot-itop+1})}\left[\text{ARMAR Z}_i(\text{dBZ}) - \text{Model Z}_i(\text{dBZ})\right]^2}{\sqrt{\text{Noise}^2(\text{ARMAR Z}_i(\text{dBZ})) + \text{Noise}^2(\text{Model Z}_i(\text{dBZ}))}} \qquad (8b)$$

where ibot and itop in equation (8b) refer to the bottom and top of the reflectivity profile, excluding the uppermost model layers which are above the height of any hydrometeors. The very large surface reflectivity signal in the ARMAR measurements (typically ~80 dBZ in clear conditions) leaks into

31

the radar reflectivity measurements at radar range gates just above the surface, dropping off to -55 dBZ of the surface value at a height of 500 m [Durden et al. (1994)]. In order to prevent the algorithm from interpreting low-level clear air returns due solely to surface contamination as real hydrometeor returns, the reflectivity at a level above the range of the surface contamination is assigned to all underlying levels down to the surface, prior to the calculation of the error function. The combined error function is then given by

$$\text{ERR (Combined)} = \text{ERR (TB, Z)} = 0.5 \ [\text{ERR (TB)} + \text{ERR (Z)}] \qquad (9)$$

The unbiased noise characteristics of the AMPR and ARMAR are given by Spencer et al. (1994) and Durden et al. (1994), respectively. If there were no biases between the model and the measurements all that would remain would be to insert these unbiased noise characteristics into equations (8). However there are biases, which is further complicated by the fact that their exact values and the circumstances under which they exist are largely unknown. Furthermore the calibration of the instruments tend to drift from the values reported in initial calibration tests, creating another source of added error. Hence instead of using the unbiased noise values reported under known conditions, larger "effective" values were used in an attempt to account for the effect of these biases and other calibration errors. The effective errors were chosen as 1 K for the AMPR TBs [Spencer (1996), personal communication], and 1.5 dBZ for the ARMAR reflectivities [Durden (1996), personal communication], which were determined from analyses of data from selected TOGA COARE cases and other field tests. These values were also prescribed to account for effective noise inherent in the model TBs and reflectivities.

2.5 Structure Function Optimization Scheme

Once the algorithm has selected an initial guess set of hydrometeor profiles from the TB-Z-Hyd-VV database using the method previously described, the first guess profiles are provided as input to an optimization scheme which seeks to iteratively alter their structure until the error function is minimized. The most straightforward method of optimization would be to alter each hydrometeor category at each level independently; with five hydrometeor categories of 42 levels each, that would result in 210 optimization variables. In order to reduce this large number of independent optimization variables, each hydrometeor profile (one for each hydrometeor category) is fit to a function which reasonably matches the structure of the hydrometeor profiles; hence their designation as "Structure Functions". The coefficients of these structure functions which represent the hydrometeor profiles are then used as the optimization control variables, rather than the complete set of hydrometeor profiles themselves.

The selection of the precise form of the structure functions was driven by three distinct criteria. First the functions should reasonably embody the shape and structure of the hydrometeor profiles found in the initial guess database. Secondly, since the hydrometeor column will have a distinct top and bottom, the structure functions should be valid over a finite interval. Thirdly, the series of functions should be mutually orthogonal, so that each function will represent independent information, and not merely be a linear combination of the others. For these reasons, Legendre Polynomials were selected as the form of the structure functions.

33

The generating function for the Legendre Polynomial of order (n), over the interval -1 < x < 1, is given by

$$P_n(x) = \frac{1}{2^n \, n!} \frac{d^n}{dx^n} (x^2 - 1)^n \qquad (10)$$

where x is the independent variable, and the function is valid over the domain $-1 \le x \le 1$ [see Arfken(1970)]. As the hydrometeor concentrations are given as a function of height, height is chosen as the independent variable, where the heights of the top and bottom of each hydrometeor column have been rescaled to -1 and 1, respectively. Then each first guess hydrometeor profile is fit to a series of Legendre polynomials, starting with order n=0 up to a finite upper limit. The specific form of the Legendre Polynomials calculated from the generating function are given in Table 2.4; likewise the graphical representation of Legendre Polynomials up to order 5 are presented in Figure 2.5.

Table 2.4: Legendre Polynomials up to 5th Order

Order	Legendre Polynomial
0	$P_0(x) = 1$
1	$P_1(x) = x$
2	$P_2(x) = \frac{1}{2}(3x^2 - 1)$
3	$P_3(x) = \frac{1}{2}(5x^3 - 3x)$
4	$P_4(x) = \frac{1}{8}(35x^4 - 30x^2 + 3)$
5	$P_5(x) = \frac{1}{8}(63x^5 - 70x^3 + 15x)$

x (independent variable)

(c) P_4 and P_5

$\cdots\cdots P_4(x)$
——— $P_5(x)$

(b) P_2 and P_3

$\cdots\cdots P_2(x)$
——— $P_3(x)$

(a) P_0 and P_1

$\cdots\cdots P_0(x)$
——— $P_1(x)$

x (independent variable)
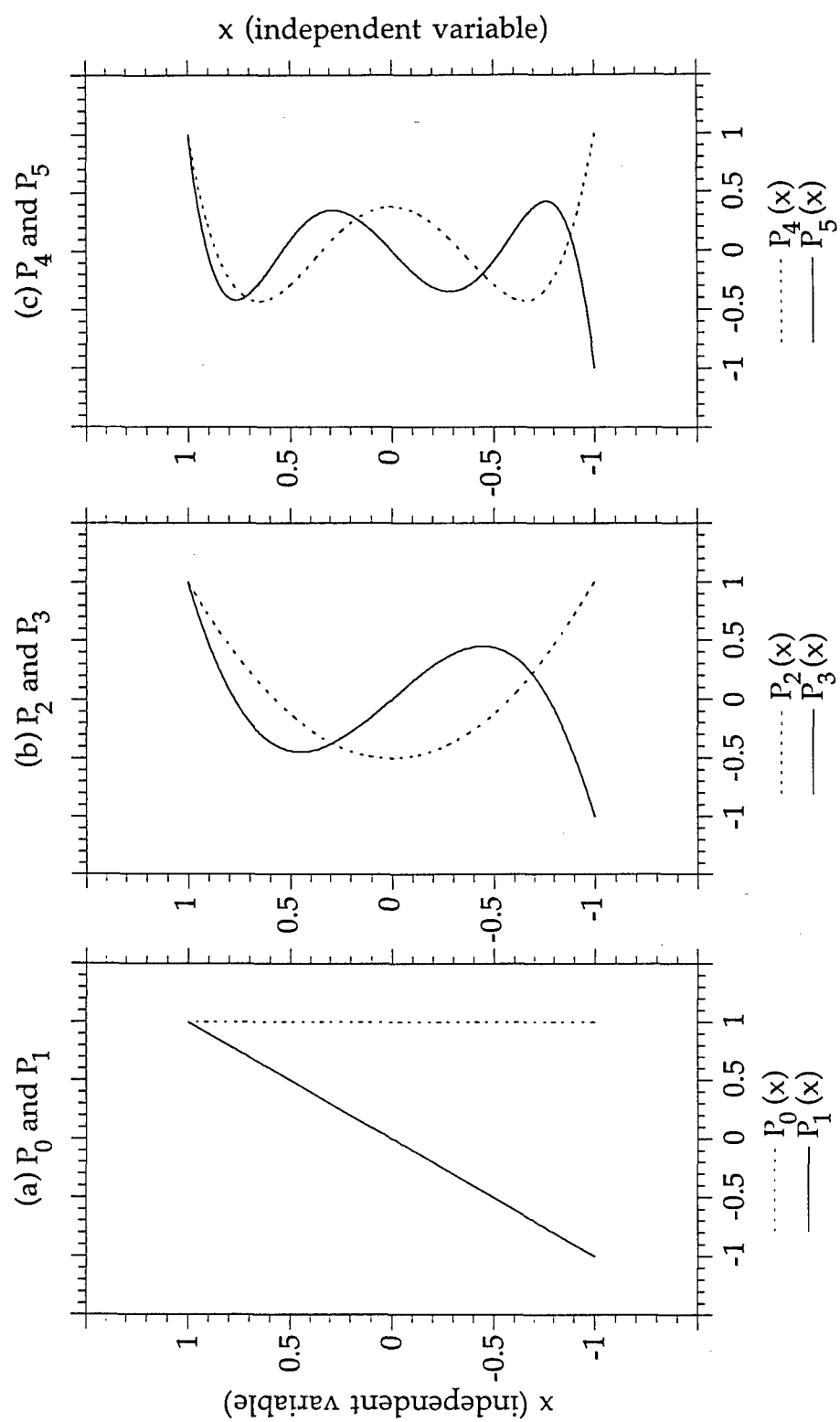
Figure 2.5: Plot of Legendre polynomials up to order 5.
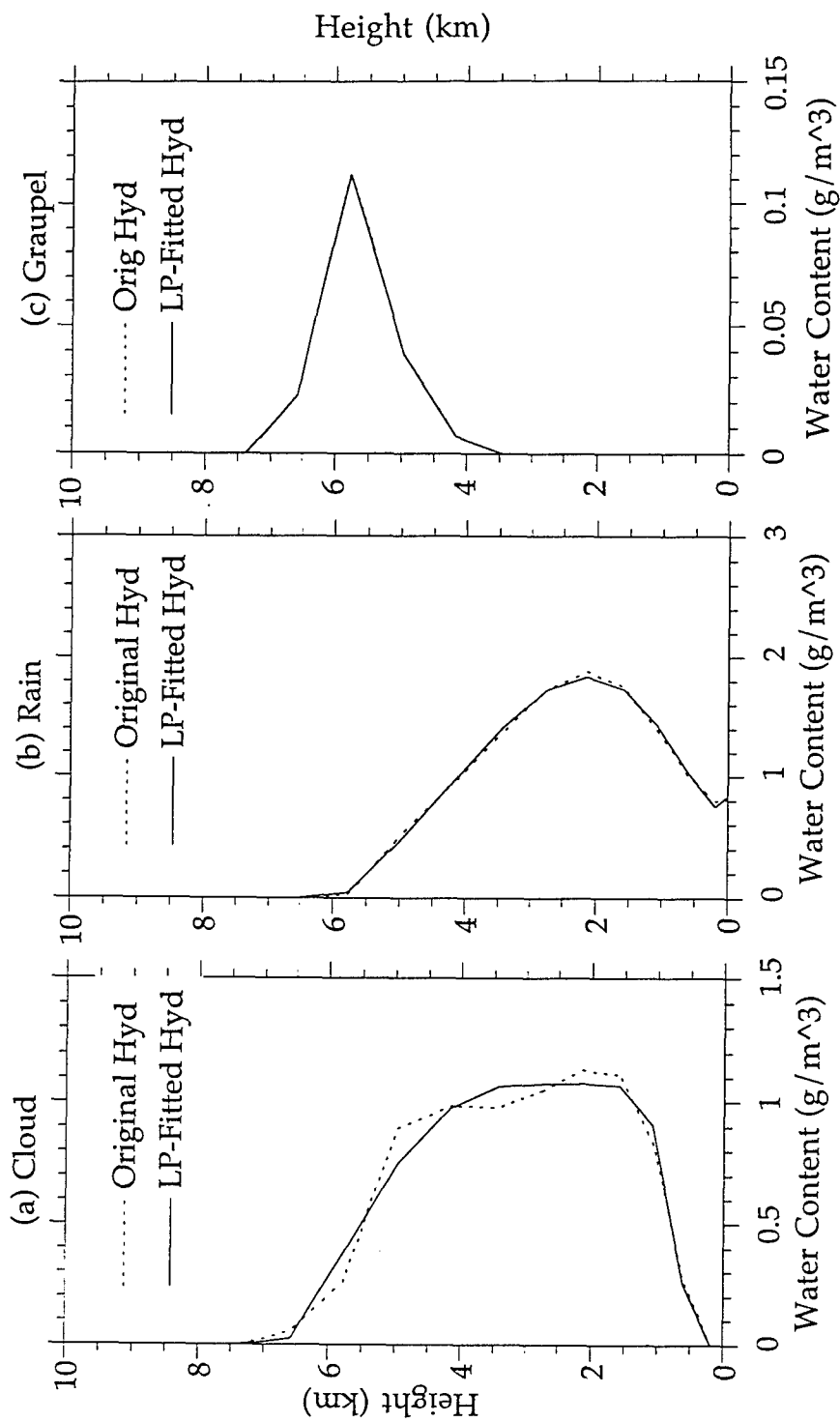
Figure 2.6: Legendre polynomial fit of an example database profile of (a) cloud, (b) rain, and (c) graupel equivalent water content.

As stated before, one of the reasons Legendre Polynomials were selected as the form for the structure functions was their mutual orthogonality over the domain interval, as expressed by

$$\int_{-1}^{1} P_m(x) P_n(x) \, dx = 0 \, , \ m \neq n \tag{11}$$

Note that while orthogonality is exactly satisfied over an explicit integration as given in the preceding equation, the Legendre Polynomial structure functions are defined at discrete intervals only, as determined by the model level heights. Hence the structure functions are more precisely described as "nearly orthogonal", as explained by Strang (1988). As the intent of the orthogonality was to maintain as much independence as possible between successive orders of the structure functions, this slight departure from exact orthogonality does not result in any detrimental effects to the optimization process.

Once fit to the series of Legendre Polynomials, the hydrometeor concentration, or equivalent Water Content (WC) as a function of height for each hydrometeor category can be expressed as

$$WC_i(x) = \sum_{n=0}^{5} c_n^i P_n(x) \, , \, -1 \leq x \leq 1 \tag{12}$$

where the hydrometeor category (i) has values 1-5, corresponding to the five hydrometeor categories described in section 2.2. Note that values of hydrometeor water content produced from the expansion equation (12) that fall below zero are set equal to zero to avoid this pathological condition, and the subsequent adverse computational effects that would result from using negative hydrometeor contents as input to the unified RTE model. The functional representation for a set of profiles taken from the TB-Z-Hyd-VV database is given in Figure 2.6 as an example. Fitting tests from a random

37

sample of the simulation database found that an upper limit of n=5 was adequate to represent the hydrometeor structures. Also note that as nearly all hydrometeor profiles from the database sample exhibited similarly simple shapes, the agreement shown for the example in Figure 2.6 is typical for most instances.

Once the first guess hydrometeor profiles have been fit to structure functions, the retrieval algorithm proceeds to the optimization phase. The error function previously defined in section 2.4 serves as the optimization function, such that the optimization parameters (here the hydrometeor profiles) are iteratively adjusted in order to minimize the error function. Since the hydrometeor profiles have been fit with the Legendre Polynomial structure functions, it is the coefficients c_n^i defined in equation (12) that are used as the optimization control parameters.

From among many types of optimization techniques designed to minimize a function, the steepest descent method, as described by Gill et al. (1981), was selected for use in the retrieval algorithm because of its simplicity. The first step in the optimization is to determine the change in the error function caused by small independent changes in the optimization control parameters, which are the Legendre Polynomial coefficients. These changes are expressed for each coefficient in the form of a derivative, namely

$$\frac{\partial ERR}{\partial c_n^i} = \frac{ERR\left(c_n^i + \Delta c_n^i\right) - ERR\left(c_n^i - \Delta c_n^i\right)}{2\,\Delta c_n^i}\,, \tag{13}$$

where Δc_n^i represents a deviation from the original value of the coefficient. If the coefficient is changed in the direction where the derivative in equation (13) is negative, then the error function is decreased. These derivatives are calculated for all optimization coefficients, and combined into an N-

dimensional gradient (where N is the number of coefficients in the optimization). The direction down this gradient is referred to as the direction of steepest descent; hence "steepest descent" optimization. The incremental change in the error function is then described as

$$\text{ERR}' = \text{ERR}_0 - k \, \nabla_N \left[\text{ERR} \left(\vec{c_n^i} \right) \right] \tag{14}$$

where ERR' is the new iterated value of the error function, ERR_0 is the original value of the error function, k is the iteration step down the gradient, and $\vec{c_n^i}$ is the vector containing all the Structure Function coefficients. The step size k is increased until a local minimum is reached, at which point the gradient is re-calculated and the optimization proceeds in a different "direction." This change of direction is illustrated for two dimensions in Figure 2.7. The error function, which involves calculations of the combined RTE model and the Mie coefficients therein, is highly non-linear with respect to the hydrometeor concentrations, and hence may require many direction changes during the optimization.

Finally, this process is repeated until one of the following conditions is satisfied: (1) the error function is reduced below a prescribed minimum threshold value; (2) the optimization exceeds a prescribed maximum number of allowable iteration steps; or (3) the error function reaches a local minimum where subsequent direction changes fail to further reduce its value. Figure 2.8 illustrates how the TBs, Zs, and surface rain rates change as the optimization proceeds. Note that even though some individual quantities may oscillate, the combined error function continues to decrease.
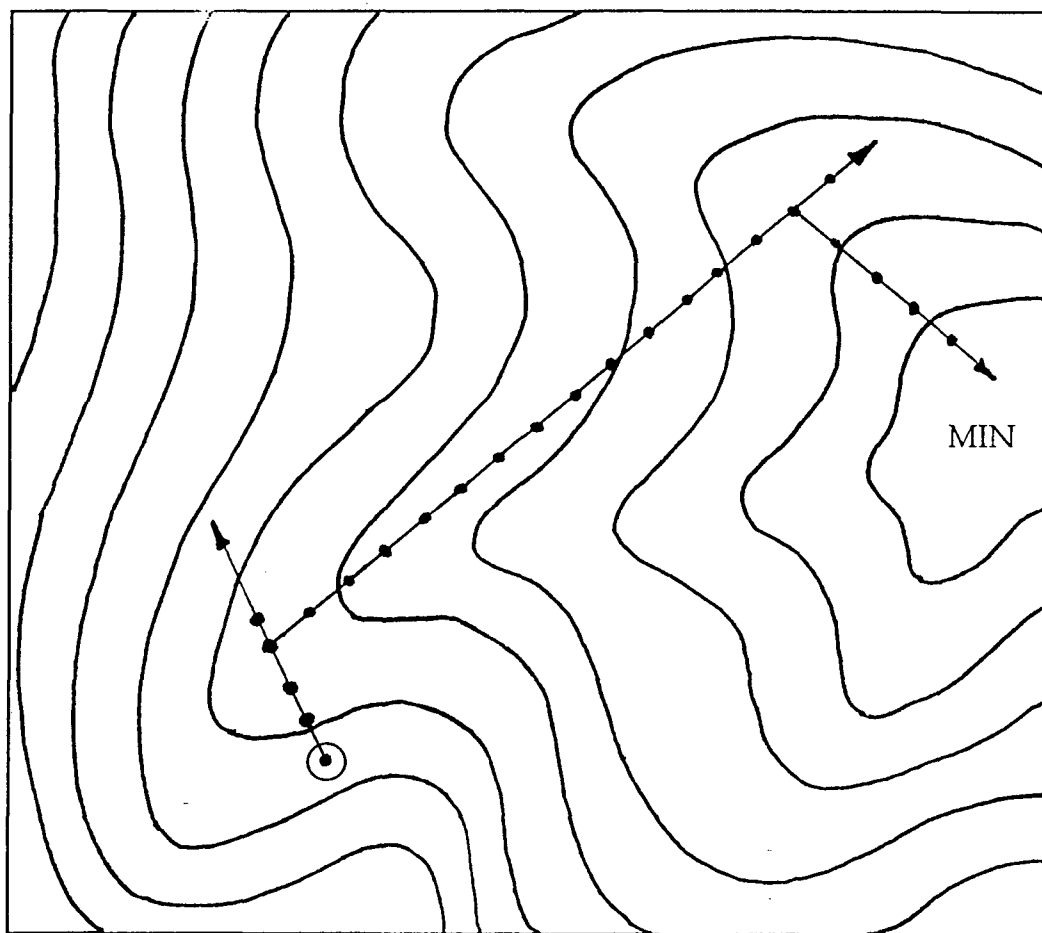
Figure 2.7: Steepest-Descent optimization in 2-dimensions
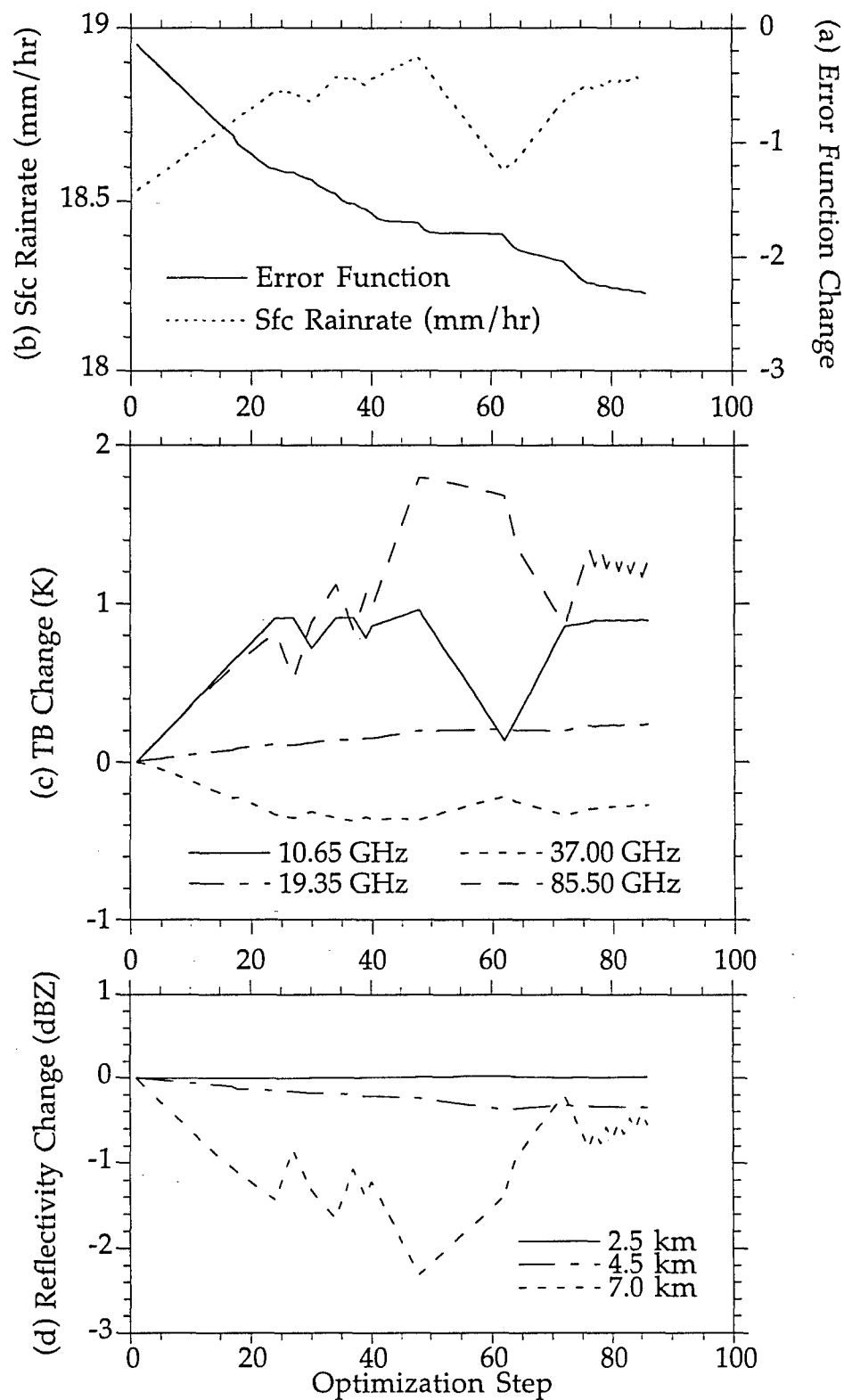
Figure 2.8: Example optimization, depicting changes in the (a) error function, (b) surface rainrate, (c) TBs, and (d) Zs from their original values.

2.6 Rainfall Fallout Submodel

Once the retrieval algorithm has produced a solution set of hydrometeor profiles, the rain hydrometeors are subjected to gravity fallout calculations which a produce a profile of rain rate. The values of the rain rate profile near the surface are then taken as the surface rainfall rate. The vertical rain rate profile RR (z) is given by

$$RR(z) = -\rho_o(z)\left[\overline{w}_{rd}(z) + \overline{W}(z)\right] q_{rd}/\rho_w \qquad (15)$$

where ρ_o is the basic state air density, ρ_w the density of water (1000 kg m^{-3}), q_{rd} the rain water mixing ratio, $\overline{W}(z)$ an externally specified cloud domain scale vertical velocity, and $\overline{w}_{rd}$ the vertically dependent mean terminal velocity, defined by

$$\overline{w}_{rd} = -1.94\left[\frac{4\,\rho_w\,D_m\,g}{3\,C_D\,\rho_o(z)}\right]^{1/2} \qquad (16)$$

where g is the gravitational acceleration, C_D is the water drop drag coefficient (0.588), and D_m is the characteristic drop diameter of the rain drops (540 mm). In equation (15), the sign convention for the vertical velocity is taken as positive upward/negative downward. Thus combining equations (15) and (16),

$$RR(z) = 3.6 \times 10^6\,\rho_o(z)\left[6.72\,\rho_o^{-1/2} - \overline{W}_z\right] q_{rd}(z)\,/\rho_w \qquad (17)$$

where the terms on the right hand side are given in SI units and RR is in mm hr^{-1}. Thus by evaluating equation (17) at the layer or layers near the surface where $\overline{W}(sfc) = 0$, the surface rain rate is obtained. This method is described by Smith et al. (1994a), as well as similar expressions for precipitating ice.

2.7 Determination of precipitation type

One of the main objectives of TRMM is to explore the impact of tropical precipitation on climate variability [Simpson et al. (1988, 1996)]. The primary

feedback mechanism by which precipitation affects weather patterns in short and long time scales is through diabatic heating. As described by Houze (1989, 1993) and Yang and Smith (1997), the heating characteristics of convective and stratiform precipitation are distinctly different, as illustrated in Figure 2.9. Hence the determination of precipitation type will be crucial if the goals of TRMM are to be fulfilled.

In order to categorize precipitation, it is important to understand the fundamental differences between categories and precisely what it is that defines precipitation as either convective or stratiform. The fundamental property that defines the type of precipitation is the mechanism by which the precipitation particles, or hydrometeors, grow, as described by Houghton (1968) and Houze (1993). Yuter and Houze (1995a) explain that stratiform precipitation grows primarily by aggregation and riming just above the melting layer, and by vapor deposition at higher levels, whereas convective precipitation grows primarily by accretion of water.

The underlying physical property that controls these growth mechanisms is the vertical motion within the precipitating column. As such, Yuter and Houze (1995a) give a definition of convective and stratiform using vertical velocity with respect to terminal fall speed of ice:

$$\text{stratiform:} \qquad |w| << |v_{ice}| \qquad\qquad (18a)$$

$$\text{convective:} \qquad |w| >> |v_{ice}| \qquad\qquad (18b)$$

where typically $v_{ice} \sim$ 1-3 m s^{-1}. For stratiform situations, the vertical velocity is weakly upward, while for convection, updraft speeds are of a greater magnitude, where typically $w \sim$ 1-10 m s^{-1}. These vertical velocity characteristics imply an associated reflectivity structure.

(a) CONVECTIVE   (b) STRATIFORM

HEIGHT →

HEATING RATE →
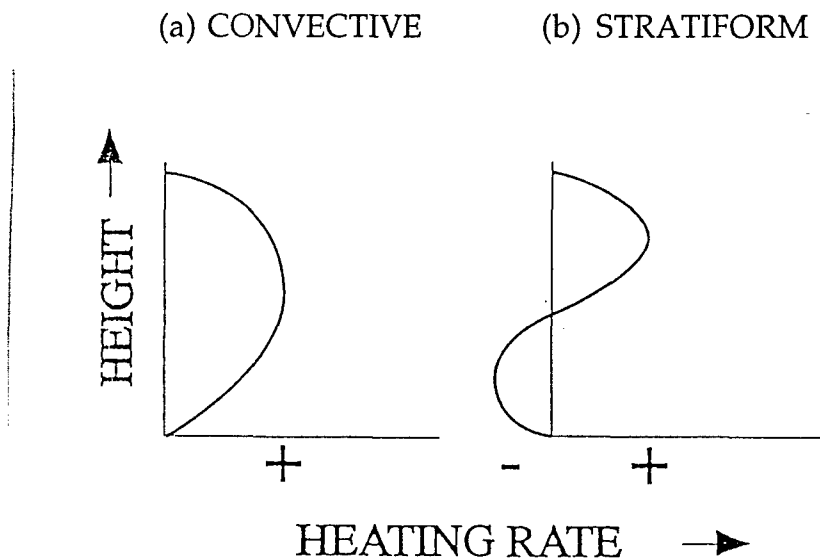
Figure 2.9: Characteristic shapes of heating profiles in (a) convective and (b) stratiform regions. Based on Houze (1989).
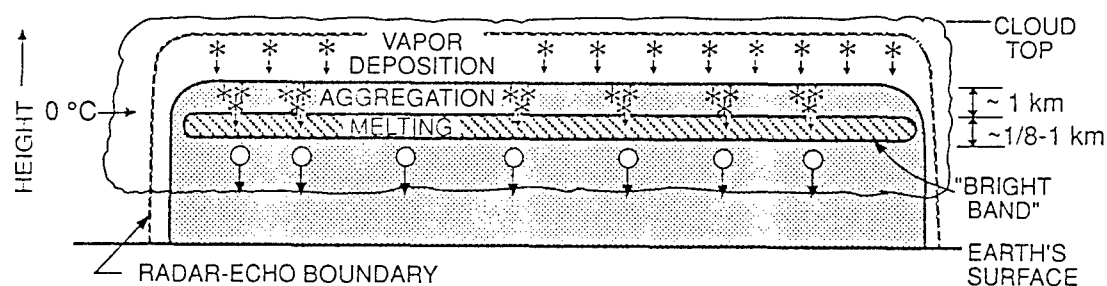
Figure 2.10: Vertical structure of hydrometeors and their growth mechanisms and the resulting "Bright Band" in a stratiform rain region. From Houze (1993).

44

The radar reflectivity from an ice particle is less than that of a water particle of the same effective size or mass, due to the fact that the dielectric constant for ice is less than that for liquid water. However when snow and ice aggregates approach the melting layer, a thin film of liquid water forms on the outside of the particles, which results in a radar reflectivity signature nearly equivalent to that of a pure liquid drop of the same effective size. Since pure liquid drops are not present at the sizes of the liquid-covered ice particles, returns from these particles are more intense than that of the liquid rain drops present in the same vicinity. As the terminal fall velocities of aggregates and snow flakes are roughly the same order as the upward motion in a stratiform system, a significant portion of these liquid-coated ice particles can remain near the melting layer. Hence the concentration of these particles in a narrow region near the melting layer, coupled with their higher reflectivities with respect to pure ice and liquid water drops, give rise to a well-defined peak in reflectivity known as the "bright band", as described by Battan (1973) and Houze (1993), and as depicted in Figure 2.10.

For convective precipitation, larger updrafts and downdrafts spread these particles in the vertical, suppressing their concentration in any narrow region. Also these updrafts support growth of the ice particles by riming, which leads to a peak in reflectivity with respect to the non-updraft background, as described by Churchill and Houze (1984). Typical profiles of reflectivity and vertical velocity for convective and stratiform rain are given in Figure 2.11.

The differences in the typical hydrometeor structures between convective and stratiform rain also result in distinctive signatures in upwelling PMW TBs. The TB signature is directly related to the type,

concentration, and size distribution of the hydrometeors, as described by Wilheit et al. (1977) and Wu and Weinman (1984). Emission signatures at lower microwave frequencies (freq. < 30 GHz) are directly related to the total amount of liquid water in the column, whereas for higher frequencies the TB values are depressed due to scattering by large ice particles [Spencer et al. (1989), Adler et al. (1991), Smith et al. (1992), and Mugnai et al. (1993)]. Note that over land, maximum updraft speeds are stronger than those present over ocean, such that ice particles can grow larger and hence the ice scattering signature can be more intense, as shown by Lemone and Zipser (1980), Zipser and Lemone (1980), and Lucas et al. (1994).
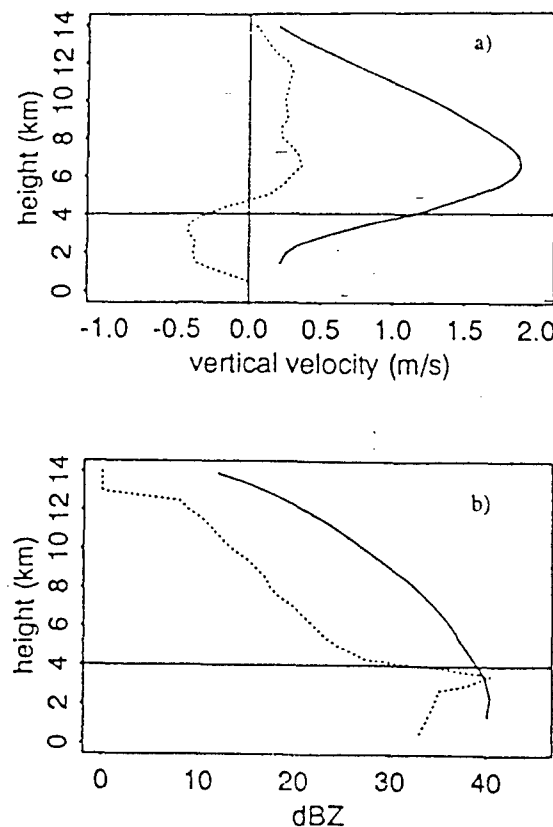
Figure 2.11: Characteristic mean profiles of (a) vertical velocity and (b) radar reflectivity for convective (solid lines) and stratiform (dotted lines) rain regions. From Yuter and Houze (1995b).

These differences in heating profiles, reflectivity, and brightness temperature signatures have led to a host of different methods to classify precipitation as either convective or stratiform. Tao et al. (1993) present a heating profile method based on region-specific heating climatologies. Other methods take advantage of the fact that for both the reflectivity and brightness temperature fields, convective regions tend to stand out from the background while stratiform regions tend to appear homogeneous. Hence such techniques are sometimes referred to as "texture" methods. Churchill and Houze (1984) and Steiner et al. (1995) separate convective from stratiform precipitation based on the intensity and sharpness in the peaks of reflectivity, while Hong et al. (1997) present a convective-stratiform index based on the variability and intensity of TB differences at multiple frequencies.

The approach chosen for the precipitation classification scheme within the combined retrieval algorithm was to diagnose only well-defined convective and stratiform regions, leaving all other candidates in an undefined "unknown" category. This is accomplished in a two-step procedure: first deep convection is separated using TB thresholds, and then stratiform rain is diagnosed with the existence of the bright band.

The first step is to identify well-defined deep convection by its brightness temperature signature. Several studies have found that TBs at 85 GHz less than 210 K are only found in convective cases [Spencer et al. (1989), Adler et al. (1991), Liu and Curry (1992)], as stratiform conditions are not capable of producing ice particles large enough to create that much of a scattering depression. This minimum threshold was confirmed by McGaughey et al. (1996) and McGaughey and Zipser (1996) for the AMPR instrument during TOGA COARE, where 220 K was the minimum AMPR 85.5 GHz TB found to

47

be associated with stratiform conditions. These authors also indicate a maximum emission peak for the AMPR 10.7 GHz TB associated with stratiform conditions to be ~ 210 K. While cases where 10.7 GHz TB < 210 K involved both stratiform rain and convection, cases with 10.7 GHz TB > 210 K were only associated with convection. In order to avoid false identification, the method requires the published threshold values not only be met but exceeded by 10 K. Hence deep convective cases are separated using the following TB threshold values:

convective: 10.7 GHz TB > 220 K   -OR-   85.5 GHz TB < 210 K   (19)

Equation (19) contains the logical "OR" notation, as only one condition is necessary to trigger the convective classification. McGaughey et al. (1996) note that the vertical tilt of precipitation sometimes causes the maximum in 10.7 GHz TB and the minimum in 85.5 GHz TB of a convective cell to not lie in the same vertical column.

The second part of the technique uses the existence of a bright band to diagnose stratiform rain. While this is reasonable for well-defined stratiform conditions, it is noted that stratiform conditions in the development and dissipation stages often do not exhibit a bright band, as described by Yuter and Houze (1995a,b,c). Hence some stratiform precipitation will not produce a bright band, and consequently not be diagnosed as stratiform by the method. In automating the determination of the existence of a bright band, the peak reflectivity in a 3 km layer centered about the freezing level (~4.5 km altitude for the TOGA COARE data) was located, and only values of 25 dBZ or greater were considered as candidates. The value of the reflectivity was then required to drop by at least 5 dBZ within 1 km above and below the peak. [All threshold values obtained from Durden (1997), personal communication].

Reflectivity profiles that met all these conditions were diagnosed as having a bright band, and consequently classified as stratiform.

Note that as decaying convection can exhibit a bright band, as described by Rinehart (1991), it is possible for a set of TBs and Zs to satisfy both the TB threshold test for convection and the bright band test for stratiform rain. Hence in those cases, the TB threshold test takes precedence and the case is classified as convective. Finally, all retrievals that fail both the TB threshold test for deep convection, and the brightband test for well-developed stratiform, are tagged as unknown.

While this method exploits differences between typical TB and Z signatures from convective and stratiform rain, these quantities are only indirect measures of the underlying dynamical and microphysical properties that distinguish these two distinctly different types of precipitation. As previously described, the fundamental property that governs precipitation growth, and therefore its type, is vertical velocity. Hence if an algorithm could correctly diagnose the vertical velocity structure of a precipitating column, the precipitation classification might proceed on a more basic level.

Previously it was explained that since no new vertical velocities were generated during the optimization, the vertical velocity profile from the database corresponding to the first guess was retained as the "solution" vertical velocity profile. In order to determine whether the initial guess vertical velocity profile would provide any value in the determination of precipitation type, it was analyzed within the retrieval in two ways. First it was compared to the ARMAR Doppler vertical velocities, which indicate the vertical motion of the hydrometeors. By subtracting a value of hydrometeor terminal fall speed in the layer consistent with the previously defined typical

values given by Yuter and Houze (1995a), the Doppler velocities of the hydrometeors were transformed to generate an estimate of the average atmospheric vertical velocity in the layer, which was then compared to the average atmospheric vertical velocity of the layer from the initial guess. Secondly the distribution of first guess vertical velocities was analyzed separately for profiles diagnosed as convective, stratiform, and unknown, as defined by the precipitation classification scheme presented above. These distributions were also compared to those generated using the corresponding ARMAR Doppler velocities. These analyses are presented, along with the other retrieval results, in Chapter 5.

CHAPTER 3

INSTRUMENTS AND DATA

3.1 Instruments

As previously discussed, the combined algorithm is being developed for use with PMW radiometer and radar measurements from the Tropical Rainfall Measuring Mission (TRMM) satellite. The PMW radiometer is the TRMM Microwave Imager (TMI), a five-frequency (10.7, 19.35, 22.2, 37.0 and 85.5 GHz) conically scanning passive microwave radiometer, and is a modification of a the Special Sensor Microwave/Imager (SSM/I) sensor now flown on the Defense Meteorological Satellite Program (DMSP) satellites. The TMI is supplemented by a first-of-its-kind satellite-borne Precipitation Radar (PR), a single-frequency (13.8 GHz) incoherent cross-track scanning radar, as described by Okamoto et al. (1991). These two instruments will provide the input for the combined retrieval. In addition to the TMI and PR, TRMM will also deploy the Visible-Infrared Scanner (VIRS), a VIS-IR radiometer similar to the AVHRR (Advanced Very High Resolution Radiometer) flown on today's NOAA operational satellites. TRMM will also deploy a Lightning Imaging Sensor (LIS), a single frequency scanning lightning detector. More details about these sensors are given by Simpson et al. (1997). Some instrument specifications for the TRMM instruments are summarized in Table 3.1.

Table 3.1: TRMM Sensor Information

(a) *Basic Sensor Information:*

Sensor	Swath (km)	Scan angle	Scan type
PR (Precipitation Radar)	215	±17°	cross-track
TMI (TRMM Microwave Imager)	760	±65°	conical (49°)
VIRS (Visible-Infrared Scanner)	720	±46°	cross-track
LIS (Lightning Imaging Sensor)	600	±41°	cross-track

(b) *Channel Information:*

Sensor	Channel freq. or wavelength	Horizontal ground resolution at nadir (km)	
PR	13.8 GHz	4.3	
TMI	10.65 GHz	38.3 x 63.2	(cross track x
	19.35	18.4 x 30.4	down-track)
	21.3	16.5 x 27.2	
	37.0	9.7 x 16.0	
	85.5	4.4 x 7.2	
VIRS	0.63 μm	2.0	
	1.6	2.0	
	3.75	2.0	
	10.8	2.0	
	12.0	2.0	
LIS	0.77765 μm	10.0	

(c) *Satellite Platform Information:*

Altitude: ~350 km
Inclination : ~35°

Table 3.2: Aircraft Sensor Information

(a) *Basic Sensor Information:*

Sensor	Aircraft platform	Altitude (km)	Swath (km)	Scan angle
ARMAR (Airborne Rain-Mapping Radar)	DC-8	12	9	±20°
AMPR (Advanced Microwave Precipitation Radiometer)	ER-2	20	40	±45°
MAS (MODIS Airborne Simulator)	ER-2	20	37	±43°

(b) *Channel Information:*

Sensor	Channel freq. or wavelength	Horizontal ground resolution at nadir
ARMAR	13.8 GHz	0.8 km
AMPR	10.7 GHz	2.8 km
	19.35	2.8
	37.1	1.5
	85.5	0.6
MAS	0.664 μm	50 m
	0.875	50
	1.621	50
	1.830	50
	2.142	50
	3.725	50
	8.563	50
	11.002	50
	12.032	50
	13.186	50
	13.952	50

As TRMM is not scheduled for launch until November 1997, measurements from the TMI, PR, VIRS, and LIS instruments are not yet available. To test and evaluate the combined algorithm prior to TRMM's launch, measurements from aircraft instruments designed mimic the performance of their TRMM counterparts are used. PMW measurements from the Advanced Microwave Precipitation Radiometer (AMPR) are used in place of data from the TMI. The AMPR is a cross-track scanning passive microwave radiometer designed primarily at NASA Marshall Space Flight Center, and is flown aboard a NASA ER-2 aircraft. The AMPR passively samples at four frequencies (10.7, 19.35, 37.1, and 85.5 GHz), and is described at length by Spencer et al. (1994). Measurements from the Airborne Rain-Mapping Radar (ARMAR) are used in place of data from the PR. The ARMAR is a coherent radar designed primarily at the NASA Jet Propulsion Laboratory (JPL), and is flown aboard a NASA DC-8 aircraft. The ARMAR actively samples at a single frequency of 13.8 GHz, and unlike the PR has a PMW radiometer at the radar frequency. The ARMAR is described in detail by Durden et al. (1994).

While VIS/IR data are not used in the rainfall retrieval algorithm, data from the MODIS Airborne Simulator (MAS) were available to be used in place of the VIRS. The MAS is an eleven channel VIS/IR sensor (1-VIS, 10-IR channels) flown on a NASA ER-2, and is described by Gumley (1993). Instrument specifications for the aircraft sensors are given in Table 3.2. (Note: no data from an instrument comparable to the LIS was available which was coincident to the AMPR, ARMAR, and MAS datasets.)

3.2 TOGA COARE Data Set

To test and evaluate the combined retrieval method, test cases were selected from aircraft radar and radiometer data taken during the Tropical Ocean Global Atmosphere - Coupled Ocean Atmosphere Response Experiment (TOGA-COARE). This experiment was designed to study the western Pacific warm pool region, in an attempt to better understand the coupling between atmosphere and ocean processes, as well as the atmospheric processes that organize convection in the region. A thorough description of the experiment and its scientific objectives is given by Webster and Lukas (1992). Of particular interest to this research is that among the many accomplishments of TOGA-COARE, it produced some of the most comprehensive observations of convection over the tropical oceans to date.

The test cases used in this research consist of four coordinated flights of the NASA ER-2 (AMPR) and DC-8 (ARMAR) aircraft, flown on 4, 8, 20, and 22 February 1993. Since the aircraft fly at different altitudes, off-nadir views from each of the instruments sample different slant paths through the atmosphere below. Hence for purposes of algorithm testing, only the nadir measurements directly below the aircraft were used. Even though nadir data was used in this study, collocation of the AMPR TBs and ARMAR Zs at nadir was not trivial, since neither the instrument clocks nor the aircraft locations were perfectly synchronized. This was overcome by overlaying plots of the AMPR TBs and the ARMAR 13.8 GHz TB, and manually aligning the data by matching the peaks and valleys found in the PMW TB signal. Further details about the TOGA COARE test cases and the how they were used in algorithm testing is given in Chapter 5.

CHAPTER 4

FORWARD RTE MODELING ANALYSES

4.1 Database distributions of TBs and Reflectivities

In creating the TB-Z-Hyd-VV database, the hydrometeor profiles from the high-resolution hurricane simulation are input to the unified RTE model to produce a set of corresponding brightness temperatures (TBs) and reflectivities (Zs), as illustrated in Figure 2.1. As retrieval tests are to be conducted using TOGA-COARE data from February 1993, average values of sea surface temperature and atmospheric profile information (i.e., temperature, pressure, and mixing ratio) from this month and region are used as input to the RTE model. In order to determine whether the simulation database will provide an adequate basis of initial guesses for the combined retrieval, a logical first step is to determine whether the range of TBs and Zs in the database generated as described above adequately represent the range of the actual instrument measurements. Hence a statistical distribution of the TBs and Zs was produced, in a similar manner to that shown in section 2.2 for the simulation hydrometeors and atmospheric parameters.

The first is the distribution of TBs, presented in Figure 4.1 in the histogram form. The most noticeable feature from these histograms are the large number of profiles having TBs concentrated at high values for 85.5 GHz, and at low TB values for the other frequencies: (a) near 125 K for 10.65 GHz, (b) near 160 K for 19.35 GHz, (c) near 170 K for 37.0 GHz, and (d) from 240-280

56

K for 85.5 GHz. These values correspond to the large number of profiles in the database with a cirrus anvil (represented with the pristine ice category), but with little or no other underlying hydrometeors. For all frequencies but 85.5 GHz, the resultant TBs are near the clear-sky values, while at 85.5 GHz the pristine ice does have a noticeable scattering effect, decreasing the TBs from the clear sky value over a range of several Kelvins. The distribution of the remainder of the TBs outside these ranges are a function of emission and scattering by hydrometeors. The broad distributions over the entire TB range indicates a well distributed sample of differing vertical distributions and hydrometeor amounts for the combined retrieval to choose from during the initial guess procedure. Further details are given in the next section.

The effect of the significant amount of cirrus-only cases is also prominent in the reflectivity distribution, given in Figure 4.2. Typically the range in reflectivities produced by the RTE model for the cirrus deck is ~15-25 dBZ, corresponding to the peaks in the distributions shown in Figure 4.2. The lowest Z values in parts (a) and (b) of Figure 4.2 are not due to minimal back-scattering from small hydrometeor amounts high in the column, but to regions near the surface which are heavily attenuated by large amounts of rain above. Finally the maximum reflectivities, near 55 dBZ as shown in Figure 4.2(c), are due solely to hydrometeor back-scattering. This is notable as the model does not produce reflectivities due to back-scattering from the surface itself, which regularly exceed 80 dBZ as measured by the ARMAR. Hence the error function (see section 2.4) does not include the surface layer in calculating the difference in reflectivity between the measured data and the model.
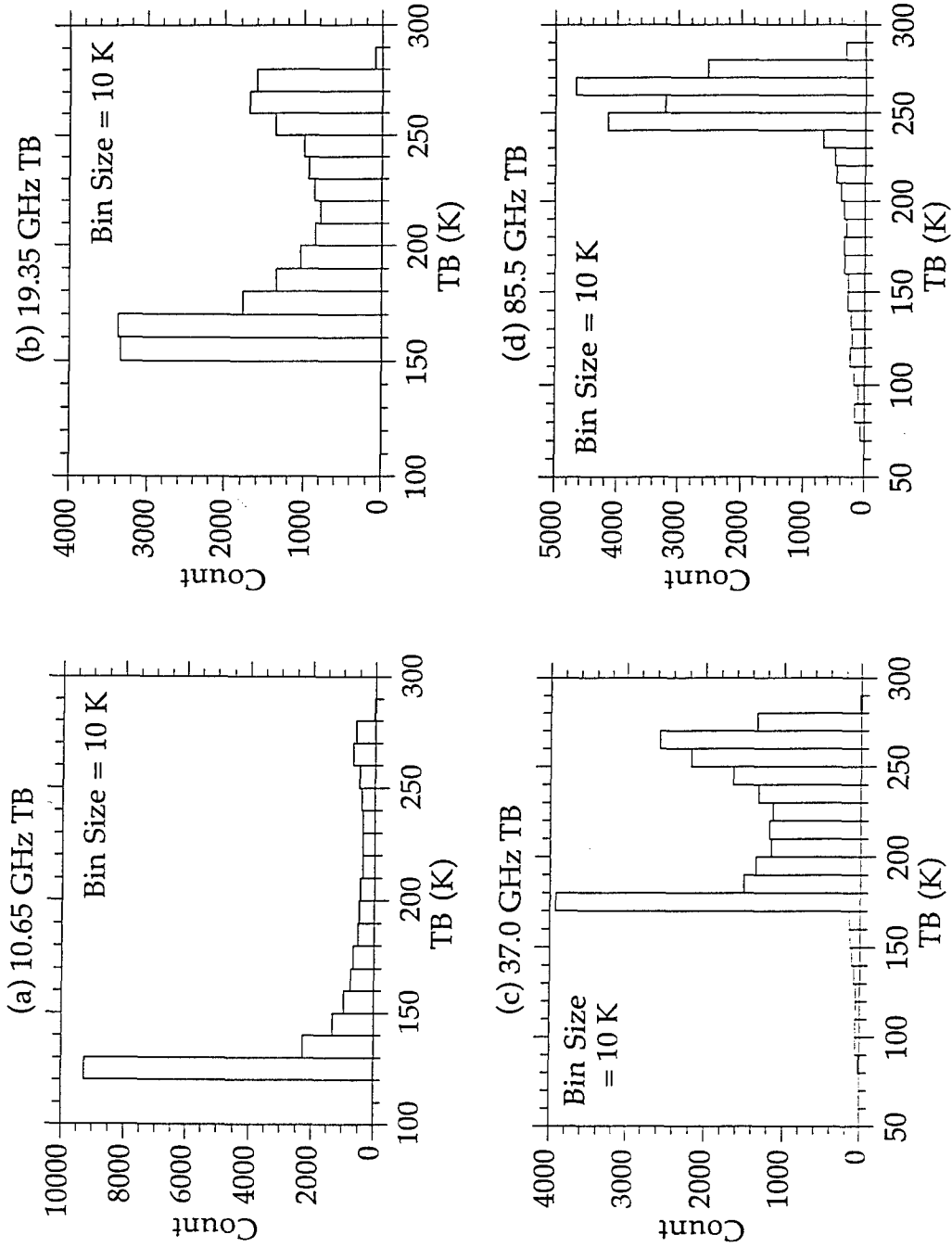
Figure 4.1: Histogram of TBs from the simulation database, which contains 20,081 sets of TBs in total.

58
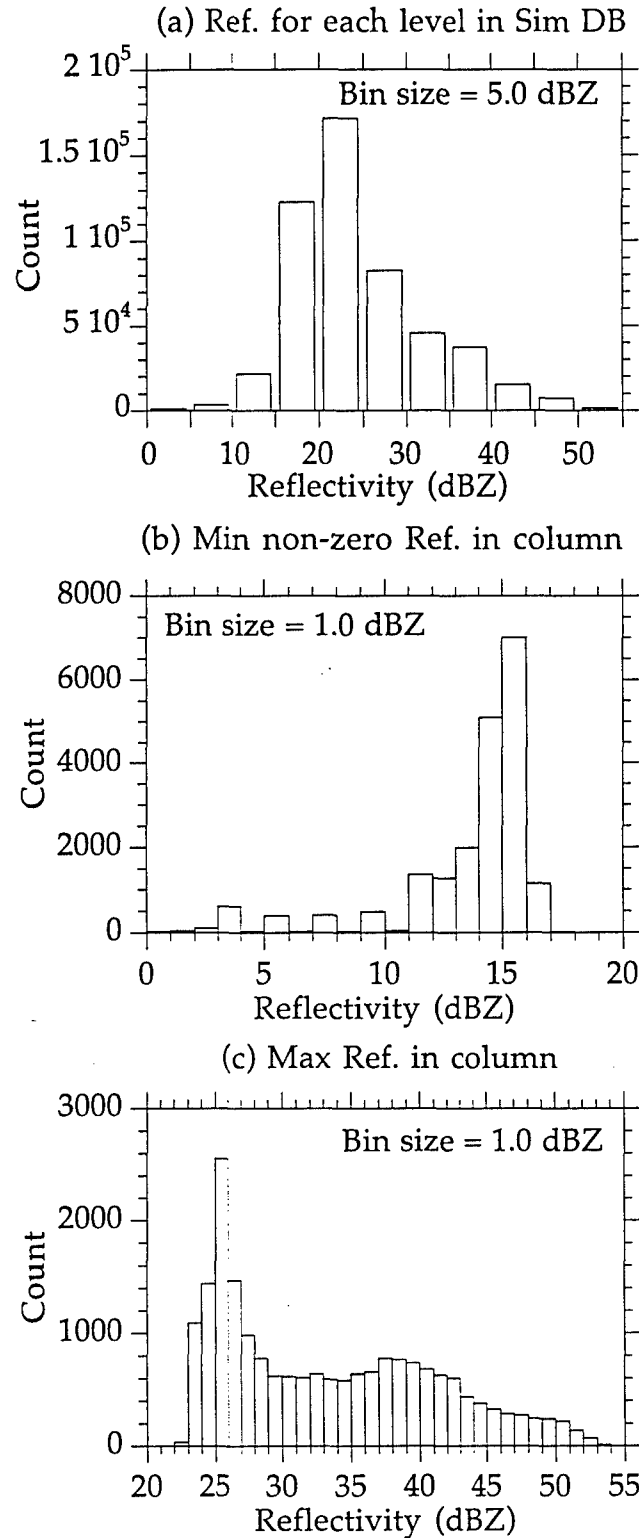
Figure 4.2: Histogram of Zs from the simulation database, including (a) all values contained in 20,081 total profiles, (b) minimum non-zero value of each profile, and (c) maximum value of each profile.
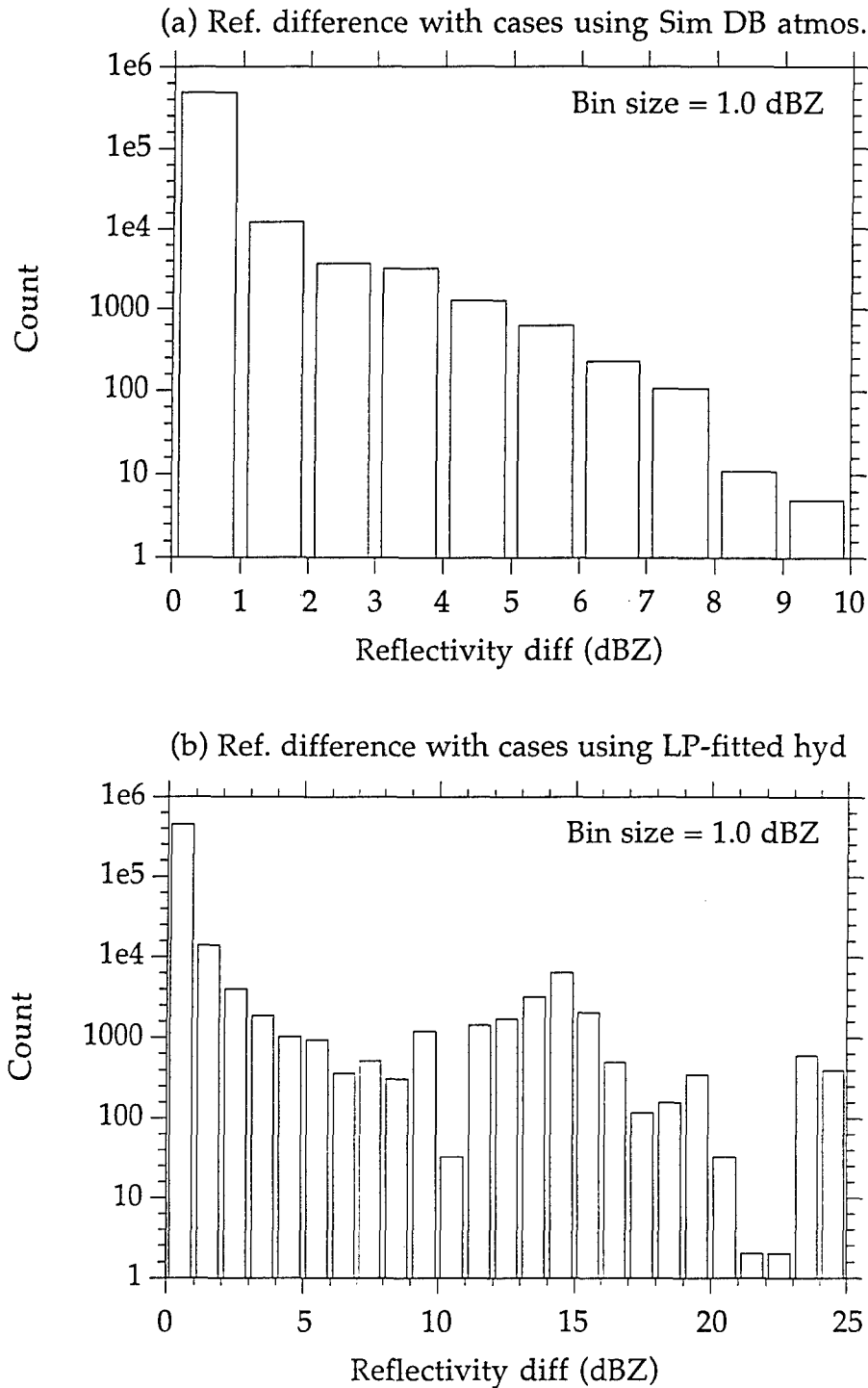
Figure 4.3: Histogram of reflectivity differences between RTE calculations using different values of (a) atmospheric profiles (TOGA-COARE vs. simulation soundings) and (b) hydrometeor profiles (original vs. Legendre polynomial-fitted profiles).
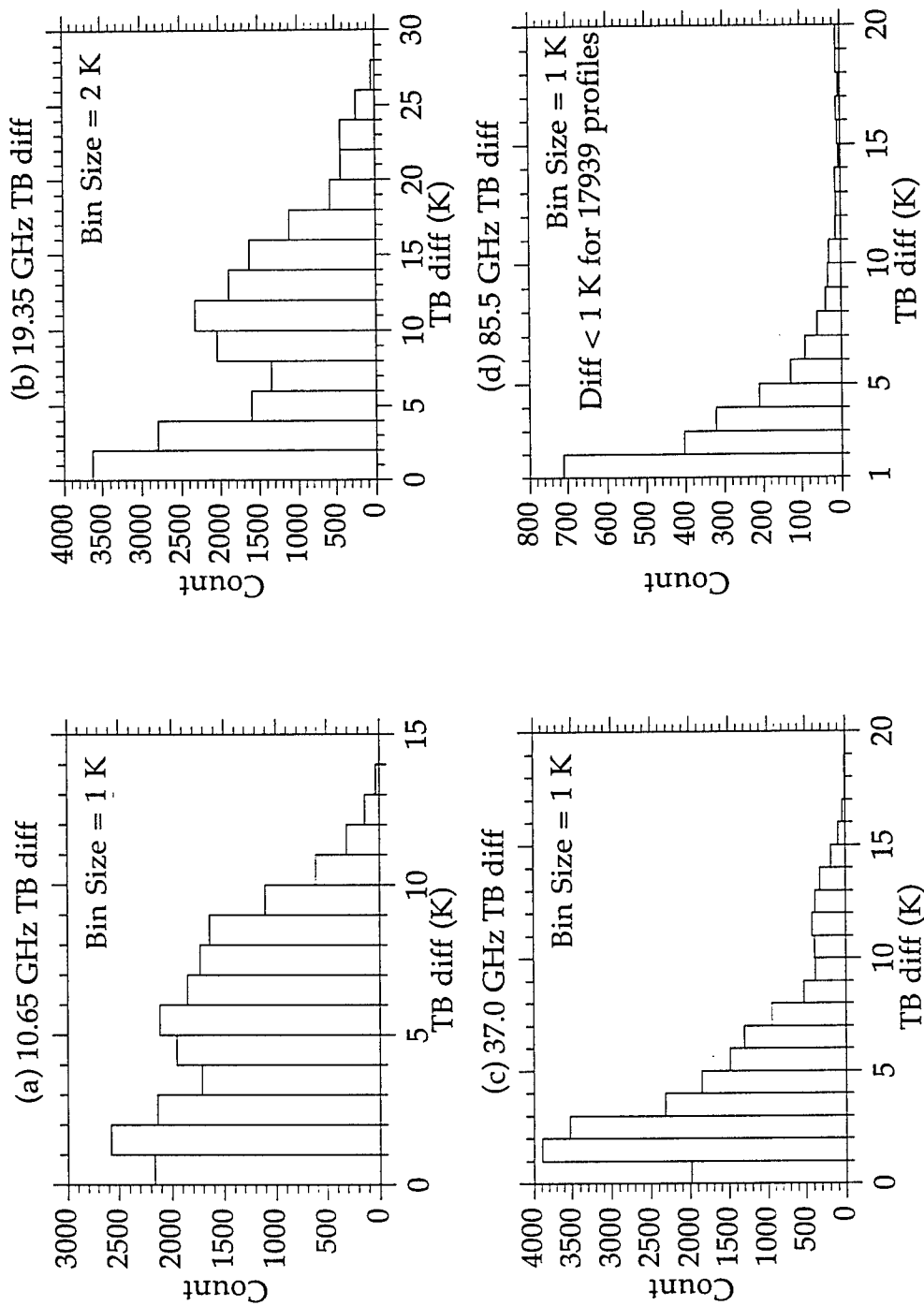
Figure 4.4: Histogram of TB differences between RTE calculations using different values of atmospheric profiles (TOGA-COARE vs. simulation soundings).

As discussed in section 2.2, the high-resolution hurricane simulation produced an atmosphere more warm and moist than is normal for a standard tropical atmosphere. Since the retrieval tests in this research are from TOGA COARE, where temperature and moisture were much closer to the climatological norm [as reported in TCIPO (1993)] than were those from the hurricane simulation database, the forward RTE calculations for producing the database TBs and Zs used average atmospheric conditions from TOGA COARE instead of those provided by the hurricane simulation. For purposes of comparison, the database was also generated using the atmospheric profiles provided by the simulation as input to the unified RTE model.

The differences between the Zs and TBs calculated using the different atmospheric conditions are given in Figures 4.3(a) and 4.4, respectively. While Figure 4.3(a) shows that most reflectivities from the database are changed no more than a few dBZ, some cases did produce larger changes. Figure 4.4 shows that the effect on the TBs is spread over a larger percentage of the cases within the database than in the case for the Zs. The effect on the TBs is due to the dependence of emission at microwave frequencies on both temperature and humidity. This effect is seen less for 85.5 GHz [Figure 4.4(d)], as emission plays less of a role on the total TB signature than at the lower frequencies, which will be discussed in further detail later in the Chapter. Given these effects, the TBs and Zs of all database profiles should be generated under atmospheric conditions similar to those where the retrieval is being conducted. Also each database entry should be calculated under the same atmospheric conditions as all the rest, lest the selection of the first guess using the error function confuse TB and Z differences due to temperature and

moisture effects with those from purely hydrometeor effects, which are the focus of the retrieval process.

Another part of the algorithm that affects the TBs and Zs is the use of structure functions to represent the hydrometeor profiles, as described in section 2.5. As these fits are not exact, the hydrometeor concentration at any given level can change as a result of the structure function fit, which in turn leads to changes in the TBs and Zs. Changes to reflectivities due to this effect are illustrated in Figure 4.3(b). While this figure only displays changes up to 10 dBZ, there are individual cases where the changes are larger. For example, in cases where small hydrometeor amounts are present at a given level (generating a reflectivity ~ 20 dBZ at that level), the structure function fitting can replace the small hydrometeor value with 0 dBZ, which drops the reflectivity generated by the RTE model from ~20 dBZ to 0 dBZ. The effect on the TBs, as shown in Figure 4.5, is less pronounced, as the TBs respond more to the total integrated amount of hydrometeors in the column than to their vertical distribution; further discussion on this point is given in the next section. Due to the TB and Z changes arising from structure function representation, the fitting is accomplished during the original creation of the TB-Z-Hyd-VV database as shown in Figure 2.1. If the database had been created using the original non-transformed hydrometeor profiles, the first step in the optimization process (as described in section 2.5), which would be to perform the structure function transformation, could produce significantly different TBs and Zs than the first guess. When the transformed profiles were then input into the error function, it could then result in a worse match with the measurements, which would immediately end the optimization as the first guess was degraded instead of improved.

63
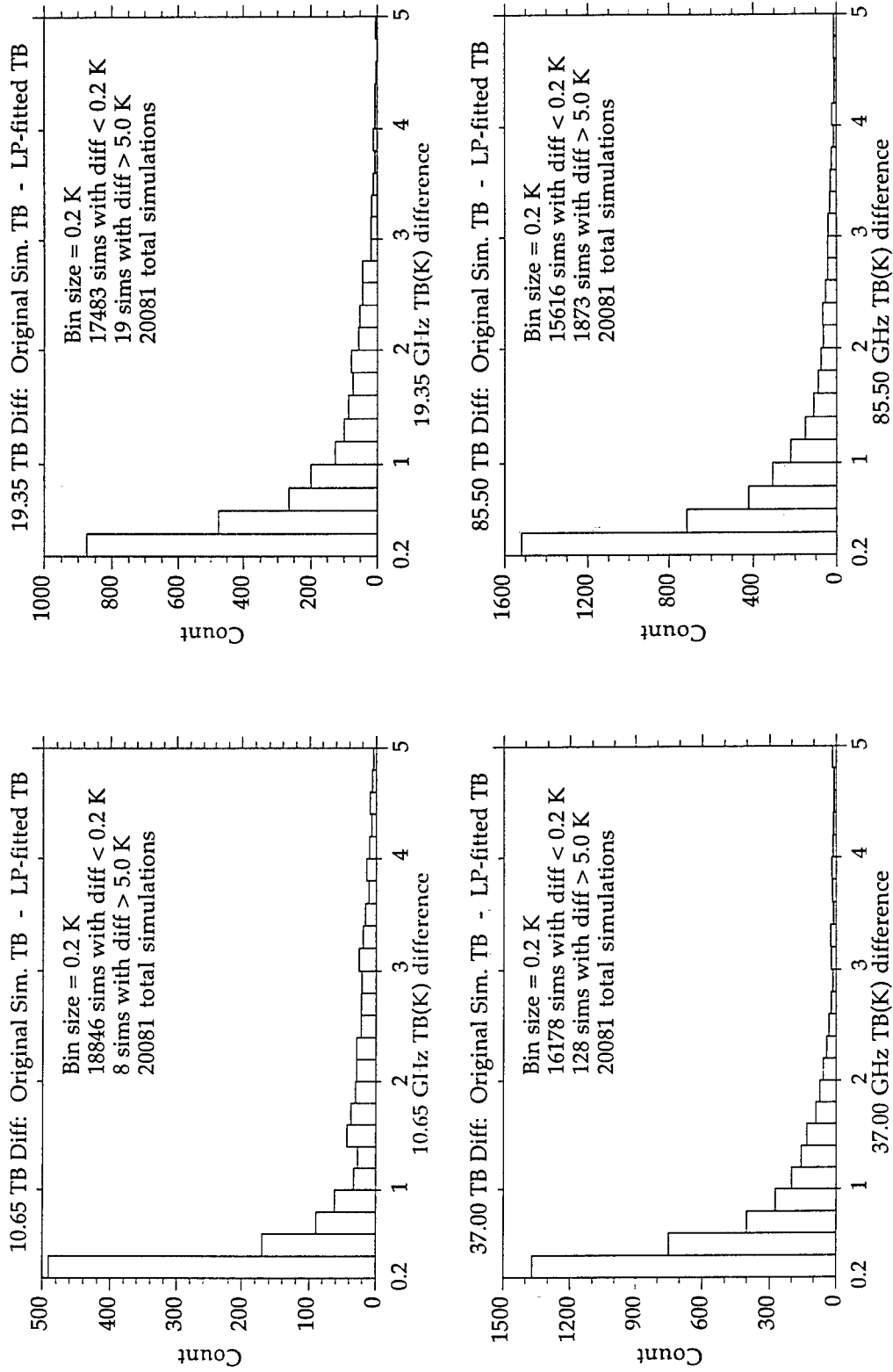
Figure 4.5: Histogram of TB differences between RTE calculations using different values of hydrometeor profiles (original vs. Legendre polynomial-fitted profiles).

64
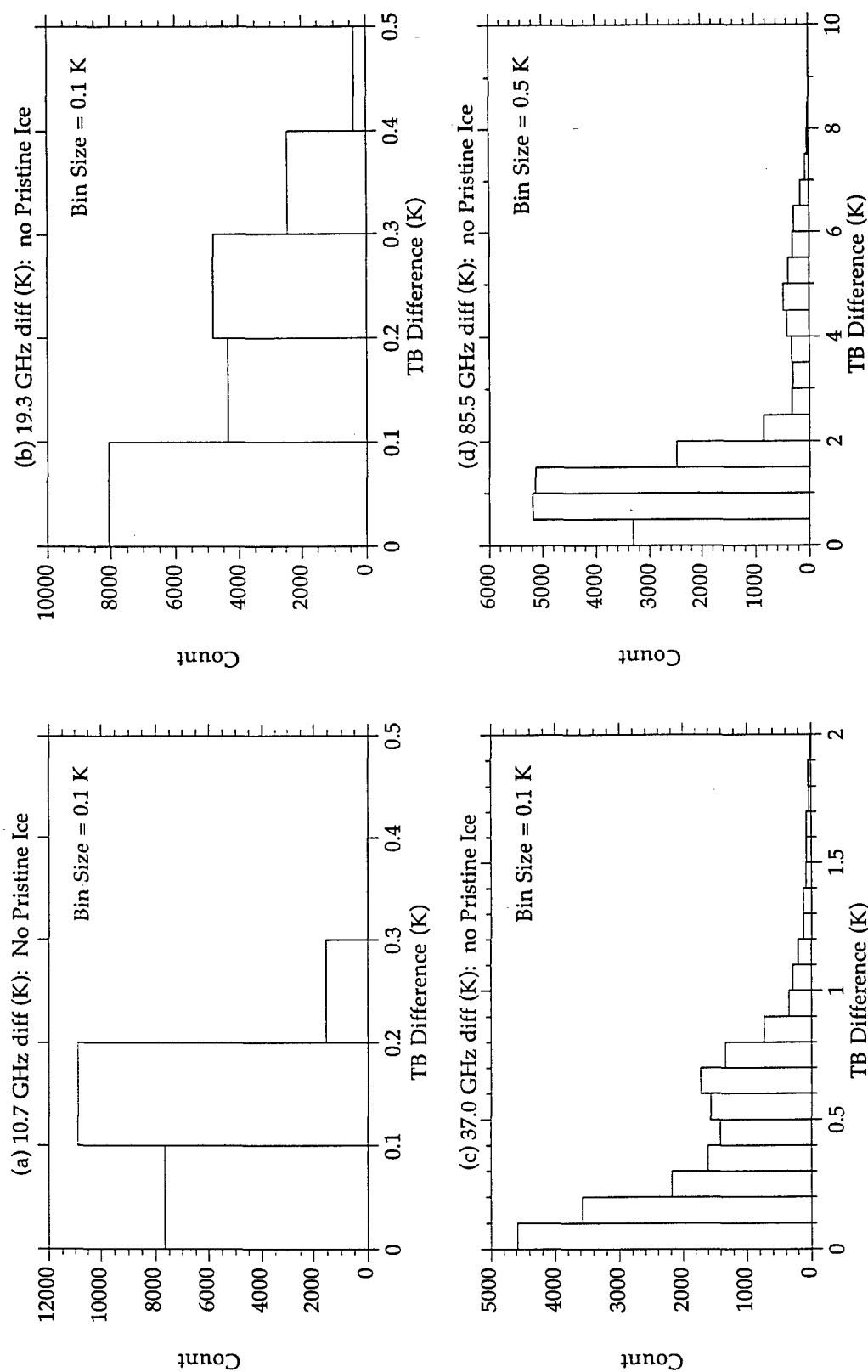
Figure 4.6: Histogram of TB differences between RTE calculations using different values of hydrometeor profiles (profiles with all hydrometeors vs. profiles with no pristine ice).
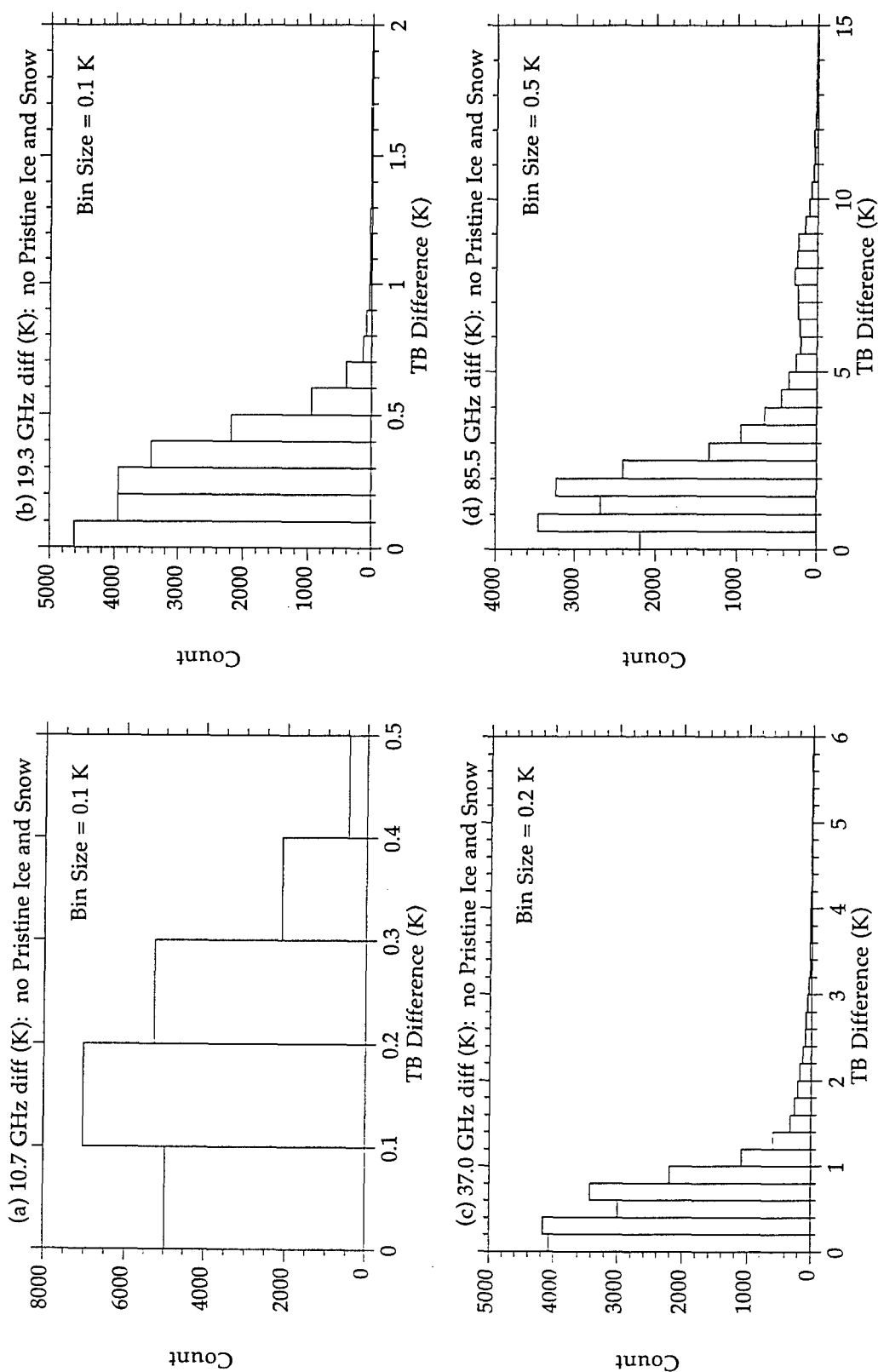
Figure 4.7: Histogram of TB differences between RTE calculations using different values of hydrometeor profiles (profiles with all hydrometeors vs. profiles with no pristine ice and snow).

One final factor contributing to TB and Z differences are the multiple versions of the database, as described in section 2.2. Due to the fact that all profiles in the database contained high level ice as a result of the cirrus anvil present throughout the simulation, pristine ice and then both pristine ice and snow were removed from the original simulation profiles in order to produce new profiles without overlying high cloud. This is primarily done to allow for better reflectivity matches at higher levels. For example, for a case of shallow precipitation with no upper level hydrometeors, the ARMAR measures zero reflectivity at levels above the shallow precipitating column, while all the original simulation profiles would have non-zero reflectivities aloft due to the cirrus anvil. Figures 4.6 and 4.7 illustrate the resultant effect on removing pristine ice, and then removing both pristine ice and snow, respectively. It is shown in Figure 4.6 that while the removal of pristine ice does have some effect at 85.5 GHz, where ice scattering is reduced somewhat, the effects at the lower frequencies is minimal. The effects of removing snow as seen in Figure 4.7 are more pronounced, due to the greater scattering cross-section of snow when compared to pristine ice. Nevertheless the effects at 10.65 and 19.35 GHz are relatively small.

Hence the three versions (#1 with all hydrometeors present, #2 without pristine ice, and #3 without pristine ice and snow) of the database, all of which are searched during the initial guess portion of the retrieval, allow a greater variety of reflectivity profiles for roughly equivalent TB values. This also aptly illustrates one of the weaknesses of passive-only retrieval, namely the non-uniqueness problem in which hydrometeor structures with different vertical distributions can produce nearly identical brightness temperatures. One of the foremost improvements of combined retrieval is that by including

the reflectivities as additional constraints on the retrieval, the non-uniqueness problems can be reduced, which will be illustrated in the next chapter.

4.2 Relationship of TBs and Reflectivities to Hydrometeor Structures

Previous modeling studies by Mugnai et al. (1988), Smith and Mugnai (1988, 1989), Adler et al. (1991b), and others have demonstrated that upwelling microwave brightness temperatures at the top of a precipitating column respond to both emission and reflection from the surface and emission and scattering by hydrometeors. For low frequencies such as 10.65 GHz, the signal is primarily driven by emission from the surface and liquid hydrometeors, while for high frequencies such as 85.5 GHz, the emission signal is obscured by the scattering by frozen hydrometeors when present in sufficient amounts. As the surface emission characteristics and atmospheric conditions were the same for all cases in the TB-Z-Hyd-VV simulation database, differences in the TBs and Zs are due solely to differences in hydrometeor structure.

In an attempt to understand the impacts of hydrometeor structure on the PMW and radar signals, analyses of the matched TB-Z-Hyd-VV simulation database were performed by comparing the hydrometeor profiles with their resultant radiative values, beginning with the TBs. The surface rain rate and total integrated water path (IWP) of each hydrometeor category is plotted against the corresponding 10.65 GHz TB in Figure 4.8; the same is done for 19.35 GHz TB, 37.0 GHz TB, and 85.5 GHz TB, in Figures 4.9, 4.10, and 4.11, respectively.
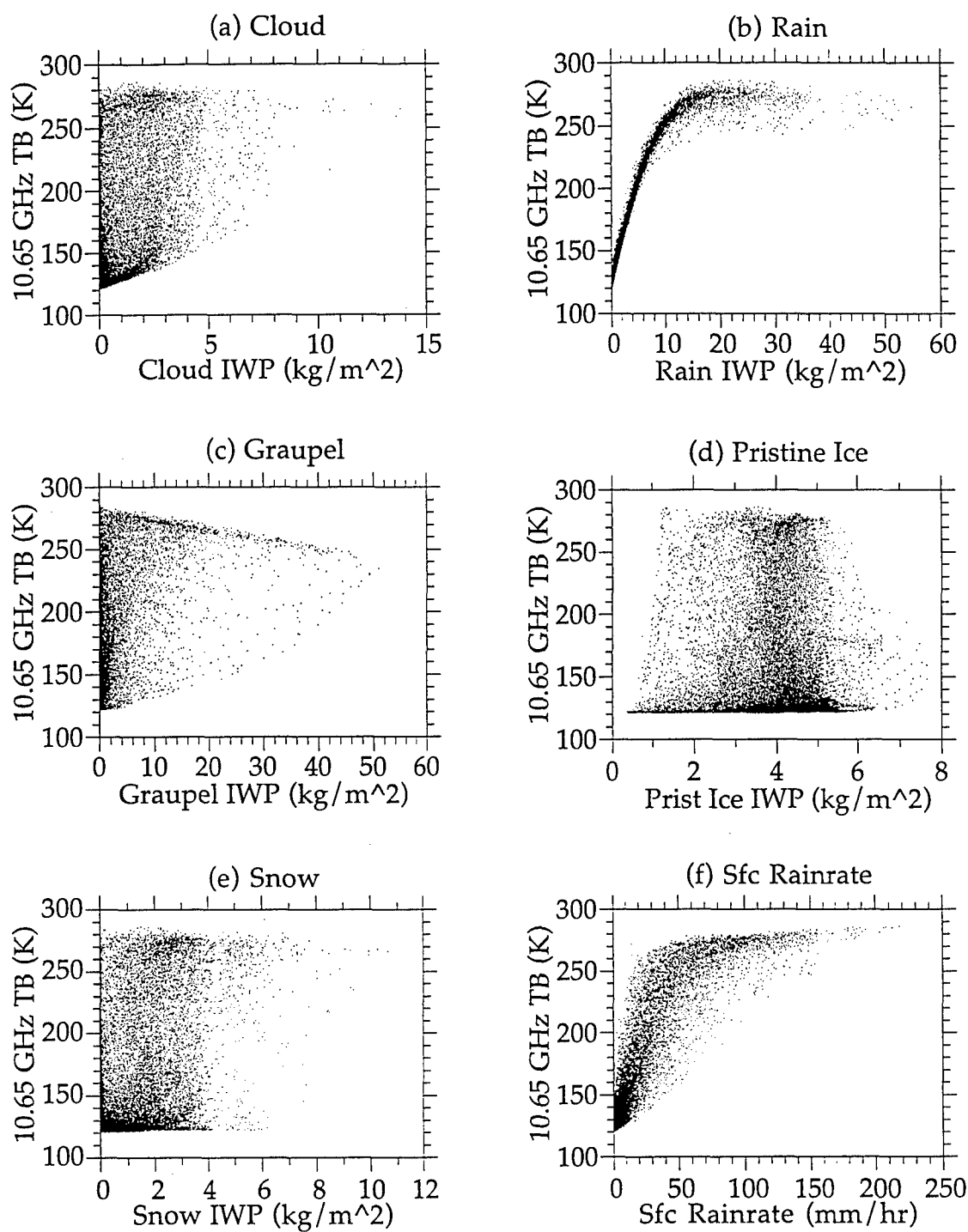
Figure 4.8: Scatterplot of simulation database values of 10.65 GHz TB vs. hydrometeor IWP (a)-(e) and surface rainrate (f).
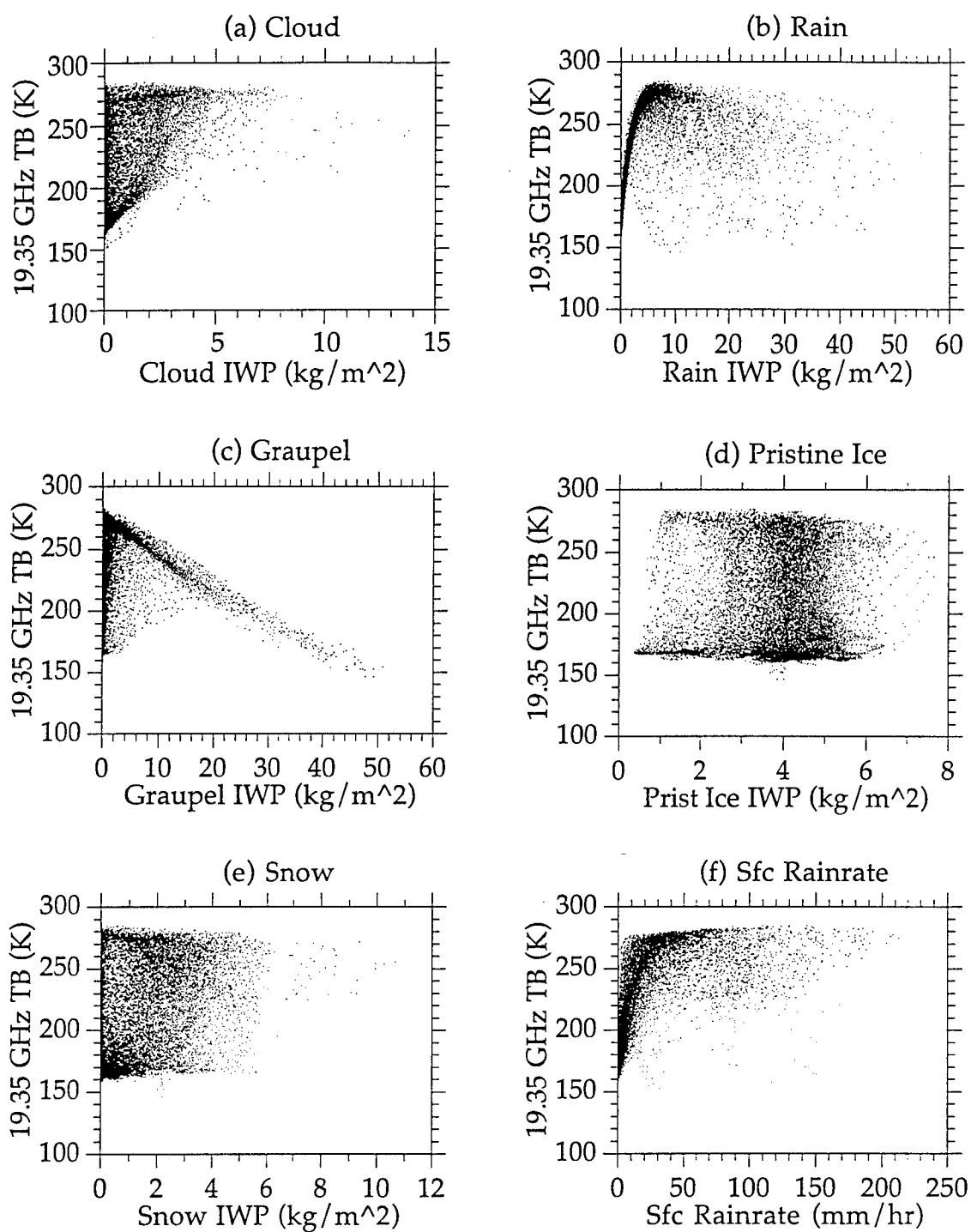
Figure 4.9: Scatterplot of simulation database values of 19.35 GHz TB vs. hydrometeor IWP (a)-(e) and surface rainrate (f).
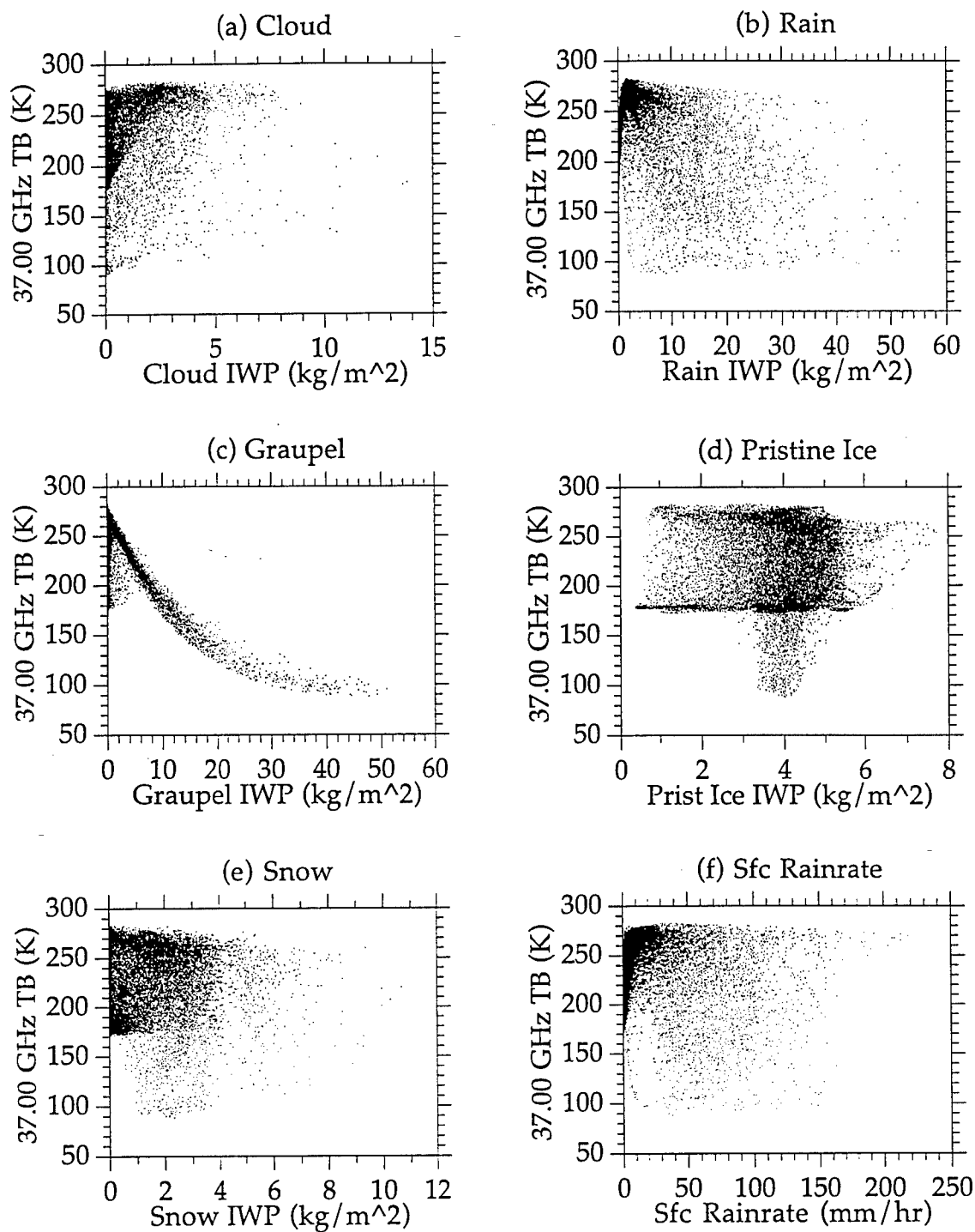
Figure 4.10: Scatterplot of simulation database values of 37.0 GHz TB vs. hydrometeor IWP (a)-(e) and surface rainrate (f).
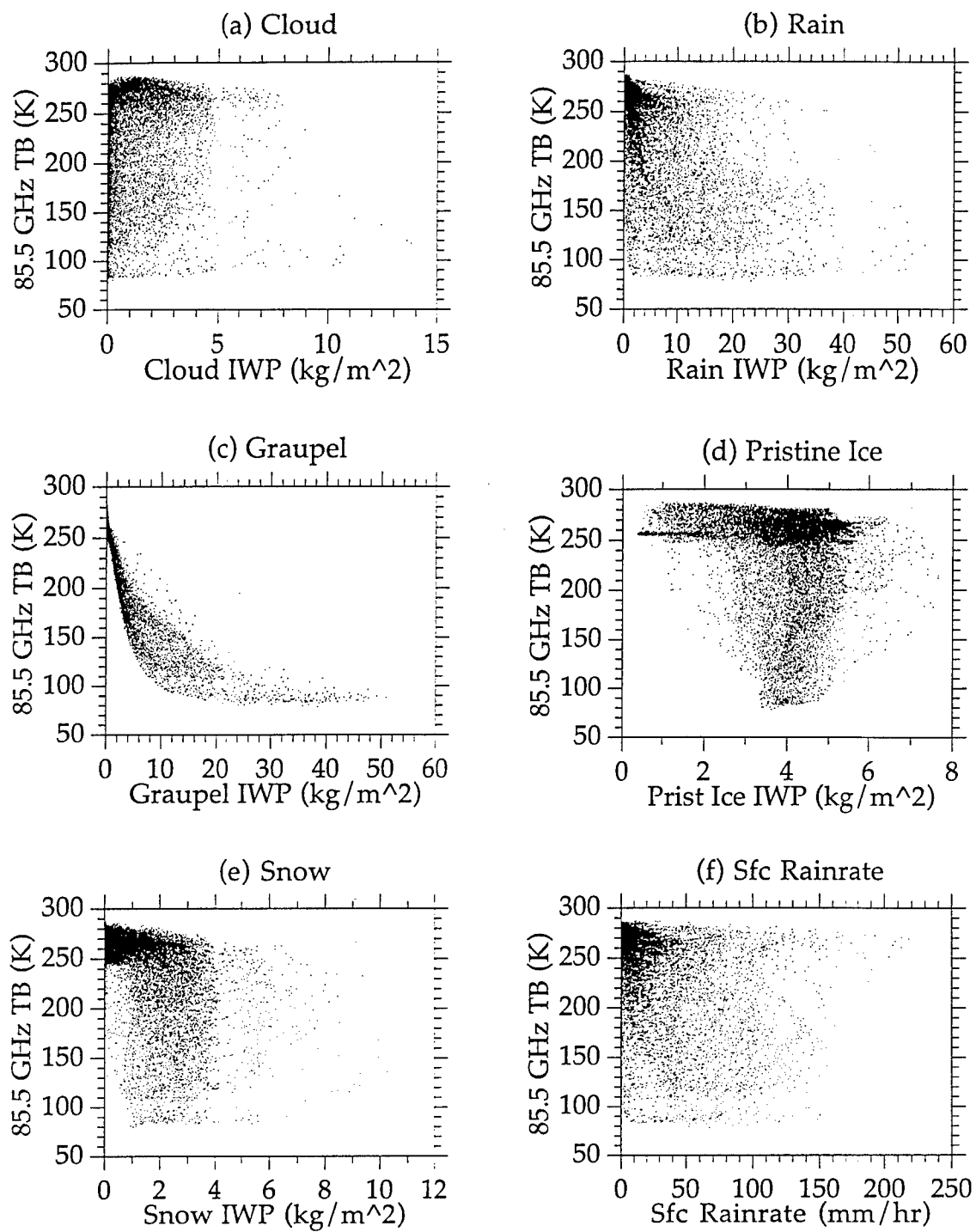
Figure 4.11: Scatterplot of simulation database values of 85.5 GHz TB vs. hydrometeor IWP (a)-(e) and surface rainrate (f).

The dependence of the 10.65 GHz TB on emission is clearly seen in Figure 4.8(b). As the amount of rain in the column increases, the brightness temperature increases due to emission until the signal saturates near 290 K, where rain IWP approaches 20 kg m^{-2}. As more rain is added the TB signal begins to decrease slightly due to the following effect. As rain is added past the point of signal saturation, the weighting function begins to move upward from its peak at the surface (as shown in Figure 1.1) to higher in the column. As atmospheric temperature decreases with increasing height above the surface, the peak of the weighting function is pushed to a level of colder temperature, which decreases the emission.

This follows closely with the relationship of 10.65 GHz TB with surface rain rate, shown in Figure 4.8(f), due to the high degree correlation with the total amount of rain in the column and the amount which reaches the surface. Also of note is the poor apparent correlation of cloud IWP with 10.65 GHz TB. While the TB is a function of emission from all suspended liquid, including cloud, the signal is dominated by the relatively larger rain drops. In addition to their larger size, the rain is also present in greater amounts, as seen in Figure 2.2(a), where the average water content in the simulation database for rain peaks at ~0.7 g•m^{-3}, while the cloud peaks at a value of ~0.15 g•m^{-3}. Their cumulative emission effects are handled by the forward RTE model, which provides a way to objectively account for their microphysical differences.

The situation for 19.35 GHz, shown in Figure 4.9, is much the same as for 10.65 GHz. However as seen in Figure 4.9(b), the TB signature saturates at a rain IWP value near 5 kg m^{-2}, a much lower value than for 10.65 GHz. The same is true for the surface rain rate in part (f) of the figure, where the TB

plateaus within a much shorter range of TBs and rain rates. Also the scattering due to graupel is much more defined than for 10.65 GHz TB, as seen in part (c), although for smaller graupel IWP values the signature is still dominated by emission effects. This transition in the TB signature from dominance by emission to scattering is more pronounced when the frequency is increased to 37.0 GHz, as illustrated by Figure 4.10. The graupel IWP signature in part (c) of the figure demonstrates a well-defined depression due to scattering, with the exception of values less than 5 kg m^{-2} where emission still makes a substantial contribution to the overall signal. Like the previous discussion of total emission as a function of all liquid, total ice scattering is affected by all frozen hydrometeors. However with the apparently poor correlation of scattering by pristine ice and snow, as seen in parts (d) and (e) of the figure, the scattering signal is clearly driven by the graupel, much like the emission which is dominated by the rain. The dominance of ice scattering over liquid emission is nearly complete for the 85.5 GHz TB, as seen in Figure 4.11. The emission signature in the rain IWP and surface rain rate, panels (a) and (f), is almost completely gone. Also the emission contribution from liquid for cases of low graupel content, seen for 37.0 GHz in Figure 4.10 (c), has vanished for 85.5 GHz, as seen in Figure 4.11(c).

The preceding figures demonstrated that the emission effects of liquid and the scattering effects of ice sometimes obscure each other. In order to sort out their independent properties, all TBs in the database were recalculated using only the liquid hydrometeors (no ice), and then again with only the frozen hydrometeors (no liquid). The results for 10.65 GHz are shown in Figure 4.12. The TBs produced using all hydrometeors as input to the RTE model are plotted versus rain IWP in panel (a); this is contrasted with a plot

74

of TBs produced omitting all ice hydrometeors versus rain IWP, plotted in panel (b). The primary difference occurs at large values of rain IWP produced by deep convection, where large amounts of ice also tend to be present. The TB signature, already saturated with respect to emission, can be reduced a little further by scattering when large amounts of ice are added. Note that this effect is small at 10.65 GHz, and is rarely seen in real measurements. Similarly the 10.65 GHz TBs produced using all hydrometeors as input to the RTE model are plotted versus graupel IWP in panel (c) of Figure 4.12, which is contrasted with the plot off TBs generated omitting all liquid hydrometeors versus graupel IWP, shown in panel (d). Considering the small scattering effects of ice at 10.65 GHz, the relatively small change in TB exhibited in Figure 4.12(d) should be expected. However the fact that TBs increase slightly as graupel IWP is increased demonstrates emission by the ice itself can be relevant in the absence of liquid hydrometeors.

Just as in the preceding discussion regarding 10.7 GHz, the behavior of the 19.35 GHz and 37.0 GHz TBs as ice and liquid are separately withheld from the RTE calculation are represented in Figures 4.13 and 4.14, respectively. While the emission signature in panel (a) of both figures is contaminated by ice scattering, the removal of the ice leads to the well-defined emission signature shown in panel (b). Similarly the removal of all liquid from the TBs in panel (c) removes the liquid emission signature seen at low graupel IWP values, resulting in panel (d) where a brief ice emission signature at low graupel IWP values turns over into a drop off of TB due to scattering. Finally the effects on 85.5 GHz are given in Figure 4.15. Unlike that for the lower frequencies, Figure 4.15 (b) shows that the TB signal does not rise as a function of IWP due to emission, but becomes immediately saturated and declines due
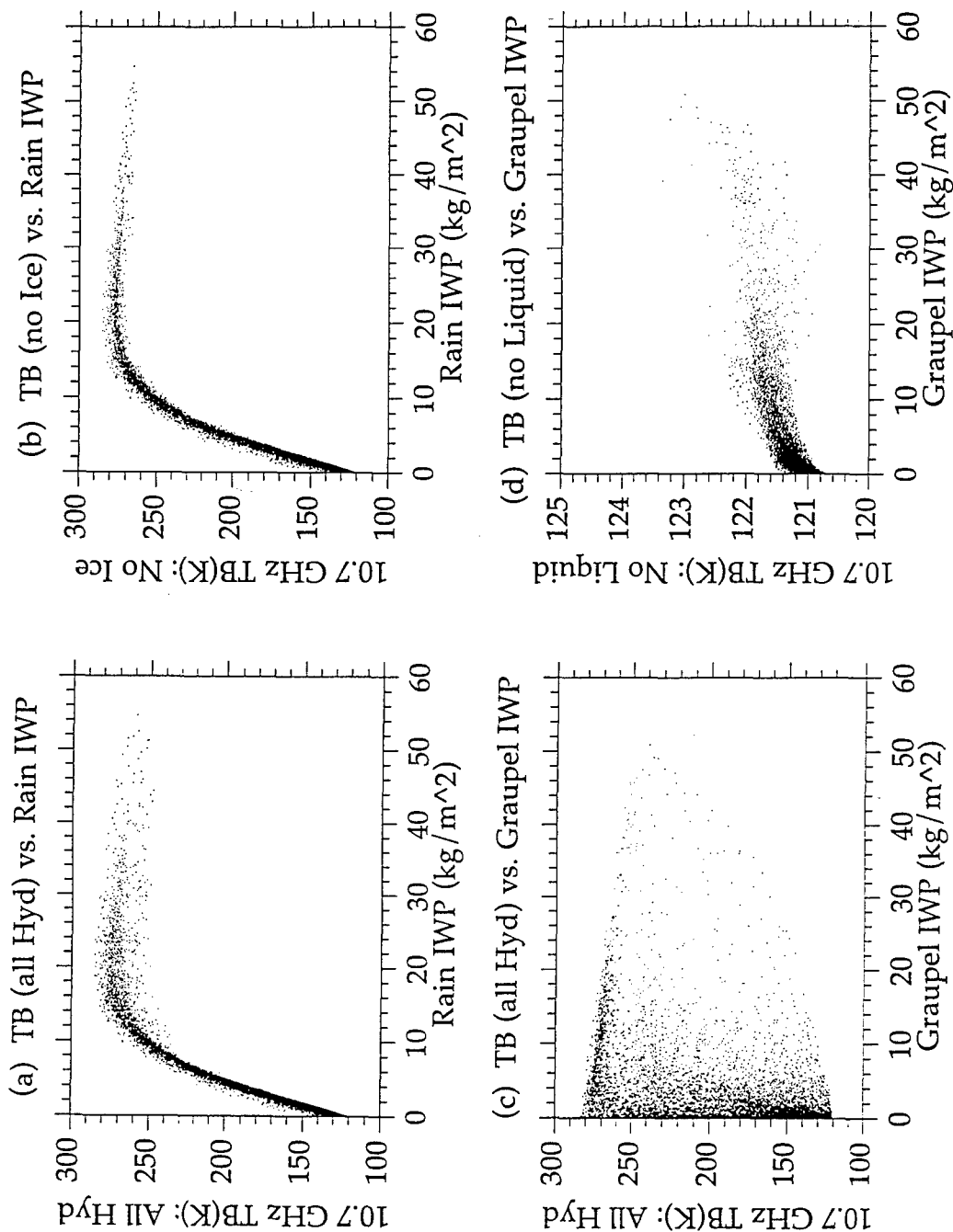
Figure 4.12: Scatterplot of database values of rain IWP vs. 10.7 GHz TB from RTE calculations using (a) all hydrometeors and (b) no ice, followed by Graupel IWP vs. 10.7 GHz TB from RTE calculations using (c) all hydrometeors and (d) no liquid.
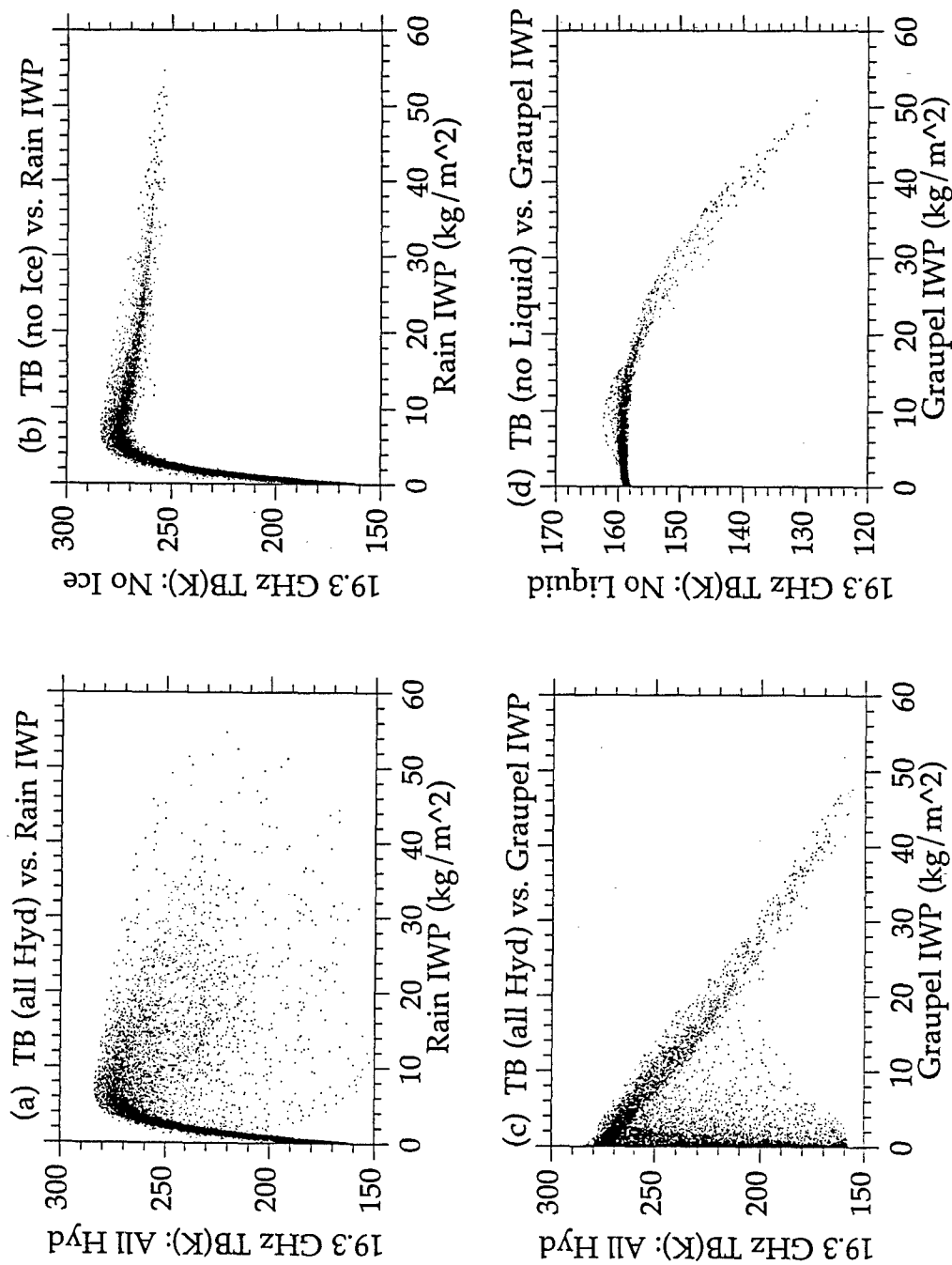
Figure 4.13: Scatterplot of database values of rain IWP vs. 19.3 GHz TB from RTE calculations using (a) all hydrometeors and (b) no ice, followed by Graupel IWP vs. 19.3 GHz TB from RTE calculations using (c) all hydrometeors and (d) no liquid.
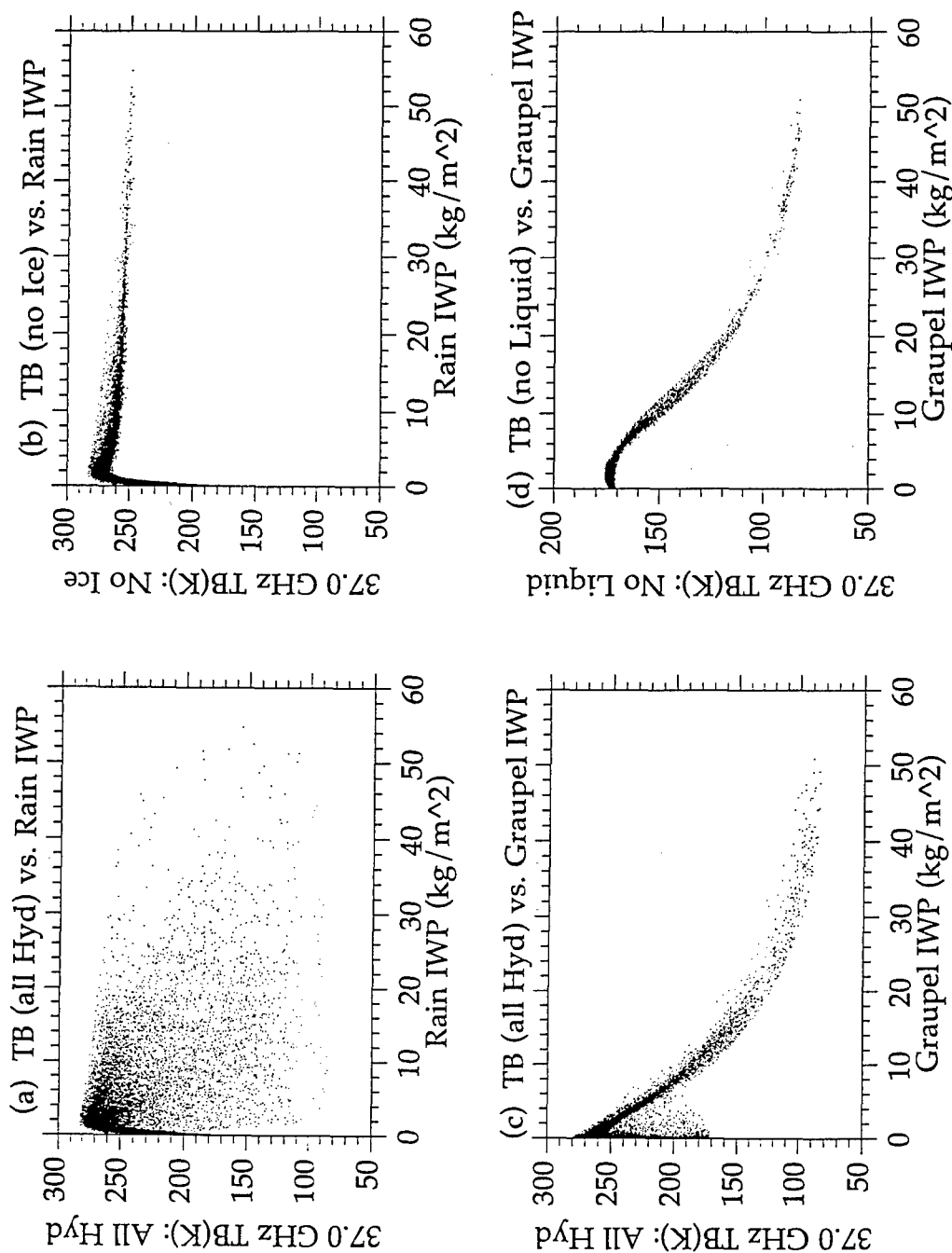
Figure 4.14: Scatterplot of database values of rain IWP vs. 37.0 GHz TB from RTE calculations using (a) all hydrometeors and (b) no ice, followed by Graupel IWP vs. 37.0 GHz TB from RTE calculations using (c) all hydrometeors and (d) no liquid.

78
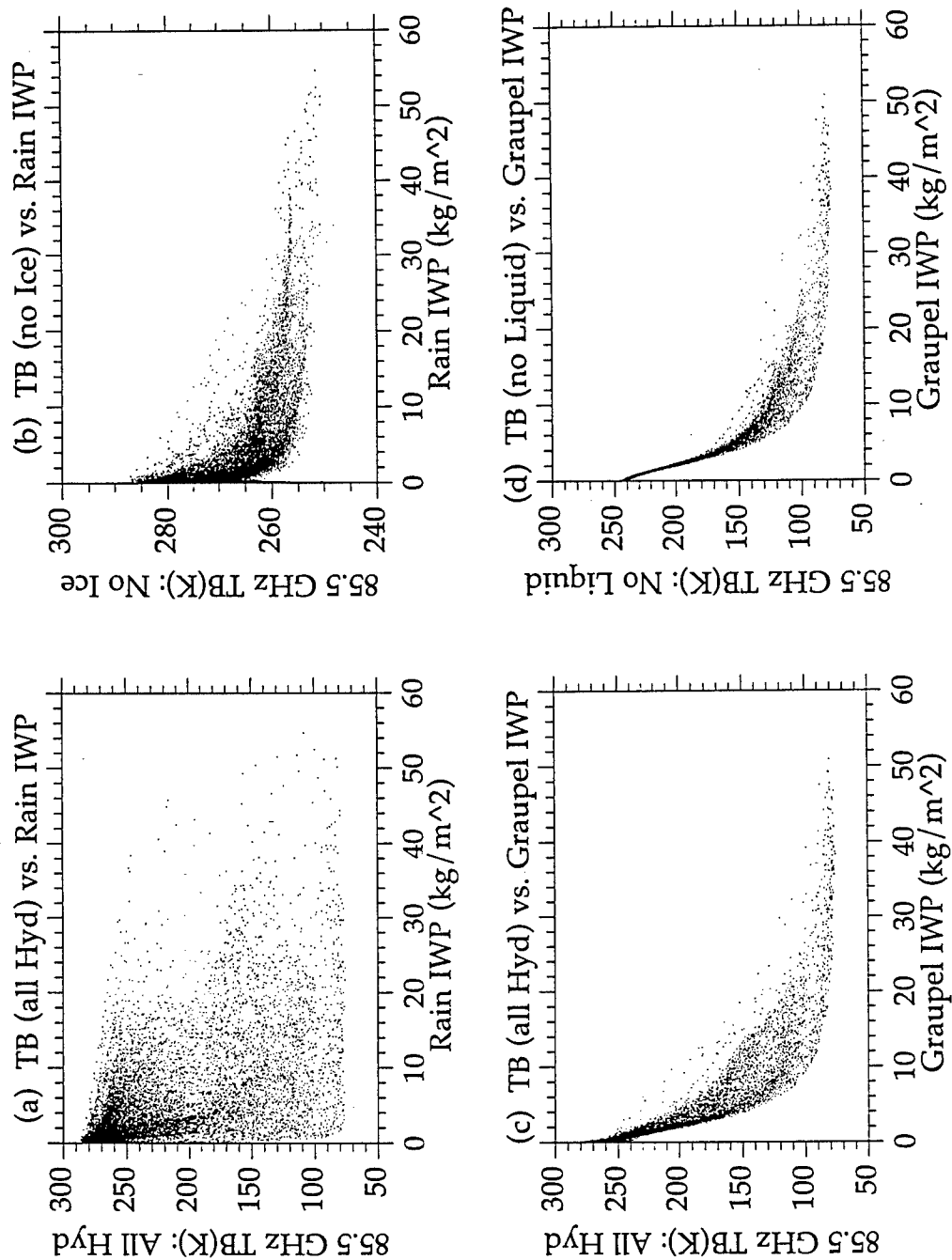
Figure 4.15: Scatterplot of database values of rain IWP vs. 85.5 GHz TB from RTE calculations using (a) all hydrometeors and (b) no ice, followed by Graupel IWP vs. 85.5 GHz TB from RTE calculations using (c) all hydrometeors and (d) no liquid.

79

to the vertical displacement of the weighting function (as previously explained). The scattering signal due to graupel, as shown in panel (c), is much less affected than for the other frequencies by the removal of the liquid, as shown in panel (d), due to the fact that even small amounts of graupel tend to obscure the underlying surface and liquid hydrometeor emission signature.

Aside from their effects on upwelling TBs, the hydrometeors also provide the back-scattering media for the down-looking radar. Scatter plots of surface rain rate, rain IWP, and graupel IWP are given in Figures 4.16, 4.17, and 4.18, respectively. One feature that stands out in these three figures is the truncation of the reflectivities near 20 dB. This is an artifact of the hydrometeor profiles present in the hurricane simulation database, where the equivalent water content at each level was truncated to zero for values less than 10^{-5} g m^{-3}, in order to avoid computational problems in some of the RTE code. This visible demarcation of reflectivities in the figures represents the corresponding value for this minimum hydrometeor content; values which drop below are due to attenuated signals deeper in the column.

The levels of the radar reflectivities chosen for analysis correspond to the peak in the average hydrometeor profiles displayed in Figure 2.2 for (a) rain (height = 0.1 km), (b) cloud (height = 2.5 km), (c) graupel (height = 6.2 km), (d) snow (height = 7.8 km), and (e) pristine ice (height = 11.8 km). Figure 4.16(a) shows a good correlation between surface rain rate and near-surface reflectivity for low values of rain rate; however for higher rain values the rain itself attenuates the radar signal. The next higher level in panel (b) mitigates the attenuation effect somewhat, as the amount of rain between that level and the radar above is less and hence the attenuation is reduced.
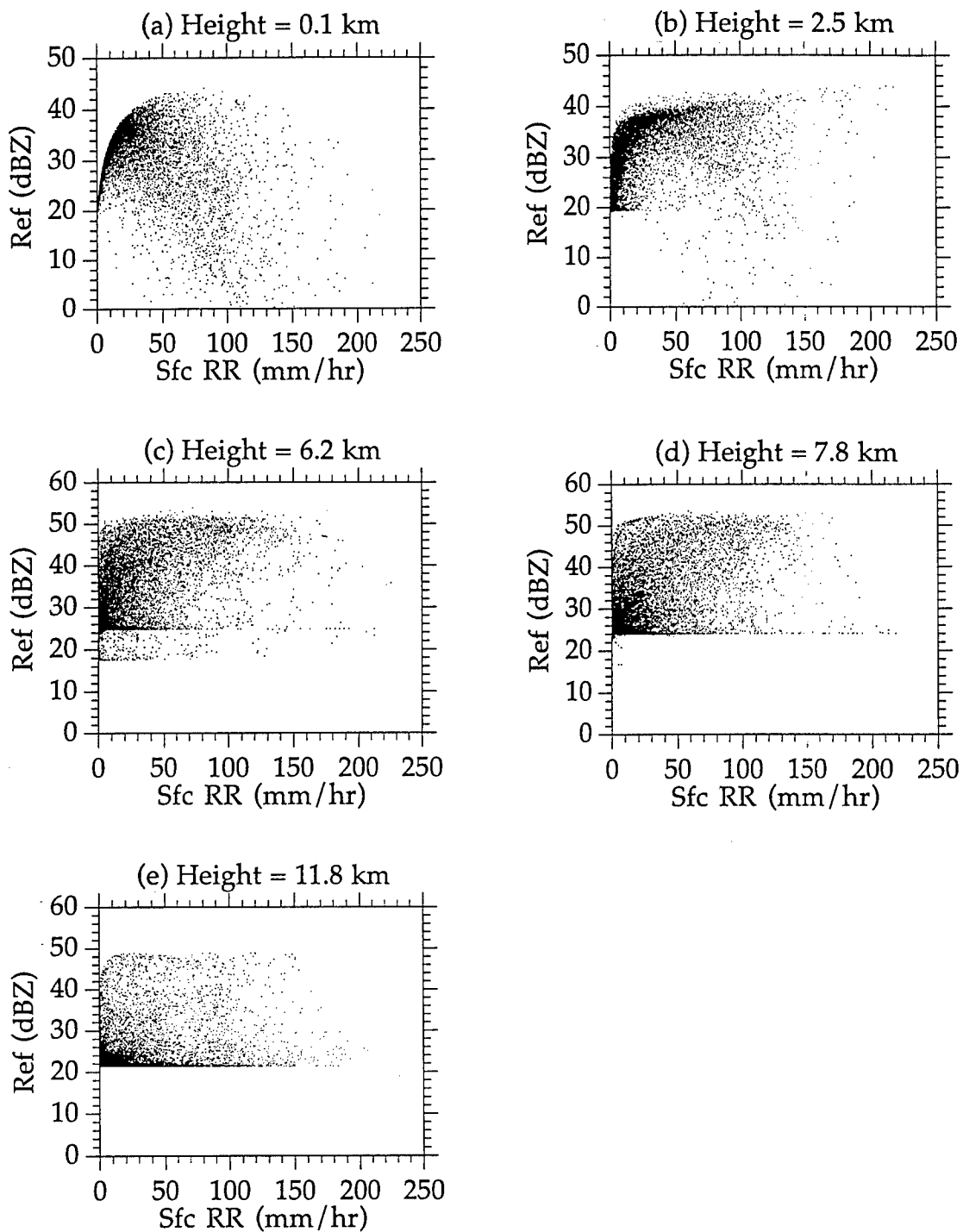
Figure 4.16: Scatterplot of database values of surface rainrate vs. radar reflectivity at heights of (a) 0.1 km, (b) 2.5 km, (c) 6.2 km, (d) 7.8 km, and (e) 11.8 km.
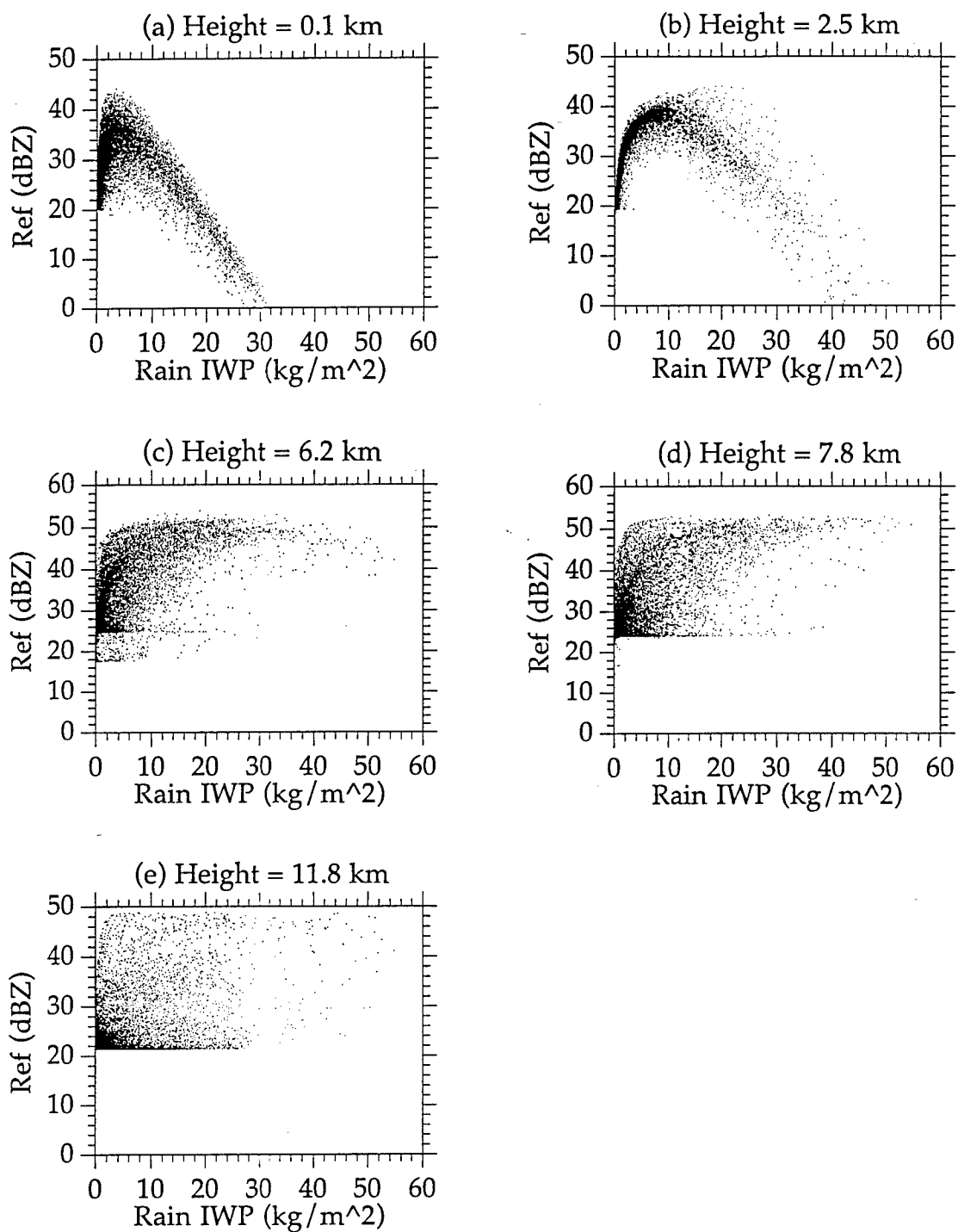
Figure 4.17: Scatterplot of database values of rain IWP vs. radar reflectivity at heights of (a) 0.1 km, (b) 2.5 km, (c) 6.2 km, (d) 7.8 km, and (e) 11.8 km.
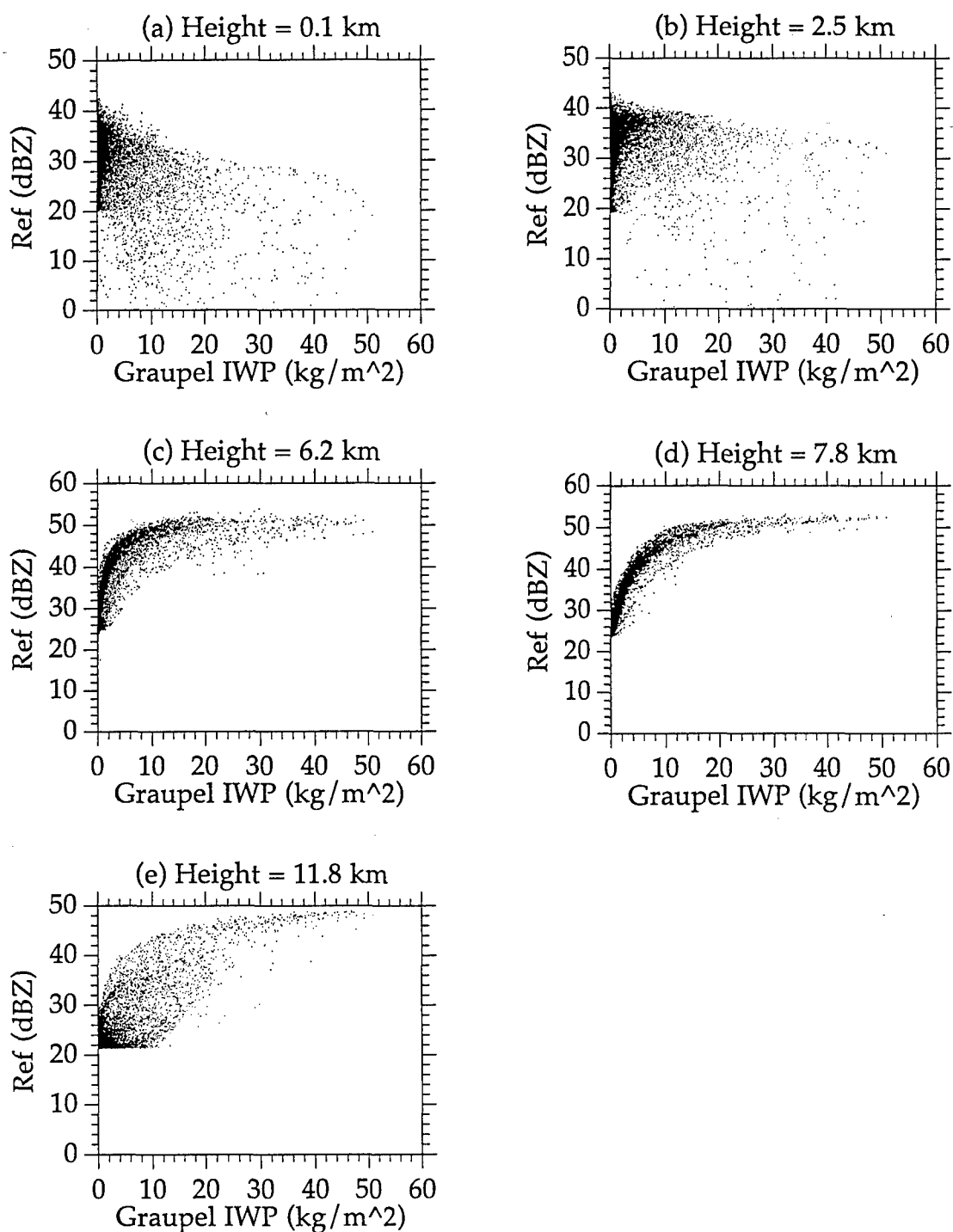
Figure 4.18: Scatterplot of database values of graupel IWP vs. radar reflectivity at heights of (a) 0.1 km, (b) 2.5 km, (c) 6.2 km, (d) 7.8 km, and (e) 11.8 km.

Also that level is low enough that the amount of rain present there is still relatively representative of the rain reaching the surface. As the level rises above the freezing level into the graupel, as shown in panel (c), the reflectivity is less representative of the surface rain rate as the radar is sampling mainly ice and not liquid; this correlation is reduced as the level is raised further, as shown in panels (d) and (e).

Nearly the same explanation can be applied to Figure 4.17, which plots the rain IWP at the same five levels. The main difference is that the apparent correlation of reflectivity is better for rain IWP than for surface rain rate as the reflectivity level is increased. This is because the total amount of ice is more highly correlated with rain IWP than it is with surface rain rate; hence the reflectivity just above the freezing level, shown in panel (c), is more representative of the total amount of rain in the column than it is for just the portion reaching the surface. However that correlation is destroyed when the level of the cirrus anvil is reached, as seen in panel (e). These analyses indicate that while a good reflectivity agreement between the retrieval solution and the measurements can lead to a good estimate of the total rain IWP, the estimate of the amount of liquid falling out as rain at the surface may not be as good, which is important as many studies use surface rain gauge measurements as ground truth in the verification of rainfall retrievals. Hence it should be noted that the surface rain rate may not be the best verification tool for evaluating the quality of a retrieval of the entire precipitating column. Furthermore as TBs appear to provide a better measure of the column-integrated hydrometeor amounts, a combined retrieval should improve the estimate of the total amount of rain in the column and the

surface rain rate, when compared to a reflectivity-only retrieval using measurements from a down-looking radar at an attenuating frequency.

The relationship of graupel IWP with reflectivities at the same five levels is given in Figure 4.18. As previously explained, the total graupel IWP is more representative of the total rain in the column than in the rain reaching the surface, as indicated further by the reflectivities in panels (a) and (b). As might be expected, the reflectivities at levels above the rain (and its associated attenuation effect on the radar returns) and in the graupel are correlated best with graupel IWP, as shown in panels (c) and (d) of Figure 4.18. Hence agreements between reflectivities in the ice layer between measurements and the solution profiles, as well as the 85.5 GHz TB matchup, are both important in the combined retrieval in diagnosis of the amount of ice present in the column. Furthermore the nature of range-gated radar sampling can diagnose the vertical placement of the large ice particles, whereas the 85.5 GHz TB measurement is only effective as inferring the total integrated amount. Hence the combined retrieval should then be able to improve the vertical distribution and IWP of the ice retrievals over that by independent TB-only or radar-only techniques.

In the discussions of the previous figures, the correlation between the hydrometeors and their corresponding TBs and Zs were discussed in qualitative terms from purely visual observations. Figure 4.19 displays these correlations in quantitative terms in the form of bar graphs, with the actual numbers provided in Table 4.1 For example, while it was clear from Figures 4.8 and 4.12 that 10.65 GHz provides a good estimate of the surface rain rate and rain IWP, the functional relationship is not linear and hence standard linear correlation will underestimate this high degree of correlation.

85
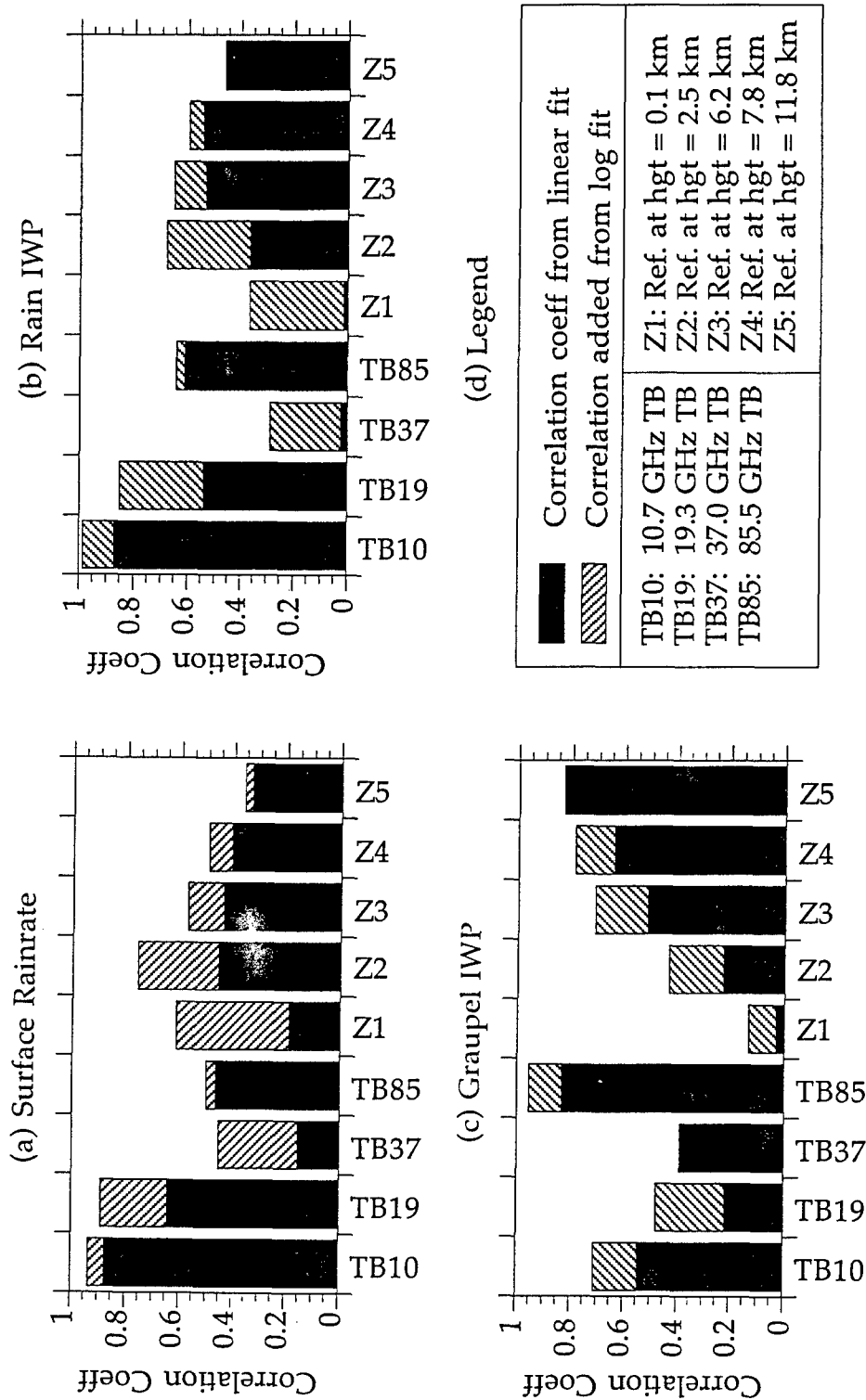
Figure 4.19: Correlations of TBs and Zs with (a) surface rainfall rate, (b) rain IWP, and (c) graupel IWP. Correlations are given for both linear fitting and logarithmic fitting.

Table 4.1: Correlations between TBs/Reflectivities and (a) Surface Rainrate, (b) Rain IWP, and (c) Graupel IWP.

(a) Surface Rainrate	---------- Correlation Coefficient ----------		
	linear	log	added
10.7 GHz TB	0.874	0.936	0.062
19.3 GHz TB	0.644	0.891	0.247
37.0 GHz TB	0.156	0.456	0.300
85.5 GHz TB	0.467	0.502	0.035
Ref at hgt = 0.1 km	0.189	0.616	0.427
Ref at hgt = 2.5 km	0.459	0.759	0.300
Ref at hgt = 6.2 km	0.441	0.576	0.135
Ref at hgt = 7.8 km	0.409	0.498	0.089
Ref at hgt = 11.8 km	0.331	0.359	0.028

(b) Rain IWP	linear	log	added
10.7 GHz TB	0.868	0.984	0.116
19.3 GHz TB	0.539	0.850	0.311
37.0 GHz TB	0.024	0.285	0.261
85.5 GHz TB	0.611	0.643	0.032
Ref at hgt = 0.1 km	0.015	0.364	0.349
Ref at hgt = 2.5 km	0.365	0.680	0.315
Ref at hgt = 6.2 km	0.536	0.653	0.117
Ref at hgt = 7.8 km	0.545	0.597	0.052
Ref at hgt = 11.8 km	0.460	0.463	0.003

(c) Graupel IWP	linear	log	added
10.7 GHz TB	0.546	0.710	0.164
19.3 GHz TB	0.217	0.479	0.262
37.0 GHz TB	0.391	0.391	0.000
85.5 GHz TB	0.833	0.955	0.122
Ref at hgt = 0.1 km	0.030	0.132	0.102
Ref at hgt = 2.5 km	0.227	0.436	0.209
Ref at hgt = 6.2 km	0.518	0.713	0.195
Ref at hgt = 7.8 km	0.643	0.788	0.145
Ref at hgt = 11.8 km	0.826	0.831	0.005

Note: The hydrometeor quantities are correlated with the TBs/Reflectivities by (a) a linear fit and then by (b) a logarithmic fit; the extra correlation gained by the log fit is given as (c) correlation "added" to the linear fit.

One practical solution is to measure the correlation with respect to a smooth function which best fits the data. This would measure the departure of the points from this functional curve instead of from the best linear fit. A logarithmic transform of the hydrometeors and rain rate was performed, which reasonably "straightened" the curves present in the relationship between these quantities and the TBs and Zs. The linear correlation using both the original values and log-transformed values are given in Figure 4.19 and Table 4.1 for the correlation of TBs and Zs with (a) surface rain rate, (b) rain IWP, and (c) graupel IWP. The results are consistent with the previous qualitative observations, namely that 10.65 GHz TB gives the highest correlation with both rain IWP and surface rain rate, and that the best correlation from a reflectivity value is up in the rain layer rather than near the surface. In a similar analysis, Smith et al. (1997) showed that the correlation between the surface rain rate and the <u>unattenuated</u> near-surface reflectivity (as opposed to the attenuated reflectivities used here and which are measured by a radar) provided an almost perfect 0.99 correlation coefficient. This demonstrates one of the drawbacks of an attenuating radar, namely that large rain amounts can attenuate the signal, resulting in lower reflectivity values which are indicative of smaller rain amounts in an unattenuated environment.

The analysis continues in a similar fashion for ice, where Figure 4.19(c) and Table 4.1 show that 85.5 GHz TB provides the best correlation with graupel IWP, followed by reflectivities in the ice layer. The correlation with graupel IWP calculated for the reflectivity at 11.8 km was higher than for the lower levels nearer the graupel peak, even though Figure 4.18 clearly illustrates more scatter around a central curve defining the relationship for

this higher level. This unexpected correlation difference is due to the fact that the curve for the higher level is more linear, and the log transform does not sufficiently straighten the curves at the 6.2 and 7.8 km levels. A better transform or functional fit would overcome this disparity.

4.3 TB Manifolds (AMPR Data vs. Model Simulations)

Another method by which to explore the combined behavior of the hurricane simulations and the forward RTE model is by the analysis of scatterplots of all TBs with one another. Analysis of these TB vs. TB scatterplots was dubbed TB "manifold" analysis by Panegrossi et al. (1997). The TB manifold is defined as the N-dimensional space enclosing the TBs, where each dimension is given by one of N TB frequencies. Panegrossi et al. (1997) performed a TB manifold analysis with a study using SSM/I TB data and a lower resolution version of the hurricane simulation used in this research. A similar analysis using the AMPR passive brightness temperature data sets from TOGA COARE was performed by McGaughey et al. (1996) and McGaughey and Zipser (1996), which focused on observations of convective and stratiform precipitation in TOGA COARE, respectively.

The model TB manifold uses TBs produced by inputting each set of microphysical hydrometeor profiles from the hurricane simulation into the unified RTE model, as described in section 2.1. Figure 4.20 illustrates the TB manifold produced by using the original hydrometeor profiles from the hurricane simulation; several features are worth discussing. The plot of 19.3 GHz TB vs. 10.7 GHz TB (lower left) shows the relatively dominant emission signatures at both lower frequencies. The drop in 19.3 GHz TB for some cases of large 10.7 GHz TB reflects the limited effects of scattering at 19.3 GHz, as

discussed in the previous section. The scattering signature is enhanced as higher frequencies are viewed. In the plots for 85.5 GHz TB vs. 19.3 GHz TB (upper left), 85.5 GHz TB vs. 37.0 GHz TB (upper right), and for 37.0 GHz TB vs. 19.3 GHz (middle right), the scattering signature of the higher frequencies can be seen as a scattering "tail". Finally no discernible pattern emerges from the plot of 85.5 GHz TB vs. 10.7 GHz TB (middle left), due to the poor correlation between the emission-dominant signature at 10.7 GHz and the scattering-dominant signature at 85.5 GHz.

Previous discussions of the methodology explained that the original simulation hydrometeors were fit to Legendre Polynomial structure functions prior to calculation of TBs and Zs for the initial guess database. Figure 4.21 illustrates TB manifold for TBs produced from structure function-transformed hydrometeors. As previously shown in Figure 4.5, hydrometeor fitting produces little change to the TBs, so it is no surprise that the structure function-transformed TB manifold (as shown in Figure 4.21) is nearly identical to the non-transformed TB manifold (as shown in Figure 4.20). If there had been significant differences, it would have indicated the structure function transform process altered the relationship between the different TBs, which in turn would alter the matchups in the selection of the first guess during the retrieval. Since this was not the case, it is further confirmation that structure function fitting of the hydrometeor profiles does not produce adverse effects on the initial guess selection within the combined retrieval.

Now that an interpretation of the shapes and structures of the model manifolds have been discussed, the next step is to compare them to the actual TB measurements, which for this study were taken airborne AMPR TBs. The AMPR data TB manifold from the TOGA COARE cases used in this research

is shown in Figure 4.22. The most noticeable difference between the model and AMPR data TB manifolds is the lesser ice scattering tails in the AMPR data manifold. While the tails at 85.5 GHz TB vs. 19.3 GHz TB (upper left) and 85.5 GHz TB vs. 37.0 GHz TB (upper right) are clearly present for the AMPR data, it is very small for the 37.0 GHz TB vs. 19.3 GHz (middle right) cross-section and non-existent for the 37.0 GHz TB vs. 10.7 GHz (bottom right) panel. This can likely be explained by the fact that the meteorological conditions present during TOGA COARE did not include the large amounts of ice present in some profiles of the hurricane simulation.

When using a simulation database in the retrieval process, one of the goals is that the database represent reality. Ideally one would want every possible combination of TBs and Zs present in actual instrument measurements to be contained within the database. If this is the case, the measured data TB manifold should be fully contained within the model TB manifold from the database; otherwise the model simulation is not representing all the conditions present in the measurements. To aid in the determination of this case, the perimeter of AMPR TB manifold for each cross-section shown in Figure 4.22 is traced in bold, and presented in Figure 4.23. This AMPR data manifold perimeter from Figure 4.23 is then overlaid on the model manifold from Figure 4.21, with the final product given as Figure 4.24. The areas within the border of the AMPR data manifold which are not represented by the model indicate TB combinations not produced in the simulation. While visual inspection indicates general agreement, two main discrepancies are noted and are discussed in the following section. The technique used to adjust the model TBs, resulting in a better match between the data and model TB manifolds, are also discussed.

91
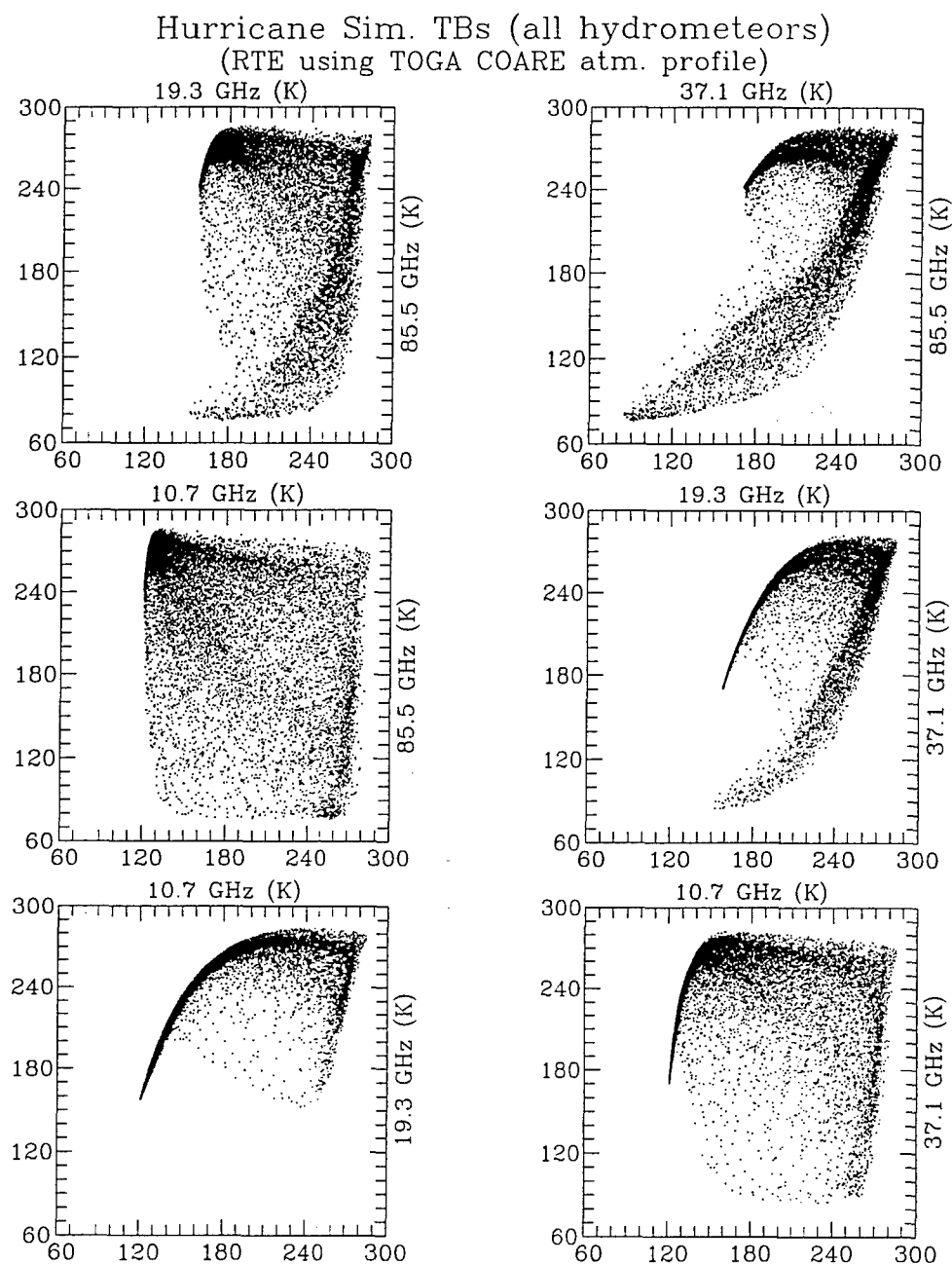
Figure 4.20: TB manifold from the simulation database using original database hydrometeor profiles.

Figure 4.21: TB manifold from the simulation database using Legendre polynomial-fitted database hydrometeor profiles.
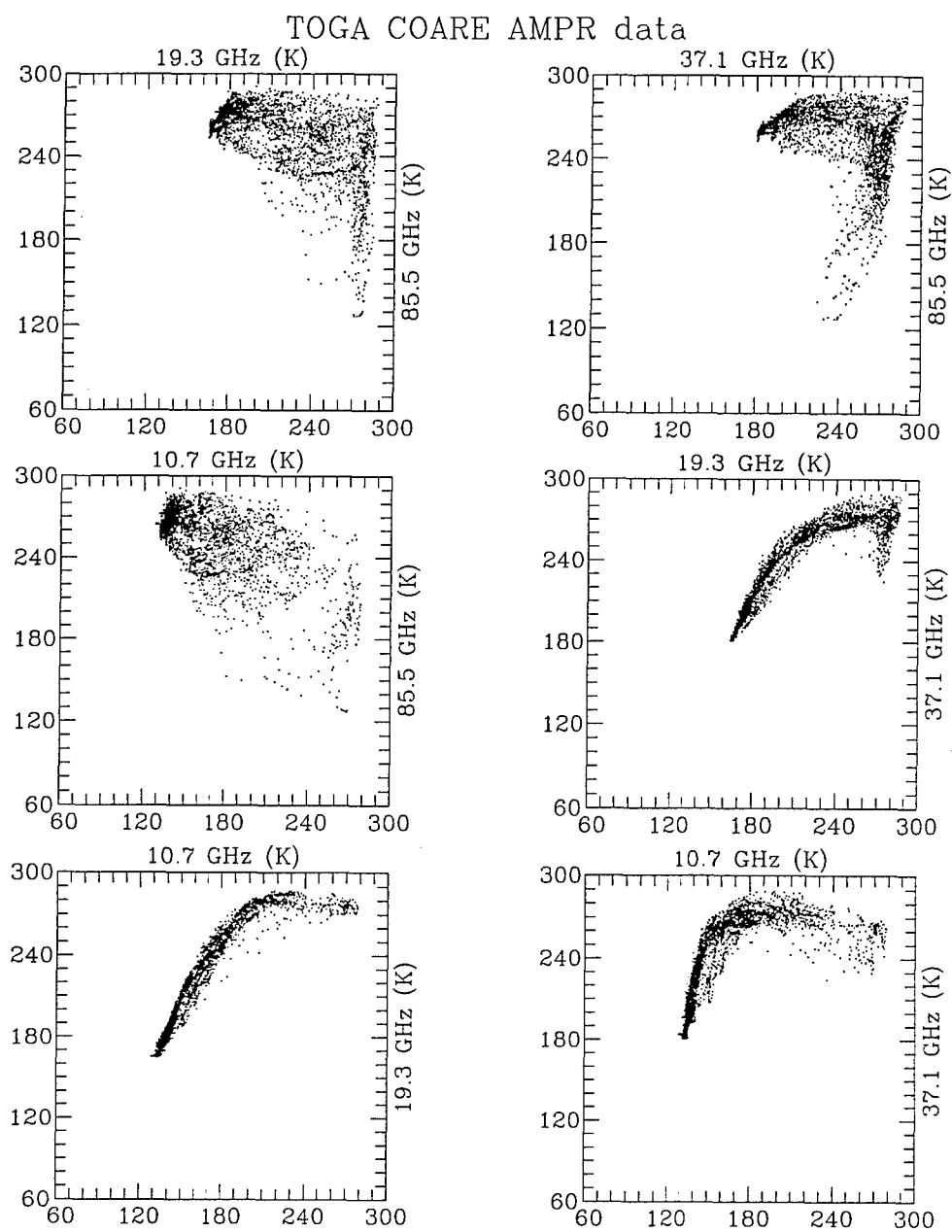
Figure 4.22: TB manifold from TOGA-COARE AMPR TB measurements.
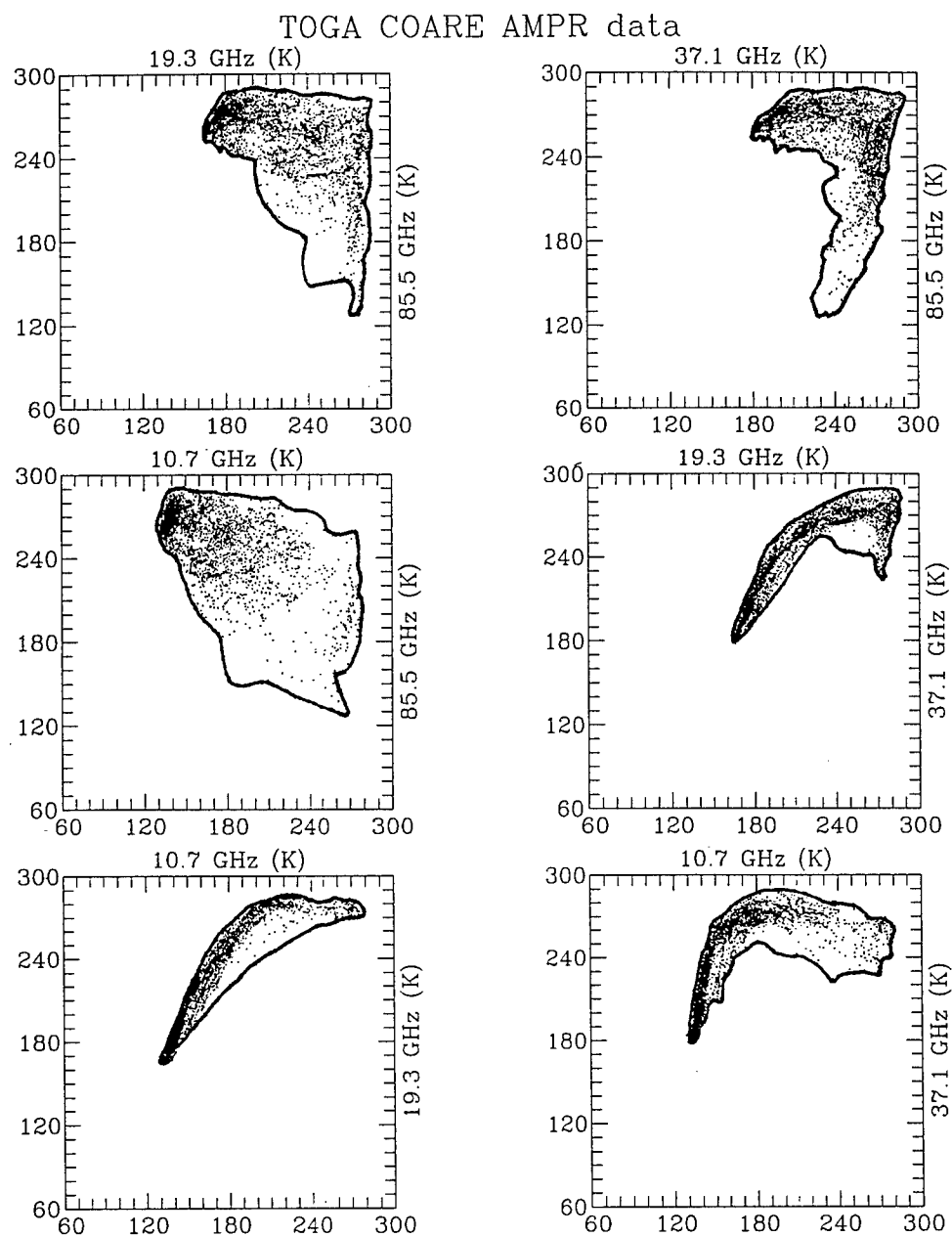
Figure 4.23: TB manifold from TOGA-COARE AMPR TB measurements, where the perimeter enclosing the manifold has been traced in bold.

4.4 Model TB Bias Adjustments

The match between the model simulation and measured TB manifolds can be seen from Figure 4.24, where the border of the AMPR TB manifold is overlaid on the model TB manifold. While several areas of mismatch can be detected, two stand out from the rest. First, the manifolds clearly indicate that the AMPR 10.7 GHz TBs are warmer than the model 10.7 GHz TB for the lower-emission/lower-TB range, possibly due to a calibration problem with the AMPR instrument during the TOGA COARE experiment [Spencer (1996), personal communication]. This is best illustrated by the TB manifold mismatches for the 19.3 GHz TB vs. 10.7 GHz (lower left) and 37.0 GHz TB vs. 10.7 GHz (lower right) cross-sections. For the RTE calculations in this study using TOGA-COARE mean surface and atmospheric conditions as input, the bias between the AMPR and model 10.7 GHz TB at the low end was found to be ~10 K. In order to adjust the model 10.7 GHz TBs to match the measurements from the AMPR, an adjustment of 10 K was added to the model 10.7 GHz TB where total rain IWP = 0, no adjustment is added for TBs corresponding to rain IWP > 20 kg m^{-2}, and a linearly-interpolated adjustment is made for TBs falling between zero and the upper threshold. McGaughey et al. (1996) report a similar discrepancy at 10.7 GHz between AMPR measurements and model-produced TBs, and made a similar bias adjustment. While from the TB manifold comparisons there also appear to be biases present at the other frequencies, their magnitudes are much less than that for 10.7 GHz, and consequently no adjustment is attempted.

The second discrepancy involves the scattering tail at 37.0 GHz, as best seen in the 85.5 GHz TB vs. 37.0 GHz TB (upper right) cross-section. The difference here is that the model produces a higher scattering depression at

96

37.0 GHz due to ice than is observed by the AMPR. While this difference affects only a small portion of the data points from TOGA COARE, as shown by the AMPR TB manifold in Figure 4.22, the discrepancy for those cases is large enough that an adjustment was deemed appropriate. The adjustment procedure is similar to that performed for 10.7 GHz, except that in this case the graupel IWP is used to scale the amount of adjustment. As the discrepancy between the model and AMPR TB manifolds at 37.0 GHz increased with increasing ice scattering, the amount of adjustment was set as a function of graupel IWP. A logarithmic function was found to provide the best adjustment, where no adjustment was made for graupel IWP = 0, and larger adjustments were made for increasing graupel IWP.

The TB manifold of the bias-adjusted simulation database is presented in Figure 4.25, and the same TB manifold is overlaid with the AMPR TB manifold perimeter in Figure 4.26. The improvements over the original model TB manifold are clearly seen, where the emission signature at 10.7 GHz and scattering signature at 37.0 GHz more closely match the performance of the AMPR instrument. Hence the selection of the first guess within the retrieval should lead to better matches, and in turn improve the quality of the rainfall retrievals. The retrieval algorithm is now complete and optimized for retrieval tests using TOGA COARE data, as presented in the next chapter.

Hurricane Sim. LP–fitted TBs (all hydrometeors)
(RTE using TOGA COARE atm. profile)
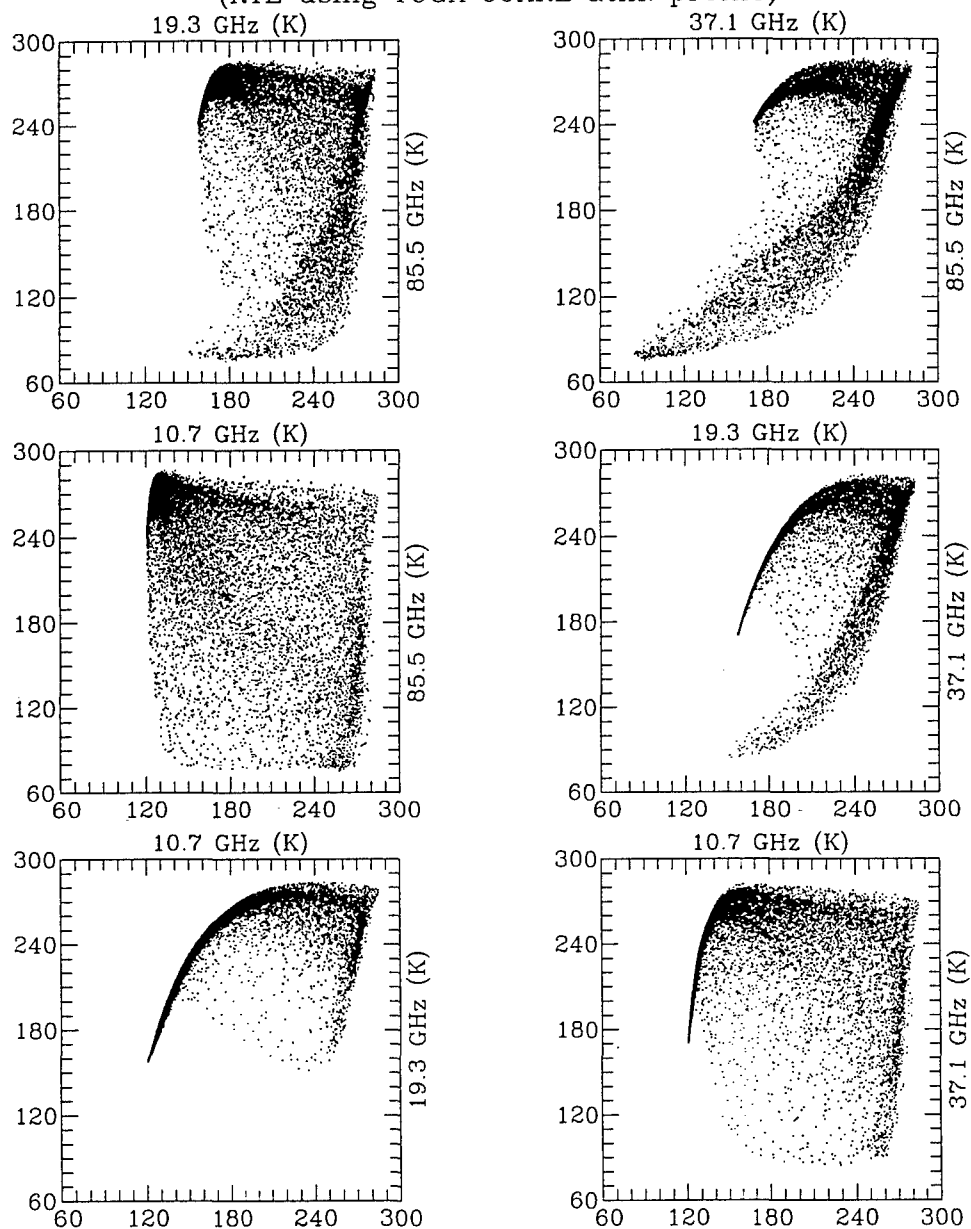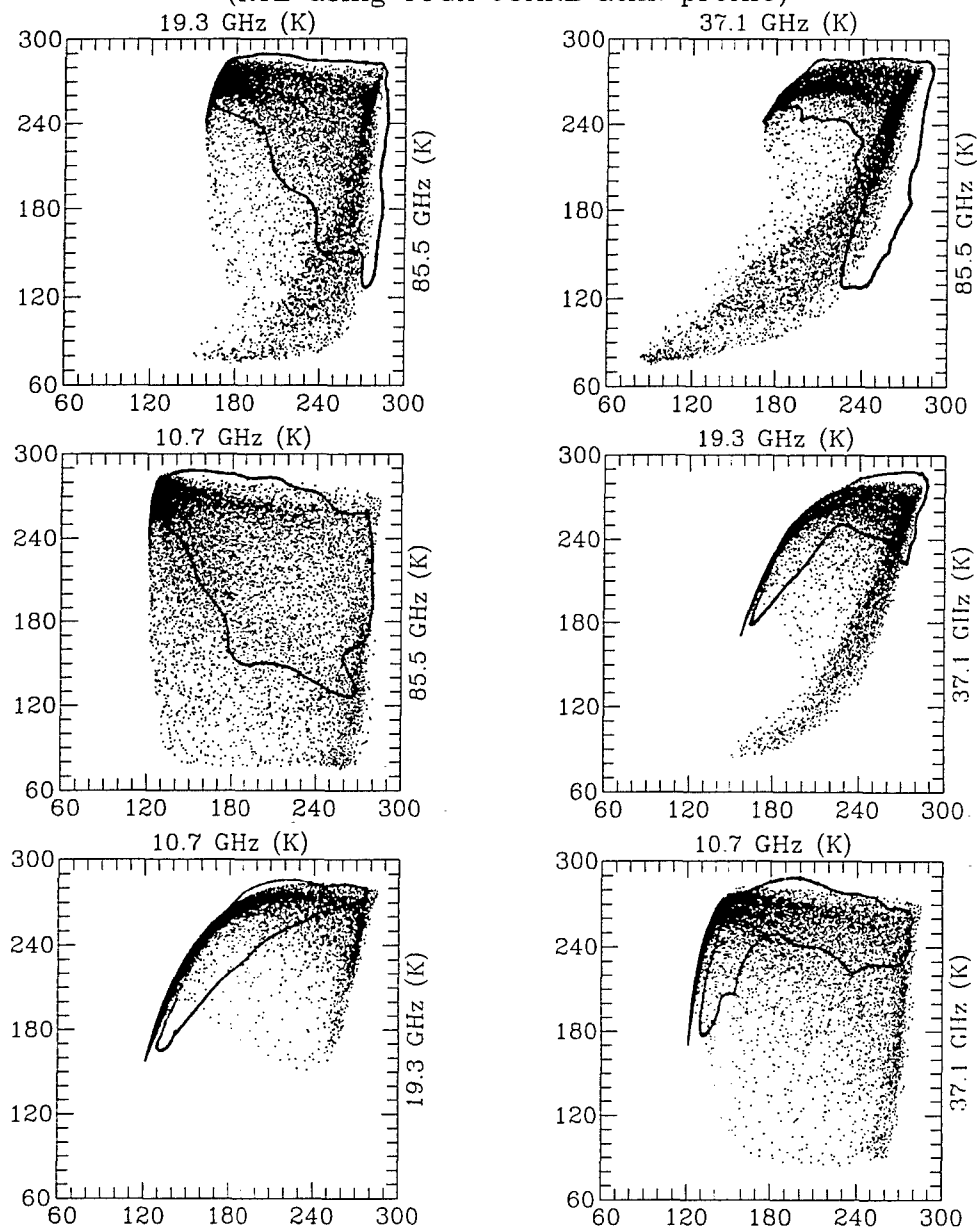
Figure 4.24: TB manifold from the simulation database using Legendre polynomial-fitted database hydrometeor profiles, overlaid with the TOGA-COARE AMPR TB manifold perimeter.

Bias Adjusted, LP–fitted, Sim. TBs (all Hyd)
(RTE using TOGA COARE atm. profile)
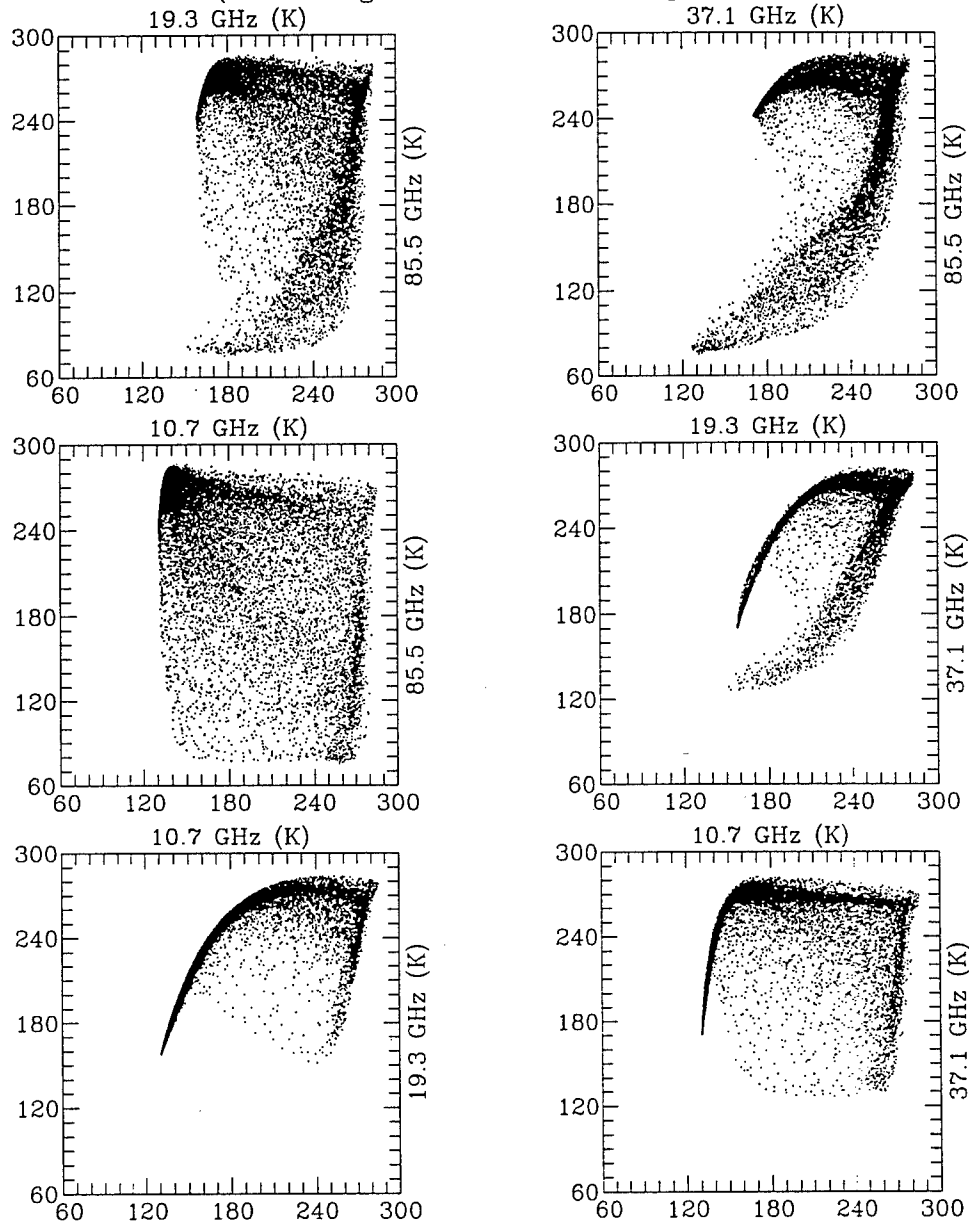
Figure 4.25: TB manifold from the simulation database using Legendre polynomial-fitted database hydrometeor profiles, which have been adjusted to match biases between it and the TOGA-COARE AMPR TB manifold.
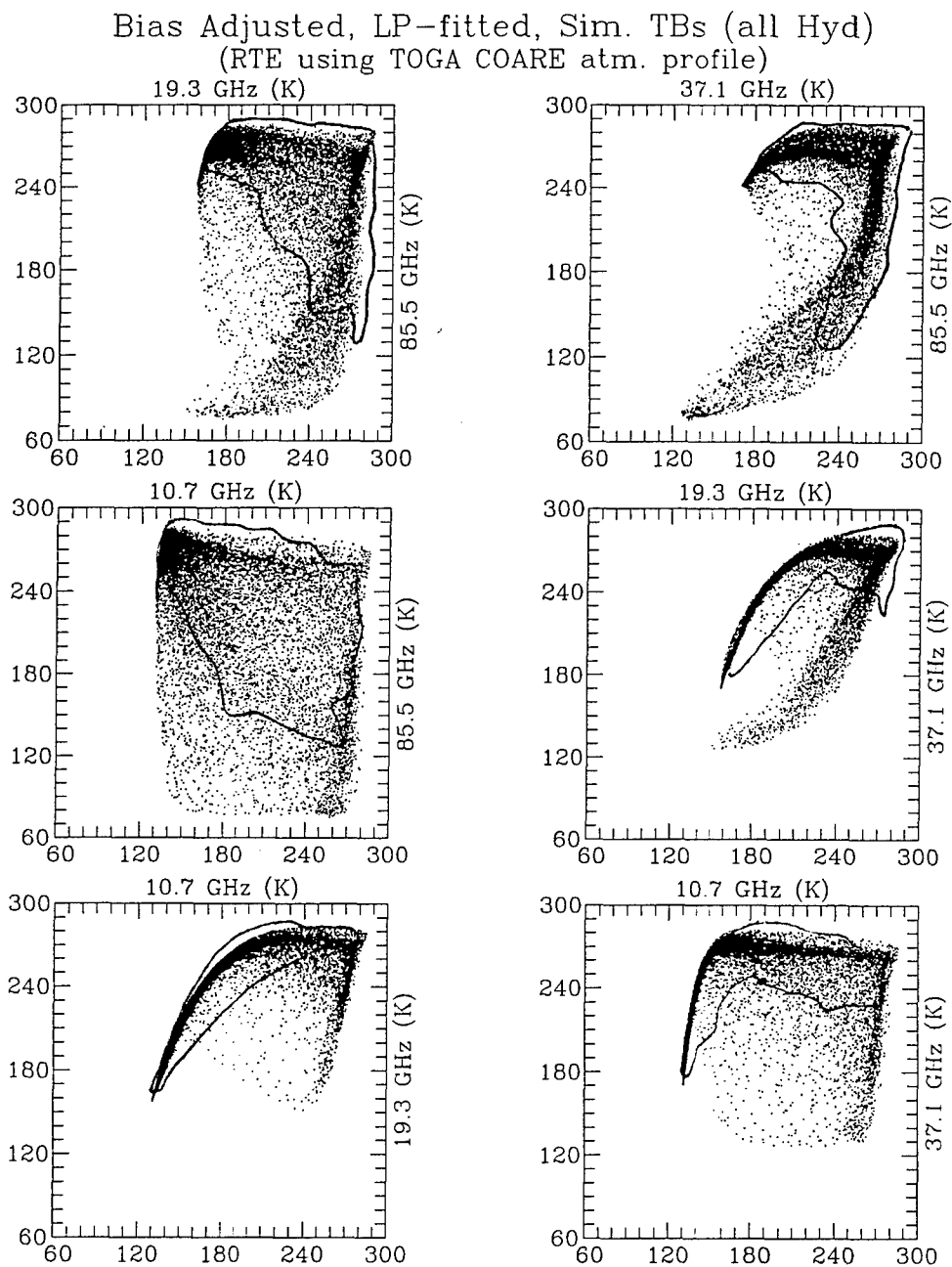
Figure 4.26: TB manifold from simulation database using Legendre polynomial-fitted, bias-adjusted database hydrometeor profiles, overlaid with the TOGA-COARE AMPR TB manifold perimeter.

100

CHAPTER 5

RETRIEVAL RESULTS

5.1 Individual TOGA-COARE Test Cases

As described in section 3.2, the TOGA-COARE field experiment measured tropical precipitation and other atmosphere-ocean processes in the western Pacific warm pool region. In addition to a network of ship-board sensors and buoys within TOGA-COARE's Intensive Flux Array (IFA), there were also several flights of research aircraft flying out of Townsville, Australia, including coordinated flights of a NASA ER-2 and DC-8. While the ER-2 and DC-8 collectively deployed several instruments, only measurements from the AMPR and ARMAR were used as input for the combined retrieval tests. Portions of coordinated flights from four days during TOGA-COARE were selected for this study: 4 Feb, 8 Feb, 20 Feb, and 22 Feb 1993.

The first ER-2/DC-8 coordinated flight selected for retrieval tests was from 4 Feb 93. The data used from this flight were from two passes over the developing Tropical Cyclone Oliver, centered approximately at 15° S, 150° E. The second coordinated flight focused again on Tropical Cyclone Oliver, which by this date had begun to weaken. Two passes over the storm, centered approximately at 19° S, 152° E, were selected for retrieval tests. The third coordinated flight used, from 20 Feb 93, focused on a mesoscale convective system located at approximately 6° S, 160° E. Four separate passes over the area were selected for retrieval tests. The fourth coordinated flight selected was from 22 Feb 93, which focused on a convective squall line and

surrounding areas near 9° S, 159° E. Three passes over this region were selected for retrieval tests. Note that for all the cases, a pass is defined as a portion of a flight in which the flight paths of both aircraft are straight and level.

Contoured TB images for the full swath of AMPR measurements are given in Figures 5.1-5.11 for the 11 passes described above. Due to the disparity in slant paths for off-nadir views between the AMPR and ARMAR caused by their different altitudes (as explained in section 3.2), only nadir measurements from these two instruments were used as input to the combined retrieval. Nadir-only AMPR TB plots are given in the top panels of Figures 5.12-5.22, which correspond to the values along the center of the TB maps in Figures 5.1-5.11. The corresponding ARMAR reflectivity profiles at nadir are displayed as contoured images in the bottom panels of Figures 5.12-5.22. Note that for all these ARMAR images, vertical lines in the ARMAR contours are caused by missing data at that location.

The combined data sets of AMPR and ARMAR nadir measurements, as displayed in Figures 5.12-5.22, were then used as input to the combined retrieval algorithm. Each paired set of AMPR TBs and ARMAR Zs from the pass were input sequentially, and processed to generate solution hydrometeor profiles, surface rainfall rates, and precipitation type, as described in Chapter 2. Retrieval results and other selected quantities are plotted for the 11 flight passes in Figures 5.23-5.33. Each figure consists of 4 panels, where the horizontal coordinate of all panels follows the equivalent ground track of the aircraft, given as either latitude or longitude, depending on the orientation of each particular pass.

AMPR TB Data from TOGA−COARE ER−2 Flight
02/04/93, Pass # 1, ER−2 Time 171400−173000 UTC
10.7 GHz   19.3 GHz   37.0 GHz   85.5 GHz

173000

172600

172200

171800

171400

80.0 95.0 110.0 125.0 140.0 155.0 170.0 185.0 200.0 215.0 230.0 245.0 260.0 275.0 290.0
AMPR TB (K)
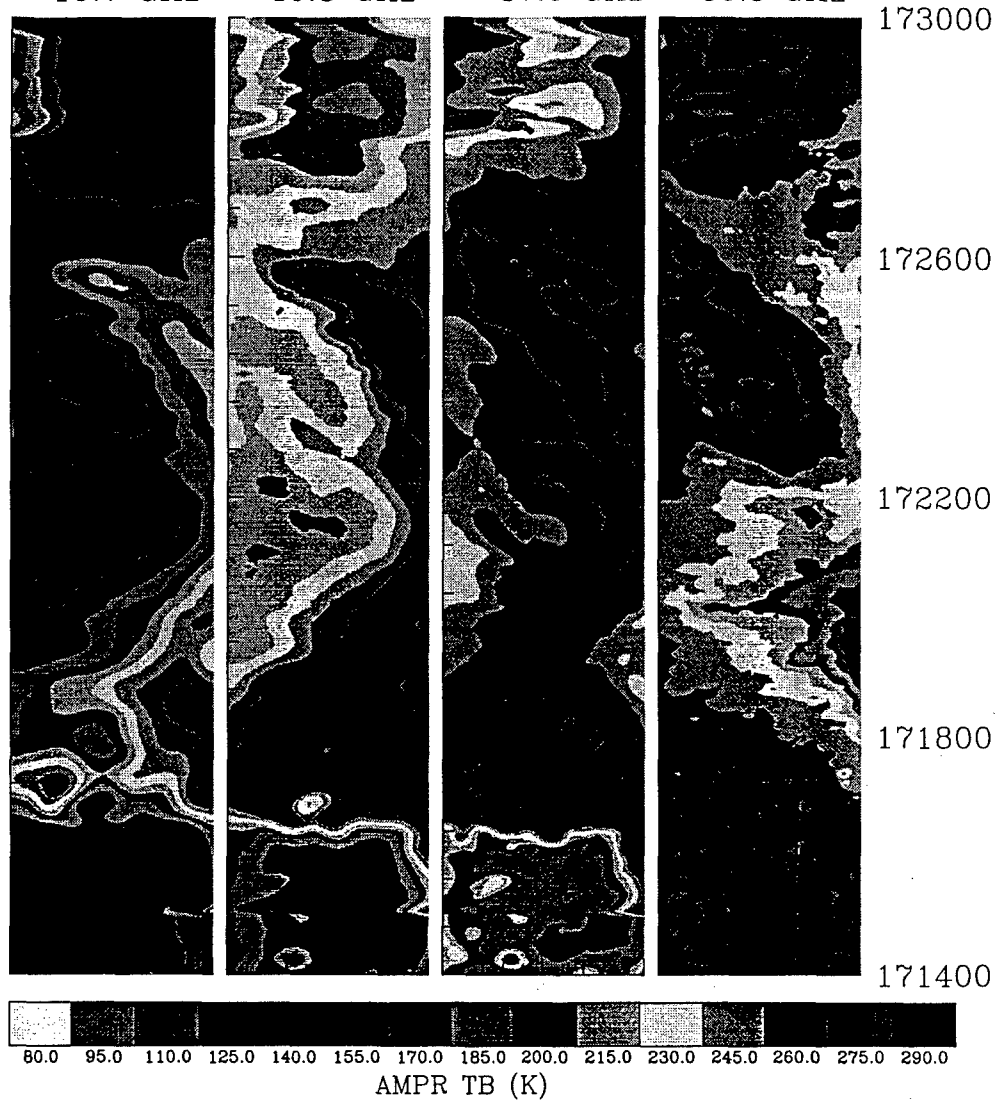
Figure 5.1: Full swath AMPR TB images from pass #1 over a developing Tropical Cyclone Oliver on 04 Feb 93.
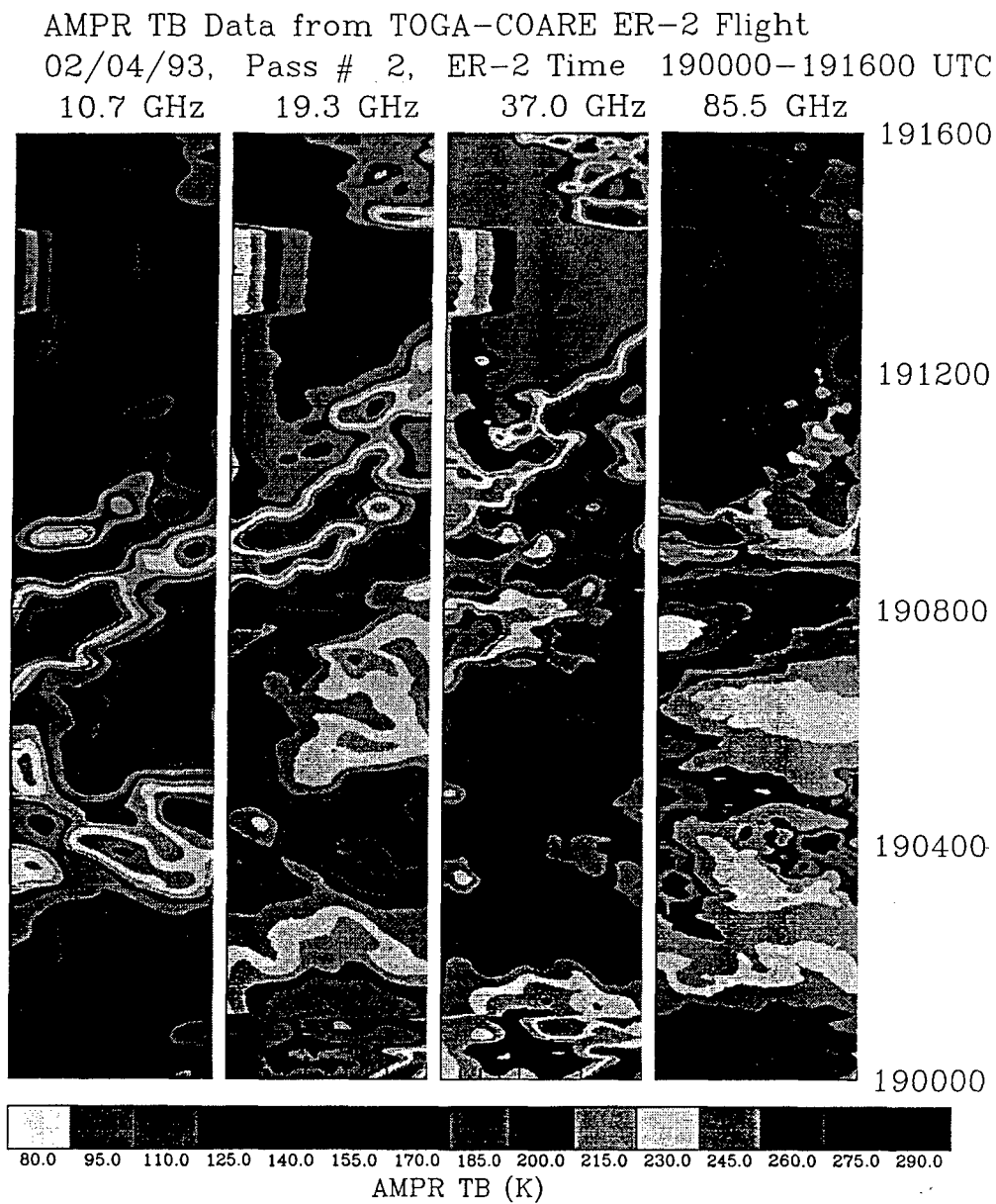
Figure 5.2: Full swath AMPR TB images from pass #2 over a developing Tropical Cyclone Oliver on 04 Feb 93.

AMPR TB Data from TOGA–COARE ER–2 Flight
02/08/93, Pass # 1, ER–2 Time 204500–210500 UTC
10.7 GHz   19.3 GHz   37.0 GHz   85.5 GHz
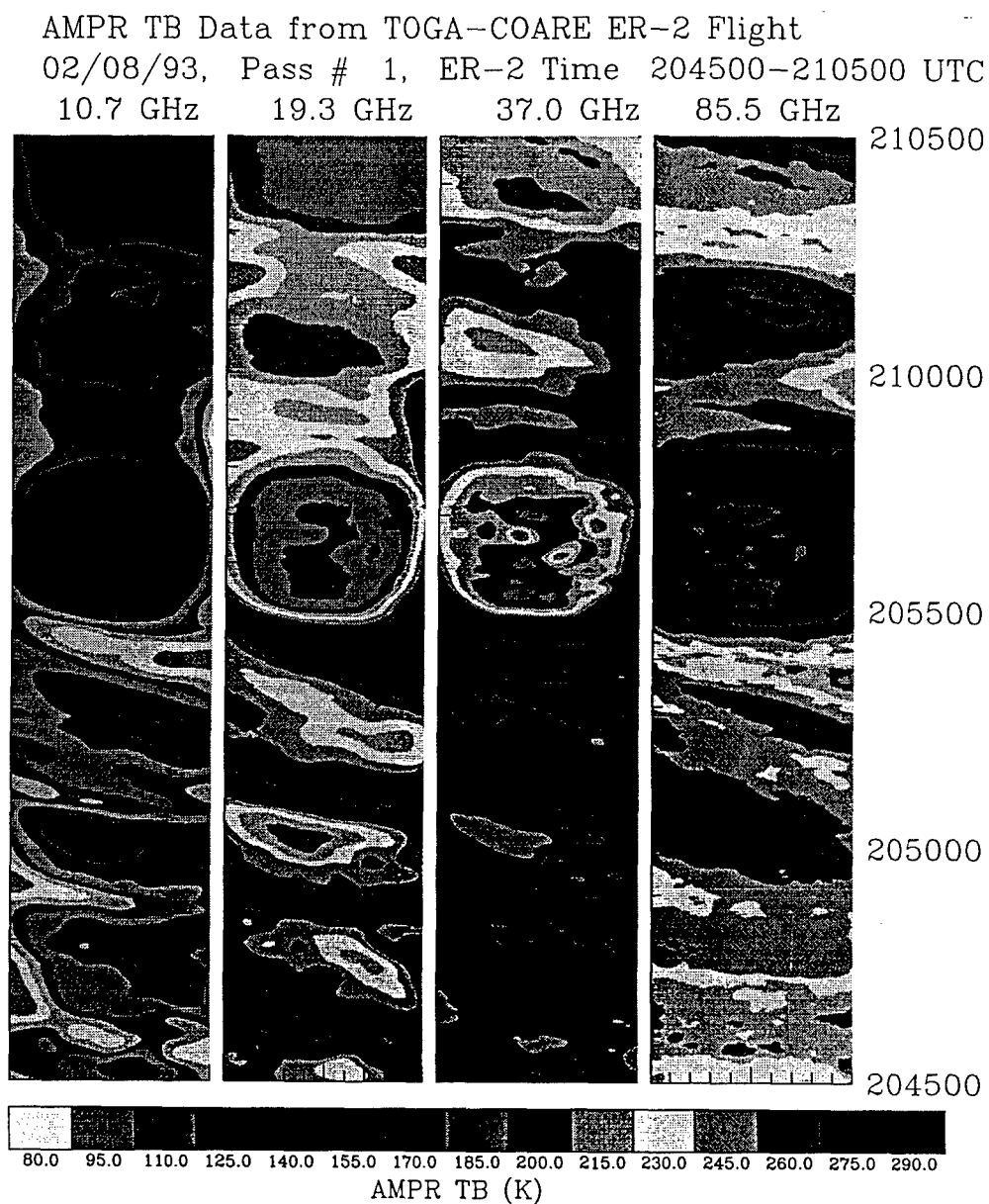
Figure 5.3: Full swath AMPR TB images from pass #1 over a weakening Tropical Cyclone Oliver on 08 Feb 93.

AMPR TB Data from TOGA−COARE ER−2 Flight
02/08/93, Pass # 2, ER−2 Time 213200−215200 UTC
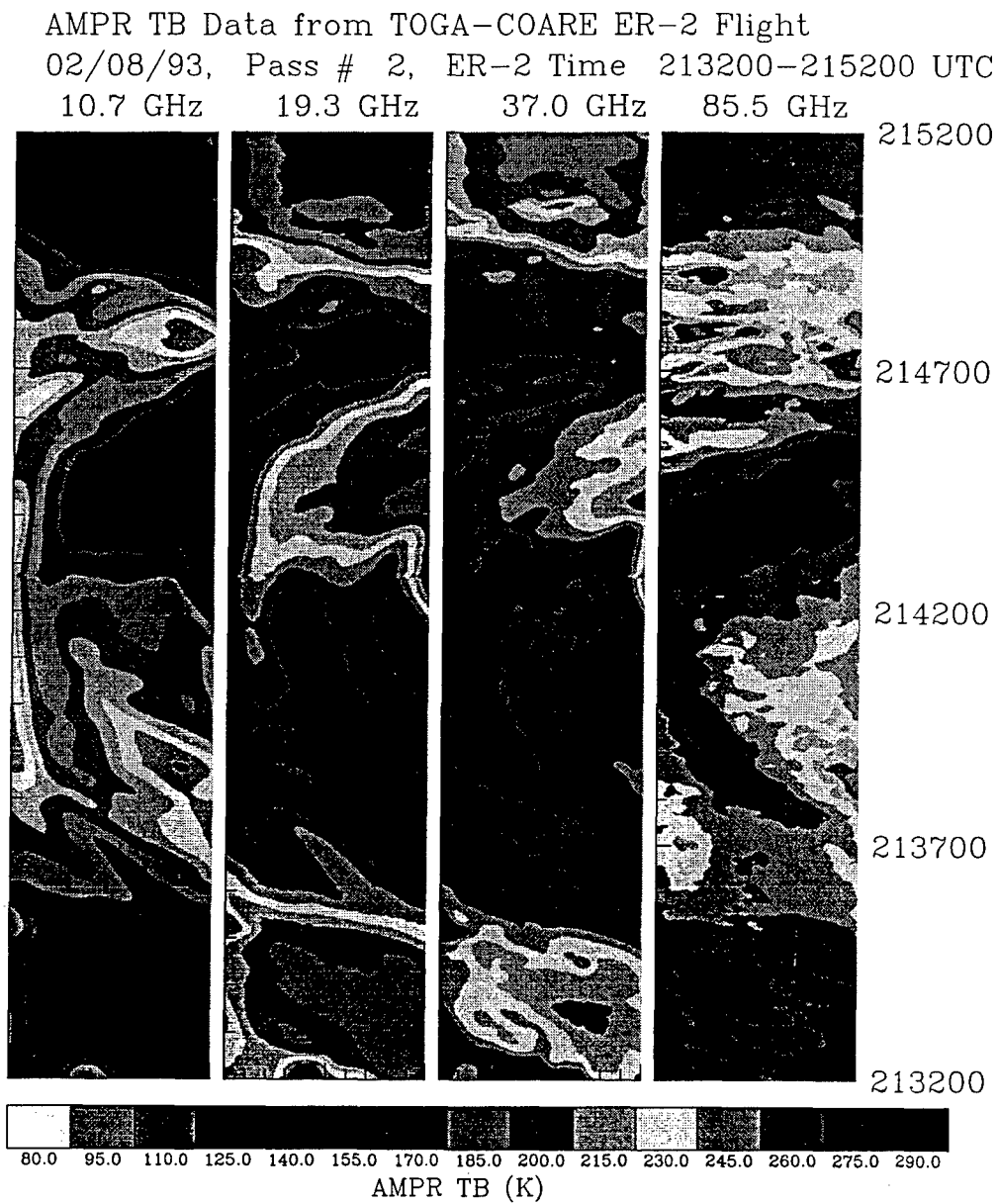
Figure 5.4: Full swath AMPR TB images from pass #2 over a weakening Tropical Cyclone Oliver on 08 Feb 93.

AMPR TB Data from TOGA–COARE ER–2 Flight
02/20/93, Pass # 1, ER–2 Time 222400–224000 UTC
10.7 GHz   19.3 GHz   37.0 GHz   85.5 GHz
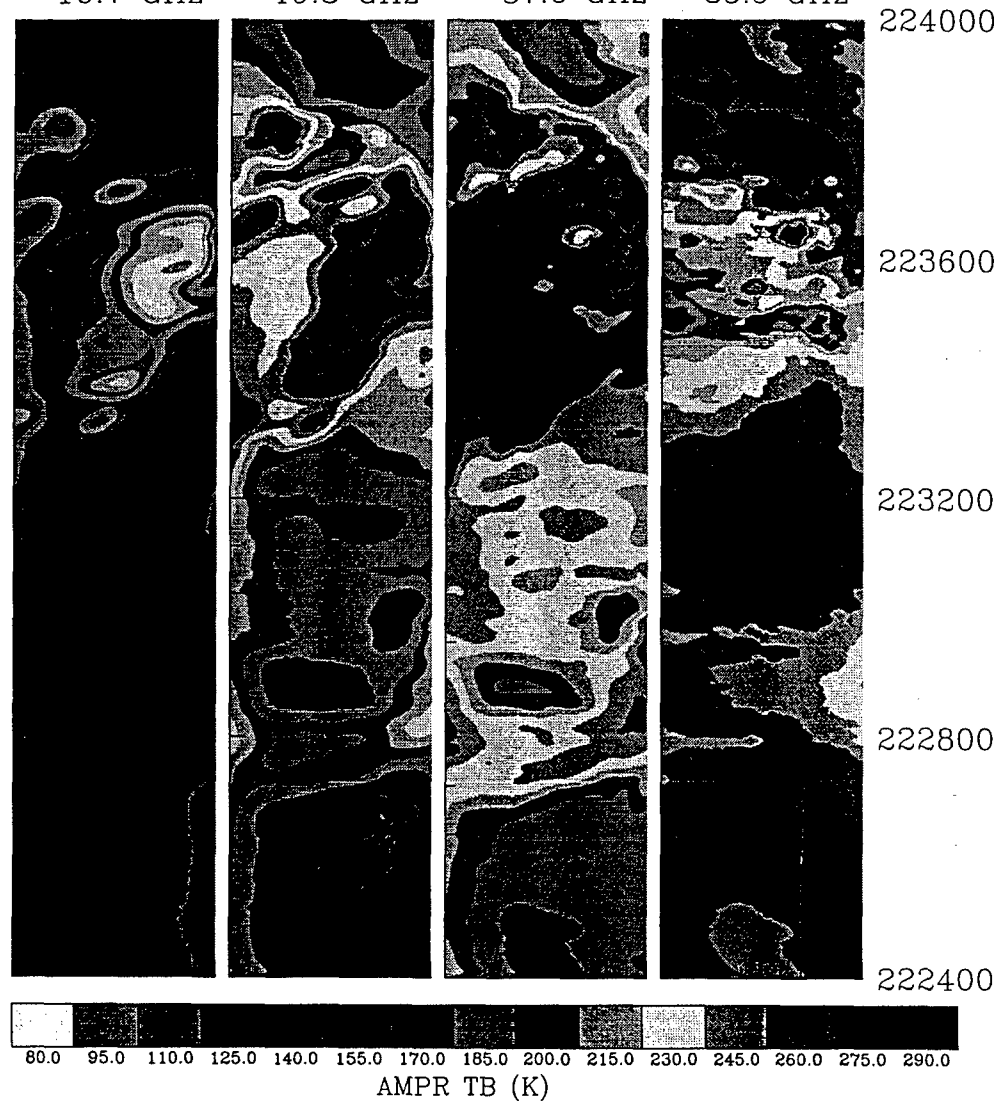
Figure 5.5: Full swath AMPR TB images from pass #1 over a mesoscale system on 20 Feb 93.

AMPR TB Data from TOGA–COARE ER–2 Flight
02/20/93, Pass # 2, ER–2 Time 224500–230100 UTC
10.7 GHz   19.3 GHz   37.0 GHz   85.5 GHz

230100

225700

225300

224900

224500

80.00 95.00 110.00 125.00 140.00 155.00 170.00 185.00 200.00 215.00 230.00 245.00 260.00 275.00 290.00
AMPR TB (K)
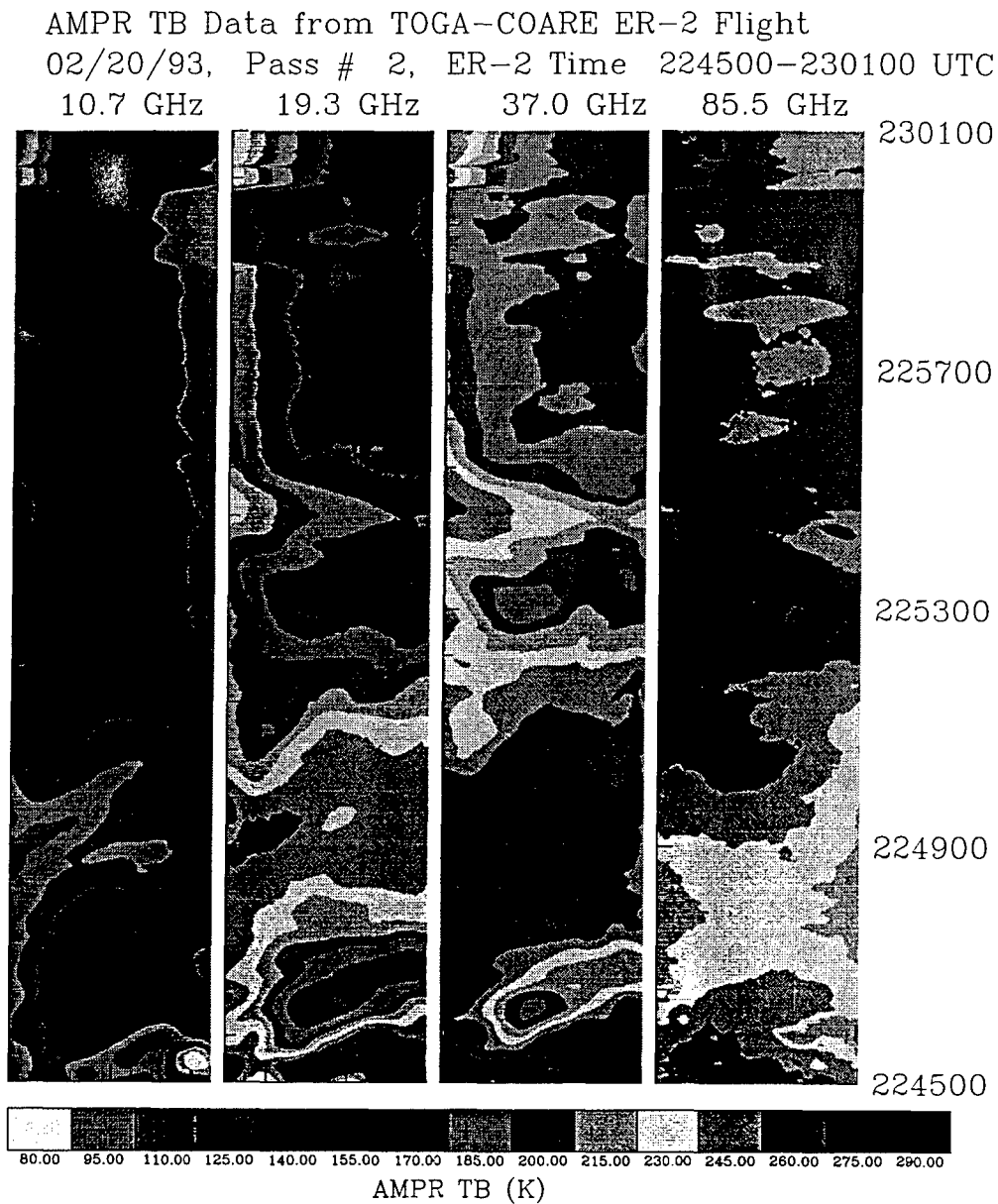
Figure 5.6: Full swath AMPR TB images from pass #2 over a mesoscale system on 20 Feb 93.

AMPR TB Data from TOGA−COARE ER−2 Flight
02/20/93, Pass # 3, ER−2 Time 230300−232300 UTC
10.7 GHz   19.3 GHz   37.0 GHz   85.5 GHz
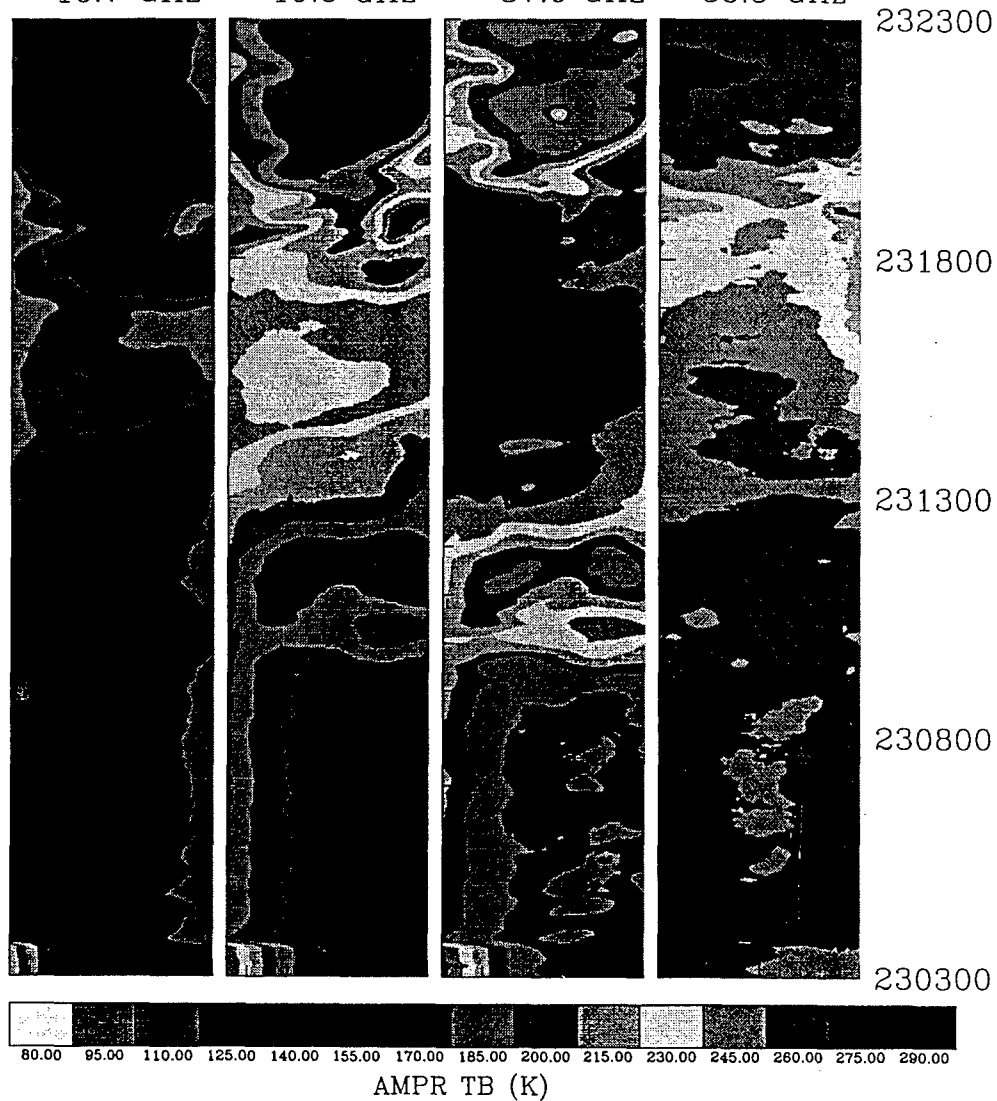
Figure 5.7: Full swath AMPR TB images from pass #3 over a mesoscale system on 20 Feb 93.

AMPR TB Data from TOGA–COARE ER–2 Flight
02/20/93, Pass # 4, ER–2 Time 233000–234600 UTC
10.7 GHz   19.3 GHz   37.0 GHz   85.5 GHz

80.00   95.00   110.00 125.00 140.00 155.00 170.00 185.00 200.00 215.00 230.00 245.00 260.00 275.00 290.00
AMPR TB (K)
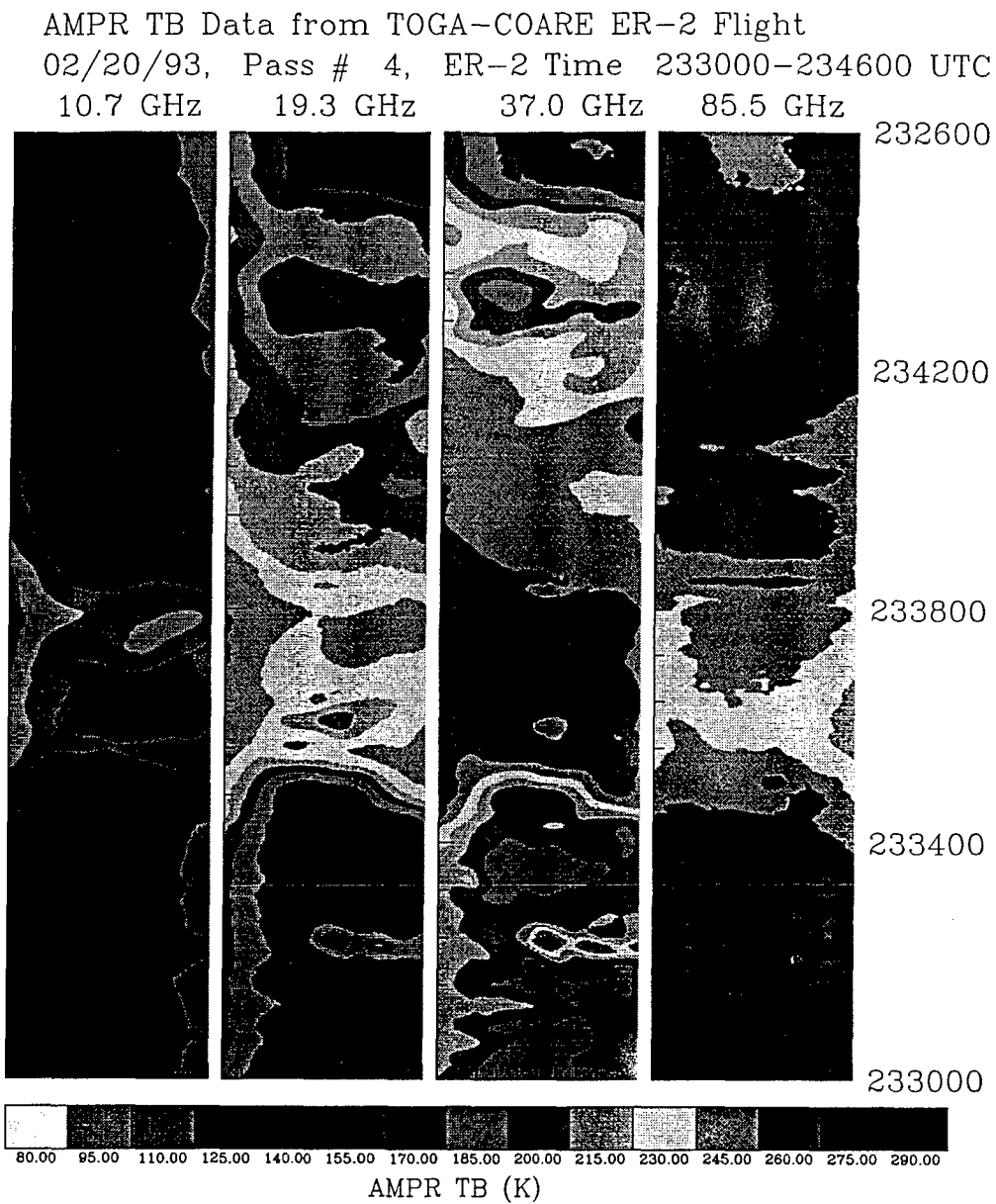
Figure 5.8:   Full swath AMPR TB images from pass #4 over a mesoscale system on 20 Feb 93.

AMPR TB Data from TOGA–COARE ER–2 Flight
02/22/93, Pass # 1, ER–2 Time 212400–214400 UTC

10.7 GHz   19.3 GHz   37.0 GHz   85.5 GHz
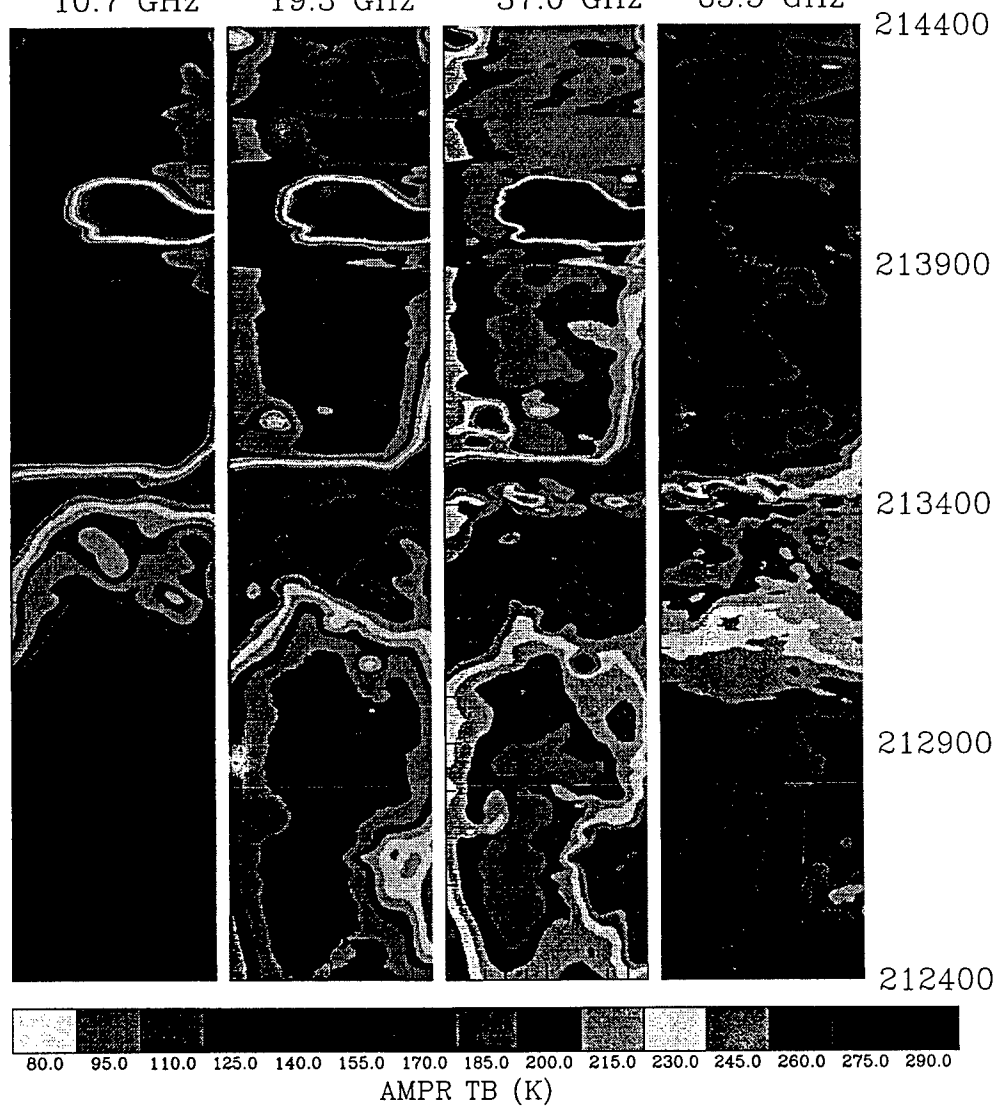
Figure 5.9: Full swath AMPR TB images from pass #1 over a squall line on 22 Feb 93.

AMPR TB Data from TOGA-COARE ER-2 Flight
02/22/93, Pass # 2, ER-2 Time 214600-215000 UTC

| 10.7 GHz | 19.3 GHz | 37.0 GHz | 85.5 GHz |
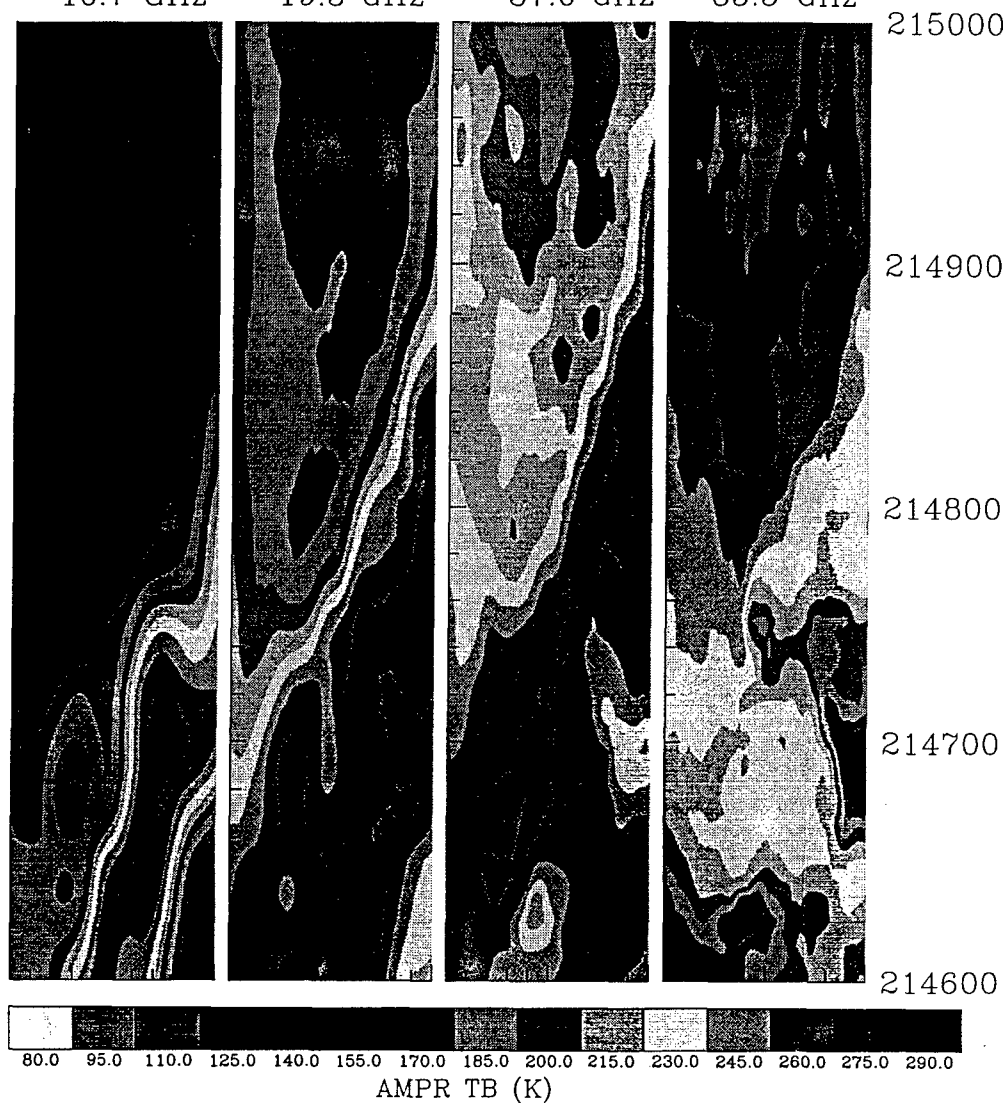
Figure 5.10: Full swath AMPR TB images from pass #2 over a squall line on 22 Feb 93.

AMPR TB Data from TOGA–COARE ER–2 Flight
02/22/93, Pass # 3, ER–2 Time 215800–221400 UTC

| 10.7 GHz | 19.3 GHz | 37.0 GHz | 85.5 GHz |
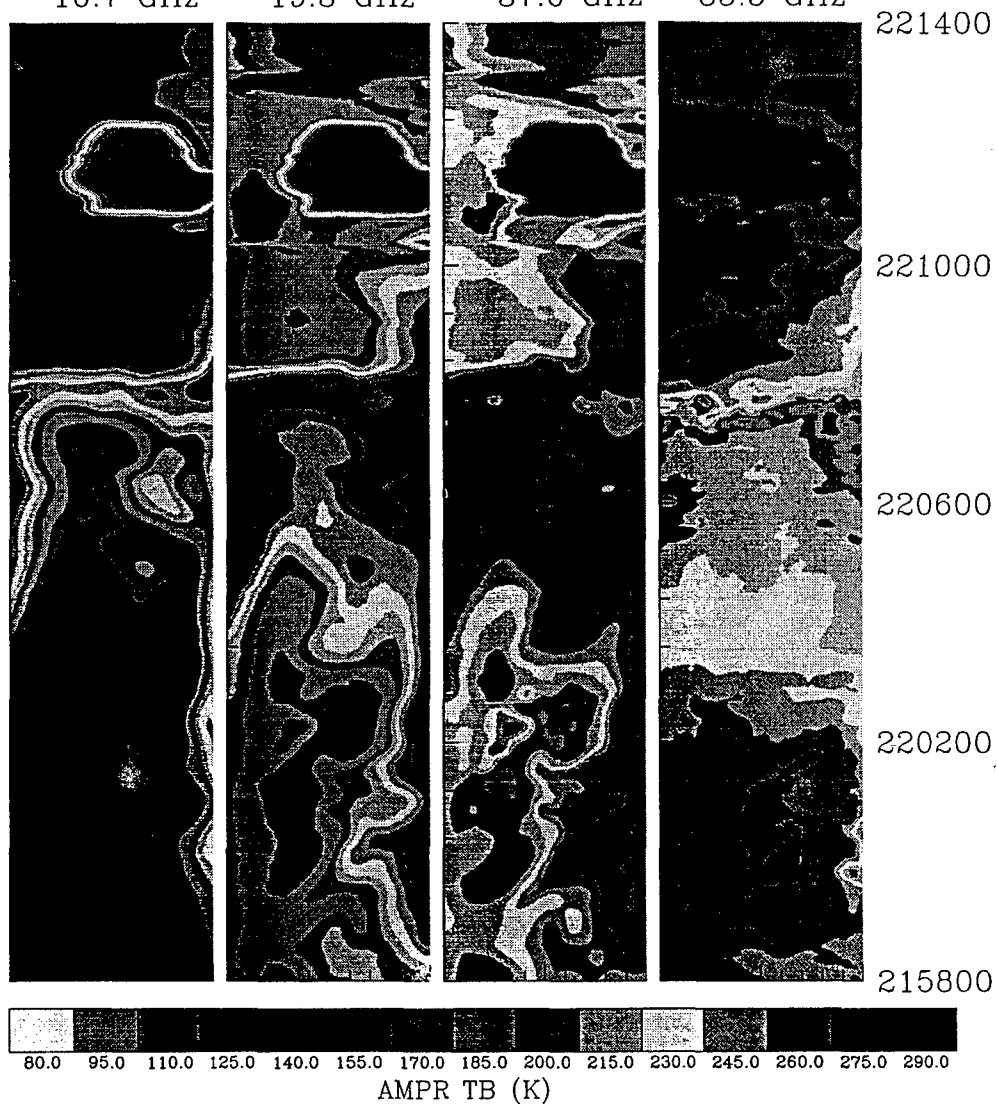
Figure 5.11: Full swath AMPR TB images from pass #3 over a squall line on 22 Feb 93.
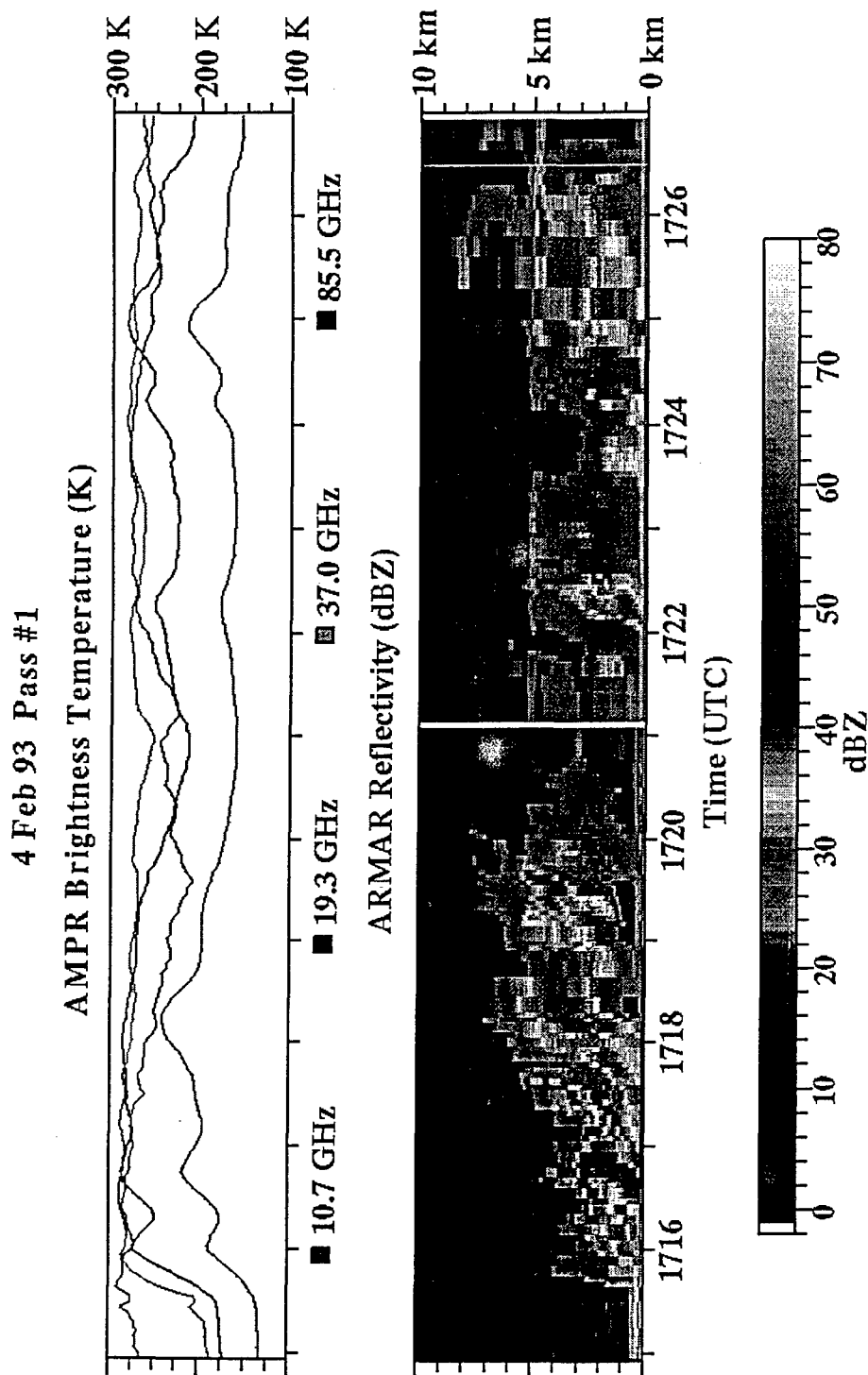
Figure 5.12: Nadir TB plots and Z profiles from pass #1 over a developing Tropical Cyclone Oliver on 04 Feb 93.

4 Feb 93 Pass #2

AMPR Brightness Temperature (K)

■ 10.7 GHz   ■ 19.3 GHz   ▩ 37.0 GHz   ■ 85.5 GHz

ARMAR Reflectivity (dBZ)
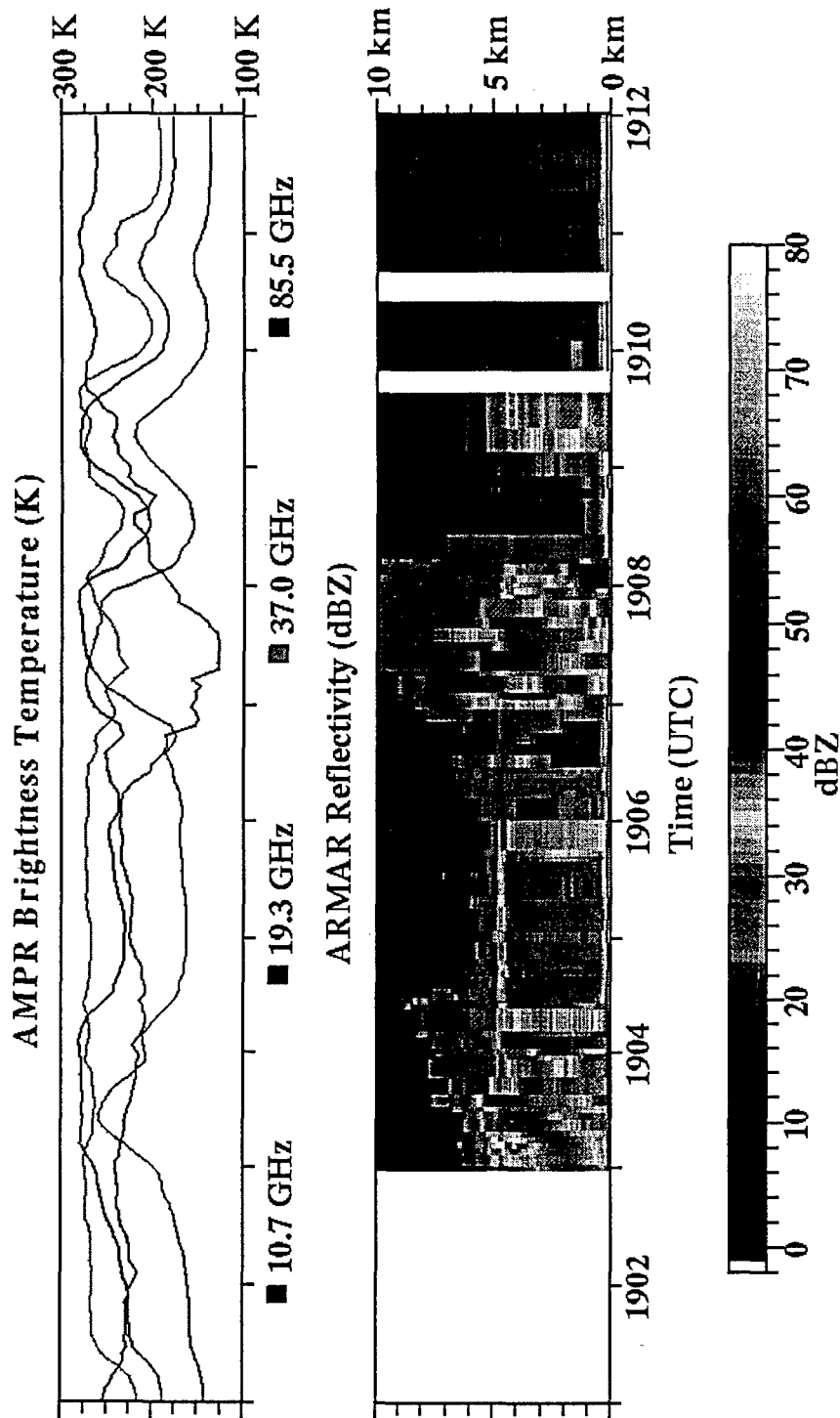
Figure 5.13: Nadir TB plots and Z profiles from pass #2 over a developing Tropical Cyclone Oliver on 04 Feb 93.

115
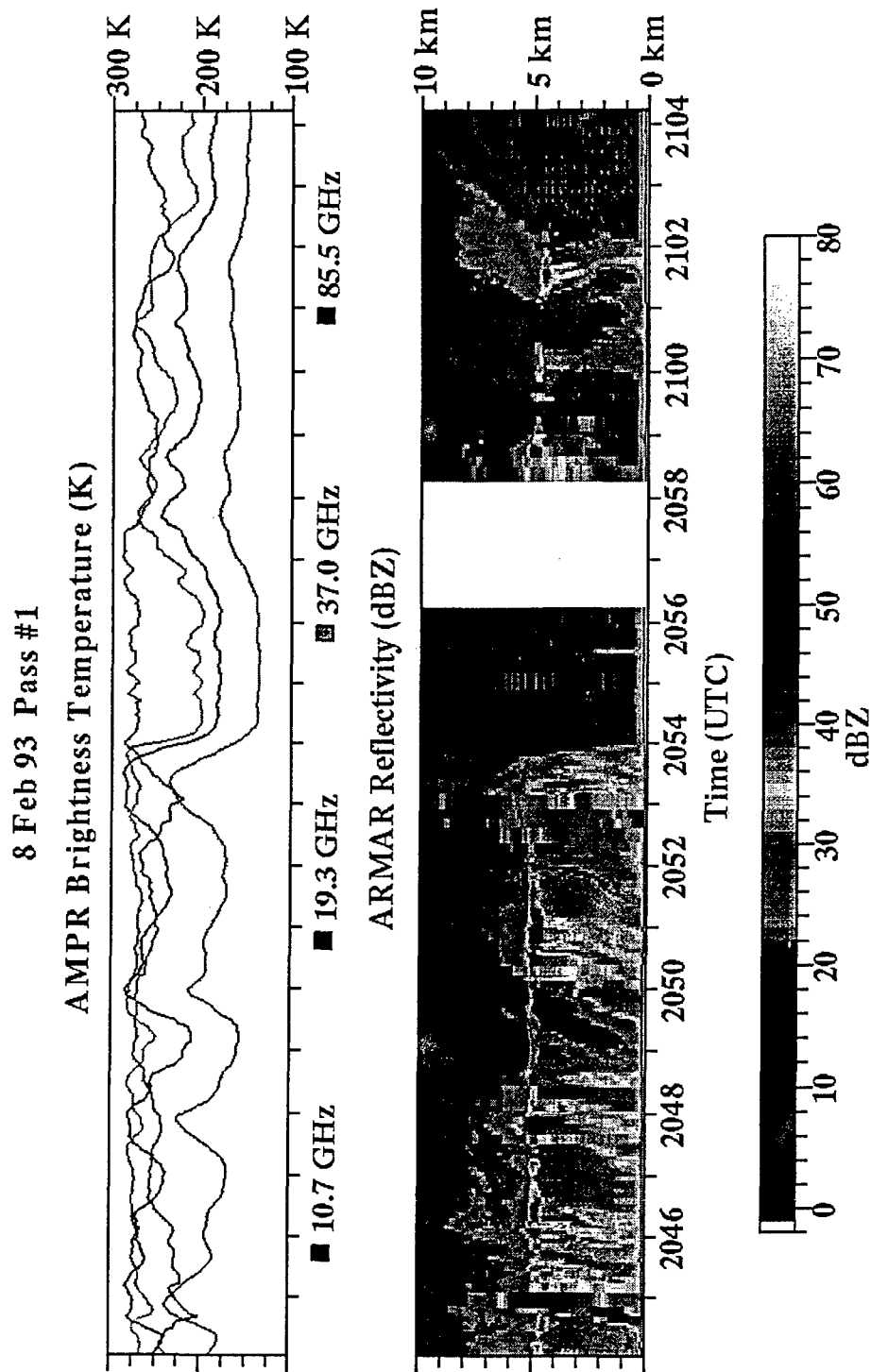
Figure 5.14: Nadir TB plots and Z profiles from pass #1 over a weakening Tropical Cyclone Oliver on 08 Feb 93.
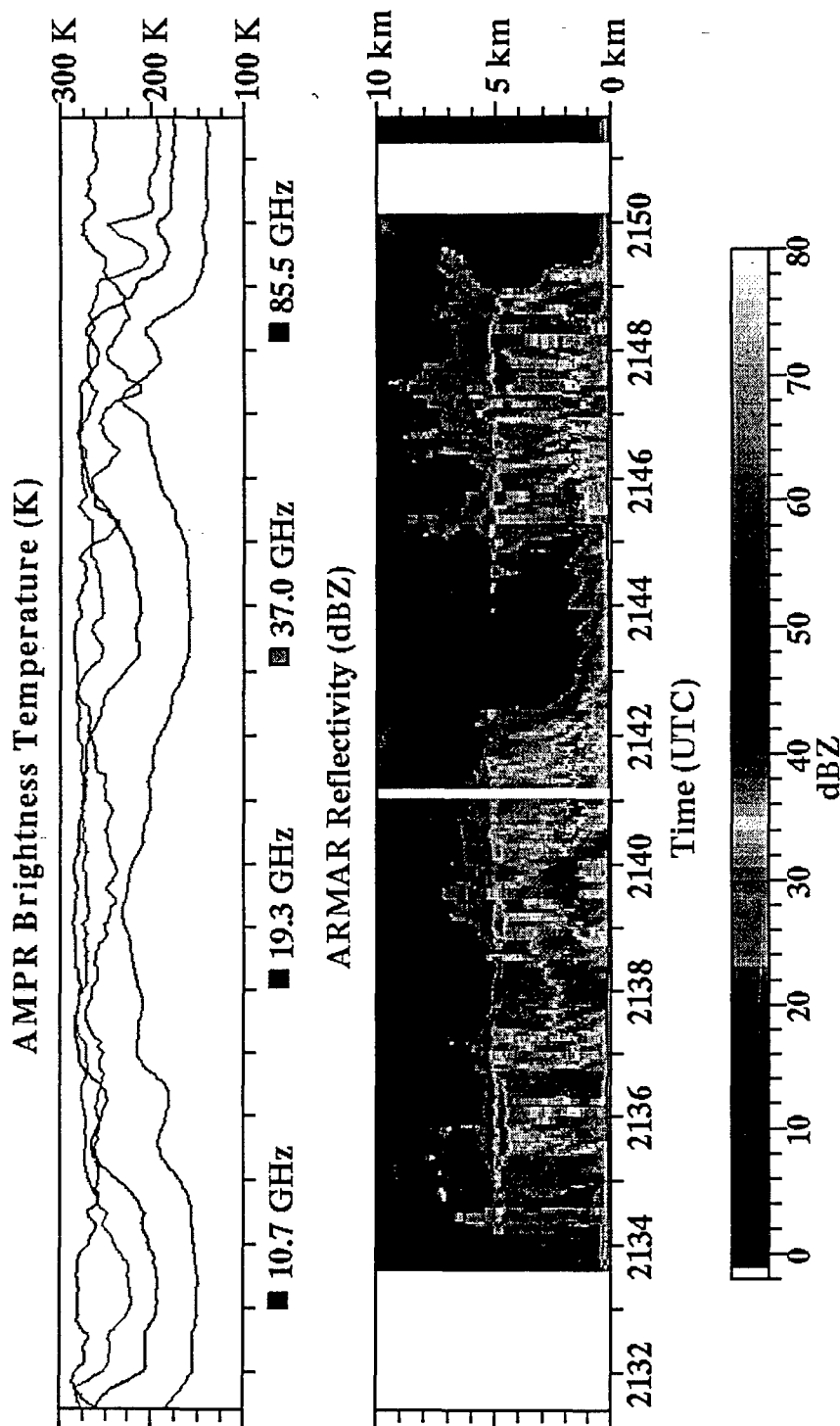
Figure 5.15: Nadir TB plots and Z profiles from pass #2 over a weakening Tropical Cyclone Oliver on 08 Feb 93.
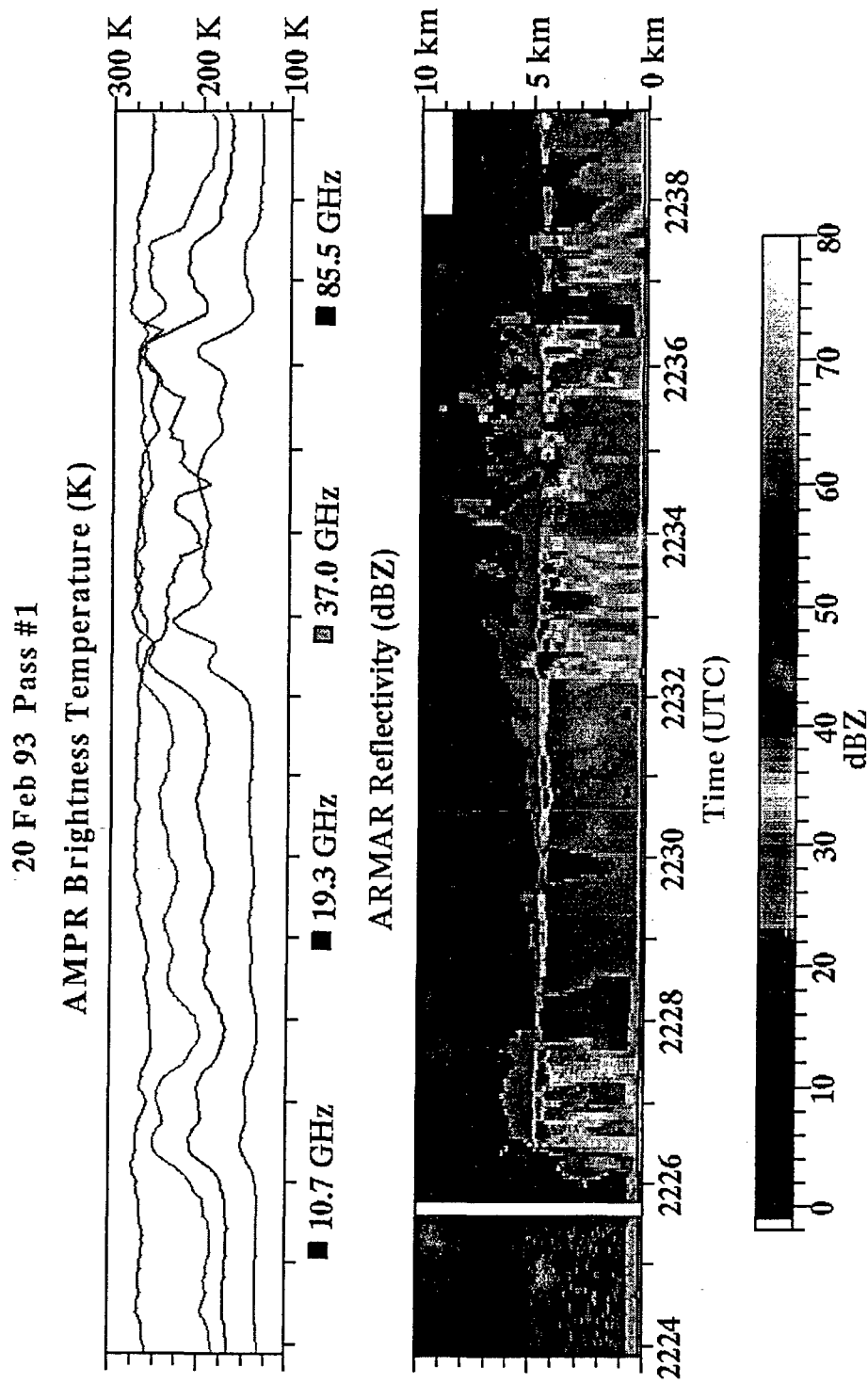
Figure 5.16: Nadir TB plots and Z profiles from pass #1 over a mesoscale system on 20 Feb 93.

118
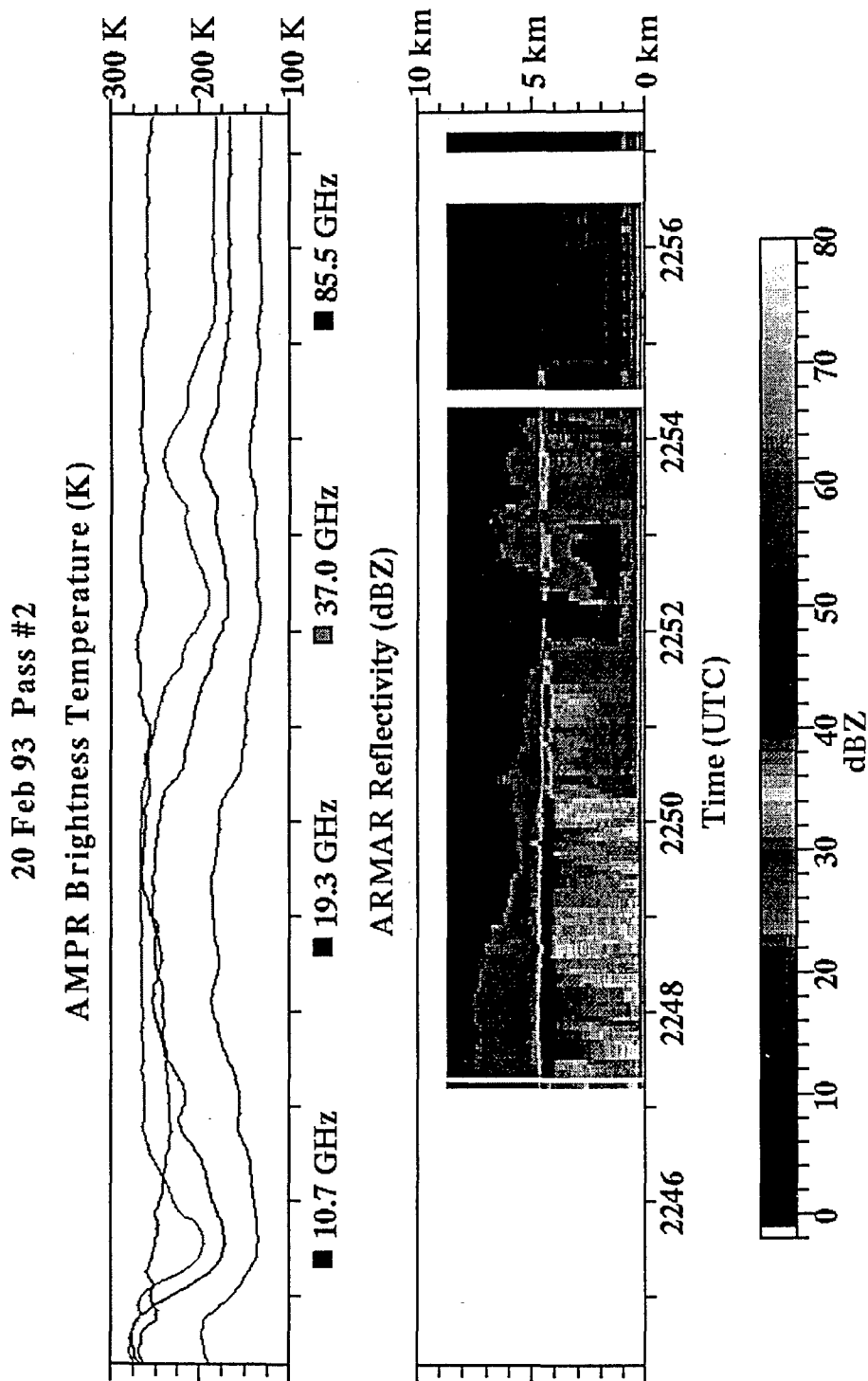
Figure 5.17: Nadir TB plots and Z profiles from pass #2 over a mesoscale system on 20 Feb 93.

119
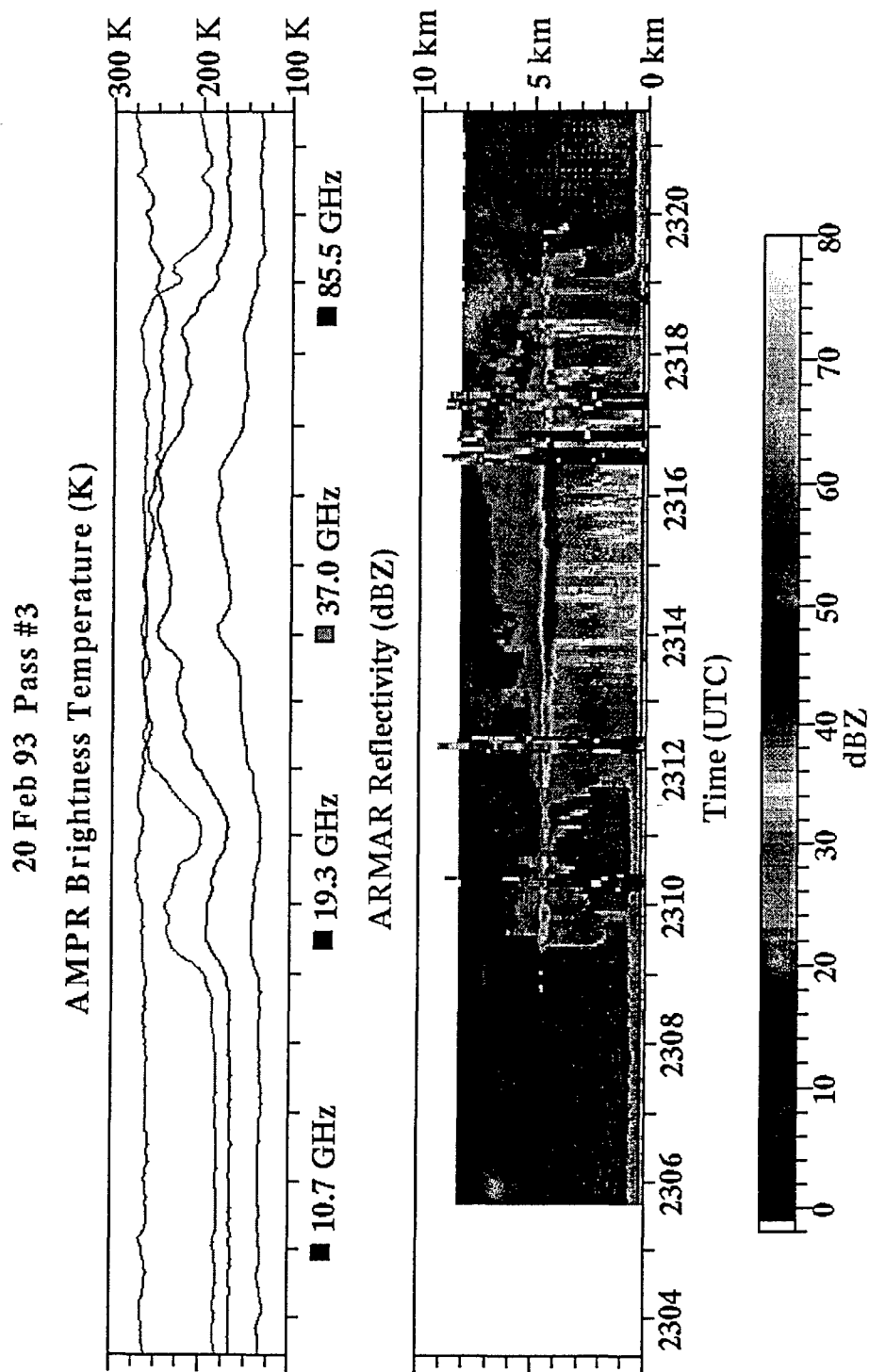
Figure 5.18: Nadir TB plots and Z profiles from pass #3 over a mesoscale system on 20 Feb 93.

20 Feb 93 Pass #4

AMPR Brightness Temperature (K)

- 10.7 GHz
- 19.3 GHz
- 37.0 GHz
- 85.5 GHz
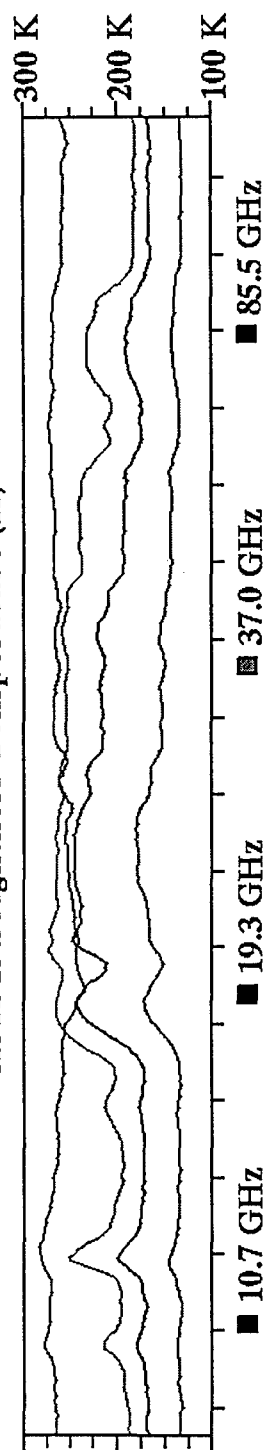
ARMAR Reflectivity (dBZ)
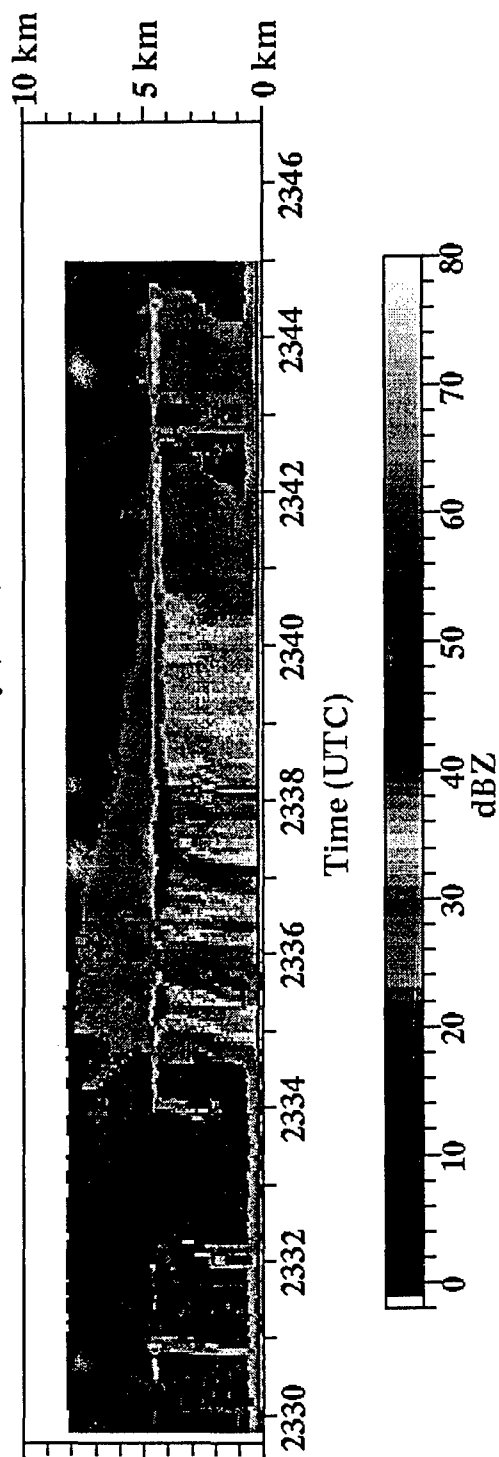
Figure 5.19: Nadir TB plots and Z profiles from pass #4 over a mesoscale system on 20 Feb 93.

22 Feb 93 Pass #1

AMPR Brightness Temperature (K)

■ 10.7 GHz   ■ 19.3 GHz   ▨ 37.0 GHz   ■ 85.5 GHz

ARMAR Reflectivity (dBZ)

Time (UTC)

dBZ
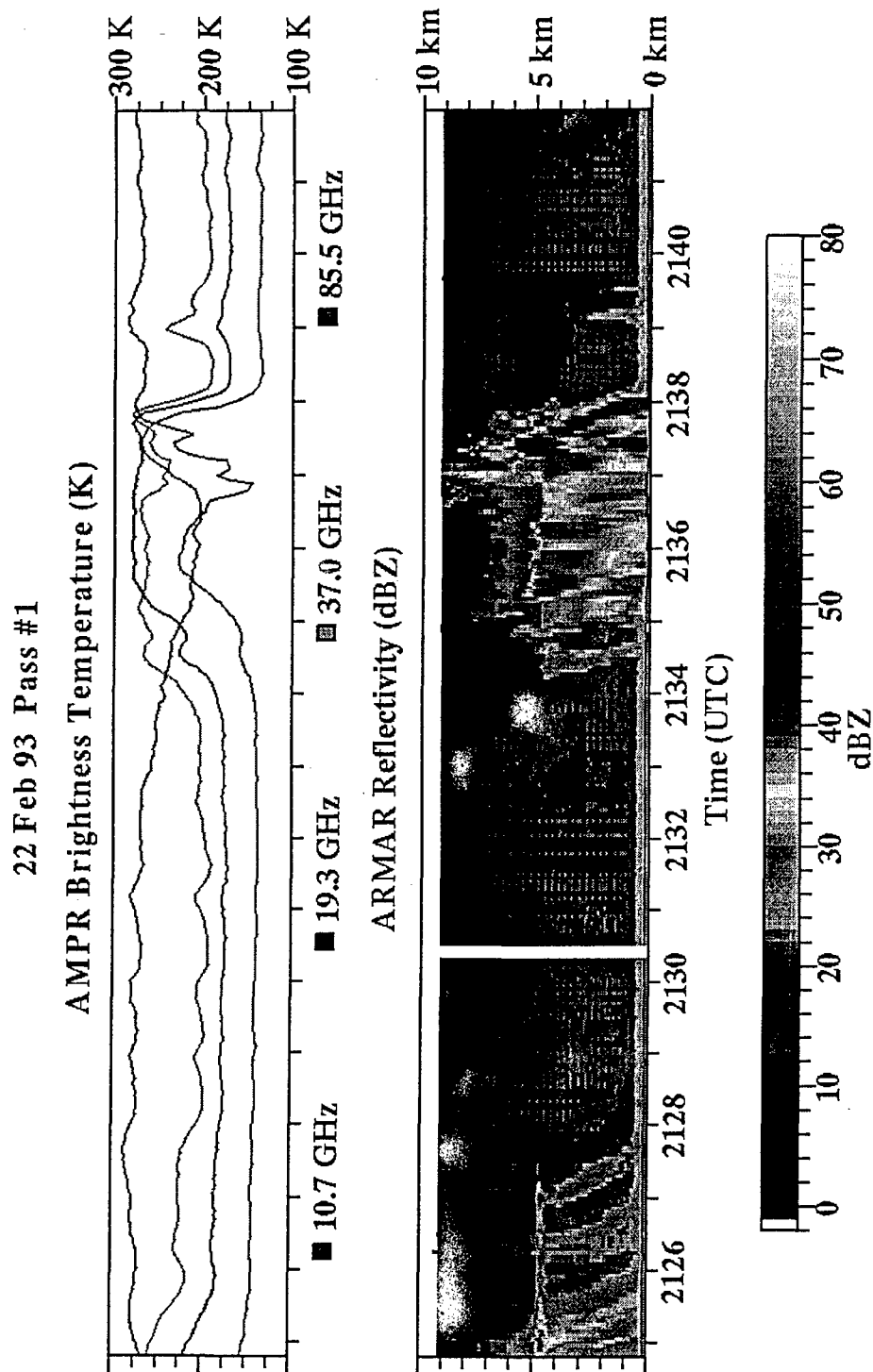
Figure 5.20: Nadir TB plots and Z profiles from pass #1 over a squall line on 22 Feb 93.

Figure 5.21: Nadir TB plots and Z profiles from pass #2 over a squall line on 22 Feb 93.

123

22 Feb 93 Pass #3

AMPR Brightness Temperature (K)

300 K
200 K
100 K

■ 10.7 GHz   ■ 19.3 GHz   ■ 37.0 GHz   ■ 85.5 GHz

ARMAR Reflectivity (dBZ)

10 km
5 km
0 km

2202 2204 2206 2208 2210 2212 2214

Time (UTC)
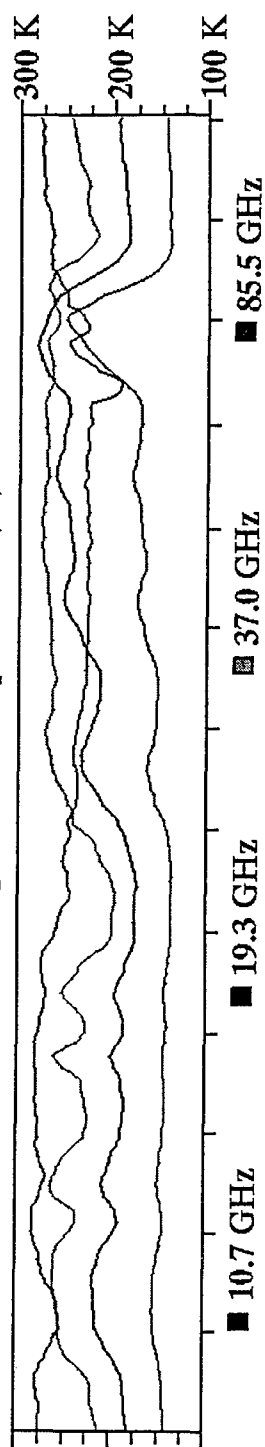
0 10 20 30 40 50 60 70 80
dBZ
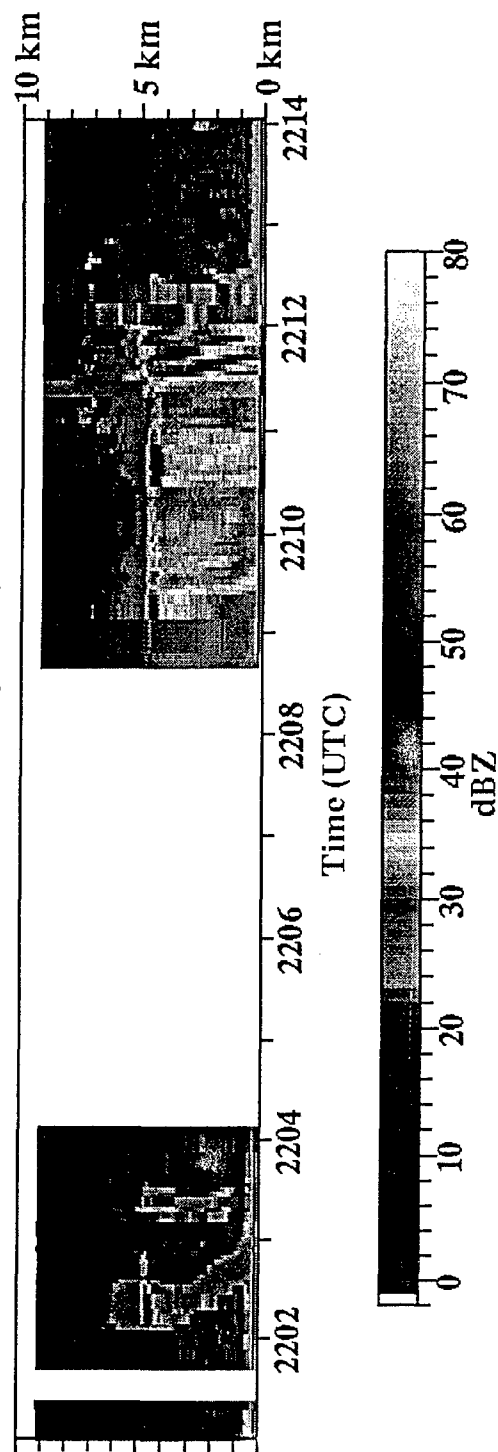
Figure 5.22: Nadir TB plots and Z profiles from pass #3 over a squall line on 22 Feb 93.

124
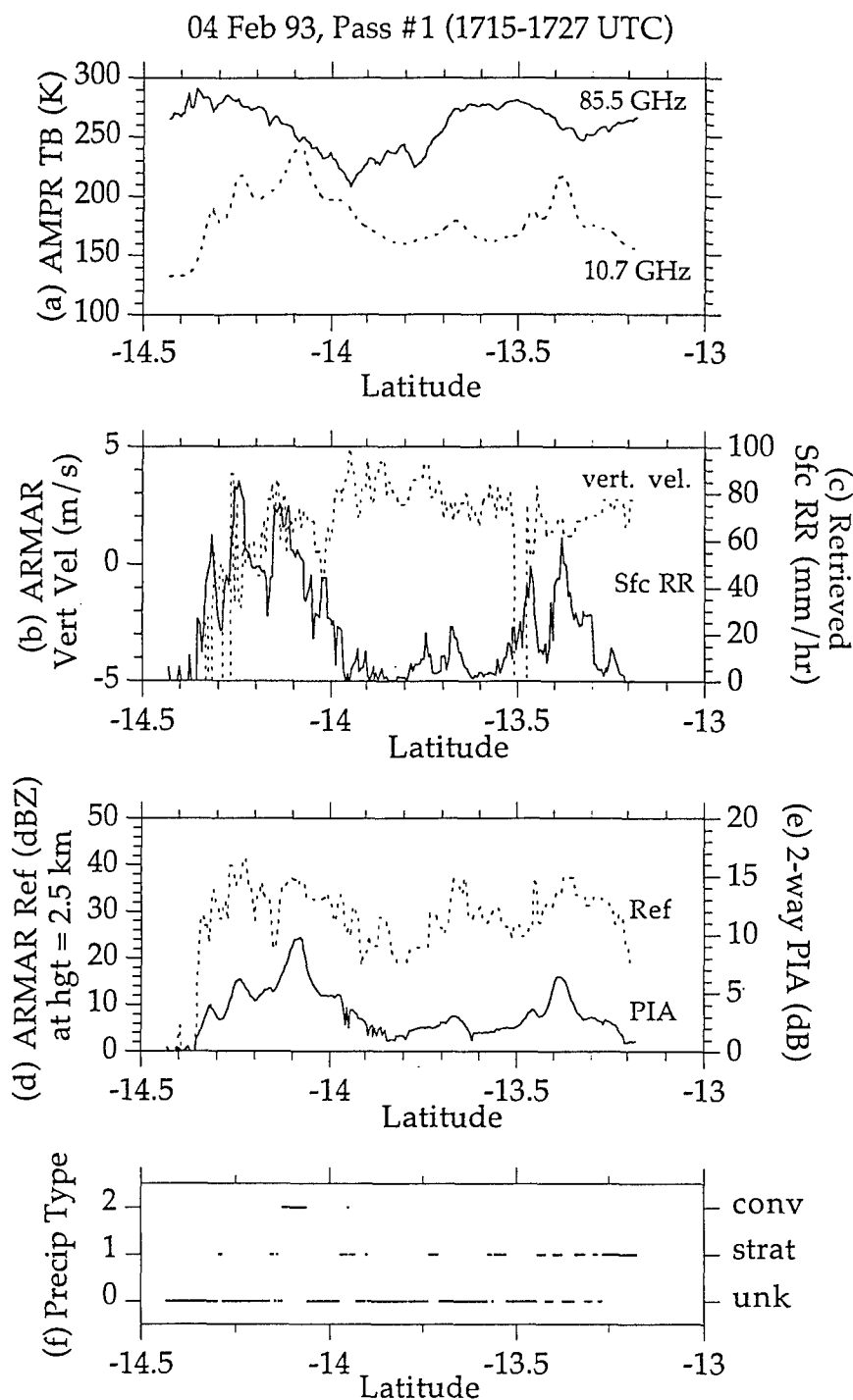
Figure 5.23: Nadir plots from pass #1, 04 Feb 93 of (a) AMPR TBs, (b) average ARMAR vertical velocity in the rain growth layer, (c) retrieved surface rainrate, (d) ARMAR reflectivity at 2.5 km height, (e) total 2-way PIA, and (f) precipitation type.

125
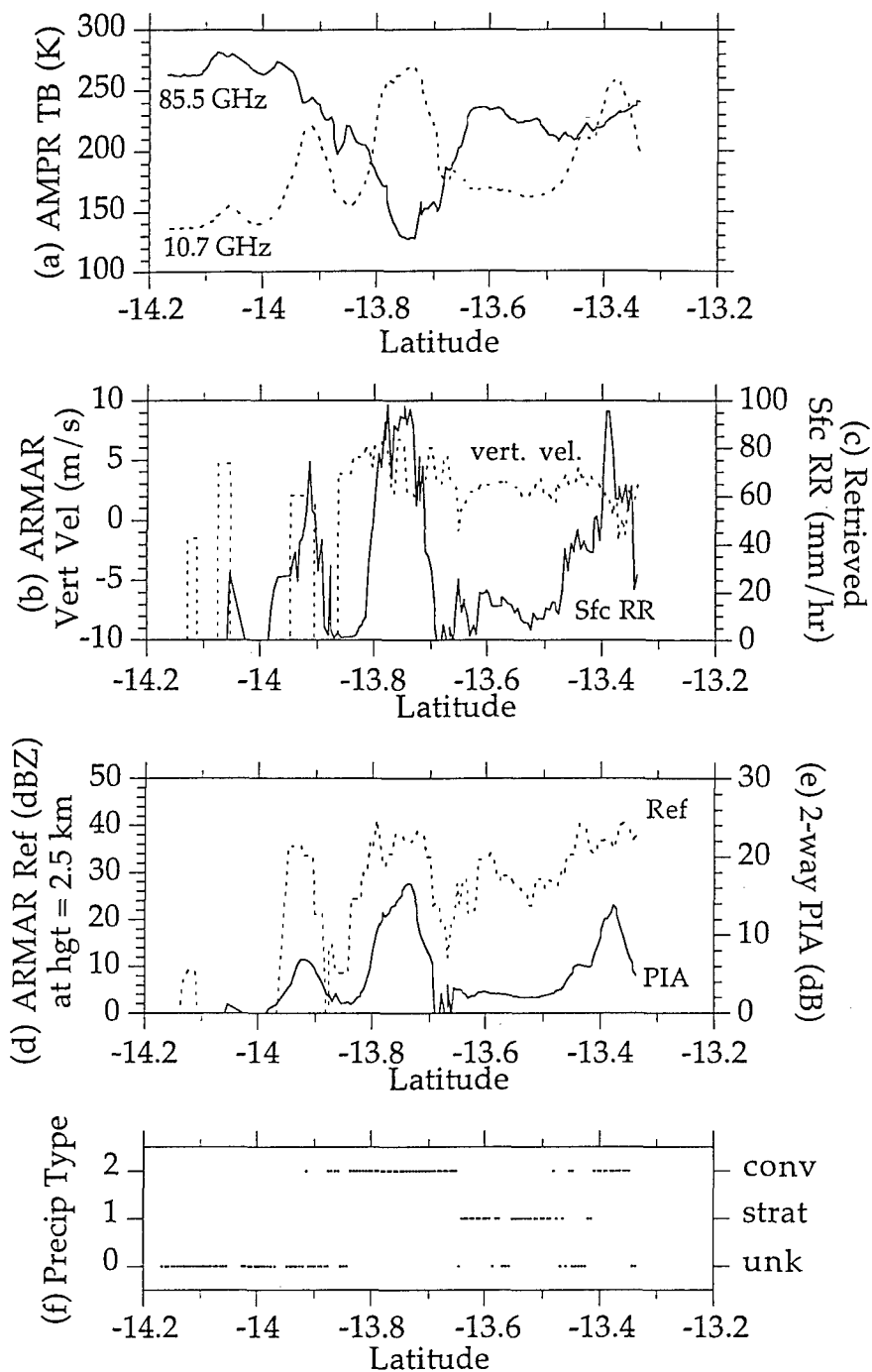
Figure 5.24: Nadir plots from pass #2, 04 Feb 93 of (a) AMPR TBs, (b) average ARMAR vertical velocity in the rain growth layer, (c) retrieved surface rainrate, (d) ARMAR reflectivity at 2.5 km height, (e) total 2-way PIA, and (f) precipitation type.

126
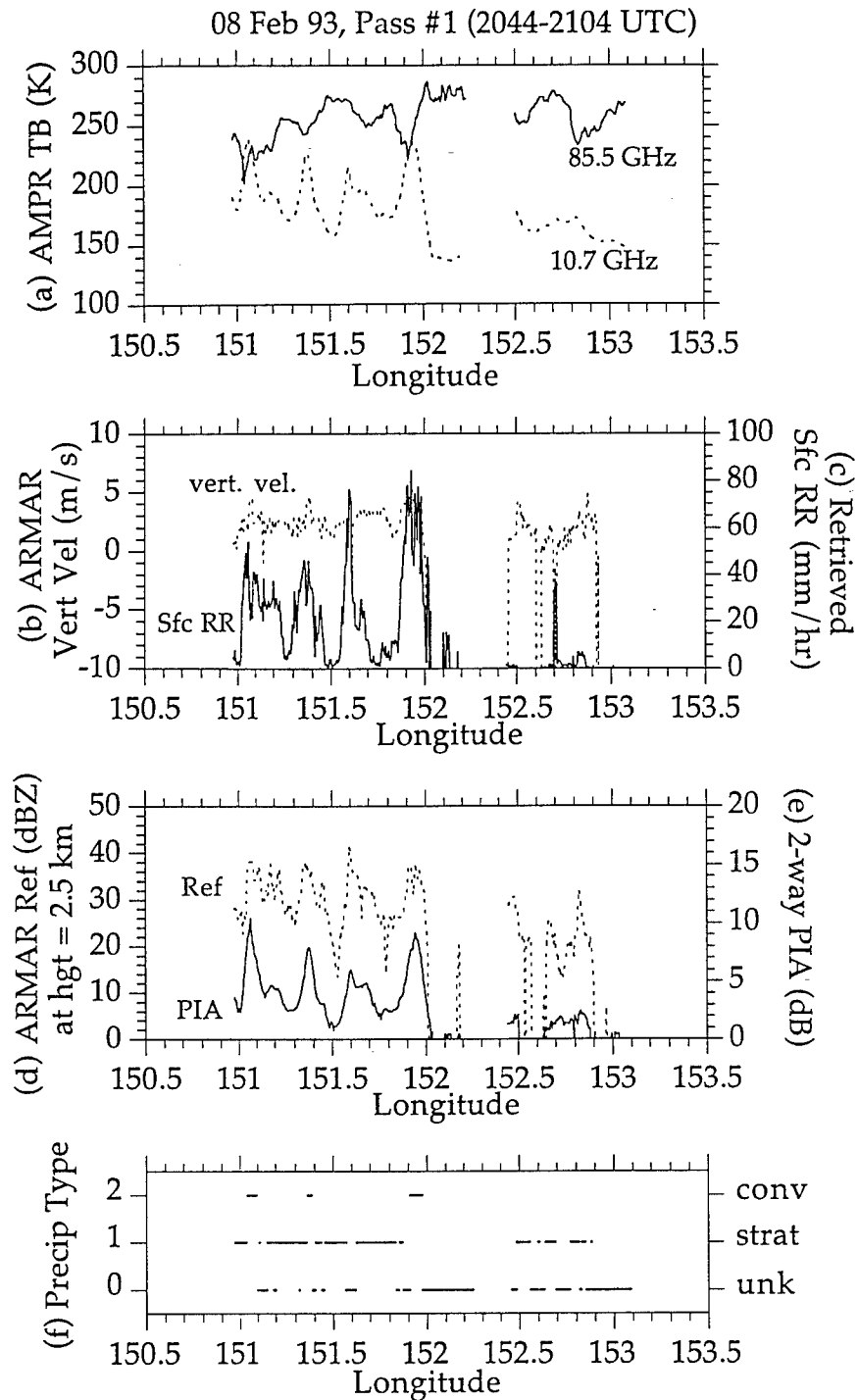
Figure 5.25: Nadir plots from pass #1, 08 Feb 93 of (a) AMPR TBs, (b) average ARMAR vertical velocity in the rain growth layer, (c) retrieved surface rainrate, (d) ARMAR reflectivity at 2.5 km height, (e) total 2-way PIA, and (f) precipitation type.

127
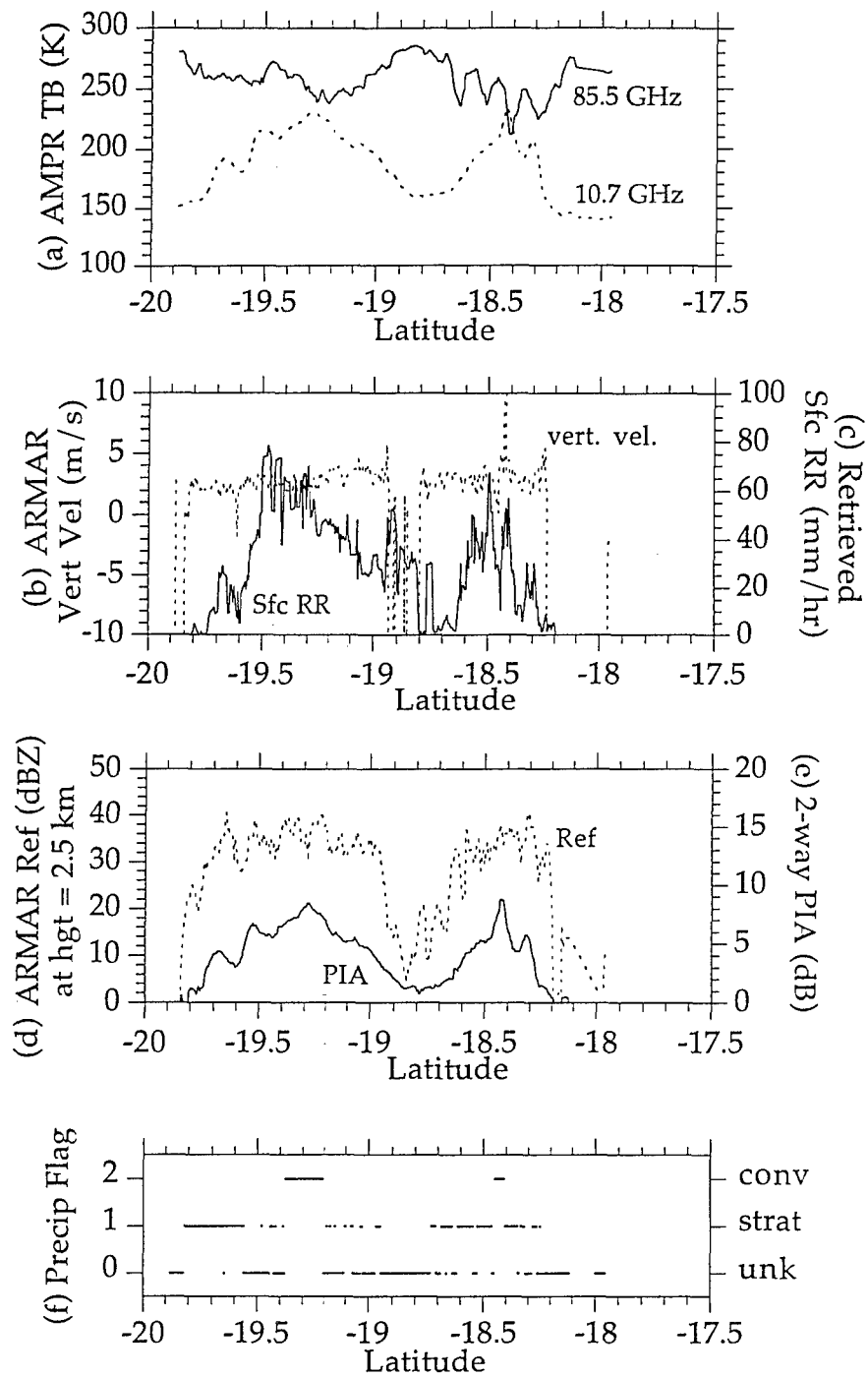
Figure 5.26: Nadir plots from pass #2, 08 Feb 93 of (a) AMPR TBs, (b) average ARMAR vertical velocity in the rain growth layer, (c) retrieved surface rainrate, (d) ARMAR reflectivity at 2.5 km height, (e) total 2-way PIA, and (f) precipitation type.
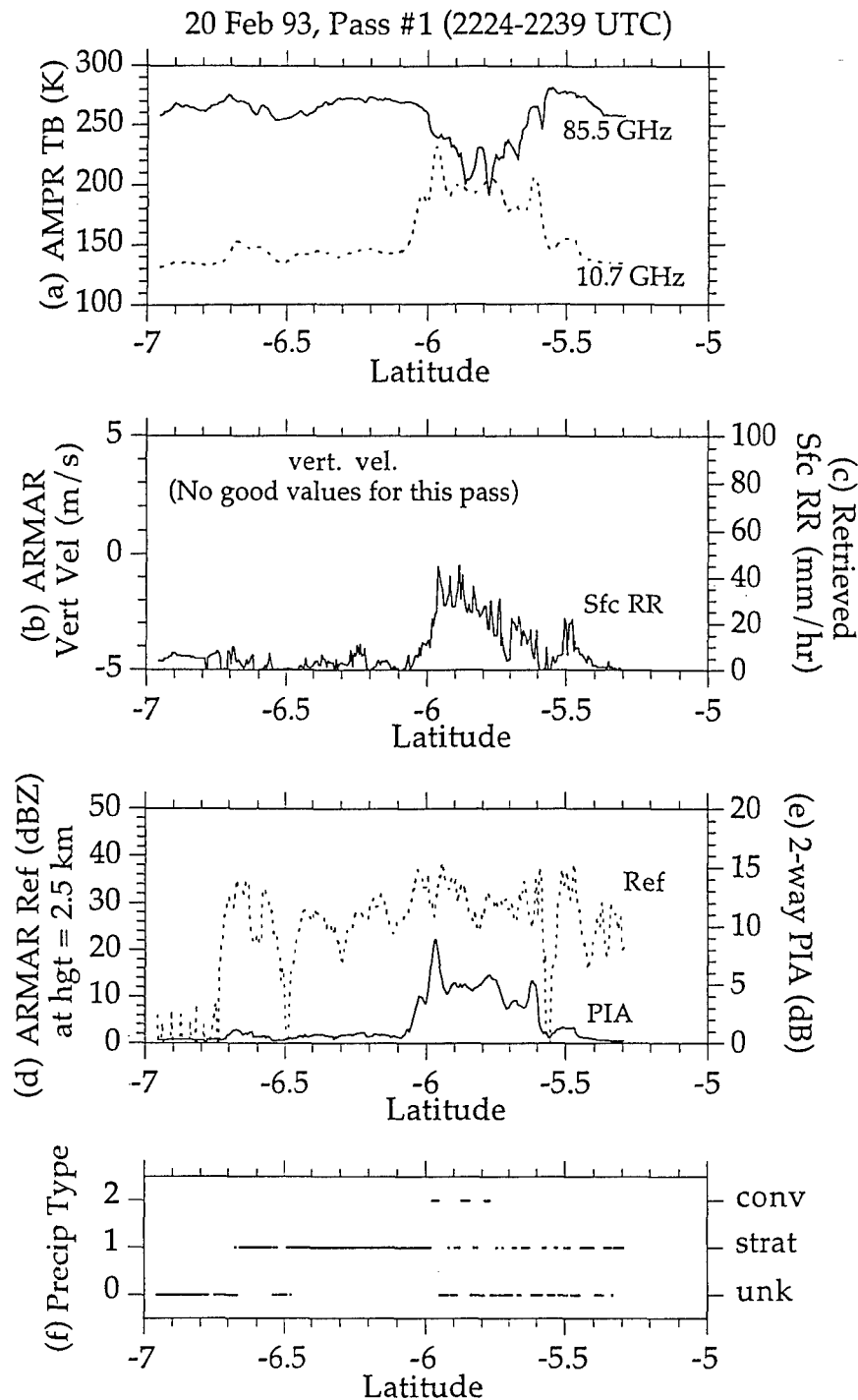
Figure 5.27: Nadir plots from pass #1, 20 Feb 93 of (a) AMPR TBs, (b) average ARMAR vertical velocity in the rain growth layer, (c) retrieved surface rainrate, (d) ARMAR reflectivity at 2.5 km height, (e) total 2-way PIA, and (f) precipitation type.

129
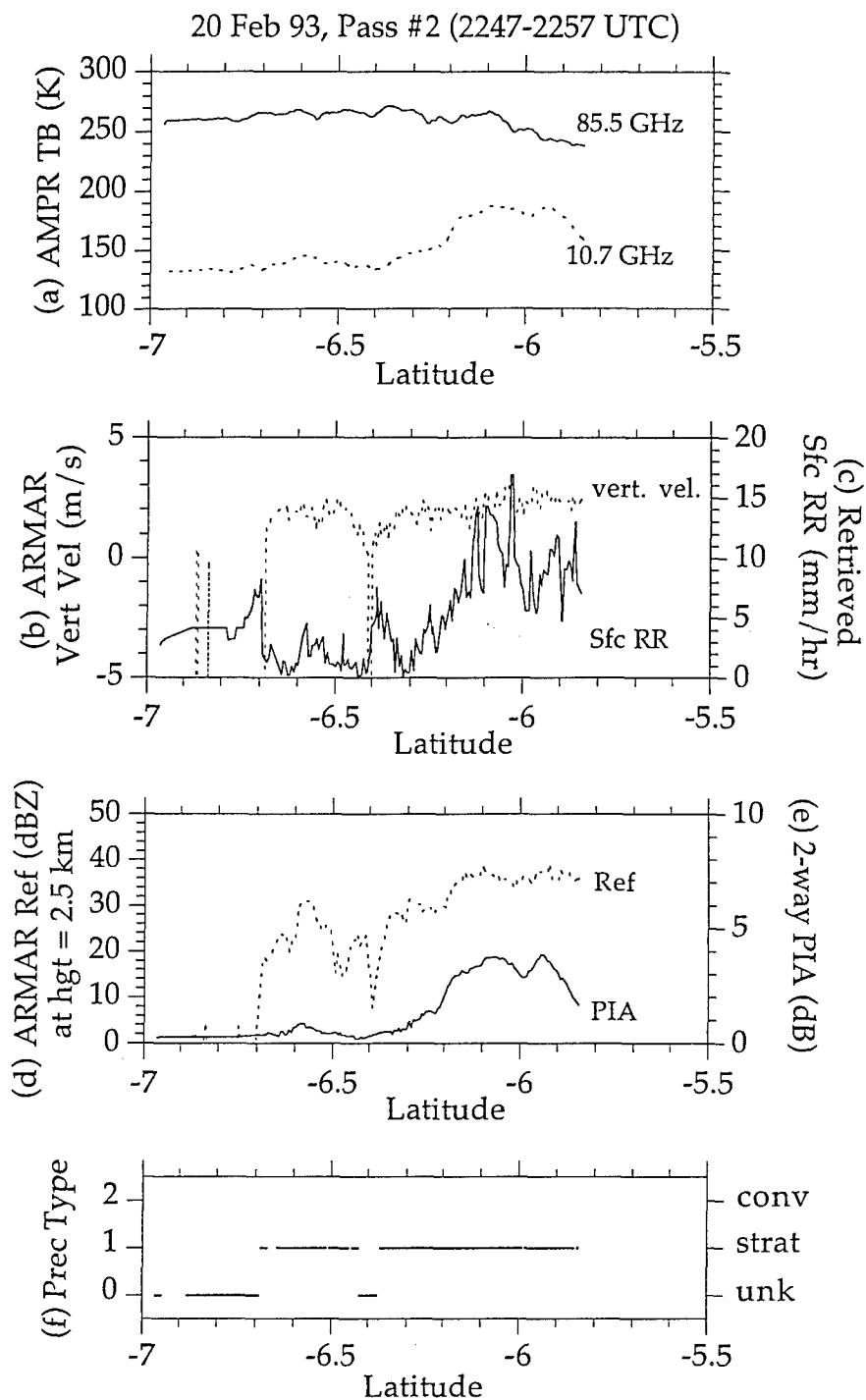
Figure 5.28: Nadir plots from pass #2, 20 Feb 93 of (a) AMPR TBs, (b) average ARMAR vertical velocity in the rain growth layer, (c) retrieved surface rainrate, (d) ARMAR reflectivity at 2.5 km height, (e) total 2-way PIA, and (f) precipitation type.
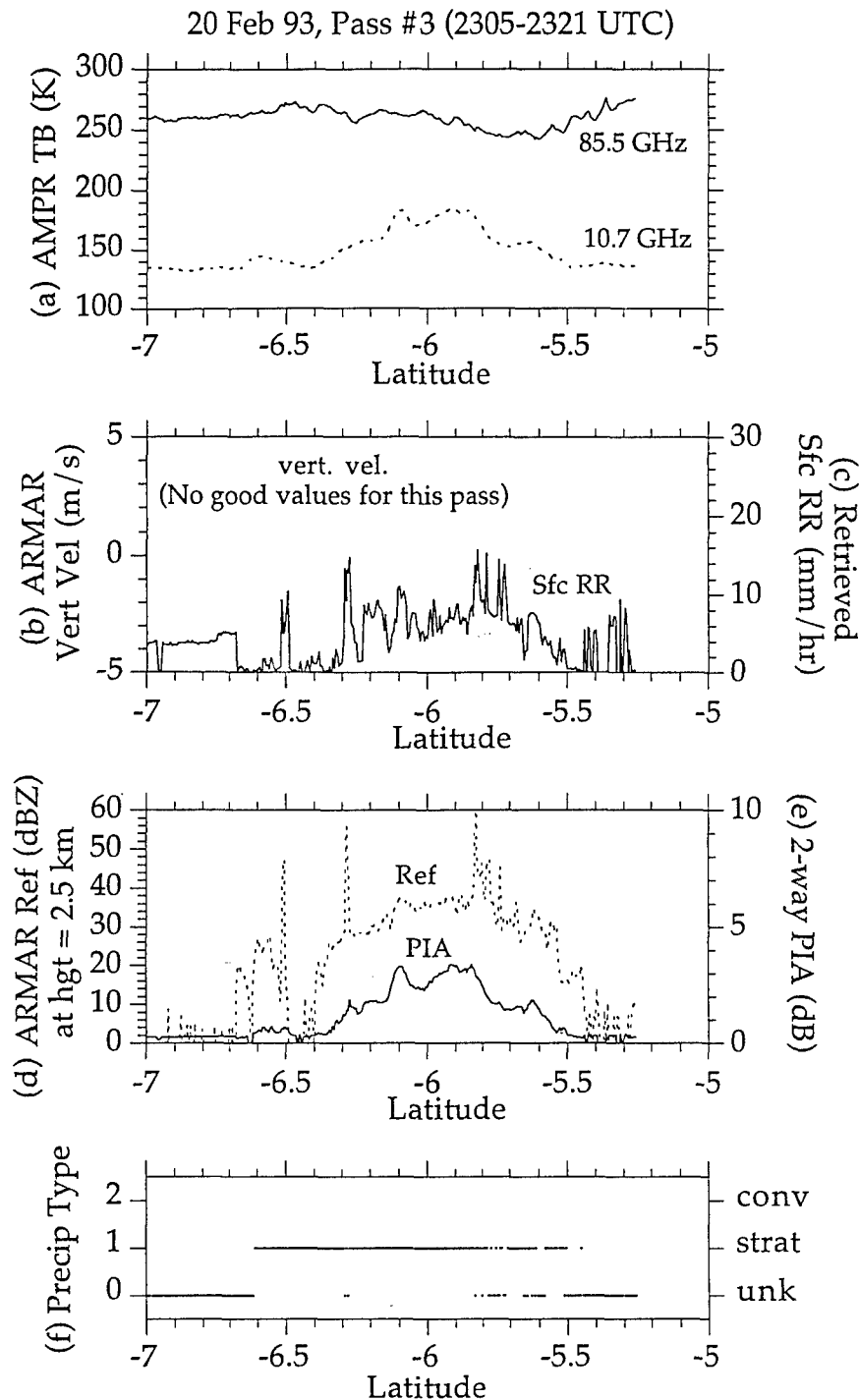
Figure 5.29: Nadir plots from pass #3, 20 Feb 93 of (a) AMPR TBs, (b) average ARMAR vertical velocity in the rain growth layer, (c) retrieved surface rainrate, (d) ARMAR reflectivity at 2.5 km height, (e) total 2-way PIA, and (f) precipitation type.

131
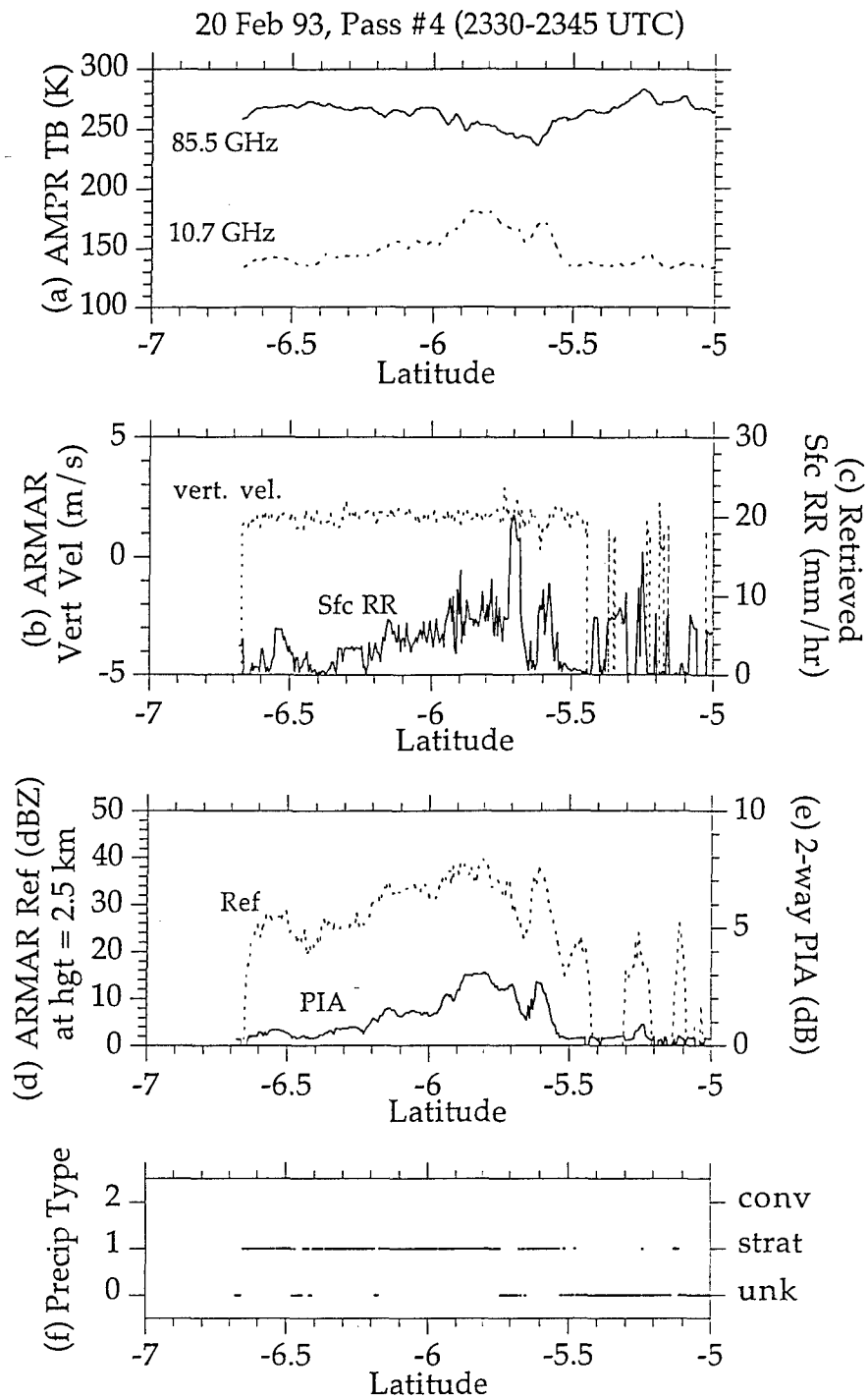
Figure 5.30: Nadir plots from pass #4, 20 Feb 93 of (a) AMPR TBs, (b) average ARMAR vertical velocity in the rain growth layer, (c) retrieved surface rainrate, (d) ARMAR reflectivity at 2.5 km height, (e) total 2-way PIA, and (f) precipitation type.
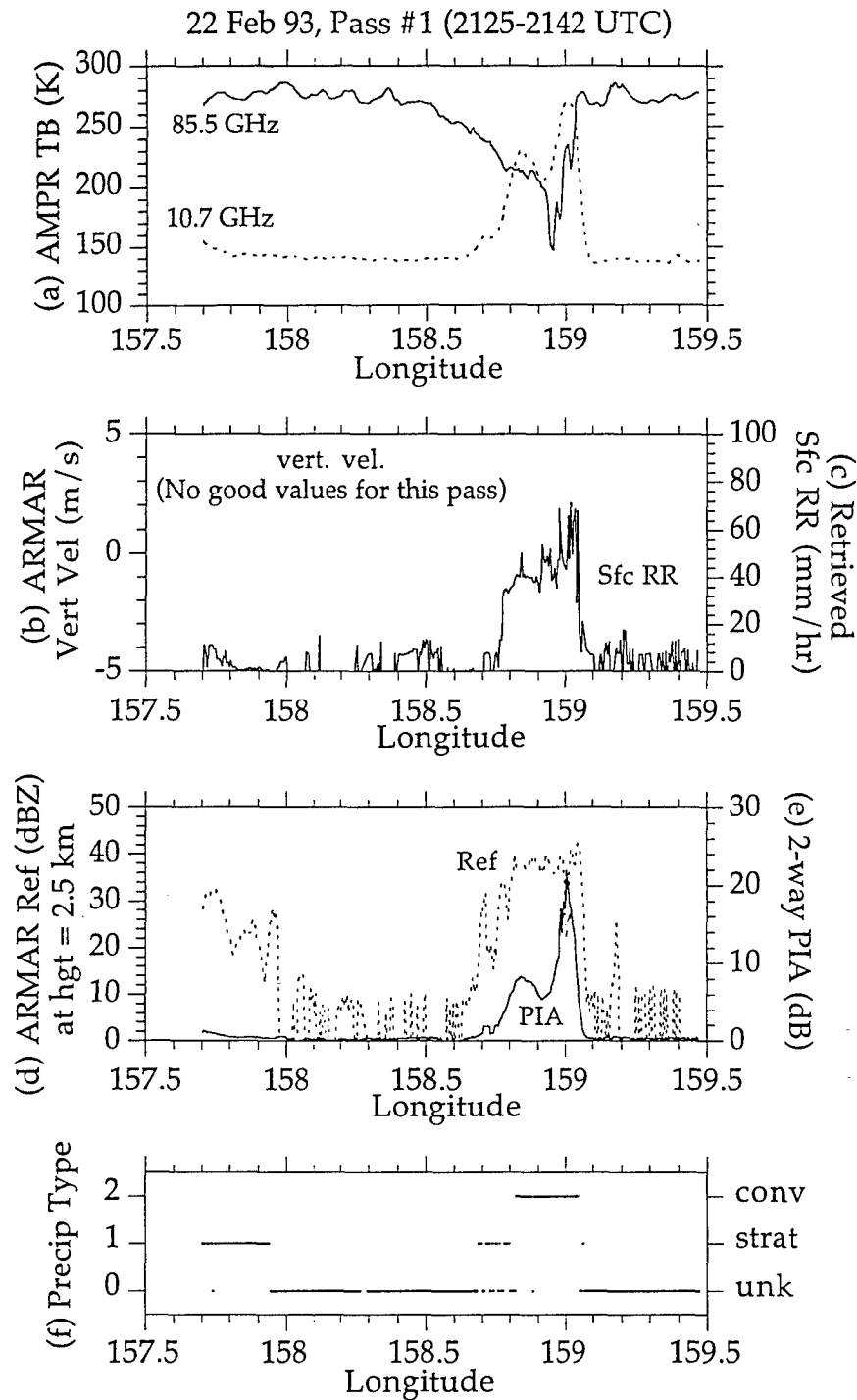
Figure 5.31: Nadir plots from pass #1, 22 Feb 93 of (a) AMPR TBs, (b) average ARMAR vertical velocity in the rain growth layer, (c) retrieved surface rainrate, (d) ARMAR reflectivity at 2.5 km height, (e) total 2-way PIA, and (f) precipitation type.
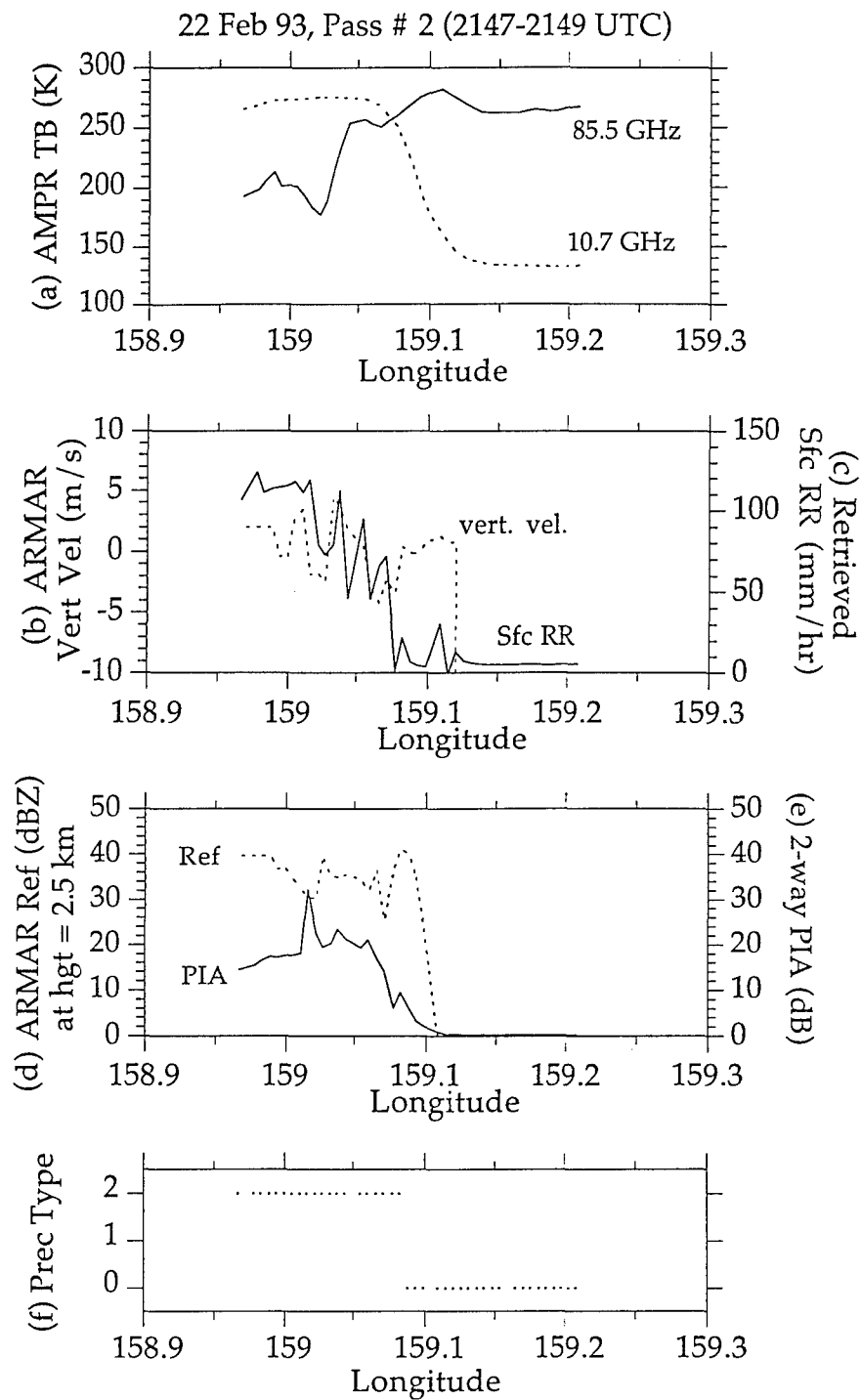
Figure 5.32: Nadir plots from pass #2, 22 Feb 93 of (a) AMPR TBs, (b) average ARMAR vertical velocity in the rain growth layer, (c) retrieved surface rainrate, (d) ARMAR reflectivity at 2.5 km height, (e) total 2-way PIA, and (f) precipitation type.
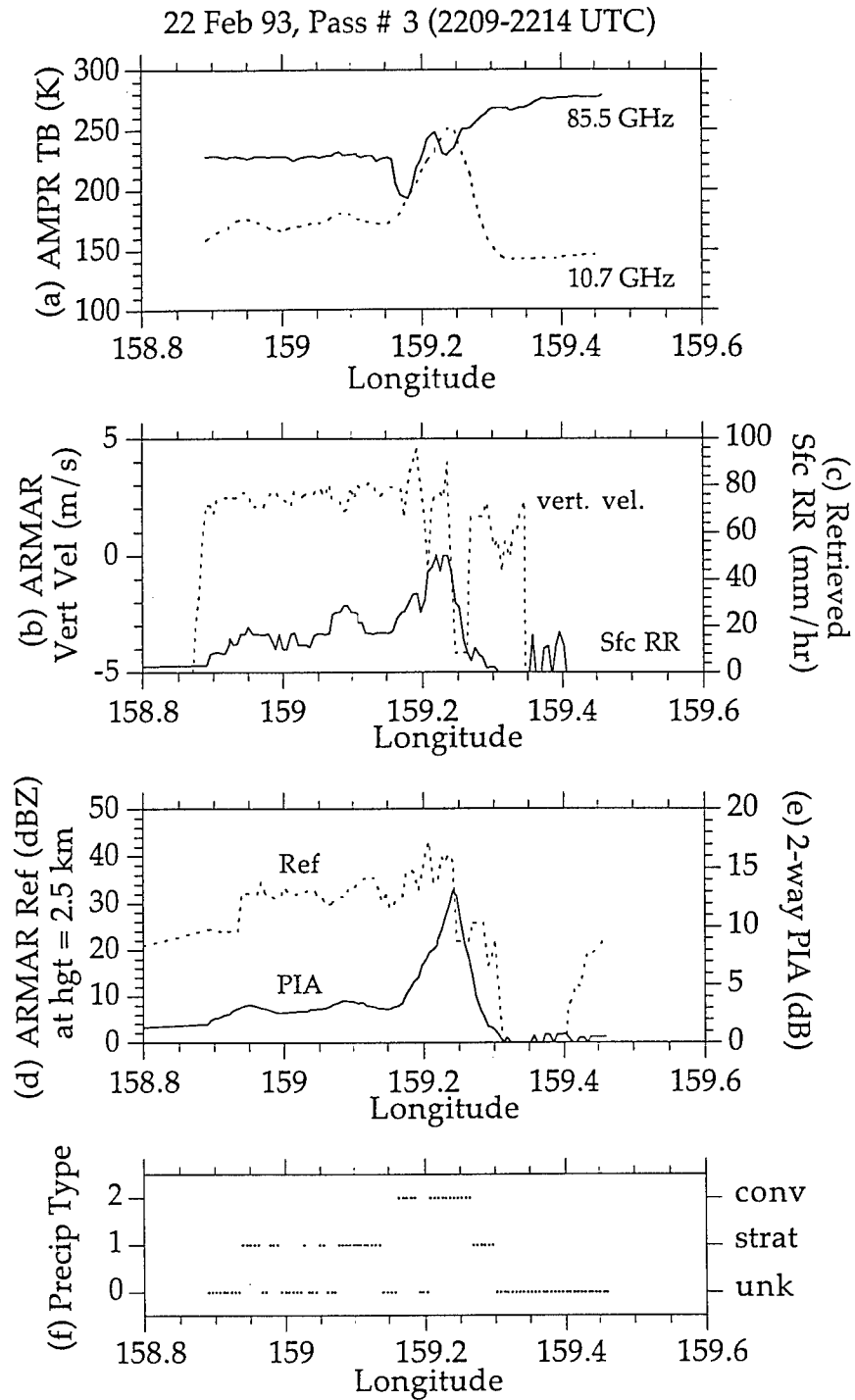
Figure 5.33: Nadir plots from pass #3, 22 Feb 93 of (a) AMPR TBs, (b) average ARMAR vertical velocity in the rain growth layer, (c) retrieved surface rainrate, (d) ARMAR reflectivity at 2.5 km height, (e) total 2-way PIA, and (f) precipitation type.

135

The top panel is a plot of the 10.7 GHz and 85.5 GHz AMPR TB measurements, similar to those displayed in Figures 5.12-5.22. The second panel displays two quantities, the first being a plot of the surface rainfall rate generated by the combined retrieval. The second is a plot of the average ARMAR Doppler velocity in the precipitation growth layer, where the growth layer is defined as having a thickness of 2 km and bounded at the bottom by the melting level. The standard sign convention for Doppler velocity is used, where velocities away from the radar are defined as positive. Hence for the case of a downlooking radar, positive values are downward, and indicate that the hydrometeors (which are the backscatterers for the radar signal) are falling in the layer.

The third panel in the series of TOGA-COARE retrieval figures also displays two quantities. The first is the ARMAR reflectivity at 2.5 km, a level roughly centered between the surface and the melting level, where the radar returns are due to liquid rain. The second is a plot of 2-way PIA, as measured by the RTE model in the following way. After the optimization is complete, the solution hydrometeors are re-run through the unified RTE model, where the model is reset to correct for attenuation, resulting in the calculation of an equivalent unattenuated Z profile. This is compared to the original solution Z profile, which is attenuated by the RTE model to match the response of the real radar, which is subject to attenuation. The difference between attenuated and unattenuated reflectivity at the surface between these two calculations is a measure of the attenuation between the surface and the radar, and hence is equivalent to total 2-way PIA.

Finally the fourth and bottom panel in these series of figures is a plot of precipitation type. At each point where a hydrometeor profile retrieval is

136

calculated in the above panels, the measured TBs and Zs are used to estimate precipitation type, by the method described in section 2.7. The diagnosed type for the case is then indicated as a point on the plot, unlike the top three panels which are all line plots.

The discussion that follows will analyze the retrieval results from each of the four TOGA-COARE flights used in this study. As each flight contains multiple passes over generally the same precipitating region, the analysis for each flight will center on a single pass to avoid a largely redundant discussion. Furthermore there are many features common between all four flights, so to limit repetitive analysis, the first flight discussed will offer an exhaustive explanation for these common features, while the discussion for the remaining three flights will be more brief and focus on outstanding features not observed in the other flights.

5.1.1 Retrieval Results from 08 Feb 93 flight

While 04 Feb 93 was the first flight to be used in this study, the discussion begins out of sequence to focus on pass #1 from 08 Feb 93, as this pass contains numerous interesting features which lends itself to an in-depth analysis. A weakening Tropical Cyclone Oliver is recognizable in the AMPR TB swath images displayed in Figure 5.3, with the eye being nearly circular and located near the middle of each image. As the eye is relatively devoid of hydrometeors and associated emission contributions to the TBs, the eye appears colder in the first three panels (10.7, 19.3, and 37.0 GHz) than the surrounding areas where hydrometeors are present. In contrast, the TBs in the eye for 85.5 GHz give the relative TB maximum, as the emission signal from the ocean surface yields warmer TBs than from hydrometeors which

137

depress the 85.5 GHz TBs by scattering, as discussed in Chapter 4. The situation is reversed for the eyewall, which appears just below the eye for the images in Figure 5.3. The convective cells within the eyewall have more liquid and frozen hydrometeors than surrounding areas. Hence the emission by liquid hydrometeors causes the eyewall TBs to be warmer than the surroundings at 10.7 and 19.3 GHz, while the ice scattering effect causes the 85.5 GHz TBs to be colder. Note that these two effects are both important at 37.0 GHz, with the net effect being slightly colder TBs in the eyewall. Similar cases of warm emission signatures for the low frequencies, collocated with cold TBs due to scattering at the high frequencies, are also seen in the convective lines in the lower half of the panels in Figure 5.3, as well as for areas of precipitation seen in the figures for the other passes.

The corresponding nadir plots of the AMPR TBs for this case, along with the aligned nadir ARMAR Z profiles, are given in Figure 5.14. The peaks and valleys in the AMPR TBs along the top portion of the figure correspond to the warm and cold contours, respectively, as described for the TB full-swath images in Figure 5.3. Several features are notable in the ARMAR Z contours, beginning with the reflectivity peak near the melting level at 4.5-5.0 km, which gives the appearance of a bright band and is evident throughout much of the pass. While a bright band is usually associated with stratiform conditions, Rinehart (1991) has noted that decaying convection can also exhibit a bright band, which may be the situation in this case of a dissipating tropical storm. Another notable feature is that the gaps in the precipitation field, as seen by vertical shafts of reflectivity minima in the image, are well aligned with valleys in the low frequency TB plots. Likewise areas of more intense precipitation, as noted by the vertical shafts of reflectivity maxima in

138

the image, are well aligned with peaks in the low frequency TB plots due to emission, and valleys in the high frequency TB plots due to scattering. Alignment of these features not only indicates behavior consistent with that predicted by the model tests discussed in Chapter 4, but it also indicates that the process of aligning the AMPR and ARMAR measurements was successful. This will be an important aspect for TRMM, as the TMI and PR will use different scanning modes, and hence will not be coincident at nadir as were the AMPR and ARMAR in the TOGA-COARE flights. Finally of note is the vertical tilt of the areas of reflectivity maxima due to radar returns from hydrometeors, which corresponds to the vertical tilt of typical convective cells due to vertical wind shear.

One final feature evident in the ARMAR Z contours is with the area of missing data in the center of the plot. Since the combined retrieval was only processed at points where both AMPR TBs and ARMAR Zs were available, there are no combined retrieval results for this portion of the pass, or for similar examples found in the other flight passes. While such problems associated with real data can be handled in a variety of ways in research studies such as this, the issue of missing or garbled data will have to be addressed more comprehensively for the operational TRMM algorithm, which is planned to be processed in near real-time.

The TB and Z data are then provided as input to the combined retrieval algorithm, with retrieval results for this case being displayed in Figure 5.25, along with selected input TB and Z values. The top panel displays the nadir plot of 10.7 GHz and 85.5 GHz TBs, with their respective emission peaks and scattering depressions corresponding to the eyewall and convective lines as previously discussed. The second panel overlays the average ARMAR

Doppler velocity in the rain growth layer, along with the retrieved instantaneous rainfall rate at the surface. The 10.7 GHz peaks due to hydrometeor emission correspond well with the peaks in rainfall rate at the surface, as expected. The magnitudes of the rainrates are also important. The rainrates peak near 80 mm•hr^{-1} in the eyewall and in other areas of intense convection, but drop to small values (< 10 mm•hr^{-1}) in areas between the convective cells. While the Doppler velocities display variability, they are generally positive (downward), indicating the hydrometeors are falling out as expected in a precipitating region.

The next plot displays the ARMAR reflectivity at 2.5 km, overlaid with a model-derived estimate of PIA, as previously explained. The peaks in reflectivity at 2.5 km, a level where rain drops are the primary backscatterers, are aligned with the peaks in 10.7 GHz TB and the retrieved surface rain rate, consistent with previous discussions and analyses. The peaks of PIA are similarly aligned, which is expected as rain drops provide the primary cause of attenuation to the radar returns at 13.8 GHz. Note also that the magnitude of PIA is on the order of 10 dB in the area of the convective cells, indicating that the total hydrometeor column can significantly attenuate the 13.8 GHz radar signal at low levels in the atmosphere. As these lower reflectivity values near the surface can be misinterpreted as lower hydrometeor values, the inclusion of TBs, which provide a good estimate of total hydrometeor content, in a combined retrieval should provide more reliable results when compared to a radar-only retrieval, especially at an attenuating radar frequency such as 13.8 GHz.
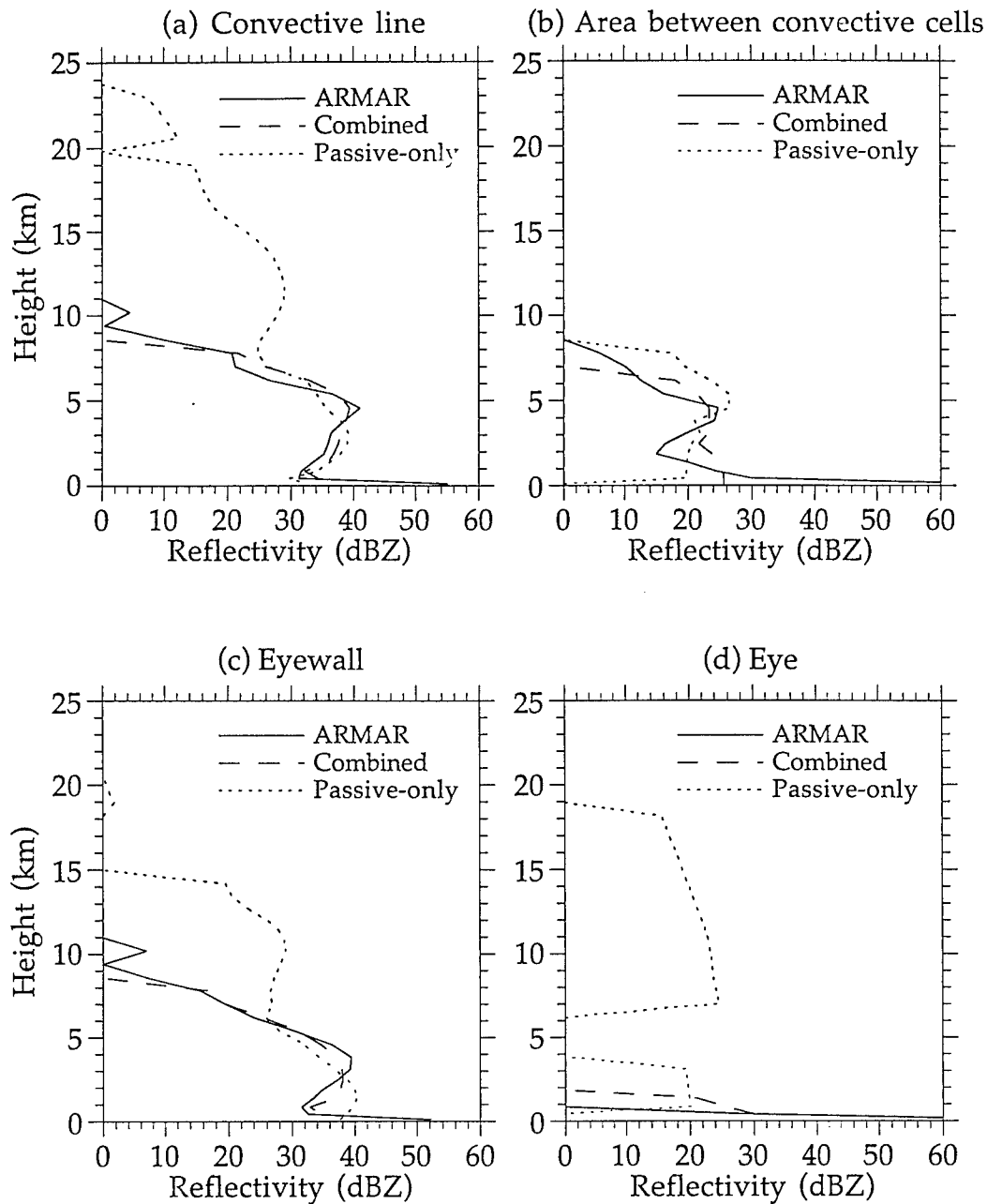
Figure 5.34: Reflectivity profiles of the combined and passive-only first guesses overlaid with the measured ARMAR profile, given for 4 selected points from the 08 Feb 93, pass #1 case.

141

The precipitation type, calculated using the technique described in section 2.7, is given in the bottom panel of Figure 5.25 for this case. The peaks in the first three panels, already described to be the eyewall and lines of convection, are properly diagnosed as convective. Other points not meeting these TB thresholds but exhibiting a bright band are labeled as stratiform, with the rest being tagged as unknown. As the TBs and Zs of the eyewall and convective lines could be considered as textbook examples of convective signatures, their designation as convective by the precipitation type algorithm is given with a high degree of confidence. However the diagnosis of the bright band cases as stratiform presents two plausible explanations; (1) the diagnosis of the precipitation is correct, indicating a case of convection embedded within a stratiform field, or (2) the diagnosis is incorrect and indicates a misclassification of dissipating convection as stratiform rain. Either explanation is plausible for this case, and hence demonstrates one aspect of the challenging nature of precipitation classification.

One final point regards the inherent non-uniqueness of TB-only retrievals, as explained in previous sections. To illustrate the effectiveness of the combined approach at mitigating this problem, example first guess retrievals from four points from pass #1 of the 08 Feb flight are displayed in Figure 5.34. For each point, the Z profile from both the combined and passive-only first guesses are overlaid with the ARMAR measurements. While the modeled TBs from the combined and passive-only first guesses are nearly equivalent, the vertical structures were found to be significantly different in 3 of the 4 cases. The first case, shown in panel (a) of Figure 5.34, is a convective line located away from the eye. Whereas the Z profile from combined first guess roughly matches the shape and vertical domain of the

ARMAR measurements, the TB-only first guess contains a much deeper layer of hydrometeors and effectively doubles the column depth indicated by the radar. A similar result occurs for points in the eyewall and in the eye, shown in Figure 5.34 (c) and (d), respectively. These three cases provide typical examples of the manifestation of non-uniqueness problems inherent to TB-only retrievals, as expressed by poor agreements between measured and modeled Z profiles.

While TB-only retrievals can produce solutions whose vertical structure is inconsistent with coincident radar measurements, this is not always the case. For a point selected between convective cells, shown in Figure 5.34 (b), the Z profiles from the TB-only and combined first guesses are much more consistent with one another than was the case for the other examples. For this case the combined retrieval does not improve the consistency of vertical structure as much, but neither does it degrade the solution. Hence overall combined retrieval is shown to generate hydrometeor solution profiles that are more consistent both in vertical structure (as measured by the Zs) and total integrated hydrometeor content (as measured by the TBs), an improvement when compared to passive-only and radar-only techniques.

5.1.2 Retrieval Results from 4 Feb 93 flight

While the 08 Feb 93 case viewed Tropical Cyclone Oliver during a weakening period, the 04 Feb passes viewed Oliver in the development stage and sampled more intense convection. A good example of such an intense convective area is seen in Figure 5.2, and is on the left hand side and centered in time (near 1908 UTC) on each AMPR TB panel. Note that the 10.7 GHz TB peaks at a value > 275 K, an indication of a near saturated emission event.

Likewise the 85.5 GHz TB drops to a value < 95 K, a significant scattering depression indicating the presence of a large amount of ice. Since this area was off-nadir, it was not a part of the nadir data input to the combined retrieval. However the area still represented a local precipitation maximum at nadir, as seen in the nadir TB and Z plots in Figure 5.13, where the TB plots indicate a TB maximum at the low frequencies and a minimum at 85.5 GHz. Similarly there is a strong reflectivity maximum at this location, which extends throughout a deep layer of the atmosphere. This region is represented in the results in Figure 5.24 by a sharp peak in surface rainrate and PIA, by large variability in the Doppler velocity consistent with the effects of convective updrafts and downdrafts, and is correctly diagnosed as convective by the precipitation type algorithm. This event is described in further detail by McGaughey et al. (1996).

5.1.3 Retrieval Results from 20 Feb 93 flight

The 20 Feb 93 flight measured a mesoscale system which contained a number of intense convective cells embedded within a field of lightly precipitating stratiform rain, as described by McGaughey and Zipser (1996). The system is seen in the full-swath AMPR TB maps (Figures 5.5-5.8) as a local maximum at the lower frequencies. While strong convective cells were present, they were mostly missed by the flight tracks of the aircraft. The strongest convective cell measured by the AMPR was in pass #1 (Figure 5.5), and is recognized by the emission peak at 10.7 GHz and the ice scattering depression at 85.5 GHz. The signature of this cell was exhibited in Figure 5.16 by a broad depression at 85.5 GHz due to scattering and a broad peak at the other frequencies due to emission. Note that unlike some of the examples

previously described for Tropical Cyclone Oliver, the TB signature at 37.0 GHz was one of an emission peak rather than a scattering depression, indicating the lack of enough ice in this case to effectively depress the 37.0 GHz TBs. Likewise the reflectivity signatures for this convective area indicate a local reflectivity maximum, most intense from the melting layer to the surface. Similarly for the results displayed in Figure 5.27, this region is indicated by a local maximum of retrieved surface rainrate and PIA, which are well aligned with the 10.7 GHz peaks and 85.5 GHz valleys.

While other areas for this flight lack a bright band and give some indications of the possibility of convection, none surpass the threshold TB values in the precipitation type algorithm indicating strong convection. Consequently, this cell provided the only instances of convection diagnosed by the precipitation type algorithm on this flight day, as seen in Figure 5.27. The precipitation type for all other passes (Figures 5.28-5.30) were diagnosed as only stratiform or unknown. The portions classified as stratiform follow from the brightband conditions evident in Figures 5.16-5.19, which were present throughout most of each pass. Also note that the magnitudes of surface rainrate were much less than those for the 04 Feb and 08 Feb retrievals for Tropical Cyclone Oliver, and consistent with that of a lightly precipitating stratiform region.

5.1.4 Retrieval Results from 22 Feb 93 flight

The last case is that of a convective squall line from 22 Feb 93, which has been the subject of several studies, including Trier et al. (1994), Jorgensen et al. (1994), Lemone et al. (1994), McGaughey et al. (1996), and McGaughey and Zipser (1996). The squall line appears in the AMPR TB maps (Figures 5.9-5.11)

145

as a line of TB maxima for 10.7 and 19.3 GHz and as a line of TB minimum for 85.5 GHz, signatures similar to those of convection previously discussed for the other flights. Similarly in the nadir plots (Figures 5.20-5.22), it appears as a TB peak for the low frequencies, a TB valley for 85.5 GHz, and a deep local reflectivity maximum. Likewise for the results (Figures 5.31-5.33), it appears as a maximum in surface rainrate and PIA, as an area of large variability in Doppler vertical velocity, and is correctly diagnosed as convective by the algorithm, all of which are consistent with previous discussions of convective regions for the other flights.

The major feature evident in both Figure 5.9 and 5.11, but not seen in the previous examples, is the warm TB maxima located near the top of the 10.7, 19.3, and 37.0 GHz panels. In addition to its very warm TBs, its sharp edges and tight TB gradients distinctively identify this area as land. Had these points not been screened from the nadir AMPR data used as input to the combined retrieval, the very warm TBs at the lower frequencies would have been interpreted as large emission signatures and the retrieval would have generated large rainrates at this location, demonstrating the importance of proper land screening to the retrieval process.

The preceding case analyses indicate reasonable agreement between measured TB and Z responses to liquid and frozen hydrometeors and that predicted by the RTE model tests. Similarly the retrieved surface rainrates and precipitation types for these individual cases are consistent with what would be expected from previous discussion. In order to facilitate further interpretation of the TOGA-COARE retrievals and to quantify the results, all retrieval cases were combined into a single bulk set of paired measurements (AMPR TBs and ARMAR Zs) and retrieved quantities (hydrometeor IWP,

surface rainrate, and precipitation type). A bulk statistical analysis as it related to the optimization, hydrometeors and rainrates, and precipitation type is presented in the sections that follow.

5.2 Effects of Optimization on Retrieval Results

The analysis begins by quantitatively assessing the value added to the retrievals by the structure function optimization as represented by a reduction of the combined error function, which quantifies the improvement in the matchup between the retrieved and measured TBs and Zs. Secondly selected case studies are discussed to illustrate the differences in the retrieved rainrate profiles and surface rainrates due to the effect of optimization, as well as rainrate differences between combined and single-instrument retrievals.

5.2.1 Effect on Error Function Reduction

Since there is no validation data for the actual hydrometeor concentration profiles or surface rain rates, the value of the optimization must be evaluated indirectly. As the optimization is specifically designed to improve the combined agreement between the measured AMPR TBs and ARMAR Zs with their retrieval counterparts (as calculated by the error function given in section 2.4), a quantitative evaluation of the improvement of TB and Z matchup provided by the optimization is given in Figure 5.35. The error improvement is expressed in terms of normalized error, defined as the error from the optimized solution divided by the error from the first guess. Hence normalized errors less than one indicate improvements over the first guess provided by the optimization, while normalized errors greater than one indicate degradations to the first guess. As the optimization is

147

designed to terminate immediately if the combined error of the first guess cannot be reduced, the normalized combined error is never degraded, and hence has a maximum value of one as shown in Figure 5.35 (a).

The average value of the normalized combined error for all TOGA-COARE retrievals was found to be 0.81, a ~20% reduction in combined error over the first guess. Figure 5.35 (b) and (c) displays the corresponding independent improvement for the TBs and Zs, which show an average improvement of ~31% and ~8% improvement, respectively. As both the TBs and Zs are individually improved, it indicates that the optimization generates a retrieval more consistent with both the TB and Z measurements than that provided by the initial guess. Also while the optimization can only reduce the combined error, the independent TBs and Zs can be degraded for some cases, as seen in the values of normalized error greater than one for the histograms in Figure 5.35 (b) and (c).

Finally it is noted that on average the TBs are improved more than the Zs. This is primarily due to the fact that the reflectivity error function calculates the RMS difference between the ARMAR measurements and the retrieved Zs for the entire column. When the top of the measured and retrieved columns are not coincident, reflectivity differences near the upper hydrometeor boundary can exceed 20 dBZ, leading to large RMS differences at that level. As the current implementation of the optimization does not allow the top boundaries to move from their initial positions as determined from the first guess, this large RMS difference does not change for most cases, leading to a smaller improvement in the Z matchup when compared to that for the TBs. One other potential contributing factor may be the combined error function itself. If the normalizing constraints between the TBs and Zs

Solution Error/First Guess Error
(a) Combined Error

Average = 0.810
Median = 0.852

(b) TB Error

Average = 0.693
Median = 0.757

(c) Reflectivity Error

Average = 0.924
Median = 0.976
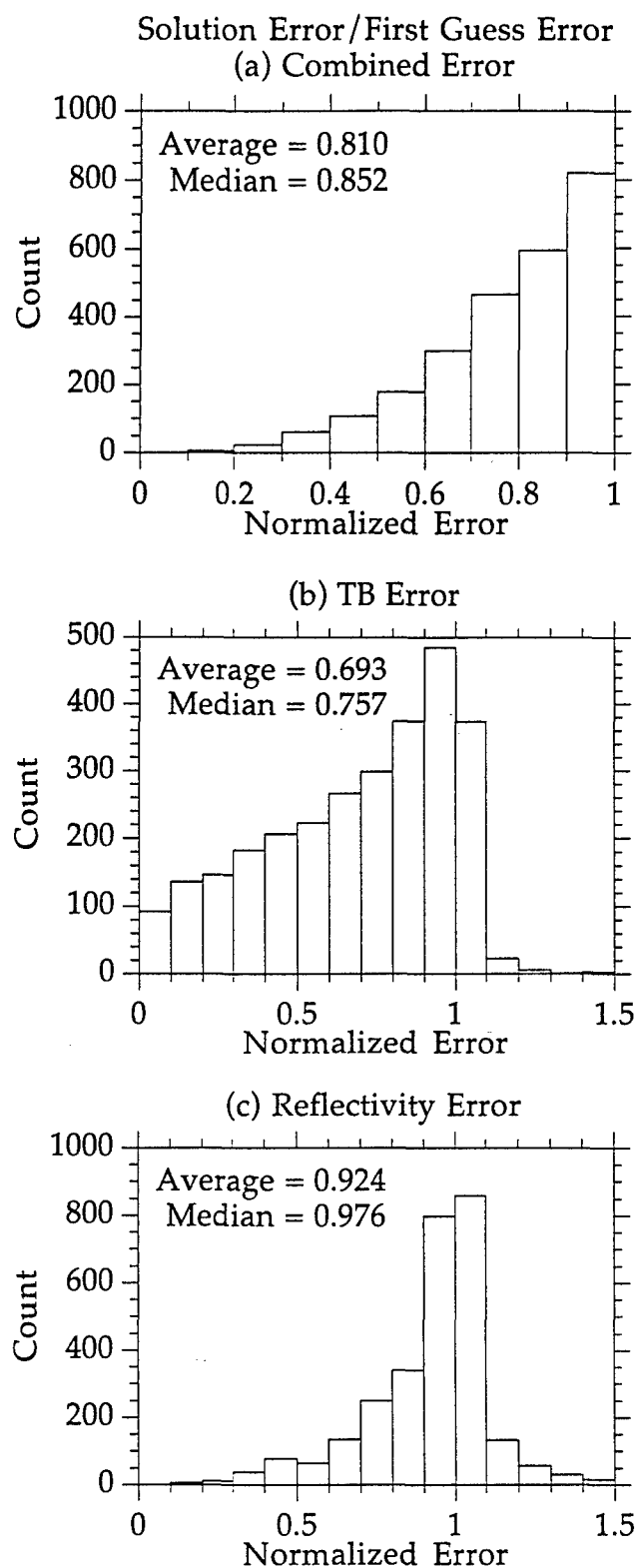
Figure 5.35: Solution error resulting from the structure function optimization divided by the first guess error, for the (a) combined (b) TB-only, and (c) Z-only error functions.
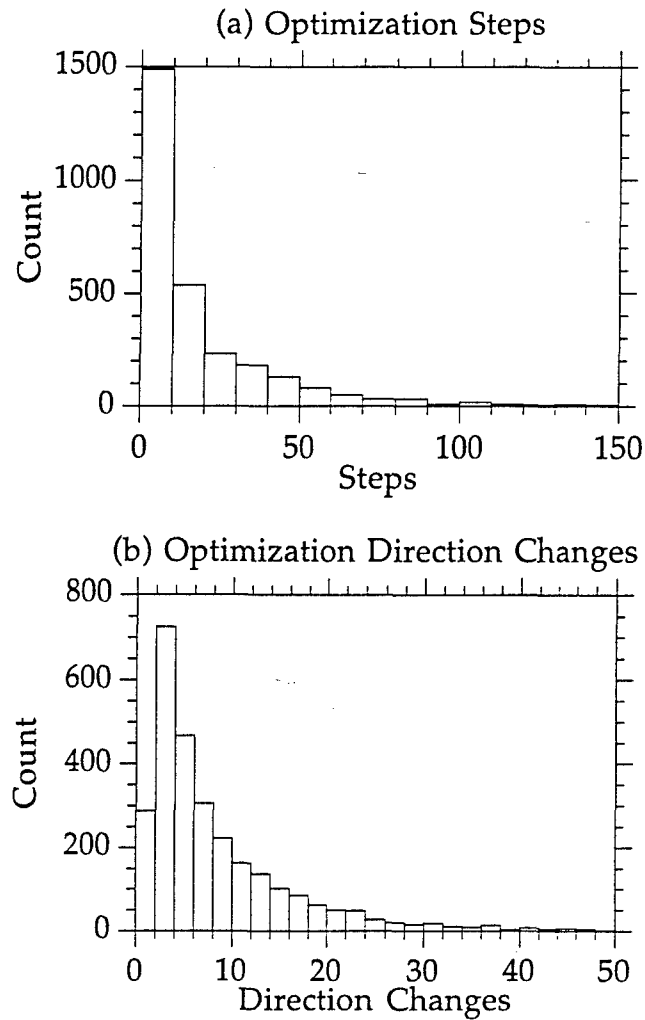
Figure 5.36: Histogram of optimization processing statistics: (a) number of optimization steps, and (b) number of optimization direction changes.

are not precise, the combined error function can overly weight either the TBs or Zs over the other, as described in section 2.4. However other algorithm improvements, such as that suggested regarding the upper hydrometeor boundaries, need to be completed before it can be determined if the error function weighting is really playing a significant role in this aspect of the retrieval results.

While the optimization has been shown to provide an improved matchup between the measured and retrieved TBs and Zs, there is a computational price to be paid. Figure 5.36 (a) and (b) gives a histogram of the total number of optimization steps and direction changes (as described in section 2.5), respectively, for the TOGA-COARE retrievals. Note that each optimization step requires one forward RTE calculation, while each direction change calculates a derivative and hence requires two RTE calculations for each structure function coefficient used in the optimization. As the forward RTE calculations are the most computationally intensive part of the algorithm, the optimization process, as currently implemented, adds computational overhead to the retrieval.

5.2.2 Effect on Retrieved Rainrate Values

Now that the overall statistical improvements of the agreement between measured and modeled TBs and Zs have been quantified, additional insight can be gained by an examination of the changes in the vertical hydrometeor structure due to optimization, as well as changes provided by combined retrieval when compared to TB-only and Z-only retrieval. While the retrieval process and the optimization has an effect on all hydrometeor types, this discussion will focus on rain rate, the main quantity of interest in most precipitation studies. Recalling from previous descriptions of the retrieval process, the retrieved rain hydrometeor profiles are input into a gravity-fallout rainfall submodel, described in section 2.6, which produces retrieved profiles of rainrate. Hence the retrieved rainrate profiles are used in the following discussion to illustrate the effects of combined retrieval and optimization on the retrieved vertical structure.

The first case to be analyzed is pass #1 from 08 Feb 93, which was examined in detail in section 5.1.1. The rainrate profiles for this case are illustrated in Figure 5.37, beginning with those from the combined and Z-only first guesses, as shown in panels (b) and (c), respectively, and their corresponding surface rainrates, shown in panel (a). Perhaps the most important feature noted is the good correlation apparent between the combined and Z-only first guesses, indicating good alignment between the PMW and radar measurements. While the location of the maximum rainrate areas, given by the eyewall and convective lines as discussed in section 5.1.1, are well correlated, the magnitudes of the maximum rainrates vary between the two retrieval types, most notably near the surface. This can result in large surface rainrate differences in the heavily raining areas, as seen in Figure 5.37 (a).

While the combined and Z-only first guess rainrate profiles exhibit relatively large magnitude differences, the rainrate profiles from the TB-only first guess and combined optimized solution do not show as large of departures from the combined first guess. Hence the rainrate profiles for the TB-only first guess and combined solution are displayed as differences from the combined first guess, and are given in Figure 5.37 (e) and (f), respectively. Similarly the corresponding surface rainrates are also shown as differences from the combined first guess values, and are given in Figure 5.37 (d). The rainrate differences between the TB-only and combined first guesses, shown in panel (e), have several interesting features, the most important of which is the vertical distribution of the rainrate differences. In most cases, positive rainrate differences at some levels are coupled with negative rainrate differences at other levels. This indicates that the rainrates present in the TB-

only first guess are effectively being vertically redistributed to better match the Zs within the combined retrieval. As many of the largest changes are found near the surface, the corresponding surface rainrate differences, as seen in panel (d), often approach 30 mm•hr^{-1}. However the resulting changes due to optimization, as seen in panel (f), are not as pronounced. While the rainrate changes are usually <10 mm•hr^{-1}, some cases in the heavily raining areas approach 20 mm•hr^{-1}, not an insignificant amount. Still the most important feature is that positive rainrate changes at one level are often coupled by negative changes at another, a reflection of the redistribution of the vertical rain structure by the optimization process.

Another example is given in Figure 5.38 for pass #2 of 04 Feb 93, a case described at length in section 5.1.2. As all of the preceding discussion for the 08 Feb pass applies to this case as well, only a single distinguishing feature will be discussed, namely the retrievals surrounding the convective region at time 1907-1908 UTC in the figure. What distinguishes this region is the large magnitude of the rainrate differences between the combined first guess and combined optimized solution, seen in panel (f). For the retrievals from this convective area, positive rainrate differences of ~20 mm•hr^{-1} near the surface are accompanied by negative rainrate differences of ~20 mm•hr^{-1} near the melting level, indicating a fairly large transfer of rain from one level to another by the optimization process. Hence while the optimization normally makes modest adjustments to the hydrometeor profiles to improve the matchup between the measured and modeled TBs and Zs, there are situations when this procedure can make significantly larger modifications, accounting for cases of error improvement much greater than the average 20% improvement reported in the previous sub-section.
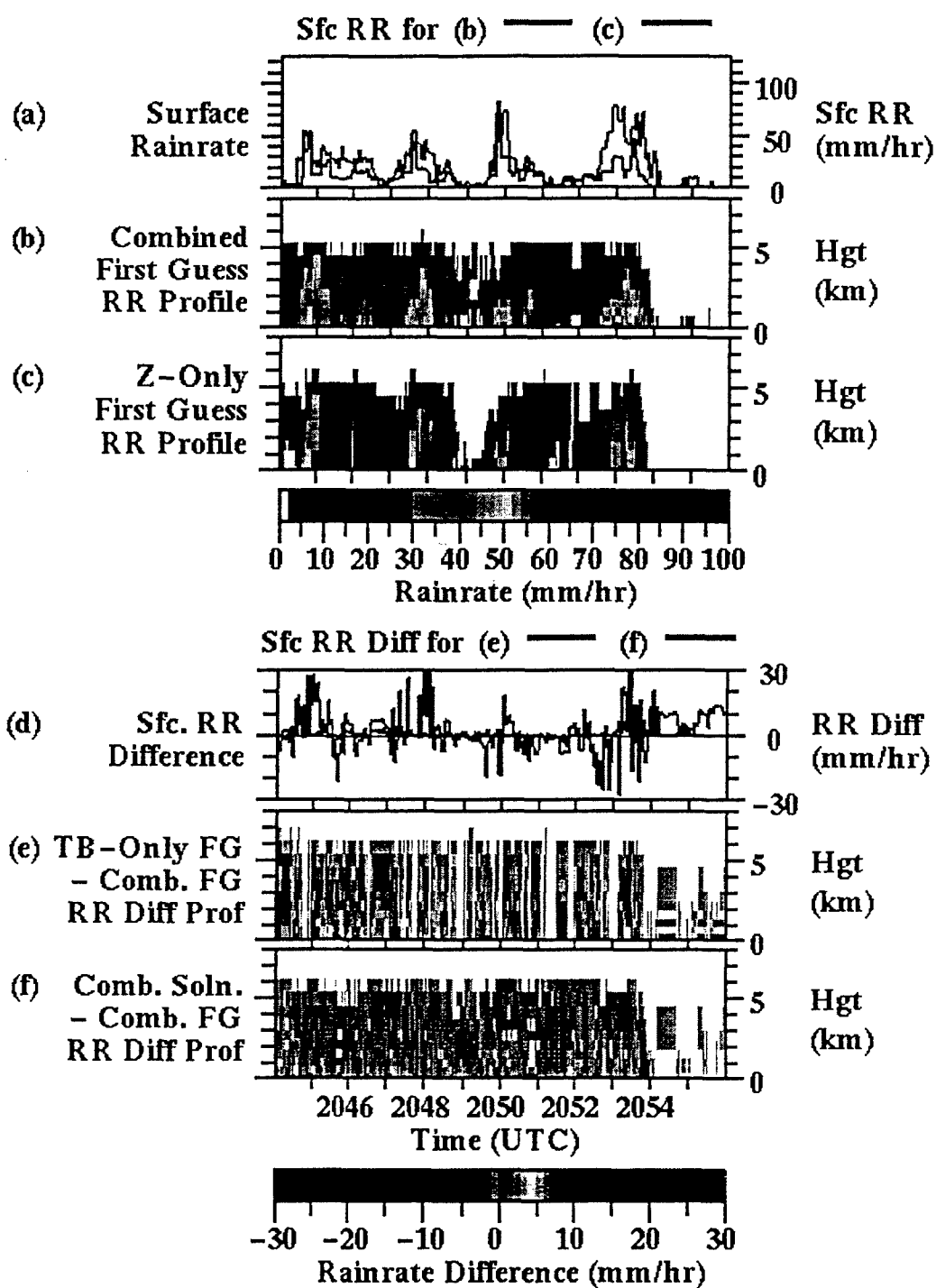
Figure 5.37: Retrieved rainrate profiles for 08 Feb, pass #1 shown for (b) combined first guess and (c) Z-only first guess rain rates, with corresponding surface rainrates shown in panel (a); rainrate differences with the combined first guess are shown for the (e) TB-only first guess and (f) combined solution rainrates, with corresponding surface rainrates shown in panel (d).
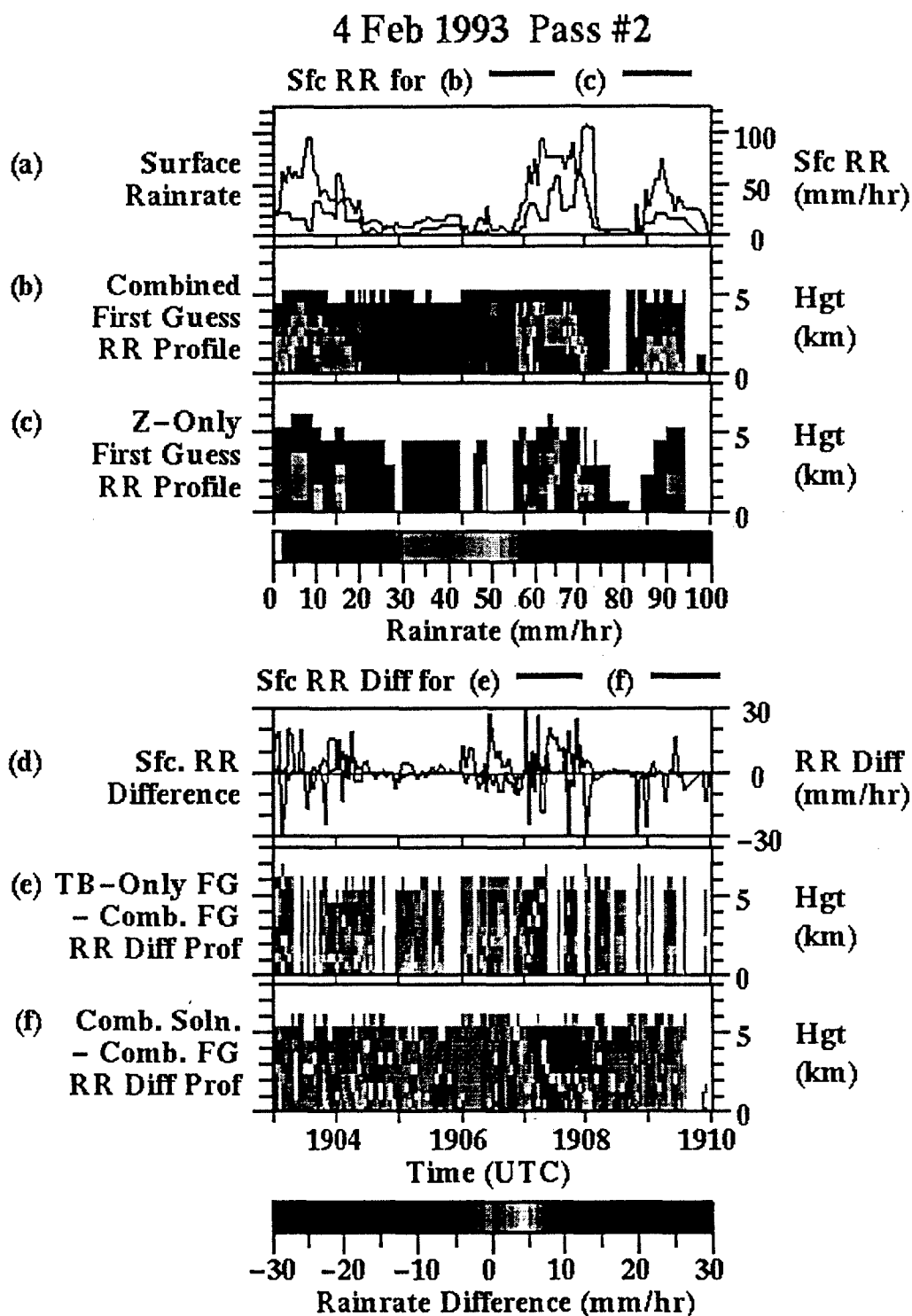
Figure 5.38: Retrieved rainrate profiles for 04 Feb, pass #2 shown for (b) combined first guess and (c) Z-only first guess rain rates, with corresponding surface rainrates shown in panel (a); rainrate differences with the combined first guess are shown for the (e) TB-only first guess and (f) combined solution rainrates, with corresponding surface rainrates shown in panel (d).

5.3 Statistical Summary of Retrieval Results

Now that the value of the optimization has been assessed, the next step is to evaluate the consistency of the retrieved quantities with expected results. This begins by directly comparing selected TB and Z relationships to hydrometeor IWP, as seen from the bulk TOGA-COARE results, with those previously accomplished from RTE model tests in Chapter 4. The first is given in Figure 5.39 (a), which depicts AMPR 10.7 GHz TB vs. retrieved rain IWP. The emission curve is well represented in this plot, where the 10.7 GHz TB reaches a saturation value near 280 K when the rain IWP approaches 20 $kg \cdot m^{-2}$. The equivalent plot from the RTE tests is given in Figure 4.8 (b), which has nearly identical saturation values. The main difference is that the maximum value of retrieved rain IWP is < 20 $kg \cdot m^{-2}$ for the TOGA-COARE cases, while the hurricane simulation contained examples of rain IWP approaching 60 $kg \cdot m^{-2}$. As the TOGA-COARE cases did not include an intense hurricane, this result is not surprising.

The same argument follows for the relationship of AMPR 85.5 GHz TB with retrieved graupel IWP, depicted in Figure 5.39 (b), when compared to the same relationship seen in the RTE model tests, as given in Figure 4.11 (c). The 85.5 GHz TB values decrease as graupel IWP increases due to scattering depression, as seen in both the retrieval results and model tests. Again the biggest difference is the maximum amount of graupel IWP present. For the TOGA-COARE retrievals, the maximum IWP was ~6 $kg \cdot m^{-2}$, whereas for some cases in the hurricane simulation, the graupel IWP approached values of 50 $kg \cdot m^{-2}$. This indicates that TOGA-COARE does not contain as much ice as can be produced by a model simulation of an intense hurricane, which like the preceding result concerning liquid is to be expected.

The relationship of radar Zs in the rain layer with rain IWP is given in Figure 5.39 (c) for the bulk TOGA-COARE results, and in Figure 4.17 (b) for the RTE model tests, which produce nearly identical curves. Similarly the relationship of radar Zs in the ice layer above the freezing level with graupel IWP is given in Figure 5.39 (d) for the bulk TOGA-COARE results, and in Figure 4.18 (c)-(d) for the RTE model tests, which also produce nearly identical curves. Aside from the differences in the maximum rain and graupel IWP as previously discussed, the main difference is in the amount of scatter in the retrieval plots compared with the corresponding examples from the RTE tests. This should be expected due to the fact that all microphysical properties of the hydrometeors (e.g., drop size distribution, particle shapes, etc.) are identical for all cases in the hurricane simulation, where these properties are undoubtedly variable in the real atmosphere. As the radar reflectivity values are sensitive to the microphysical characteristics of the backscatterers [Battan (1973)], it is should be expected that the relationship of retrieved hydrometeor IWP to the radar Zs is not as smooth and well-defined as for a controlled model simulation.

Due to the correlation between hydrometeor concentrations and surface rainrates, as discussed in Chapter 4, a comparison between retrieved surface rainrates and TB/Z measurements should provide similar results as those just discussed for the hydrometeor IWPs. Instead of using a scatter plot as in the previous discussion, various quantities were sorted according to rainrate values, and the average from each 10 mm•hr^{-1} bin is plotted in Figure 5.40. The 10.7 and 85.5 GHz TBs are plotted as a function of rainrate in Figure 5.40 (a). The increasing value of 10.7 GHz with increasing rainrate is consistent with the similar relationship for rain IWP and 10.7 GHz TB presented in

157

Figure 5.39 (a), due to the correlation between total rain IWP in the column and the amount falling out to the surface. Similarly the decreasing value of 85.5 GHz with increasing rainrate is consistent with that shown between graupel IWP and 85.5 GHz TB shown in Figure 5.39 (b), due to the generally good correlation between liquid and frozen hydrometeor concentrations, as discussed in Chapter 4. Also the noisy nature of the plots at high rainrate values (> 60 mm•hr^{-1}) is due to the fact that the sample size for these bins is small. There are only a small number of cases with very large rainrates found in the TOGA-COARE retrieval tests, such that the average within those bins can be effected by only a few extreme data points.

As discussed in the previous case study analyses, total PIA of the radar signal is due mainly to the rain, and hence is correlated well with rain IWP, surface rainrate, and 10.7 GHz TB. Hence the increasing value of PIA with increasing rainrate seen in Figure 5.40 (b) is as expected. The relationship between average Doppler vertical velocity in the rain growth layer with retrieved rainrate is not as well behaved, as seen in Figure 5.40 (c). At low rainrate values, most cases are stratiform as previously discussed. As the rainrate is increased, the average hydrometeor fall speed as indicated by the average Doppler velocity also increases as expected. However at larger rainrates, the relationship breaks down. This is due to two factors: (1) the large rainrates are primarily in convective cells, where the actual vertical velocity distribution cannot be expressed by a well-defined Gaussian shape, as it contains both updrafts and downdrafts, and (2) the sample size of the highest rainrates within the flight passes is small, as previously discussed.
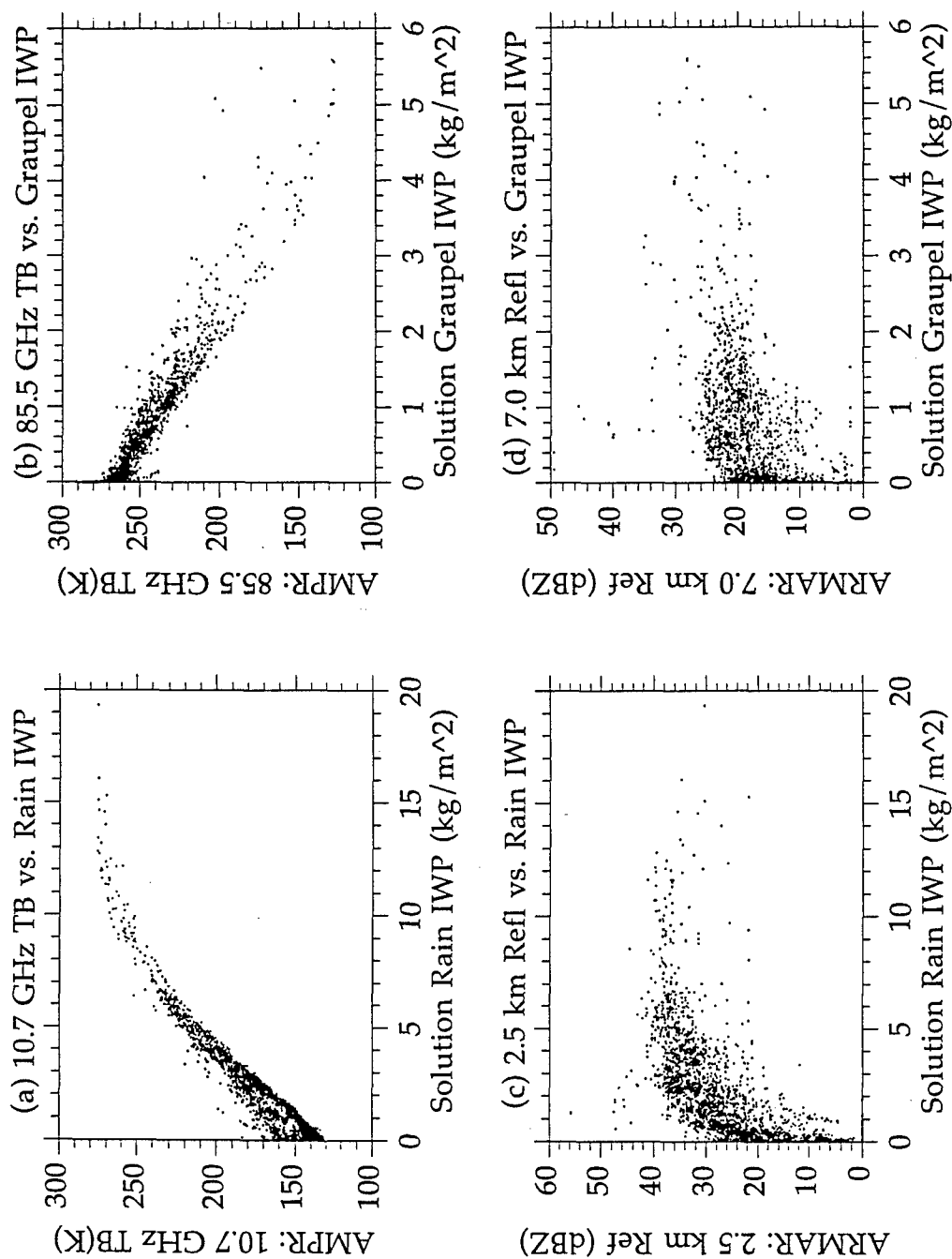
Figure 5.39: Scatter plot of measured TBs/Zs vs. retrieved hydrometeor IWP: (a) AMPR 10.7 GHz TB vs. rain IWP, (b) AMPR 85.5 GHz TB vs. graupel IWP, (c) ARMAR Z at 2.5 km vs. rain IWP, and (d) ARMAR Z at 7.0 km vs. graupel IWP.
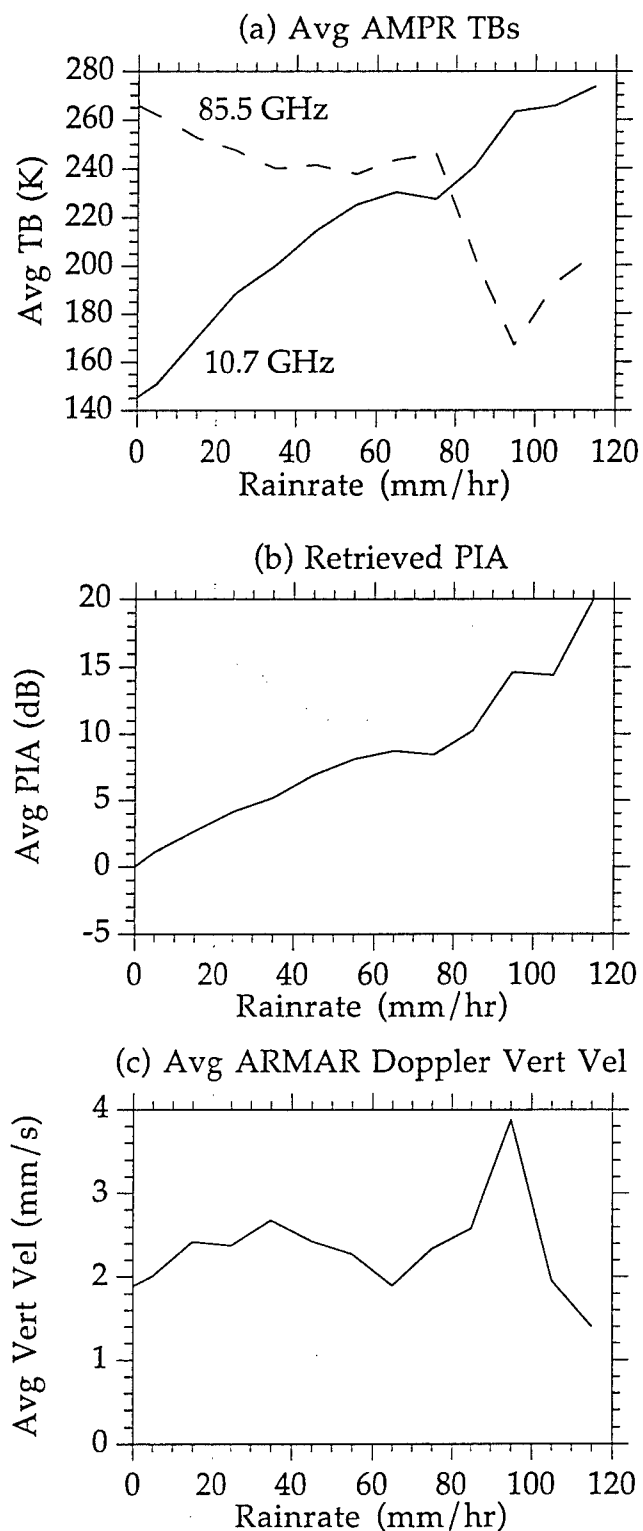
Figure 5.40: Values averaged over 10 mm/hr bins of retrieved surface rainrate for (a) AMPR TBs, (b) retrieved PIA, and (c) average ARMAR vertical velocity in rain growth layer, where all averaged values are plotted vs. retrieved surface rainrate.

5.4 Results for Precipitation Classification Algorithm

Having verified the consistency of retrieved surface rainrates with the TBs and Zs, it is useful to analyze the statistical distribution of the rainrate values themselves, as presented in Figure 5.41 (a). The distribution contains mostly small rainrate values, trailing off to a small number of high values. As such a log-normal rainrate distribution has been measured in previous rainfall studies [e.g., Goldhirsch (1983) and Kedem et al. (1990)], this result is expected. The next step is to analyze the results separately by precipitation type, as determined by the precipitation type algorithm, which classified 10.3% of the TOGA-COARE cases as convective, 45.5% as stratiform, and the remaining 44.2% as unknown, as shown in Figure 5.41 (b).

Recall that in the TB threshold technique for diagnosing convection, given in equation (19) in section 2.7, previously published observed threshold values were required to be exceeded by 10 K in order to ensure that cases diagnosed as convective were done so with a high degree of confidence. Furthermore cases selected as convective under this scheme could be considered as intense convection, with less intense convective cases failing to meet the threshold tests being diagnosed as either unknown or stratiform. For purposes of comparison, the threshold values in equation (19) were relaxed by 10 K, and the TOGA-COARE cases were re-diagnosed for precipitation type using these new threshold values, which yielded the following distribution by precipitation type: 15.3 % convective, 43.8 % stratiform, and 40.9 % unknown. Hence an additional 5% from the total number were diagnosed as convective, which could be referred to as cases of "probable" convection. As these additional convective cases came from cases previously tagged as unknown (3.3%) and stratiform (1.7%) using the original

161

threshold values, it is clear that many cases can exhibit properties consistent with both convective and stratiform precipitation, and as such the inclusion of a significant portion in an unknown category is a prudent option.

After grouping the retrievals in these three categories, the average rainrates for each are shown in Figure 5.41 (c). The average rainrate for the convective cases was 50 mm•hr^{-1}, while the stratiform cases had an average of ~9 mm•hr^{-1}. This is consistent with the typically larger rainrates in intense convection, when compared with the smaller rainrates in a typical stratiform region. Note that non-raining cases, defined here as rainrates < 0.1 mm•hr^{-1}, were not included for any of the distributions displayed in Figure 5.41.

After the cases were separated by precipitation type, the rainrate distributions were then calculated independently for each category to determine their consistency with expected values, as seen in Figure 5.42. The stratiform rainrate distribution is as expected, with a log-normal distribution containing mostly small rainrate values. The unknown category displays similar characteristics, except with the inclusion of slightly larger values, which is expected as the unknown category undoubtedly contains cases which are convective but not intense enough to meet the threshold criteria for convection specified in the algorithm. Finally, the rainrate distribution for the convective cases exhibits a peak at ~50 mm•hr^{-1}. Since the algorithm attempted to classify as convective only intense convective cells, it was anticipated that the peak in the rainrate values would be at a larger value, and not at zero as it is for the log-normal distribution for mostly stratiform rain.

(a) Rainrate Distribution

Bin Size = 5 mm/hr

(b) Precip Type Distribution

44.2 %   45.5 %

10.3 %

(c) Average Rainrate

50.0

14.4

9.3
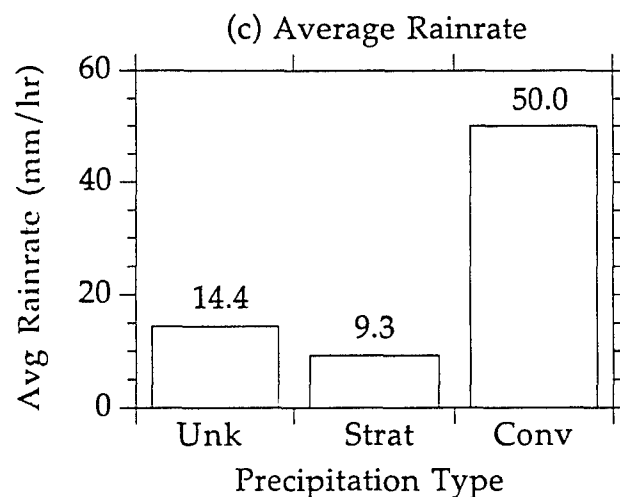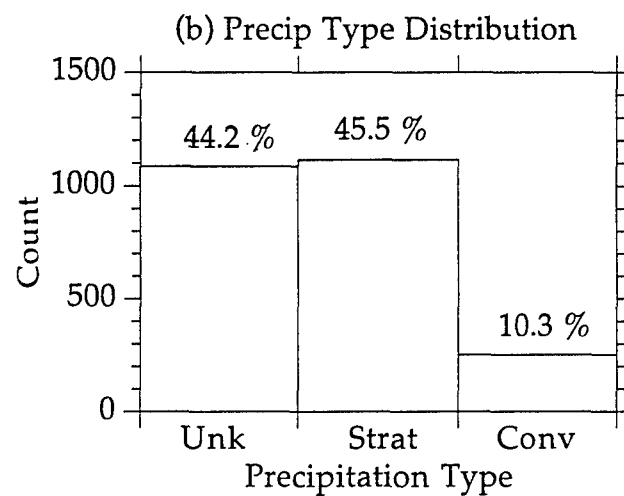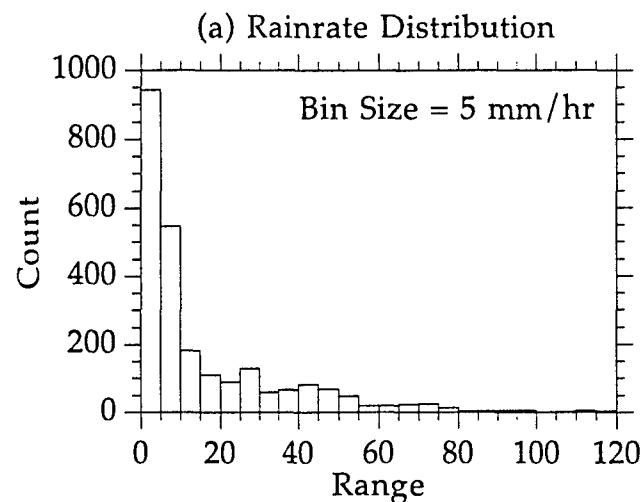
Figure 5.41: Retrieved surface rainrate and precipitation type distributions: (a) distribution of retrieved surface rainrate, (b) distribution of retrieved precipitation type, and (c) average rainrate by precipitation type. Non-raining cases (retrieved surface rainrate < 0.1 mm/hr) not included.
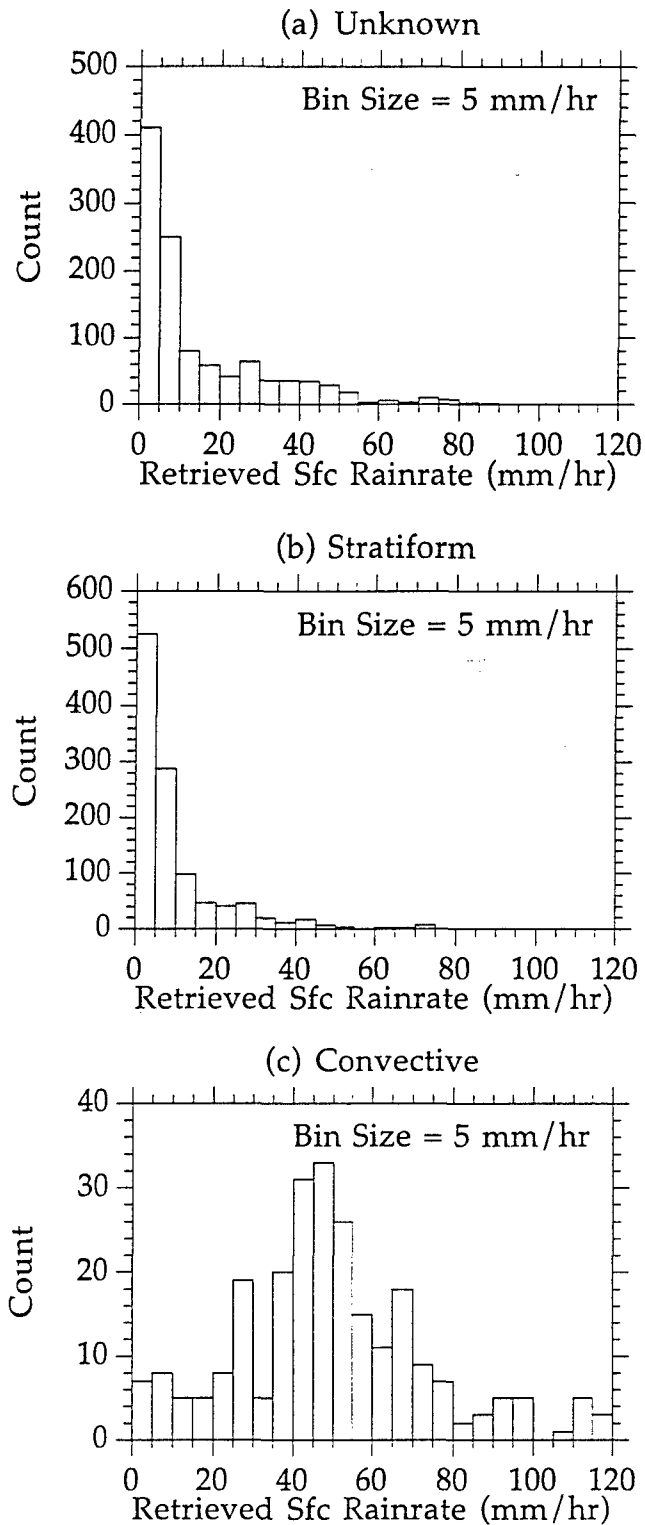
Figure 5.42: Distribution of retrieved surface rainrate separated by precipitation types (a) unknown, (b) stratiform, and (c) convective. Non-raining cases (retrieved surface rainrate < 0.1 mm/hr) not included.
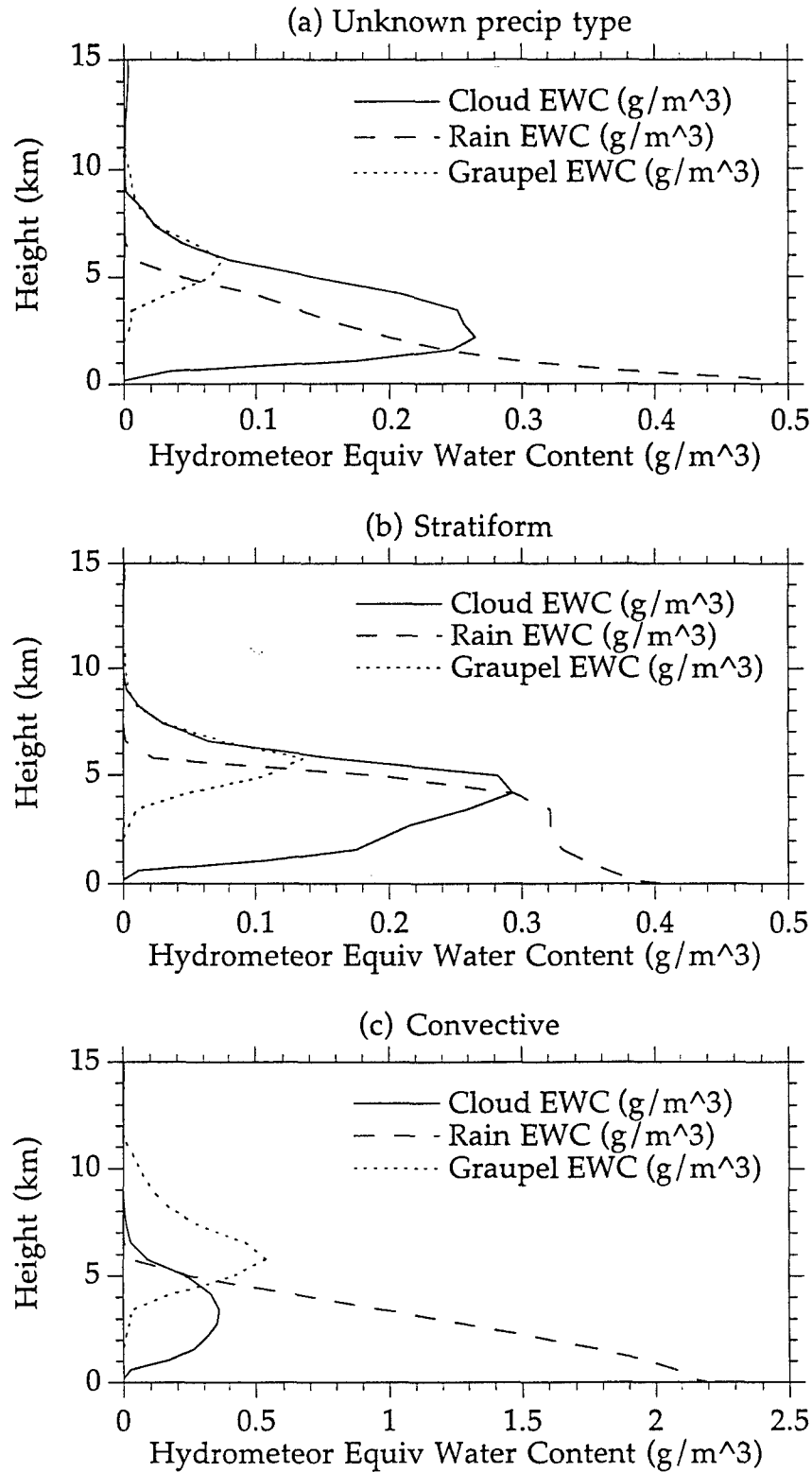
Figure 5.43: Average of retrieved cloud, rain, and graupel profiles separated by precipitation types (a) unknown, (b) stratiform, and (c) convective.

In addition to surface rainrates, the retrieved hydrometeor profiles separated by precipitation type was also explored. The comparison is given by the average retrieved hydrometeor profile for each type, as seen in Figure 5.43. The main difference between the average convective and stratiform hydrometeor profile is one of magnitude, where the peak value of both rain and graupel equivalent water content is ~5 times larger for convection than for stratiform rain, which is consistent with the known physical differences between stratiform regions and intense convective cells. As the unknown category contains convective cells (with greater hydrometeor content than the average stratiform case), non-raining cases (with little or no hydrometeors), and stratiform cases without a brightband, the net effect is that its average profile does not drastically depart from that of the stratiform category for the circumstances present in the TOGA-COARE dataset.

The preceding analyses indicated that the precipitation type classification scheme is physically consistent with such properties as surface rainrate and hydrometeor concentration. A similar analysis was also conducted for vertical velocity. Unlike the TRMM PR, the ARMAR is a coherent radar and measures Doppler velocity, which indicates the vertical motion of the hydrometeors. A histogram of average ARMAR hydrometeor velocities for the rain growth layer is given separately for each precipitation category from the TOGA-COARE retrievals in Figure 5.44. Note that the sign of the Doppler velocities have been reversed to indicate the motion of the hydrometeors in the atmospheric standard sign convention (positive upward/negative downward). The hydrometeor vertical velocities for precipitation diagnosed as stratiform, shown in Figure 5.44 (b), is the type of distribution expected from the conceptual theory described in section 2.7, namely small magnitude

downward velocities on the order of the terminal velocities of snow and aggregates. Likewise the hydrometeor vertical velocity distribution of the cases diagnosed as convective also follows observations and conceptual theory, as it contains larger downward velocities and some upward velocities, corresponding to the updrafts and downdrafts known to exist in convective systems. The greater magnitudes of the fall speeds, compared to the stratiform distribution, are indicative of the higher concentrations of graupel and other large ice particles found in convection. Finally the hydrometeor vertical velocity distribution of the unknown precipitation cases, given in Figure 5.44 (a), appears to have values consistent with a mixture of convective and stratiform cases.

While the diagnosis by the algorithm of precipitation type is consistent with the distributions of hydrometeor vertical velocities measured from the ARMAR, this is not the case for the distributions of first guess atmospheric vertical velocities from the simulation database. Figure 5.45 depicts the distribution by precipitation type of the first guess vertical velocities averaged over the rain growth layer. Unlike the case for the ARMAR Doppler-measured hydrometeor vertical velocities, the first guess atmospheric vertical velocity distributions offer no separation by precipitation type, and hence would clearly not be useful for the determination of precipitation type. However as the quality of cloud models improve, this technique may merit another evaluation at some future date.

Whereas the growth mechanism of hydrometeors is governed by the atmospheric vertical velocities, Doppler velocities indicate the vertical motion of the hydrometeors, not the atmosphere. However from Doppler-measured hydrometeor fall speeds, the atmospheric vertical can be estimated

167

if one assumes an average terminal fall velocity for the hydrometeors, as expressed by the following equation:

$$v_{atm} \text{ (estimated)} \approx v_{hyd} \text{ (Doppler-measured)} - v_{term} \text{ (assumed)} \quad (20)$$

Using this equation with the convective cases from the retrieval tests, the estimated atmospheric vertical velocity distribution is given in Figure 5.46, where a hydrometeor terminal velocity of 3 m•s^{-1} is assumed.

This is compared with the atmospheric vertical velocity distribution of selected convective cases from the National Hail Research Experiment given in Figure 5.47, where the atmospheric vertical velocities where directly measured from aircraft instruments [see Fankhauser (1981)]. The reasonably good agreement between these two independent distributions indicates that a reasonable estimate of atmospheric vertical velocity can be obtained from Doppler vertical velocities, provided that the assumed value of hydrometeor terminal fall velocity is also reasonable. Note that the hydrometeor terminal fall velocity is dependent on the drag coefficient of the hydrometeor, which is dependent on the mass, density, and shape of the hydrometeors, which in turn are related to precipitation type. Hence the combination of indirect measures of precipitation type and Doppler hydrometeor vertical velocity information can provide a potential improvement to the diagnosis of precipitation type, which previews a possible enhancement to combined precipitation retrieval should a coherent radar capable of measuring vertical velocity ever be deployed on a satellite.
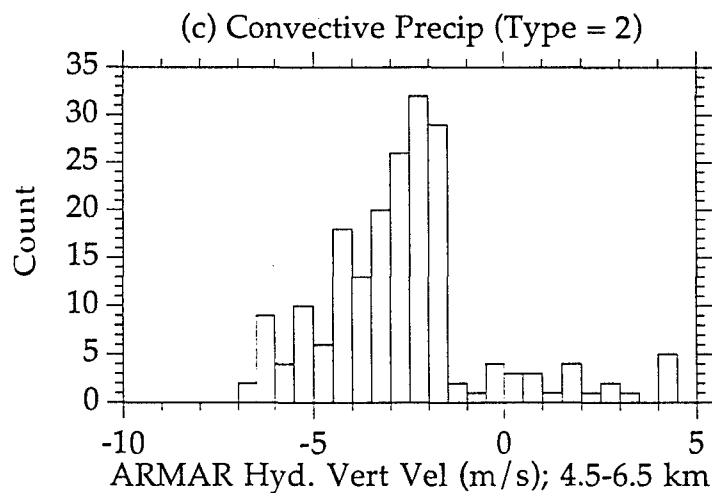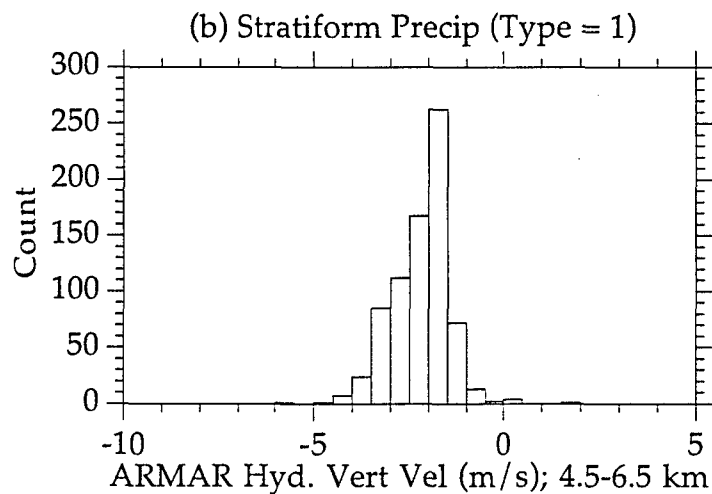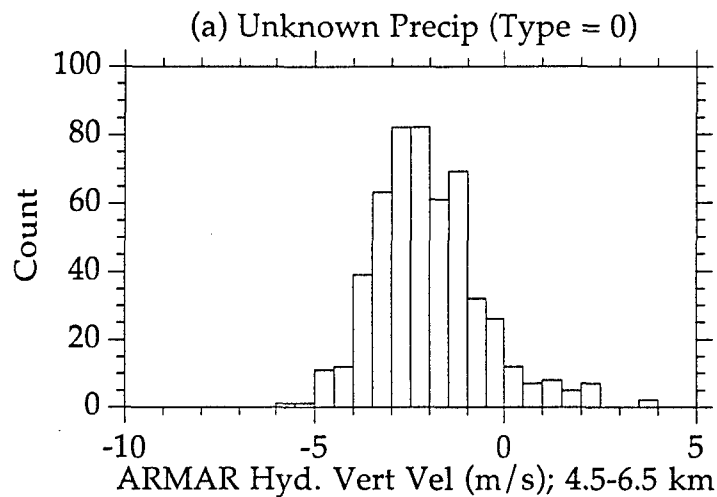
Figure 5.44: Distribution of average ARMAR hydrometeor vertical velocity in the rain growth layer separated by precipitation types (a) unknown, (b) stratiform, and (c) convective.
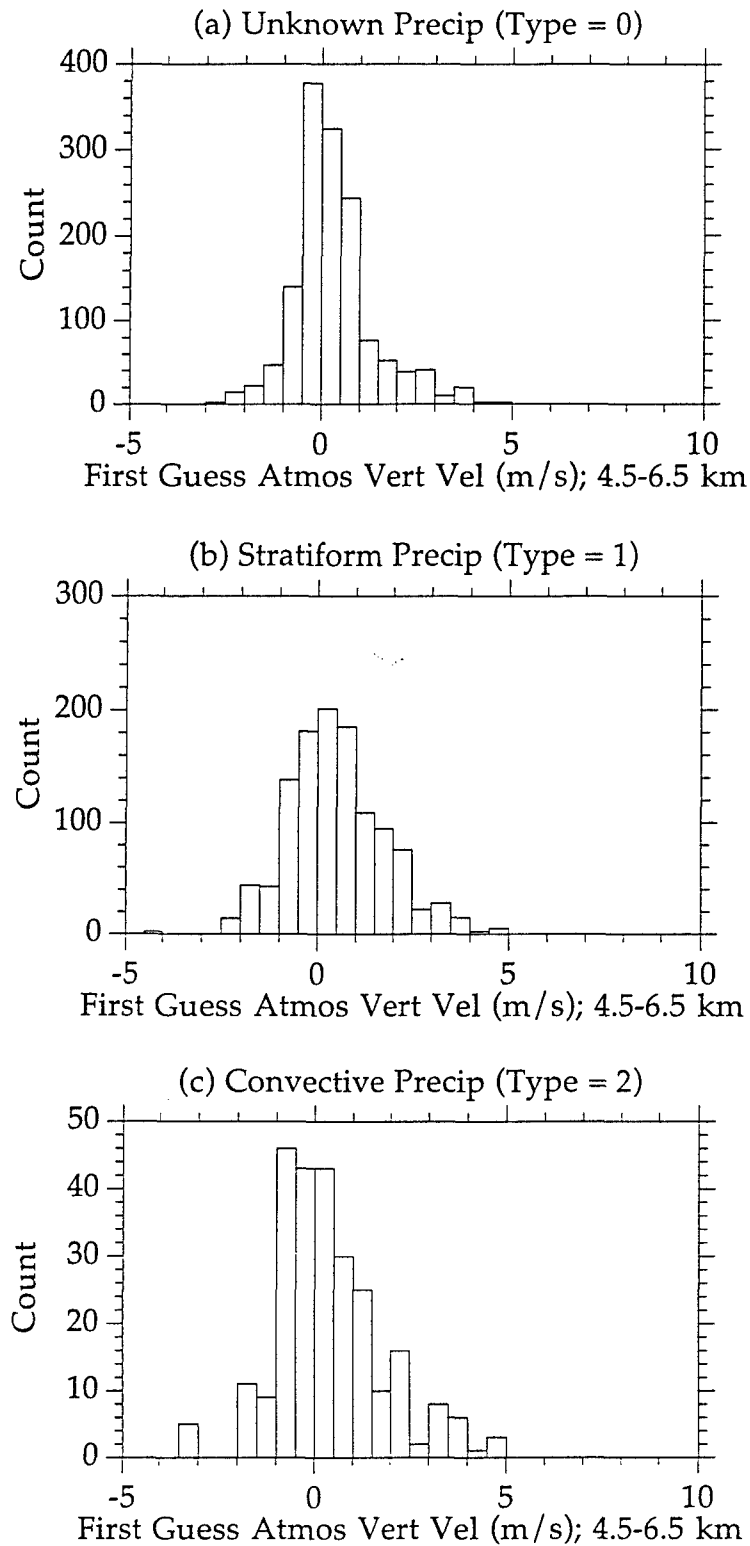
Figure 5.45: Distribution of average first guess simulation atmospheric vertical velocity in the rain growth layer separated by precipitation types (a) unknown, (b) stratiform, and (c) convective.

Est. Atmos. Vert. Vel. for Retrieval Tests
(precip type = convective)
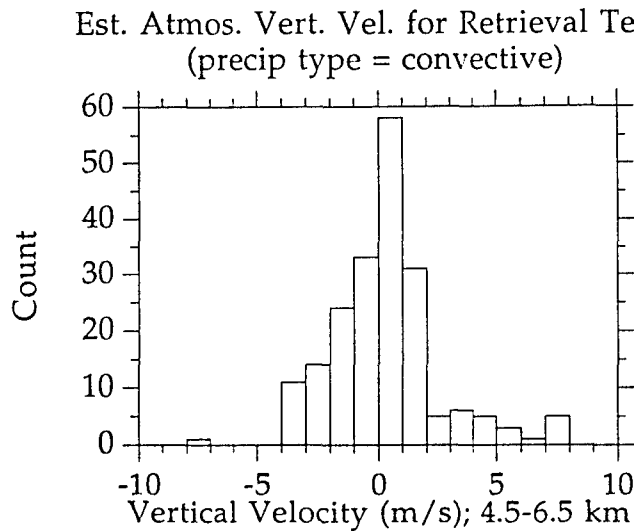
Figure 5.46: Atmospheric vertical velocity distribution for cases diagnosed as convective from TOGA-COARE retrieval tests. Atmospheric velocities estimated from ARMAR Doppler hydrometeor fall velocities and assuming hydrometeor terminal fall speed = 3 m/s. Bin size = 0.5 mm/hr.
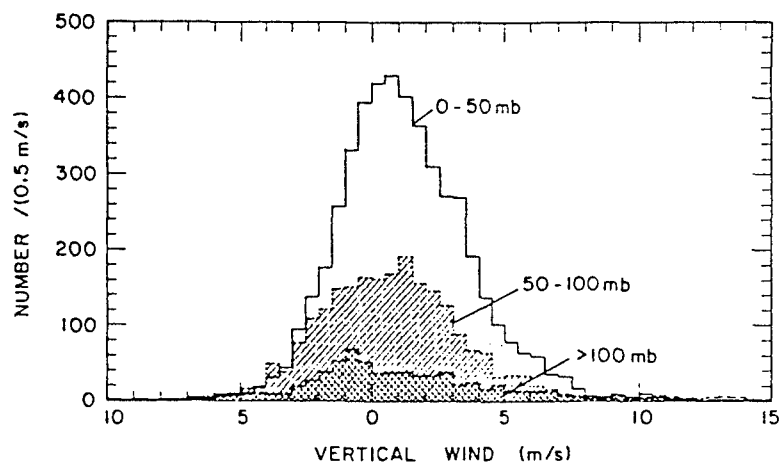
Figure 5.47: Atmospheric vertical velocity distribution for cases of significant cloud water concentration from the National Hail Research Experiment. Atmospheric velocities measured with aircraft instruments. Distribution given for measurements from 0-50, 50-100, and more than 100 mb above cloud base. Bin size = 0.5 mm/hr. From Fankhauser et al. (1982).

CHAPTER 6
DISCUSSION AND CONCLUSIONS

The Tropical Rainfall Measuring Mission (TRMM) satellite, designed to measure tropical rainfall and its effects on climate and atmospheric circulations, will deploy a sensor suite containing a passive microwave (PMW) radiometer and precipitation radar, a first for an earth-viewing satellite. In anticipation of the launch of TRMM, a combined radar-radiometer precipitation profile retrieval algorithm has been developed which uses aircraft PMW radiometer brightness temperature (TB) and radar reflectivity (Z) measurements as input. The TB and Z measurements are compared with values from a database of profiles produced by a cloud model simulation of a tropical storm. Database values that most closely match the measurements, as measured by a combined normalized RMS error function, are selected as the initial guess of the solution profiles. The initial guess profiles, represented as a series of structure functions, are modified in an optimization scheme which uses the structure function coefficients as the optimization control parameters, yielding a solution set of hydrometeor profiles whose TB and Z signatures agree more closely with the measurements than did the first guess. The solution hydrometeor profiles are then input to gravity fallout equations to generate solution rain rate profiles and surface rainrates. Finally the TB and Z measurements are input into a combined precipitation type algorithm, which identifies stratiform rain

by a radar-derived bright band calculation and convective rain by TB threshold values.

For a series of retrieval tests, using aircraft radar and PMW radiometer measurements from TOGA-COARE as input, the combined algorithm generated solution hydrometeor profiles and surface rainrates that were found to be consistent with model tests and previous observations. The relationship between the retrieved hydrometeors and the TB and Z measurements yielded nearly identical functional relationships as those from simulation and RTE model tests. Likewise the retrieved surface rainrates were correlated well with the TBs and retrieved radar PIA in a manner consistent with the model tests. Also the retrieved surface rainrate values followed a log-normal distribution, as found in previous observational studies.

While these results validate the physical consistency of the retrieval method with respect to theoretical considerations, model tests, and observations, it should be noted that these general conclusions could also be drawn from a combined retrieval without optimization. Hence it is important to note the specific value added to the retrieval results by the optimization procedure. For the TOGA-COARE retrieval tests, the optimization scheme provided an average 20% improvement over the first guess in the combined agreement between the measured and retrieved TBs and Zs. While this average improvement represents modest adjustments to the hydrometeor profiles when averaged over all the retrieval tests, it is noted that under some circumstances the effect of optimization can be much more pronounced. One case detailed in this study, illustrating a retrieved rain hydrometeor profile by an equivalent rainrate profile, showed that

rainrates on the order of 20 mm•hr^{-1} can be added to the first guess at some levels, while similar amounts are subtracted from other levels, indicating the ability of the optimization to redistribute significant hydrometeor amounts in order to improve agreement between the measured and modeled TBs and Zs. The improved agreement is a result of the non-linear optimization scheme, a process which generates a new set of profiles which are *independent* from those in the database, a feature which distinguishes it from other techniques.

In contrast, an alternate technique for profile-based retrieval is the Bayesian approach, which weights profiles in a database using a priori probability density functions constrained by statistical information from the cloud and RTE models and the hydrometeor distributions, and applies the weights to the database profiles to generate a solution. The Bayesian method has been applied to profile retrieval using PMW-only, radar-only, and combined measurements, as described by Evans et al. (1995), Haddad et al. (1996), Kummerow et al. (1996), and Olson et al. (1996). While these methods are computationally efficient as they do not require iterative forward RTE calculations, their solutions are ultimately weighted combinations of the database profiles, and hence not independent from the simulation database.

In a sense, this is similar to the first-guess procedure of the optimization-based combined algorithm, which effectively assigns a weight of 1.0 to the single set of database profiles which provide the best match between measured and simulated TBs and Zs, and a weight of 0.0 to the rest. This suggests the possibility of a hybrid technique which could combine some of the advantages of both methods. The Bayesian method generates solution profiles with improved statistical properties when compared to any individual set of profiles from the database. Hence the solution profiles from

a Bayesian algorithm could provide an improved initial guess to an optimization-based retrieval algorithm, whereby the optimization process would improve the agreement between the measured and simulated quantities from that of the Bayesian first guess.

Another issue regarding combined retrieval addressed by this study is the determination of precipitation type. The precipitation type algorithm categorized observed rain events as either convective, stratiform, or unknown, based on the measured TB and Z signatures. The retrieved rainrate distributions, calculated separately for each category, were found to be consistent with distributions calculated from surface rain rate observations. Likewise the distribution of hydrometeor fall velocities by precipitation type, determined from coincident ARMAR Doppler velocities, also exhibited characteristics consistent with previous observations. As the vertical velocity field is the underlying dynamical factor governing precipitation growth, which is what fundamentally distinguishes between stratiform and convective precipitation and the associated heating structure, this result affirms the sound nature of the precipitation type scheme. Furthermore the analysis demonstrates the usefulness of Doppler velocities in diagnosing precipitation type, which suggests that the addition of a coherent radar to future satellite platforms could provide improvements to current techniques.

One final issue regards the usefulness of the basic approach of combined retrieval when compared to single-instrument retrievals. There currently exist a number of radar-only and PMW-only techniques to retrieve hydrometeor profiles and the corresponding surface rain rates, and while many perform well under certain conditions, each has specific limitations due to the physical nature of the measuring instrument. The vertical

resolution of TB-only retrievals are limited due to the fairly broad and extended weighting functions of the TB measurements, while the accuracy of the rain rate magnitudes from Z-only retrievals are limited by the sensitivity of the Zs to the assumptions regarding the particle size distributions and other microphysical properties of the backscattering hydrometeors.

This study has demonstrated that by combining both types of measurements within a unified retrieval framework, some of the problems specific to each type can be reduced. One example is that while PMW radiometer measurements respond well to the total integrated amount of hydrometeors within a precipitating column, they can be relatively insensitive to the vertical hydrometeor distribution under some circumstances. This leads to non-uniqueness problems in PMW-only retrievals, namely that different vertical hydrometeor distributions can lead to nearly equivalent TBs. In contrast, the reflectivities from a down-looking radar, by the very nature of their range-gated samples, provide better information on vertical structure.

It was demonstrated for several TOGA-COARE test cases that by incorporating TBs and Zs into a combined retrieval, the non-uniqueness problems inherent to TB-only retrievals can be reduced. Similarly it was shown that the magnitudes of the rainrates derived from Z-only retrievals, which are sensitive to microphysical assumptions, can be significantly impacted by the inclusion of TBs within a combined retrieval. These and other examples presented within this study demonstrate the fundamental improvement of combined retrieval, namely its synergistic ability to plumb the strengths of both the active-only and passive-only methods, while at the same time reducing their weaknesses.

176

REFERENCES

Adler, R.F., A.J. Negri, and I.M. Hakkarinen, 1991a: Rain estimation from combining geosynchronous IR and low-orbit microwave data. *Paleogeography, Paleoclimatology, Paleoecology (Global and Planetary Change Section)*, **90**, 87-92.

Adler, R.F, H.Y.M. Yeh, N. Prasad, W.K. Tao, and J. Simpson, 1991b: Microwave simulations of a tropical rainfall system with a three-dimensional cloud model. *J. Appl. Meteor.*, **30**, 924-953.

Adler, R.F., P.R. Keehn, and I.M. Hakkarinen, 1993: Estimation of monthly rainfall over Japan and surrounding waters from a combination of low-orbit microwave and geosynchronous IR data. *J. Appl. Meteor.*, **32**, 335-356.

Adler, R.F., G.J. Huffman, and P.R. Keehn, 1994: Global tropical rain estimates from microwave adjusted geosynchronous IR data. *Remote Sens. Rev.*, **11**, 125-152.

Alishouse, J.C., 1983: Total precipitable water and rainfall determinations from Seasat Scanning Multichannel Microwave Radiometer (SMMR). *J. Geophys.* Res., **88**, 1929-1935.

Arfken, G., 1970: *Mathematical methods for physicists*. Academic Press, New York, 815 pp..

Arkin, P.A., and B.N. Meisner, 1987: The relationship between large-scale convective rainfall and cold cloud cover over the Western hemisphere during 1982-1984. *Mon. Wea. Rev.*, **115**, 51-74.

Barrett, E.C., 1970: The estimation of monthly rainfall from satellite data. *Mon. Wea. Rev.*, **98**, 322-327.

Barrett, E.C., 1973: Forecasting daily rainfall from satellite data. *Mon. Wea. Rev.*, **101**, 215-222.

Battan, L.J., 1973: *Radar Observation of the Atmosphere*. University of Chicago Press, Chicago, 324 pp.

CalVal, 1989: DMSP Special Sensor Microwave/Imager Calibration/Validation. Final Report Volume I. CalVal Final Report Volume I. (J.P. Hollinger, ed.) Naval Research Laboratory, Washington, DC, 176 pp.

CalVal, 1991: DMSP Special Sensor Microwave/Imager Calibration/Validation. Final Report Volume II. CalVal Final Report Volume I. (J.P. Hollinger, ed.) Naval Research Laboratory, Washington, DC, 277 pp.

Churchill, D.D., and R.A. Houze, 1984: Development and structure of winter monsoon cloud clusters on 10 Dec 78. *J. Atmos. Sci..*, **41**, 933-960.

Cotton, W.R., M.A. Stephens, T. NehrKorn, and G.J. Tripoli, 1982: The Colorado State University three-dimensional cloud/mesoscale model. Part II: An ice phase parameterization. *J. Rech. Atmos.*, **16**, 295-320.

Durden, S.L., E. Im, F.K. Li, W. Ricketts, A. Tanner, and W. Wilson, 1994: ARMAR: an airborne rain-mapping radar. *J. Atmos. Oceanic Tech.*, **11**, 727-737.

Evans, K.F., J. Turk, T. Wong, and G.L. Stephens, 1995: A Bayesian approach to microwave precipitation profile retrieval. *J. Appl. Meteor.*, **34**, 260-279.

Fankhauser, J.C., I.R. Paluch, W.A. Cooper, D.W. Breed, and R.E. Rinehart, 1981: Air motion and thermodynamics. *Hailstorms of the Central Plains, Volume 1: The National Hail Research Experiment* (C.A. Knight and P. Squires, eds.), Colorado Assoc. Univ. Press, Boulder, CO, 95-149.

Farrar, M.R., E.A. Smith, and X. Xiang, 1994: The impact of spatial resolution enhancement of SSM/I microwave brightness temperatures on rainfall retrieval algorithms,. *J. Appl. Meteor.*, **33**, 313-333.

Farrar, M.R., E.A. Smith, and X. Xiang, 1996: Combined radar-radiometer precipitation retrieval for TRMM. Part II: The Retrieval Algorithm. Preprints, *Eighth Conf. on Satellite Meteor. and Ocean..*, [Jan 28-Feb2; Atlanta, GA], AMS, 259-260.

Flatau, P.J., G.J. Tripoli, J. Berlinder, and W.R. Cotton, 1989: The CSU-RAMS cloud microphysics module: General theory and code documentation. *Department of Atmospheric Sciences Report*, No. 451, Colorado State Univ., Ft Collins, CO, 88 pp.

Fujita, M., K. Okamoto, H. Masuko, T. Ojima, and N. Fugono, 1985a: Quantitative measurements of path-integrated rain rate by an airborne microwave radiometer over ocean. *J. Atmos. Oceanic Tech.,* **2**, 285-292.

Fujita, M., K. Okamoto, S. Yoshikado, and K. Nakamura, 1985b: Inference of rain rate profile and path-integrated rain rate by an airborne microwave rain scatterometer. *Radio Science,* **20**, 631-642.

Fujiwara, M., 1965: Raindrop-size distributions from individual storms. *J. Atmos. Sci..,* **22**, 585-591.

Gill, P.E., W. Murray, and M.H. Wright, 1981: *Practical Optimization.* Academic Press, London, 401 pp.

Gloersen, P., C.J. Cavalieri, A.T.C. Chang, T.T. Wilheit, W.J. Campbell, O.M. Johannessen, K.B. Katsaros, K.F. Kunzi, D.R. Ross, D. Staelin, E.P.L. Windsor, F.T. Barath, P. Gudmandsen, E. Langham, and R.O. Ramseier, 1984: A summary of results from the first Nimbus 7 SMMR observations. *J. Geophys. Res.,* **89**, 5335-5344.

Goldhirsch, J., 1983: Yearly variations of rain rate statistics at Wallops Island and their impact on modeled slant path attenuation distributions. *IEEE Trans. Geosci. Rem. Sens.,* **28**, 781-790.

Gumley, L.E., 1993: MODIS Airborne Simulator Level-1B data user's guide. NASA/Goddard Space Flight Center, 31 pp.

Haddad, Z.S., E.A. Smith, C. Kummerow, T. Iguchi, M.R. Farrar, and M. Alves, 1997: The TRMM 'Day-1' radar-radiometer combined rain-profiling algorithm. Submitted to *J. Meteor. Society of Japan.*

Haddad, Z.S., E. Im, S.L. Durden, and S. Hensley, 1996: Stochastic filtering of rain profiles using radar, surface-referenced radar, or combined radar-radiometer measurements. *J. Appl. Meteor.,* **35**, 229-242.

Hai, L., X. Miaoxin, W. Chong, H. Yaokui, and Z. Shouxiang, 1985: Ground-based remote sensing of LWC in cloud and rainfall by a combined dual-wavelength radar-radiometer system. *Adv. Atmos. Sciences,* **2**, 93-103.

Hinton, B.B., W.S. Olson, D.W. Martin, and B. Auvine, 1992: A passive microwave algorithm for tropical ocean rainfall. *J. Appl. Meteor.,* **31**, 1379-1395.

Hitschfeld, W., and J. Bordan, 1954: Errors inherent in the radar measurement of rainfall at attenuating wavelengths. *J. Meteor.,* **11**, 58-67.

Hollinger, J.P, J.L. Pierce, and G.A. Poe, 1990: SSM/I instrument evaluation. *IEEE Trans. Geosci. Rem. Sens.*, **GE-28**, 781-790.

Hong, Y., C.D. Kummerow and W.S. Olson, 1997: Separation of convective/ stratiform precipitation using microwave brightness temperatures. Preprints, *22nd Conf. on Hurricanes and Trop. Meteor.*, [May 19-23; Ft Collins, CO], AMS.

Houghton, H.G., 1968: On precipitation mechanisms and their artificial modification. *J. Appl. Meteor.*, **7**, 851-859.

Houze, R.A., 1993: *Cloud Dynamics*. Academic Press, San Diego, CA, 573 pp.

Houze, R.A., 1989: Observed structure of mesoscale convective systems and implications for large-scale heating. *Quart. J. Roy. Meteor. Soc.*, **115**, 425-461.

Iguchi, T., and R. Meneghini, 1994: Intercomparison of single-frequency methods for retrieving a vertical rain profile from airborne or spaceborne radar data. *J. Atmos. Oceanic Tech.*, **11**, 1507-1511.

Jung, H.J., 1980: The determination of rainfall rates from satellite measurements of the thermal microwave emission. *Contrib. Atmos. Phys.*, **53**, 366-388.

Kedem, B., L. Chiu, and G. North, 1990: Estimation of mean rain rates: applications to satellite observations. *J. Geophys. Res.*, **95**, 1965-1972.

Kozu, T., and K. Nakamura, 1991: Rainfall parameter estimation from dual-radar measurements combining reflectivity profile and path-integrated attenuation. *J. Atmos. Ocean. Tech.*, **8**, 259-270.

Kozu, T., K. Nakamura, R. Meneghini, and W.C. Boncyk, 1991: Dual-parameter radar rainfall measurement from space: A test result from an aircraft experiment. *IEEE Trans. Geosci. Rem. Sens.*, **29**, 584-592.

Kumagai, H., R. Meneghini, and T. Kozu, 1993: Preliminary results from multiparameter airborne rain radar measurement in the western Pacific. *J. Appl. Meteor.*, **32**, 431-440.

Kummerow, C., R.A. Mack, and I.M. Hakkarinen, 1989: A self-consistency approach to improve microwave rainfall rate estimation from space. *J. Appl. Meteor.*, **28**, 869-884.

Kummerow, C., and L. Giglio, 1994a: A passive microwave technique for estimating rainfall and vertical structure information from space. Part I: Algorithm description. *J. Appl. Meteor.*, **33**, 3-18.

Kummerow, C., and L. Giglio, 1994b: A passive microwave technique for estimating rainfall and vertical structure information from space. Part II: Applications to SSM/I data. *J. Appl. Meteor.*, **33**, 19-34.

Kummerow, C., and L. Giglio, 1995: A method for combining passive microwave and infrared rainfall observations. *J. Atmos. Ocean. Tech.*, **12**, 33-45.

Kummerow, C., W.S. Olson, and L. Giglio, 1996: A simplified scheme for obtaining precipitation and vertical hydrometeor profiles from passive microwave sensors. *IEEE Trans. Geosci. Rem. Sens.*, **34**, 1213-1232.

Lemone, M.A., and E.J. Zipser, 1980: Cumulonimbus vertical velocity events in GATE. Part I: Diameter, intensity, and mass flux. *J. Appl. Meteor.*, **37**, 2444-2457.

Lethbridge, M., 1967: Precipitation probability and satellite radiation data. *Mon. Wea. Rev.*, **95**, 487-490.

Liou, K.N., 1980: *An introduction to atmospheric radiation.* Academic Press, 392 pp.

Liu, G., and J.A. Curry, 1992: Retrieval of precipitation from satellite microwave measurements using both emission and scattering. *J. Geophys. Res.*, **97**, 9959-9974.

Lu, D., and L. Hai, 1980: Comparisons of radar and microwave radiometer in precipitation measurements and their combined use (in Chinese). *Acta Atmos. Sinica*, **1**, 30-39.

Lucas, C., E.J. Zipser and M.A. Lemone, 1994: Vertical velocity in oceanic convection off tropical Australia. *J. Atmos. Sci..*, **51**, 53183-3193.

Marshall, J.S., R.C. Langille, and W.M. Palmer, 1947: Measurement of rainfall by radar. *J. Meteorology*, **4**, 186-192.

Marshall, J.S., and W.M. Palmer, 1948: The distribution of raindrops with size. *J. Meteorology*, **5**, 165-166.

Marzano, F.S., A. Mugnai, E.A. Smith, X. Xiang, J.E. Turk, and J. Vivekanandan, 1994: Active and passive remote sensing of precipitation

storms during CaPE. Part II: Intercomparison of precipitation retrievals from AMPR radiometer and CP-2 radar. *Meteorol. Atmos. Phys.*, **54**, 29-52.

Marzoug, M., and P. Amayenc, 1991: Improved range profiling algorithm of rainfall rate from a spaceborne radar with path-integrated attenuation constraint. *IEEE Trans. Geosci. Rem. Sens.*, **29**, 584-592.

Meneghini, R.J., J. Eckerman, and D. Atlas, 1983: Determination of rain rate from a spaceborne radar technique. *IEEE Trans. Geosci. Rem Sens.*, **21**, 34-43.

Meneghini, R.J., A. Jones, and L.H. Gesell, 1987: Analysis of dual-wavelength surface reference radar technique. *IEEE Trans. Geosci. Rem Sens.*, **25**, 456-471.

Meneghini, R., K. Nakamura, C.W. Ulbrich, and D. Atlas, 1989: Experimental tests of methods for the measurement of rainfall rate using an airborne dual-wavelength radar. *J. Atmos. Oceanic Tech.*, **6**, 637-651.

Meneghini, R., and K. Nakamura, 1990: Range profiling of the rain rate by airborne weather radar. *Rem. Sens. Environ.*, **31**, 193-209.

Meneghini, R., T. Kozu, H. Kumagai, and W.C. Boncyk, 1992: A study of rain estimation methods from space using dual-wavelength radar measurements at near nadir incidence over ocean. *J. Atmos. Oceanic Tech.*, **9**, 364-382.

McGaughey, G., E.J. Zipser, R.W. Spenser, and R.E. Hood, 1996: High resolution passive microwave observations of convective systems over the tropical Pacific ocean. *J. Appl. Meteor.*, **35**, 1921-1947.

McGaughey, G., and E.J. Zipser, 1996: Passive microwave observations of the stratiform regions of two tropical oceanic mesoscale convective systems. *J. Appl. Meteor.*, **35**, 1949-1962.

Mohr, K. and E.J. Zipser, 1996: Mesoscale convective systems defined by their 85-GHz ice scattering signature: size and intensity comparison over tropical oceans and continents. *Mon. Wea. Rev.*, **124**, 2417-2437.

Mugnai, A., H.J. Cooper, E.A. Smith, and G.J. Tripoli, 1990: Simulation of microwave brightness temperatures of an evolving hail storm at SSM/I frequencies. *Bull. Amer. Meteor. Soc.*, **71**, 2-13.

Mugnai, A., E.A. Smith, and G.J. Tripoli, 1993: Foundations for statistical-physical precipitation retrieval from passive microwave satellite measurements. Part II: Emission source and generalized weighting function properties of a time dependent cloud-radiation model. *J. Appl. Meteor.*, **32**, 17-39.

Negri, A.J., R.F. Adler, and P.J. Wetzel, 1984: Satellite rain estimation: an analysis of the Griffith-Woodley technique. *J. Clim. Appl. Meteor.*, **26**, 1565-1576.

Okamoto, K., T. Ihara, T. Kozu, K. Nakamura, J. Awaka, and M. Fujita, 1991: Development status of the rain radar in the Tropical Rainfall Measuring Mission. Preprints, *25th Conf. on Radar Meteor.*, [June 24-28; Paris, France], AMS, 388-391.

Olson, W.S., 1989: Physical retrieval of rainfall rates over the ocean by multispectral microwave radiometry: Application to tropical cyclones. *J. Geophys. Res.*, **94**, 2267-2280.

Olson, W.S., C.D. Kummerow, G.M. Heymsfield, and L. Giglio, 1996: A method for combined passive-active microwave retrievals of cloud and precipitation profiles. *J.Appl. Meteor.*, **35**, 1763-1789.

Panegrossi, G., S. Dietrich, F.S. Marzano, A. Mugnai, E.A. Smith, X. Xiang, G.J. Tripoli, P.K. Wang, and J.P.V. Baptista, 1997: Use of cloud model microphysics for passive microwave-based precipitation retrieval: significance of consistency between model and measurement manifolds. *J. Atmos. Sci*, in press.

Prabhakara, C., D.A. Short, W. Wiscombe, R.S. Fraser, and B.E. Vollmer, 1986: Rainfall over oceans inferred from Nimbus 7 SMMR: application to 1982-1983 El Nino. *J. Clim. Appl. Meteor.*, **25**, 1464-1474.

Rinehart, R.E., 1991: *Radar for Meteorologists* Knight Printing Company, Fargo, ND, 334 pp.

Rodgers, E.B., H. Siddalingaiah, A.T.C. Chang, and T.T. Wilheit, 1979: A statistical technique for determining rainfall over land employing Nimbus 6 ESMR measurements. *J. Appl. Meteor.*, **18**, 978-991.

Schols, J.L., and J.A. Weinman, 1994: Retrieval of hydrometeor distributions over the ocean from airborne single-frequency radar and multi-frequency radiometric measurements. *Atmospheric Research*, **34**, 329-346.

Simpson, J., R.F. Adler, and G.R. North, 1988: A proposed tropical rainfall measuring mission (TRMM) satellite. *Bull. Amer. Meteor. Soc.*, **69**, 278-295.

Simpson, J., C. Kummerow, W.K. Tao, and R.F. Adler, 1996: On the tropical rainfall measuring mission (TRMM). *Meteor. Atmos. Phys.*, **60**, 19-36.

Smith, E.A., and A. Mugnai, 1988: Radiative transfer to space through a precipitating cloud at multiple microwave frequencies. Part II: Results and analysis. *J. Appl. Meteor.*, **27**, 1074-1091.

Smith, E.A., and A. Mugnai, 1989: Radiative transfer to space through a precipitating cloud at multiple microwave frequencies. Part III: Influence of large ice particles. *J. Meteor. Soc. Japan*, **67**, 739-755.

Smith, E.A., A. Mugnai, H.J. Cooper, G.J. Tripoli, and X. Xiang, 1992: Foundations for statistical - physical precipitation retrieval from passive microwave satellite measurements. Part I: Brightness temperature properties of a time dependent cloud - radiation model. *J. Appl. Meteor.*, **31**, 506-531.

Smith, E.A., X. Xiang, A. Mugnai, and G.J. Tripoli, 1994a: Design of an inversion-based precipitation profile retrieval algorithm using an explicit cloud model for initial guess microphysics. *Met. Atmos. Phys.*, **54**, 53-78.

Smith, E.A., X. Xiang, A. Mugnai, R.E. Hood, and R.W. Spencer, 1994b: Behavior of an inversion-based retrieval algorithm with high-resolution AMPR measurements including a low-frequency 10.7 GHz channel. *J. Atmos. Oceanic Tech.*, **11**, 858-873.

Smith, E.A., C. Kummerow, and A. Mugnai, 1994c: The emergence of inversion-type precipitation profile algorithms for estimation of precipitation from satellite microwave measurements. *Remote Sensing Reviews*, **11**, 211-242.

Smith, E.A., A. Mugnai, and G.J. Tripoli, 1994d: Theoretical foundations and verification of a multispectral, inversion-type microwave precipitation profile retrieval algorithm. *ESA/NASA Intnl Workshop.*, 599-621.

Smith, E.A., M. Farrar, X. Xiang, and J. Turk, 1995: Prospects for advanced radar-radiometer precipitation retrieval algorithms during the TRMM era. Conference Proceedings, Second Combined Optical-Microwave Earth and Atmosphere Sensing Symposium [April 3-6, Atlanta, GA], IEEE/LEOS, ISBN 0-7803-2402-1, Piscataway, NJ, 177.

Smith, E.A., J. Turk, M. Farrar, A. Mugnai, and X. Xiang, 1997a: Estimating 13.8 GHz path integrated attenuation from 10.7 GHz brightness temperatures for TRMM combined PR-TMI precipitation algorithm *J. Appl. Meteor.*, **36**, 365-388.

Smith, E.A., X. Xiang, and M.R. Farrar, 1997b: Combined radar-radiometer precipitation retrieval for TRMM. Part I: A unified RTE model for active and passive radiative transfer calculations. To be submitted to *J. Appl. Meteor.*

Spencer, R.W., H.M. Goodman, and R.E. Hood, 1989: Precipitation retrieval over land and ocean with the SSM/I. Part I: Identification and characteristics of the scattering signature. *J. Atmos. Oceanic Tech.*, **6**, 254-273.

Spencer, R.W., R.E. Hood, F.J. LaFontaine, E.A. Smith, R. Platt, J. Galliano, V.L. Griffith, and E. Lobl, 1994: High resolution imaging of rain systems with the Advanced Microwave Precipitation Radiometer. *J. Atmos. Oceanic Tech.*, **11**, 849-857.

Steiner, M., R.A. Houze, and S.E. Yuter, 1995: Climatological characterization of three-dimensional storm structure from operational radar and rain gauge data. *J. Appl. Meteor.*, **34**, 1978-2007.

Strang, G., 1970: *Linear algebra and its applications.* Harcourt Brace Jovanovich, Orlando, FL, 505 pp..

Stout, G.E. and E.A. Mueller, 1968: Survey of relationships between rainfall rate and radar reflectivity in the measurement of precipitation. *J. Appl. Meteor.*, **7**, 465-474.

Tao, W.-K., S. Lang, J. Simpson, and R. Adler, 1993: Retrieval algorithms for estimating the vertical profiles of latent heat release: their applications for TRMM. *J. Meteor. Soc. Japan*, **71**, 685-700.

Tripoli, G.J., and W.R. Cotton, 1982: The Colorado State University three-dimensional cloud/mesoscale model. Part I: General theoretical framework and sensitivity experiments. *J. Rech. Atmos.*, **16**, 185-200.

Tripoli, G.J., 1992a: A non-hydrostatic model designed to simulate scale interaction. *Mon. Wea. Rev.*, **120**, 1342-1359.

Tripoli, G.J., 1992b: An explicit three-dimensional non-hydrostatic numerical simulation of a tropical cyclone. *Met. Atmos. Phys.*, **49**, 229-254.

185

Turk, J., J. Vivekanandan, F.S. Marzano, R.E. Hood, R.W. Spencer, and F.J. LaFontaine, 1994: Active and passive microwave remote sensing of precipitating storms during CaPE. Part I: Advanced Microwave Precipitation Radiometer and polarimetric radar measurements and models. *Meteor. Atmos. Phys.*, **54**, 3-27.

Vivekanandan, J., J. Turk, and V.N. Bringi, 1993: Advanced Microwave Precipitation Radiometer (AMPR) and multiparameter radar comparisons of precipitation. *IEEE Trans. Geosci. Rem. Sens.*, **31**, 860-870.

Webster, P.J., and R. Lukas, 1992. TOGA COARE: The Coupled Ocean-Atmosphere Response Experiment. *Bull. Amer. Meteor. Soc.*, **73**, 1377-1416.

Weinman, J.A., and P.J. Guetter, 1977: Determination of rainfall distributions from microwave radiation measured by Nimbus 6 ESMR. *J. Appl. Meteor.*, **16**, 437-442.

Weinman, J.A., R. Meneghini, and K. Nakamura, 1990: Retrieval of precipitation profiles from airborne radar and passive radiometer measurements: Comparison with dual-frequency radar measurements. *J. Appl. Meteor.*, **29**, 981-993.

Wexler, R, 1947: Radar detection of a frontal storm 18 June 1946. *J. Meteorology*, **4**, 38-44.

Wexler, R, 1948: Rain intensities by radar. *J. Meteorology*, **5**, 171-173.

Wexler, R. and D. Atlas, 1963: Radar reflectivity and attenuation of rain. *J. Appl. Meteor.*, **2**, 276-280.

Wilheit, T.T., A.T.C. Chang, M.S.V. Rao, E.B. Rodgers, and J.S. Theon, 1977: A satellite technique for quantitatively mapping rainfall rates over the oceans. *J. Appl. Meteor.*, **16**, 551-560.

Wilheit, T.T., 1986: Some comments on passive microwave measurements of rain. *Bull. Amer. Meteor. Soc.*, **67**, 1226-1232.

Wilheit, T., R. Adler, S. Avery, E. Barrett, P. Bauer, W. Berg, A. Chang, J. Ferriday, N. Grody, S. Goodman, C. Kidd, D. Kniveton, C. Kummerow, A. Mugnai, W. Olson, G. Petty, A. Shibata, E. Smith, and R. Spencer, 1994: Algorithms for the retrieval of rainfall from passive microwave measurements. *Remote Sensing Rev.*, **11**, 163-194.

Wu, R., and J.A. Weinman, 1984: Microwave radiances from precipitating clouds containing aspherical ice, combined phase, and liquid hydrometeors. *J. Geophys.* Res., **89**, 7170-7178.

Xiang, X., E.A. Smith, and C.G. Justus, 1994: A rapid radiative transfer model for reflection of solar radiation. *J. Atmos. Sci.*, **51**, 1978-1988.

Yang, S. and E.A. Smith, 1997: Moisture budget analysis of TOGA-COARE IFA using SSM/I retrieved latent heating and large scale Q2 estimates. Submitted to *J. Atmos. Sci.*

Yuter, S.A. and R.A. Houze, 1995a: Three-dimensional kinematic and microphysical evolution of Florida cumulonimbus. Part I: Spatial distribution of updrafts, downdrafts, and precipitation. *Mon. Wea. Rev.*, **124**, 1921-1940.

Yuter, S.A. and R.A. Houze, 1995b: Three-dimensional kinematic and microphysical evolution of Florida cumulonimbus. Part II: Frequency distributions of vertical velocity, reflectivity, and differential refelectivity. *Mon. Wea. Rev.*, **124**, 1941-1963.

Yuter, S.A. and R.A. Houze, 1995c: Three-dimensional kinematic and microphysical evolution of Florida cumulonimbus. Part III: Vertical mass transport, mass divergence, and synthesis. *Mon. Wea. Rev.*, **124**, 1964-1983.

Zipser, E.J., and M.A. Lemone, 1980: Cumulonimbus vertical velocity events in GATE. Part II: Synthesis and model core structure. *J. Appl. Meteor.*, **37**, 2458-2469.

BIOGRAPHICAL SKETCH

Michael Ray Farrar

Background and experience:

Michael Ray Farrar ███████████████████████████████████,
the son of James ████████ Carolyn ████████████ After graduation from
Purdue University in 1986, Michael was commissioned as a Second
Lieutenant in the U.S. Air Force, where he has served as a weather officer
until the present.

In addition to the locations Michael has attended school (see Education
below), he has been assigned to Headquarters U.S. Air Forces in Europe
(Ramstein Air Base, Germany), Headquarters Strategic Air Command and Air
Force Global Weather Center (Offutt Air Force Base, Nebraska), and to Riyadh
Air Base, Saudi Arabia. After completion of his Ph. D., Michael was assigned
at the Weather Flight Commander at Kunsan Air Base, South Korea.

Michael was married to the former Tammy Jane Violka of South Bound
Brook, New Jersey, on August 12, 1989. Michael and Tammy have two sons,
Nicholas Raymond ████████████████████████ and Jacob Francis ████
██████████

Education:

Ph. D., Meteorology, Florida State University, 1997.
M. S., Meteorology, Florida State University, 1991.
B. S., Meteorology, Pennsylvania State University, 1987.
B. S., Physics, Purdue University, 1986.

Publications (Peer-reviewed Journals):

Farrar, M.R., E.A. Smith and X. Xiang, 1997: Combined radar-radiometer
precipitation retrieval for TRMM. Part II: Applications with ARMAR-
AMPR measurements from TOGA COARE. To be submitted to *J. Appl.
Meteor.*

Farrar, M.R., E.A. Smith, and X. Xiang, 1994: The impact of spatial resolution enhancement of SSM/I microwave brightness temperatures on rainfall retrieval algorithms,. *J. Appl. Meteor.*, **33**, 313-333.

Farrar, M.R., and E.A. Smith, 1992: Spatial resolution enhancement of terrestrial features using deconvolved SSM/I microwave brightness temperatures. *IEEE Trans. Geosci. Rem. Sens.*, **30**, 349-355.

Haddad, Z.S., E.A. Smith, C. Kummerow, T. Iguchi, M.R. Farrar, and M. Alves, 1997: The TRMM 'Day-1' radar-radiometer combined rain-profiling algorithm. Submitted to *J. Meteor. Society of Japan*.

Smith, E.A., J. Turk, M. Farrar, A. Mugnai, and X. Xiang, 1997a: Estimating 13.8 GHz path integrated attenuation from 10.7 GHz brightness temperatures for TRMM combined PR-TMI precipitation algorithm *J. Appl. Meteor.*, **36**, 365-388.

Smith, E.A., X. Xiang, and M.R. Farrar, 1997b: Combined radar-radiometer precipitation retrieval for TRMM. Part I: A unified RTE model for active and passive radiative transfer calculations. To be submitted to *J. Appl. Meteor.*

Publications (Scientific Conference Proceedings):

Farrar, M.R., E.A. Smith, and X. Xiang, 1996: Combined radar-radiometer precipitation retrieval for TRMM. Part II: The Retrieval Algorithm. Preprints, *Eighth Conf. on Satellite Meteor. and Ocean..*, [Jan 28-Feb 2; Atlanta, GA], Amer. Meteor. Soc., Boston, MA, 259-260.

Farrar, M.R., and E.A. Smith, 1992: Impact of SSM/I resolution enhancement on satellite rainfall estimation from tropical storms. Preprints, *Sixth Conf. on Satellite Meteor. and Ocean..*, [Jan 5-10; Atlanta, GA], Amer. Meteor. Soc., Boston, MA, 276-279.

Farrar, M.R., and E.A. Smith, 1991: Impact of resolution enhancement of SSM/I microwave brightness temperatures on satellite estimation of rainfall from Super Typhoon Thelma. Preprints, *19th Conf. on Hurricanes and Tropical Meteor.*, [May 6-10; Miami, FL], Amer. Meteor. Soc., Boston, MA, 396-399.

Smith, E.A., M. Farrar, and X. Xiang, 1997: The use of a unified active-passive radiative transfer model to reduce ambiguities in physical inversion of precipitation profiles. Presentation, *9th Conf. on Atmos. Radiation*, [Feb 2-7; Long Beach, CA], Amer. Meteor. Soc., Boston, MA.

189

Smith, E.A., M. Farrar, and X. Xiang, 1995: An emerging satellite microwave technology for tropical rainfall measurement. Presentation, *21st Conf. on Hurricanes and Tropical Meteor.*, [Apr 24-28; Miami, FL], Amer. Meteor. Soc., Boston, MA.

Smith, E.A., M. Farrar, X. Xiang, and J. Turk, 1995: Prospects for advanced radar-radiometer precipitation retrieval algorithms during the TRMM era. Conference Proceedings, Second Combined Optical-Microwave Earth and Atmosphere Sensing Symposium [April 3-6, Atlanta, GA], IEEE/LEOS, ISBN 0-7803-2402-1, Piscataway, NJ, 177.

Smith, E.A., M.R. Farrar, and A. Mugnai, 1991: Spatial enhancement of 19 & 37 GHz SSM/I brightness temperatures. Presentation, *WetNet Science and Analysis Colloquium* , [Feb 19-22; Santa Barbara, CA].

Turk, J., F.S. Marzano, E.A. Smith, M.R. Farrar, and A. Mugnai, 1995: Radar and radiometric measurements from TOGA-COARE: Application to a combined TRMM rainfall algorithm. Preprints, *27th Conference on Radar Meteorology* [Oct. 9-13; Vail, CO], Amer. Meteor. Soc., Boston, MA, 786-788.

Turk, J., M. Farrar, E.A. Smith, and F.S. Marzano, 1995: Measurements and implications for combined radar-passive microwave rainfall profiling techniques. Conference Proceedings, Second Combined Optical-Microwave Earth and Atmosphere Sensing Symposium [April 3-6, Atlanta, GA], IEEE/LEOS, ISBN 0-7803-2402-1, Piscataway, NJ, 183-185.

Xiang, X., M.R. Farrar, and E.A. Smith, 1996: Combined radar-radiometer precipitation retrieval for TRMM. Part I: A unified RTE model for active and passive radiative transfer calculations. Preprints, Vol., *Eighth Conf. on Satellite Meteor. and Ocean..*, [Jan. 28-Feb. 2; Atlanta, GA], Amer. Meteor. Soc., Boston, MA, p. 266-267.